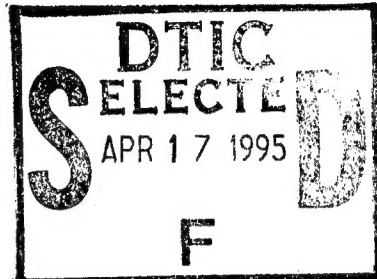


**MATERIALS FOR ADAPTIVE STRUCTURAL
ACOUSTIC CONTROL**

Period February 1, 1994 to January 31, 1995

Annual Report

VOLUME II



OFFICE OF NAVAL RESEARCH
Contract No.: N00014-92-J-1510

APPROVED FOR PUBLIC RELEASE — DISTRIBUTION UNLIMITED

Reproduction in whole or in part is permitted
for any purpose of the United States Government

L. Eric Cross

19950417 070

PENNSTATE



DTIC QUALITY INSPECTED 6

**THE MATERIALS RESEARCH LABORATORY
UNIVERSITY PARK, PA**

REPORT DOCUMENTATION PAGE

Form Approved
OMB No. 0704-0188

Public reporting burden for this collection of information is estimated to average 1 hour per response, including the time for reviewing instructions, searching existing data sources, gathering and maintaining the data needed, and completing and reviewing the collection of information. Send comments regarding this burden estimate or any other aspect of this collection of information, including suggestions for reducing this burden, to Washington Headquarters Services, Directorate for Information Operations and Reports, 1215 Jefferson Davis Highway, Suite 1204, Arlington, VA 22202-4302, and to the Office of Management and Budget, Paperwork Reduction Project (0704-0188), Washington, DC 20503.

1. AGENCY USE ONLY (Leave blank)	2. REPORT DATE	3. REPORT TYPE AND DATES COVERED	
	4/6/95	ANNUAL REPORT 02/1/94 TO 01/31/95	
4. TITLE AND SUBTITLE		5. FUNDING NUMBERS	
MATERIALS FOR ADAPTIVE STRUCTURAL ACOUSTIC CONTROL			
6. AUTHOR(S)			
L. ERIC CROSS			
7. PERFORMING ORGANIZATION NAME(S) AND ADDRESS(ES)		8. PERFORMING ORGANIZATION REPORT NUMBER	
MATERIALS RESEARCH LABORATORY THE PENNSYLVANIA STATE UNIVERSITY UNIVERSITY PARK, PA 16802			
9. SPONSORING/MONITORING AGENCY NAME(S) AND ADDRESS(ES)		10. SPONSORING/MONITORING AGENCY REPORT NUMBER	
OFFICE OF NAVAL RESARCH GERALD T. SMITH CODE 1513:NRJ OFFICE OF NAVAL RESARCH RES. REP. 800 NORTH QUINCY STREET 536 SOUTH CLARK STREET, RM 286 ARLINGTON, VA 22217 CHICAGO, ILLINOIS 60606-1588			
11. SUPPLEMENTARY NOTES			
12a. DISTRIBUTION/AVAILABILITY STATEMENT		12b. DISTRIBUTION CODE	
13. ABSTRACT (Maximum 200 words)			
SEE FOLLOWING TWO PAGES			
14. SUBJECT TERMS			15. NUMBER OF PAGES
			16. PRICE CODE
17. SECURITY CLASSIFICATION OF REPORT	18. SECURITY CLASSIFICATION OF THIS PAGE	19. SECURITY CLASSIFICATION OF ABSTRACT	20. LIMITATION OF ABSTRACT

GENERAL INSTRUCTIONS FOR COMPLETING SF 298

The Report Documentation Page (RDP) is used in announcing and cataloging reports. It is important that this information be consistent with the rest of the report, particularly the cover and title page. Instructions for filling in each block of the form follow. It is important to *stay within the lines* to meet *optical scanning requirements*.

Block 1. Agency Use Only (Leave blank).

Block 2. Report Date. Full publication date including day, month, and year, if available (e.g. 1 Jan 88). Must cite at least the year.

Block 3. Type of Report and Dates Covered.

State whether report is interim, final, etc. If applicable, enter inclusive report dates (e.g. 10 Jun 87 - 30 Jun 88).

Block 4. Title and Subtitle. A title is taken from the part of the report that provides the most meaningful and complete information. When a report is prepared in more than one volume, repeat the primary title, add volume number, and include subtitle for the specific volume. On classified documents enter the title classification in parentheses.

Block 5. Funding Numbers. To include contract and grant numbers; may include program element number(s), project number(s), task number(s), and work unit number(s). Use the following labels:

C - Contract	PR - Project
G - Grant	TA - Task
PE - Program Element	WU - Work Unit
	Accession No.

Block 6. Author(s). Name(s) of person(s) responsible for writing the report, performing the research, or credited with the content of the report. If editor or compiler, this should follow the name(s).

Block 7. Performing Organization Name(s) and Address(es). Self-explanatory.

Block 8. Performing Organization Report Number. Enter the unique alphanumeric report number(s) assigned by the organization performing the report.

Block 9. Sponsoring/Monitoring Agency Name(s) and Address(es). Self-explanatory.

Block 10. Sponsoring/Monitoring Agency Report Number. (If known)

Block 11. Supplementary Notes. Enter information not included elsewhere such as: Prepared in cooperation with...; Trans. of...; To be published in.... When a report is revised, include a statement whether the new report supersedes or supplements the older report.

Block 12a. Distribution/Availability Statement.

Denotes public availability or limitations. Cite any availability to the public. Enter additional limitations or special markings in all capitals (e.g. NOFORN, REL, ITAR).

DOD - See DoDD 5230.24, "Distribution Statements on Technical Documents."

DOE - See authorities.

NASA - See Handbook NHB 2200.2.

NTIS - Leave blank.

Block 12b. Distribution Code.

DOD - Leave blank.

DOE - Enter DOE distribution categories from the Standard Distribution for Unclassified Scientific and Technical Reports.

NASA - Leave blank.

NTIS - Leave blank.

Block 13. Abstract. Include a brief (*Maximum 200 words*) factual summary of the most significant information contained in the report.

Block 14. Subject Terms. Keywords or phrases identifying major subjects in the report.

Block 15. Number of Pages. Enter the total number of pages.

Block 16. Price Code. Enter appropriate price code (*NTIS only*).

Blocks 17. - 19. Security Classifications. Self-explanatory. Enter U.S. Security Classification in accordance with U.S. Security Regulations (i.e., UNCLASSIFIED). If form contains classified information, stamp classification on the top and bottom of the page.

Block 20. Limitation of Abstract. This block must be completed to assign a limitation to the abstract. Enter either UL (unlimited) or SAR (same as report). An entry in this block is necessary if the abstract is to be limited. If blank, the abstract is assumed to be unlimited.

ABSTRACT

The objectives of this ONR sponsored University Research Initiative (URI) entitled "Materials for Adaptive Structural Acoustic Control" concern both basic fundamental studies and highly applied development of the piezoelectric and electrostrictive ferroelectric ceramics which carry both the sensing and actuation functions for adaptive control. The report documents work over the third year of this five year program. For convenience and continuity, the activities are grouped under the headings" General Summary Papers, Materials Studies, Composite Sensors, Actuator Studies, Integration Issues, Processing Studies, Thin Film Ferroelectrics, and the Abstracts of graduating students on the program.

The first general papers illustrate the educational role undertaken by MRL faculty both in the basic understanding of ferroics, and in the philosophy of their application in 'smart' systems. It is interesting that through work pioneered on earlier ONR programs in MRL, it is now possible to measure both direct and converse electrostrictive response in simple solids, and to thus explore models to explain the signs and magnitudes of these striction constants. The relaxor ferroelectrics have been a topic of study for more than 30 years in the laboratory, but recent breakthroughs have revolutionized the level of understanding and opened a vista for further potential application of size (scale) effects in ferroics. Electrical control of shape memory has been achieved in a number of electro-ferroic solids, but full exploitation will need more complete understanding of both ferroelectric and ferroelastic:ferroelectric domain wall processes. Photostriction, the combination of photovoltaic and piezoelectric effects in ceramics promises an interesting range of new device possibilities.

In material studies, the elegant work on lanthanum modified lead titanate has now been fully written up, and the vital role of strain coupling in the onset of diffuse response underscored. New experimental methods have been applied to separating and measuring intrinsic and extrinsic components of response in PZT ceramics and to the measurement of microwave properties in these high K systems. Soft, intermediate, and hard modified lead zirconate and PZT composition have been under study for new and more interesting morphotropic phase boundaries which could be fabricated in single crystal form. Both optical birefringence and Raman studies are being used to explore domain and phase changes.

In sensing studies, the focus has been maintained upon flexensional (Moonie) structures and the enhanced performance which new end cap designs are affording. The polyvinylidene fluoride/trifluoethylene piezoelectrics are themselves an interesting composite system where the lower symmetry demands more complete characterization. The 1:3 rod and tube type composites have many performance advantages and trade-offs which will ensure wider scale application now that economical assembly techniques are at hand.

For actuation, the flexextensional (Moonie) offers a number of advantages which merit further study. Both material and multilayer device related fatigue and destruction mechanisms are under study, and modes to control and alleviate microcracking and space change degradation are examined. More detailed studies of the photostriction effects and their control by doping effects in PZTs have also been accomplished.

Integration studies have continued to explore the components which must be co-processed in the smart material or adaptive assemblage. Examples are the thick film conductors in copper or silver/palladium, the 0:3 high density piezoelectric polymer composites and the filter functions required to eliminate cross talk in the wiring system.

Processing studies are essential to the fabrication of the very wide range of materials demanded by all elements of the program. Relaxor materials have formed the focus for many processing activities but more recently the needs for high strain actuation are refocusing interest on phase switching antiferroelectric:ferroelectric compositions in the high lead zirconate PLZTs and PSnZTs with mounting evidence for multiple ferroelectric phases appearing under high fields.

Thin film papers have been selected from the extensive work in MRL on ferroelectric films because of their relevance to transduction in piezoelectric or phase switching compositions.

MATERIALS FOR ADAPTIVE STRUCTURAL ACOUSTIC CONTROL

Period February 1, 1994 to January 31, 1995

Annual Report

VOLUME II

OFFICE OF NAVAL RESEARCH
Contract No.: N00014-92-J-1510

APPROVED FOR PUBLIC RELEASE — DISTRIBUTION UNLIMITED

Reproduction in whole or in part is permitted
for any purpose of the United States Government

L. Eric Cross

Accession For	
NTIS	CRA&I
DTIC	TAB
Unannounced	
Justification	
By	
Distribution /	
Availability Codes	
Dist	Avail and/or Special
A-1	

PENNSTATE



**THE MATERIALS RESEARCH LABORATORY
UNIVERSITY PARK, PA**

TABLE OF CONTENTS

ABSTRACT	8
INTRODUCTION	9
1.0 GENERAL SUMMARY PAPERS	12
2.0 MATERIALS STUDIES	12
3.0 COMPOSITE SENSORS	14
4.0 ACTUATORS STUDIES	14
5.0 INTEGRATION ISSUES	15
6.0 PROCESSING STUDIES	15
7.0 THIN FILM FERROELECTRICS	16
8.0 GRADUATING STUDENTS IN THE PROGRAM	16
9.0 HONORS AND AWARDS	17
10.0 APPRENTICE PROGRAM	17
11.0 PAPERS PUBLISHED IN REFEREED JOURNALS	18
12.0 INVITED PAPERS PRESENTATIONS AT NATIONAL AND INTERNATIONAL MEETINGS	21
13.0 INVITED PAPERS PRESENTED AT UNIVERSITY, INDUSTRY AND GOVERNMENT LABORATORIES	24
14.0 CONTRIBUTED PAPERS AT NATIONAL AND INTERNATIONAL MEETINGS	26
15.0 BOOKS (AND SECTIONS THEREOF)	33

APPENDICES

VOLUME I

General Summary Papers

1. Newnham, R.E., S. Trolier-McKinstry and J.R. Giniewicz, "Piezoelectric, Ferroelectric and Ferroic Crystals, *J. Mater. Educ.* **15**, 189-223 (1993).
2. Newnham R.E., "Electroceramics in the 1990s and Beyond, *Euroceramics II*, Vol. 3, Deutsche Keramische Gesellschaft Köln, Germany, 1771-1782 (1994).
3. Newnham, R.E. and V. Sundar, "Anisotropy in Electrostriction and Elasticity," *J. Mat. Sci. Lett.* **13**, 799-801, Chapman and Hall, London, England (1994).

General Summary Papers (continued) –Volume I

4. Cross, L.E., "Relaxor Ferroelectrics: An Overview," *Ferroelectrics* **151**, 305-320 (1994).
5. Cross, L.E., Boundary Conditions for Shape Memory in Ceramic Material Systems, *J. Intelligent Material Systems on Structures* **6**, 55 (1994).
6. Uchino, K. and S.Y. Chu, "Photostriction and Its Applications," Proc. Amer. Ceram. Soc. Pac. Rim Conf., *Ferroic Materials*, 287-293 (1994).
7. Kumar, S., A.S. Bhalla and L.E. Cross, "Smart Ceramics for Broadband Vibration Control," *J. Intelligent Materials Systems and Structures* **5**(5), 673 (1994).
8. Kumar, S., A.S. Bhalla and L.E. Cross, "Smart Ferroelectrics for Acoustic and Vibration Control," *J. Intelligent Materials Systems and Structures* **5**(5), 678 (1994).

Materials Studies

9. Rossetti, G., L.E. Cross and J.P. Cline, "Structural Aspects of the Ferroelectric Phase Transition in Lanthanum-Substituted Lead Titanate," *J. of Mat. Sci.* **30**(1), 24-34 (1995).
10. Rossetti, G.A., Jr., M.A. Rodriguez, A. Navrotsky, L.E. Cross and R.E. Newnham, "Structure of the Defect Perovskite $[Pb_{0.85}La_{0.10}]TiO_3$ between 10 and 1023K," *J. Appl. Phys.* **77**(4), 1683 (1994).
11. Zhang, Q.M., H. Wang, N. Kim and L.E. Cross, "Direct Evaluation of Domain-Wall and Intrinsic Contributions to the Dielectric and Piezoelectric Response and Their Temperature Dependence on Lead Zirconate-Titanate Ceramics," *J. Appl. Phys.* **75**(1), 454-9 (1994).
12. Li, Shaoping, A.S. Bhalla, R.E. Newnham, L.E. Cross and C.-Y. Huang, "90° Domain Reversal in $Pb(Zr_xTi_{1-x})O_3$ Ceramics," *J. Mater. Sci.* **29**(5), 1290-4 (1994).
13. Li, S., J. Sheen, S.-J. Jang, A.S. Bhalla, R.E. Newnham and L.E. Cross, "Modified Lumped Parameter Method for Measurements of Dielectric Susceptibility in Ferroelectrics," *Jpn. J. Appl. Phys.*, Part 1 **33**(6A), 3617-21 (1994).
14. Troilo, L.M., D. Damjanovic and R.E. Newnham, "Modified Lead Titanate Ceramics with a Relatively Large Dielectric Constant for Hydrophone Applications," *J. Am. Cer. Soc.* **77**(3), 857-59 (March 1994).
15. Subbarao, E.C., V. Srikanth, W. Cao and L.E. Cross, "Domain Switching and Microcracking During Poling of Lead Zirconate Titanate Ceramics," *Ferroelectrics* **145**, 771-781 (1993).
16. Jiang, Q.Y., E.C. Subbarao and L.E. Cross, "Dielectric Properties of Single Grain in PLZT Ferroelectric Ceramics," *Ferroelectrics Lett.* **17**, 41-46 (1994).

Materials Studies (continued) –Volume I

17. Wang, J.F., J. Gineiwicz and A.S. Bhalla, "Soft Piezoelectric $(1-x)Pb(Sc_{0.5}Ta_{0.5})O_3-xPbTiO_3$ Ceramics with High Coupling Factors and Low Q_m ," *Ferroelectrics Lett.* **16**, 113-118 (1993).
18. Alberta, E.F., A.S. Bhalla and T. Takenaka, "The Complex Piezoelectric, Elastic, and Dielectric Coefficients for a Lead Zirconate-Based Ceramic Under Electrical Bias," *Ferroelectrics* **154**, 11 (1994).

VOLUME II

19. Alberta, E.F., A.S. Bhalla and T. Takenaka, "The Piezoelectric, Elastic and Dielectric Constants for Ceramics in the Solid Solution $(x)PbZrO_3-(1-x-z)PbZn_{1/3}Nb_{2/3}O_3 - (z) PbTiO_3$," *Ferroelectrics* (in press).
20. Alberta, E.F and A.S. Bhalla, "An Evaluation of Lead-Zirconate Based Ceramics For Use In Non-Volatile Ferroelectric Memory Devices," *Proceedings of the 9th Annual International Symposium on the Applications of Ferroelectrics* (1994).
21. Alberta, E.F. and A.S. Bhalla, "Dielectric and Piezoelectric Properties of Ceramics in the Lead Indium Niobate Lead Scandium Tantalate Solid Solution System," *Proceedings of the 9th Annual International Symposium on the Applications of Ferroelectrics* (1994).
22. Jin, B.-M., A.S. Bhalla, J.-B. Kim and J.-N. Kim, "Dielectric Response of $Li_{0.4}K_{0.6}NbO_3$ Crystal in the Frequency Domain," *J. Mat. Sci. Mat. Electronics* **4**, 225-228 (1993).
23. Jin, B.-M., A.S. Bhalla, B.-C. Choi and J.-N. Kim, "Dielectric Anomalies in $Li_{0.4}K_{0.6}NbO_3$ Crystals," *Physica Sta. Solidi.* **140**, 239-245 (1993).
24. Oh, K.Y., K. Uchino and L.E. Cross, "Optical Study of Domains in $Ba(Ti,Sn)O_3$ Ceramics," *J. Amer. Ceram. Soc.* **77**(11), 2809-16 (1994).
25. Idink, H., V. Srikanth, W.B. White and E.C. Subbarao, "Raman Study of Low Temperature Phase Transitions in Bismuth Titanate, $Bi_4Ti_3O_{12}$," *J. Appl. Phys.* **76**(3), 1819-1823 (1994).

Composite Sensors

26. Newnham, R.E. and K.A. Markowski, "Composite Sensors and Actuators," Submitted for Proceedings of the Japan-U.S. Workshop on Functional Fronts in Advanced Ceramics, Tsukuba, Japan, December 6-8, 1994.
27. Dogan, A., S. Yoshikawa, K. Uchino and R.E. Newnham, "The Effect of Geometry on the Characteristics of the Moonie Transducer and Reliability Issues," *Proceedings of the IEEE Ultrasonics Symposium* **2**, 935-939 (1994).
28. Xu, Q.C., A. Dogan, J. Tressler, S. Yoshikawa and R.E. Newnham, "Ceramic-Metal Composite Actuator," *Ferroelectrics Special Issue on Piezoelectric and Electrostrictive Actuators* **160** (1994).

Composite Sensors (continued) –Volume II

29. Onitsuka, K., A. Dogan, Q.C. Xu, S. Yoshikawa and R.E. Newnham, "Design Optimization for Metal-Ceramic Composite Actuator, 'Moonie,'" *Ferroelectrics* **156**, 37-42 (1994).
30. Tressler, J.F., Q.C. Xu, S. Yoshikawa, K. Uchino and R.E. Newnham, "Composite Flextensional Transducers of Sensing and Actuation," *Ferroelectrics* **156**, 67-72 (August 1994).
31. Meyer, R., H. Weitzing, Q.C. Xu, Q.M. Zhang, R.E. Newnham and J.K. Cochran, "Lead Zirconate Hollow-Sphere Transducers," *J. Am. Ceram. Soc.* **77**(6), 1669-72 (1994).
32. Wang, H., Q.M. Zhang, L.E. Cross and A.O. Sykes, "Piezoelectric, Dielectric, and Elastic Properties of Poly (Vinylidene Fluoride/Trifluoroethylene)," *J. Appl. Phys.* **74**(5), 3394-3398 (1993).
33. Wang, H., Q.M. Zhang and L.E. Cross, "Piezoelectric Relaxation of P(VDF-TrFE) Copolymer," *Ferroelectrics* **159**, 218-286 (1994).
34. Zhang, Q.M., W. Cao, H. Wang and L.E. Cross., "Characterization of the Performance of 1-3 Type Piezocomposites for Low-Frequency Applications," *J. Appl. Phys.* **73**(3), 1403-1410 (1993).
35. Zhang, Q.M., H. Wang and L.E. Cross, "Piezoelectric Tubes and 1-3 Tubular Composites as Tunable Actuators and Sensors," *Proc. SPIE-Int. Soc. Opt. Eng.* (1993), 1916 (Smart Materials), 244-54.
36. Zhang, Q.M., H. Wang and L.E. Cross, "Piezoelectric Tubes and Tubular Composites for Actuator and Sensor Applications," *J. Mater. Sci.* **28**(14), 3962-3968 (1993).

Actuator Studies

37. Newnham, R.E., A. Dogan, Q.C. Xu and S. Yoshikawa, "Flextensional 'Moonie' Actuators," *IEEE 1993 Ultrasonics Symposium Proc.*, Baltimore, Maryland, Vol. 1, 509-514 (Oct. 31-Nov. 3, 1993).
38. Dogan, A., Q. Xu, K. Onitsuka, S. Yoshikawa, K. Uchino and R.E. Newnham, "High Displacement Ceramic Metal Composite Actuators (Moonies)," *Ferroelectrics* **156**, 1 (1994).
39. Uchino, K., "Manufacturing Technology of Multilayered Transducers," *Proc. Amer. Ceram. Soc.* (in press).
40. Furuta, A. and K. Uchino, "Destruction Mechanism of Multilayer Ceramic Actuators: Case of Antiferroelectrics," *Ferroelectrics* **160**, 277-285 (1994).
41. Aburatani, H., S. Harada, K. Uchino, A. Furuta and Y. Fuda, "Destruction Mechanisms in Ceramic Multilayer Actuators," *Jpn. J. Appl. Phys.* **33**, 3091-3094 (1994).

Actuator Studies (continued) –Volume II

42. Uchino, K. and H. Aburatani, "Destruction Detection Techniques for Safety Piezoelectric Actuator Systems," *Proc. 2nd Int'l Conf. Intelligent Mater.*, pp. 1248-56 (1994).

VOLUME III

43. Takahashi, S., S. Hirose and K. Uchino, "Stability of PZT Piezoelectric Ceramics Under Vibration-Level Change," *J. Amer. Ceram. Soc.* **77**(9), 2429-32 (1994).

44. Jiang, Q.Y., E.C. Subbarao and L.E. Cross., "Effect of Composition and Temperature on Electric Fatigue of La-Doped Lead Zirconate Titanate Ceramics," *J. Appl. Phys.* **75**(11), 7433-7443 (1994).

45. Srikanth, V. and E.C. Subbarao, "Acoustic Emission Study of Phase Relations in Low Y_2O_3 Portions of ZrO_2 - Y_2O_3 System," *J. Mater. Sci.* **29**, 3363-3371 (1994).

46. Chu, S.Y., Z. Ye and K. Uchino, "Impurity Doping Effect on Photostriction in PLZT Ceramics," *J. Adv. Performance Mater.* **1**, 129-143 (1994)..

47. Chu, S.Y., Z. Ye and K. Uchino, "Photovoltaic Effect for the Linearly Polarized Light in $(Pb,La)(Zr,Ti)O_3$ Ceramics," *Smart Mater. Struct.* **3**, 114-117 (1994).

48. Chu, S.Y., M.L. Mulvihill, Z. Ye and K. Uchino, "Bulk Photovoltaic Effect for the Linearly Polarized Light in $Pb(Zn_{1/3}Nb_{2/3})O_3$ Single Crystals," *Jpn. J. Appl. Phys.* **34** (Part 1, No. 2A) (1995).

49. Mulvihill, M.L., L.E. Cross and K. Uchino, "Low Temperature Dynamic Observation of Relaxor Ferroelectric Domain in Lead Zinc Niobate," *J. Amer. Ceram. Soc.* (in press).

50. Uchino, K., "Electrooptic Ceramics and Their Display Applications," *Ceramics International* (in press).

51. Lee, D., J. Yuk, N. Lee and K. Uchino, "Humidity-Sensitive Properties of Nb_2O_5 -Doped $Pb(Zr,Ti)O_3$," *Sensor and Mater.* **5**(4), 231-240 (1994).

52. Lee, N.Y., N. Usuki, H. Aburatani, Y. Ito and K. Uchino, "Pb/Ti Ratio of RF-Magnetron Sputtered $PbTiO_3$ Thin Films," *Jpn. J. Appl. Phys.* (accepted).

Integration Issues

53. Dougherty, J.P. and Y. Chen, "Tailoring Materials for Smart Applications," Invited Paper, *Proc. 1994 Int'l. Conf. on Intelligent Materials*, June 5-8, 1994, Williamsburg VA.

54. Hackenberger, W.S., T.R. Shrout, J.P. Dougherty and R.F. Speyer, "The Effect of Differential Shrinkage on the Sintering and Microstructural Development of Low-Temperature Co-Firable Multilayer Substrates," *Proc. SAMPE/ISHM 7th International Electronics Conference*, pp. 643-650, Parsippany, NJ, June 20-23, 1994

Integration Issues (continued) –Volume III

55. Wang, S.F., J.P. Dougherty, W. Huebner, and J.G. Pepin, "Silver-Palladium Thick Film Conductors," published as the feature article in *Journal of the American Ceramic Society* 77(12), 3051-72 (December 1994).
56. Sample, D.R., P.W. Brown and J.P. Dougherty, "The Microstructural Evolution of Copper Thick Films Observed by Environmental Scanning Microscopy," *J. American Ceramic Society* (in press).

VOLUME IV

57. Fiallo, H.H., J.P. Dougherty, S.J. Jang, R.E. Newnham and L. Carpenter, "Transmission Properties of Metal-Semiconductor-Relaxor Microstrip Lines", *IEEE Trans. Microwave Theory & Techniques* 42(7), 1176-1182, (July 1994).
58. Dougherty, J.P., M. Megherhi, and H.H. Fiallo, "Integrated Filters and Over Voltage Protection in Multilayer Ceramic Packaging Materials," *Proc. Eighth Cimtec World Ceramics Conference*, Florence, June 29-July 4, 1994.

Processing Studies

59. Miller, D.V., C.A. Randall, A.S. Bhalla, R.E. Newnham and J.H. Adair, "Electrorheological Properties of BaTiO₃ Suspensions," *Ferroelectrics Lett.* 15, 141-151 (1993).
60. Fielding, J.T., Jr., T.R. Shrout and S.J. Jang, "Increased Operating Temperature Range in La-Modified Pb(Mg_{1/3}Nb_{2/3}O₃-PbTiO₃ Relaxor Ferroelectric-Based Transducers," *Proc. 9th ISAF*, State College, PA (August 1994).
61. Fielding, J.T., Jr., S.J. Jang and T.R. Shrout, "Field-Induced Piezoelectric Materials for 100 kHz-10 MHz Transducer Applications," *Proc. 9th ISAF*, State College, PA (August 1994).
62. Brodeur, Russell P., Kamau wa Gachigi, Philip M. Pruna and Thomas R. Shrout, "Ultra-High Strain Ceramics with Multiple Field-Induced Phase Transitions," *J. Am. Ceram. Soc.* 77(11), 3042 (1994).
63. Yoshikawa, S., N. Kim, T. Shrout, Q. Zhang, P. Moses and L.E. Cross, "Field-Induced Lead Zirconate Titanate Stannate Antiferroelectric-to-Ferroelectric Phase Switching Ceramics," *Proc. 9th ISAF*, State College, PA (August 1994).
64. Gururaja et al., "Electrostrictive Ultrasonic Probe Having Expanded Operating Temperature Range," United States Patent, Patent Number: 5,345,139, Date of Patent: September 6, 1994.
65. Yoon, K.H., Y.S. Cho, D.K. Kang, K. Uchino and K.Y. Oh, "Effect of Eutectic Lithium Sulphate-Sodium Sulphate Flux on the Synthesis of Lead Magnesium Niobate," *Ferroelectrics* 160, 255-264 (1994).

Thin Film Ferroelectrics –Volume IV

66. Brooks, K.G., J. Chen, K.R. Udayakumar and L.E. Cross, "Electric Field Forced Phase Switching in La-Modified Lead Zirconate Titanate Stannate Thin Films," *J. Appl. Phys.* **75**(3), 1699-704 (1994).
67. Ghosh, P.K., A.S. Bhalla and L.E. Cross, "Surface Morphology of r.f. Sputtered Bismuth Titanate Thin Films," *J. Materials Science* **29**, 4659-4662 (1994).
68. Lee, N.Y., T. Sekine, Y. Ito and K. Uchino, "Deposition Profile of RF-Magnetron-Sputtered BaTiO₃ Thin Films," *Jpn. J. Appl. Phys.* **33** (Part 1, No. 3A), 1484-88 (1994).

Graduating Students in the Program

69. Dogan, Aydin. PhD Thesis (Abstract), Materials Program. Flextensional "Moonie and Cymbal" Actuators. December 1994.
70. Wang, Hong. PhD Thesis (Abstract), Materials Program. Electromechanical Effects in Polymeric Materials. August 1994.
71. Tressler, James F. Master of Science (Abstract), Ceramic Science. Smart Ceramic-Metal Composites for Active Vibration Control. December 1993.

MATERIALS STUDIES

(continued)

APPENDIX 19

The Piezoelectric, Elastic and Dielectric Constants For Ceramics In The Solid Solution: (x) PbZrO_3 - (1-x-z) $\text{Pb}(\text{Zn}_{1/3}\text{Nb}_{2/3})\text{O}_3$ - (z) PbTiO_3

Edward F. Alberta and Amar S. Bhalla

The Pennsylvania State University, Materials Research Laboratory
University Park, Pennsylvania 16802 USA

T. Takenaka

Faculty of Science and Technology, Science University of Tokyo.
Noda, Chiba-ken 278 Japan

ABSTRACT

In earlier work the existence of a morphotropic phase boundary separating an antiferroelectric and a ferroelectric phase has been found in the solid solution system (x) PbZrO_3 - (1-x-z) $\text{Pb}(\text{Zn}_{1/3}\text{Nb}_{2/3})\text{O}_3$ - (z) PbTiO_3 [PZNT (x/z)]. This paper further explores the electrical field dependence of various material properties near this boundary. Some of those properties measured are the piezoelectric coefficients (d_{31} , k_{31} and k_p), the dielectric constant (ϵ_{33}), and the elastic constant (s_{11}^E). In addition, the pyroelectric effect and hysteresis behavior are also examined.

INTRODUCTION

Material systems capable of altering their physical properties in response to environmental changes are becoming increasingly attractive. Applications of these very smart systems are indeed numerous. A few of these are: mechanical vibration control, acoustic damping, aerodynamic flow control, micro-positioning, chemical detection, and temperature control. Piezoelectric sensor/actuator materials seem to be promising candidates for use in many of these applications.¹

Control over the piezoelectric response is the key to the operation of such a device. Previous work by Kumar² has shown that the elastic properties of a multilayer piezoelectric transducer can be altered in response to an applied stress. This was accomplished by sensing the stress applied to the device and subsequently altering the applied driving voltage. Another of smart piezoelectric devices is the tunable transducer. This type of transducer exploits the non linearity in the piezoelectric response that is found in some materials. Previous work by Taylor³ has shown that the morphotropic phase boundary composition $0.9 \text{ Pb}(\text{Mg}_{1/3}\text{Nb}_{2/3})\text{O}_3 - 0.1 \text{ PbTiO}_3$ [PMN:PT] displays this form of nonlinear piezoelectric response. By applying a small dc bias to the material, d_{33} can be seen to increase from 0 pC/N at zero field to a maximum of 1500 pC/N at 3.7 kV/cm.

The PZNT system, due to similarities with PMN:PT, was thought to possibly exhibit analogous behavior. Takenaka⁴ first explored this system near the room temperature orthorhombic to rhombohedral morphotropic phase boundary. Remanent polarizations of approximately $30 \text{ } \mu\text{C/cm}^2$ and piezoelectric coupling factors of $k_{15}\sim 58\%$, $k_{33}\sim 30\%$ and $k_{31}\sim 10\%$ were found. The system was also thought to be promising for pyroelectric applications due to relatively large values of the pyroelectric coefficient and low dielectric constant in compositions with this rhombohedral phase transition near room temperature.

This paper reports the electric field dependence of various material parameters. Among these are the real and imaginary parts of the dielectric constant (ϵ_{33}), elastic compliance (s_{11}^E), and the piezoelectric coefficient d_{31} . Also, hysteresis and pyroelectric properties are addressed.

EXPERIMENTAL PROCEDURES

Ceramic samples of various PZNT (x/z) compositions near the room temperature morphotropic phase boundary were prepared. Those samples containing 0 mol% PT (i.e. $y=0$) were referred to as PZZN (x). For all experiments the samples were polished to a 1 μm finish using diamond paste.

The polarization versus electric field hysteresis loops were generated at 10 Hz using a modified Sawyer-Tower circuit. During the experiment the samples were immersed in a silicone oil bath. The bath temperature was controlled by a nitrogen fed furnace. Data was acquired using an automated measurement system controlled by a desk top computer.

The temperature dependence of the dielectric constant was measured at various frequencies in a temperature range from -100 °C to 250 °C using a computer controlled measurement system. This system consisted of a multifrequency LCR meter (HP4274A, Hewlett Packard Co.), desktop computer (HP 9816) and a nitrogen fed furnace. Various electrical bias voltages were then applied to the sample by an external power supply.

For piezoelectric measurements, the samples were prepared as thin disks with typical dimensions of 20 x 0.2 mm or as long thin bars with typical dimensions of 20 x 2 x 0.2 mm. All resonance measurements were made using an HP 4192A Impedance Analyzer. The calculations of the compliance, s_{11}^E , piezoelectric coefficient, d_{31} , dielectric constant, ϵ_{33} , and coupling coefficient, k_{31} , were made using the appropriate admittance equation of either a bar or disk resonator. For the bar shaped resonators, the imaginary values of these parameters were found by assuming the s_{11}^E , d_{31} and ϵ_{33} to be complex values as follows:

$$Y = j \frac{\omega i w}{t} \left(\epsilon_{33}^T - \frac{d_{31}^2}{s_{11}^E} \right) + j \frac{2 w d_{31}^2}{s_{11}^E t \sqrt{\rho s_{11}^E}} \tan \left(\frac{\omega l \sqrt{\rho s_{11}^E}}{2} \right) \quad (1)$$

where:

w = width, ρ = density, t = thickness,
 ω = frequency and l = length

and:

$$s_{11}^E = s_{11}^E + j s_{11}^{E''} \quad (2)$$

$$d_{31} = d_{31}^{\prime} + j d_{31}^{\prime\prime} \quad (3)$$

$$\epsilon_{33}^T = \epsilon_{33}^T + j \epsilon_{33}^{T''} \quad (4)$$

The complex admittance equation is then solved by the method described by Smits⁵ and latter by Damjanovic.⁶ This method involves an iterative calculation using an initial guess of the elastic constant and three values of the admittance near resonance.

The pyroelectric data was obtained using the Byer-Roundy method. The pyroelectric coefficient, p_3 , and spontaneous polarization, P_s , for the ceramic specimens were measured using an HP-4140B picammeter controlled by an HP-9121 computer. Temperature was regulated by a Delta D. gn 2300 furnace with a working temperature range of -175 °C to 250 °C. Samples were poled in the sample holder at 100 °C and

poled during cooling to the starting temperature. The samples were then heated at +4 °C/min as the data was taken.

RESULTS AND DISCUSSION

(a) Hysteresis Measurements.

Hysteresis data was taken for six PZZN compositions. These were $x=92.5, 92.8, 93.0, 93.2, 93.5$ and 95.0 mol% PZ. Initially, the hysteresis loops were made using samples with no prior heat treatment. The results showed the antiferroelectric to ferroelectric phase transition (A_α to F_α) to be located between the compositions PZZN (93.0) and PZZN (93.2) (figure 3). The ferroelectric compositions showed coercive fields between 15 kV/cm and 16 kV/cm. The remanent polarization in both PZZN (92.8) and PZZN (92.5) was approximately $28 \mu\text{C}/\text{cm}^2$ and decreased slightly with increasing concentration of PZ. For PZZN (93.0) the remanent polarization was found to be $32.2 \mu\text{C}/\text{cm}^2$. This was slightly higher than that would have been predicted based on the previously mentioned values and is probably due to the morphotropic phase boundary and its increase number of domain states. With further increases in concentration of PZ above 93.0% (i.e., PZZN(93.2), PZZN (93.5), etc.) the remanent polarization falls to $0.00 \mu\text{C}/\text{cm}^2$.

The room temperature antiferroelectric phase compositions, PZZN (93.2), PZZN (93.5) and PZZN (95.0) showed no hysteresis initially. Typical antiferroelectric behavior was found for PZNT (95/5). The antiferroelectric hysteresis loop for this composition is shown in figure 5.

Next, the samples were poled at 100°C for 15 minutes and then cooled, with the field still applied, to room temperature. Following this treatment, all three showed ferroelectric hysteresis loops comparable to those of the ferroelectric samples studied. This implies that the F_α phase is metastable at room temperature in these compositions. The coercive field for this induced phase was found to be between 15 kV/cm and 16 kV/cm. The induced remanent polarization decreased with increasing concentration of PZ to a low of $6.13 \mu\text{C}/\text{cm}^2$ in PZZN (95.0).

The temperature dependence of P_r for PZZN (93.5) is shown in figure 6. This confirms that the F_α phase is stable during cooling to 20°C . During heating, however, the F_α phase is not stable until 75°C . After combining the heating and cooling data, a thermal hysteresis of 55°C is observed.

(b) Dielectric Measurements.

Due to the large concentration of PZ in the compositions studied, the relaxor nature of the PZN component was suppressed. To illustrate this the frequency dependence of PZZN (93.5) from the dielectric data taken during cooling at -4 °C/min is used. Figure 7 shows the dielectric constant and loss measured at frequencies of 1 kHz, 10 kHz and 100 kHz. This shows very little frequency dispersion, and the phase transitions are typically affected by less than 0.2 °C. From these data, it has been determined the PZNT ceramics with $y < 8.0\%$ PZN do not show any relaxor behavior.

The thermal hysteresis found in these compositions can be as much as 120 °C in the lower temperature phase transitions. However, at the Curie point the hysteresis is limited to ~2 °C. Figure 8 shows the thermal hysteresis for heating and cooling rates of ±4 °C/min in PZZN (93.5).

Figure 9 shows the average maximum dielectric constant at the Curie temperature (T_c) from heating and cooling cycles as a function of mol% PZ. Maximum dielectric constant decreases as the concentration of PZN is decreased. Also, as expected, increasing the concentration of PT increases the maximum dielectric constant at T_c . The variation in T_c with mol% PZ can be seen in figure 10. This, for example shows an increase of 10 °C between PZNT (93.5/2.6) and PZNT (93.5/3.9) which is an increase in PT of 1.3 mol%.

Figures 9 and 10 also show the influence of electric bias. The average dielectric constant at T_c for PZNT (93.5/2.6) can be seen to decrease with bias. The bias field also causes a shift in T_c which can be seen in figure 10. This shows the increase in T_c for various compositions in the PZNT system as the bias field is increased. The effect of bias on the dielectric constant and loss in PZZN (93.2) for the whole temperature range studied is shown in figure 11.

(c) Piezoelectric Measurements

The electric bias dependence of real part of d_{31} after poling at room temperature is shown in figure 12. This shows that the piezoelectric effect is linear as a function of bias. The room temperature antiferroelectric to ferroelectric phase boundary can be located between PZZN (93.2) and PZZN (93.0) by plotting $-d'_{31}$ versus composition. Using a Berlincourt meter, the value of d_{33} was found to be between 55 and 60 pC/N in all the ferroelectric samples. The temperature dependence of k_{31} and k_p was found for a morphotropic phase boundary composition. The composition used was PZZN (93.0) and the measurements were conducted using an incremental cooling run with no applied bias.

The results for the PZZN compositions showed little if any dependence on electric bias. The real part of $-d_{31}$ was found to be 6-7 pC/N and the imaginary part to be 0.35 to 0.45 pC/N. The coupling coefficient, k_{31} , was found to be 5-8% at room temperature. From the compositions studied, PZNT(93.5/2.6) was found to have the optimum properties. For this composition, the values of d'_{31} , k_{31} and k_p were found to be 16.0 pC/N, 4% and 6%, respectively. Again, these values were nearly bias independent.

(d) Pyroelectric Measurements.

PZZN (92.5) showed the largest pyroelectric coefficient and remanent polarization of the compositions studied. Figure 14 shows the variation in these parameters as a function of temperature. At room temperature, the spontaneous polarization was found to be 28.9 $\mu\text{C}/\text{cm}^2$ and agrees with the data from hysteresis measurements. The F_a to F_a transitions in this composition was found at -15°C and the F_a to Paraelectric transition is located at 215.09°C .

CONCLUSIONS

Various compositions in the PZ-PZN-PT ternary system have been studied to determine their weak field piezoelectric and dielectric response at room temperature. Some of the conclusions that have been made are as follows:

Hysteresis results indicate that the location of the AF-FE boundary is between $x = 93.0\%$ and $x = 93.2\%$ PZ. Large values of P_r ($\sim 30 \mu\text{C}/\text{cm}^2$) and low values of E_c ($\sim 10 \text{ kV}/\text{cm}$) for $x < 92.8\%$ PZ have been obtained. Also, with decreasing PZ concentrations hysteresis loops become increasingly square in nature.

Room temperature dielectric constants near 250 have been measured and can be altered with suitable compositional adjustments. Large hysteresis in heating and cooling cycles has been displayed, especially in the low to high temperature rhombohedral phase transition. Curie temperatures near 225°C have been found to decrease with both increasing bias field and increasing concentrations of PT.

Piezoelectric coefficient d'_{31} at 25°C was found to be between -5 pC/N and -10 pC/N and linear with electrical bias fields of up to 20 kV/cm . The real elastic

coefficient s'_{11}^E was found to be between 7 and $9 \times 10^{-10} \text{ m}^2/\text{N}$ and constant for electric bias fields of up to 20 kV/cm. The piezoelectric coupling coefficient k_{31} was found to be between 2% and 8%.

The PZNT phase diagram has been refined to show the AF-FE boundary at room temperature. In addition, after poling at elevated temperatures, the ferroelectric phase has been shown to be stable when cooled to room temperature. Finally, the composition PZZN (92.5) has been shown to have strong pyroelectric properties.

REFERENCES

- [1] R.E. Newnham and G.R. Ruschau, "Smart Electroceramics," *J. Am. Ceram. Soc.*, **74** [3] 463-80, (1991).
- [2] S. Kumar, Smart Materials for Acoustic Vibration Control, Ph.D. Thesis, The Pennsylvania State University, 1991.
- [3] D.J. Taylor, Electric and Elastic Coefficients of PMN-Based Ceramics Under DC Bias For Smart Sensor Applications, Ph.D. Thesis, The Pennsylvania State University, 1992.
- [4] T. Takenaka, A.S. Bhalla and L.E. Cross, "Dielectric Piezoelectric and Pyroelectric Properties of Lead Zirconate-Lead Zinc Niobate Ceramics," *J. Am. Ceram. Soc.*, **72** [6] 1016-23, (1989).
- [5] J. Smits, "Iterative Method for Accurate Determination of the Real and Imaginary Parts of the Materials Coefficients of Piezoelectric Ceramics," *IEEE Transactions on Sonics and Ultrasonics*, **SU-23** p 393, (1976).
- [6] D. Damjanovic, Highly Anisotropic Electromechanical Properties in Modified Lead Titanate Ceramics, Ph.D. Thesis, The Pennsylvania State University, 1987.
- [7] D.J. Taylor, D. Damjanovic, and A.S. Bhalla, "Pyroelectric and Dielectric Properties of PMN-Based Ceramics Under DC Bias," *Ferroelectrics*, **118** 143 (1990).

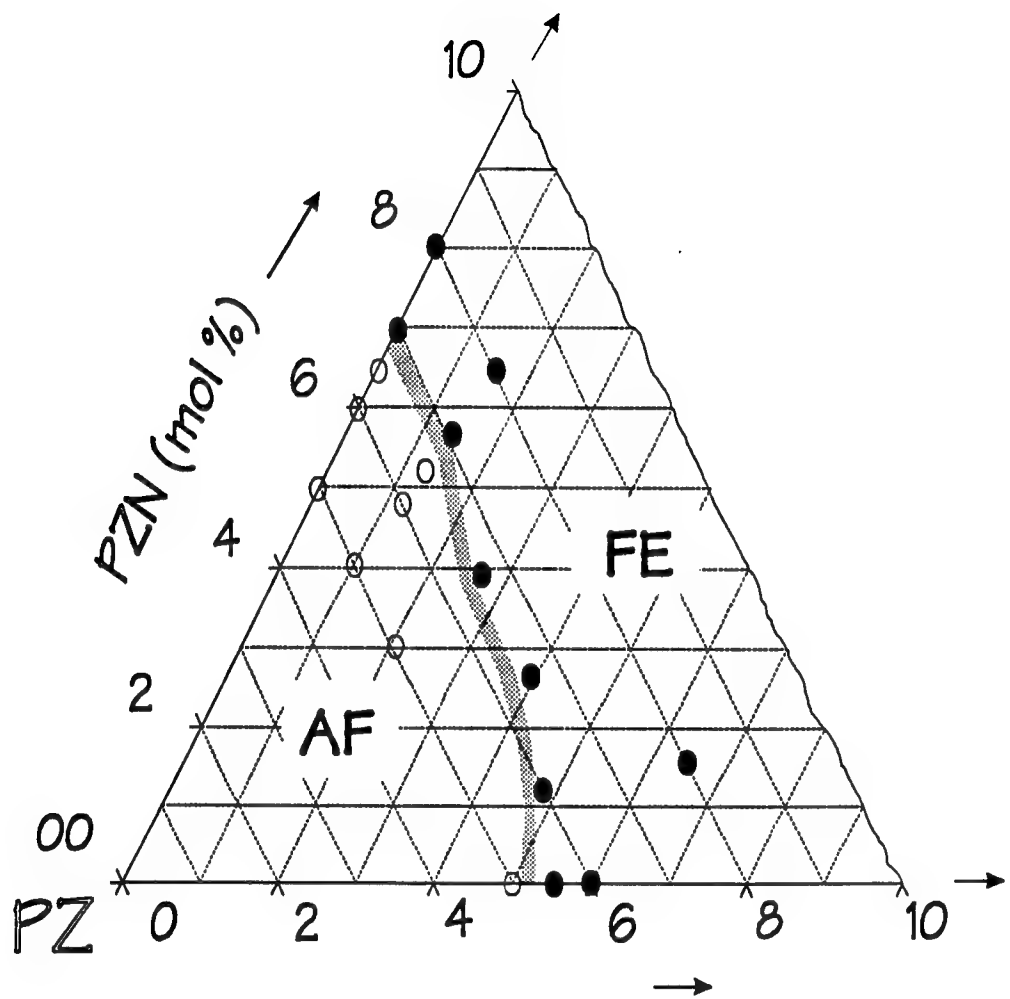


Figure 1: Ternary phase diagram of the PZN-PZ-PT system showing the room temperature antiferroelectric - Ferroelectric morphotropic phase boundary.

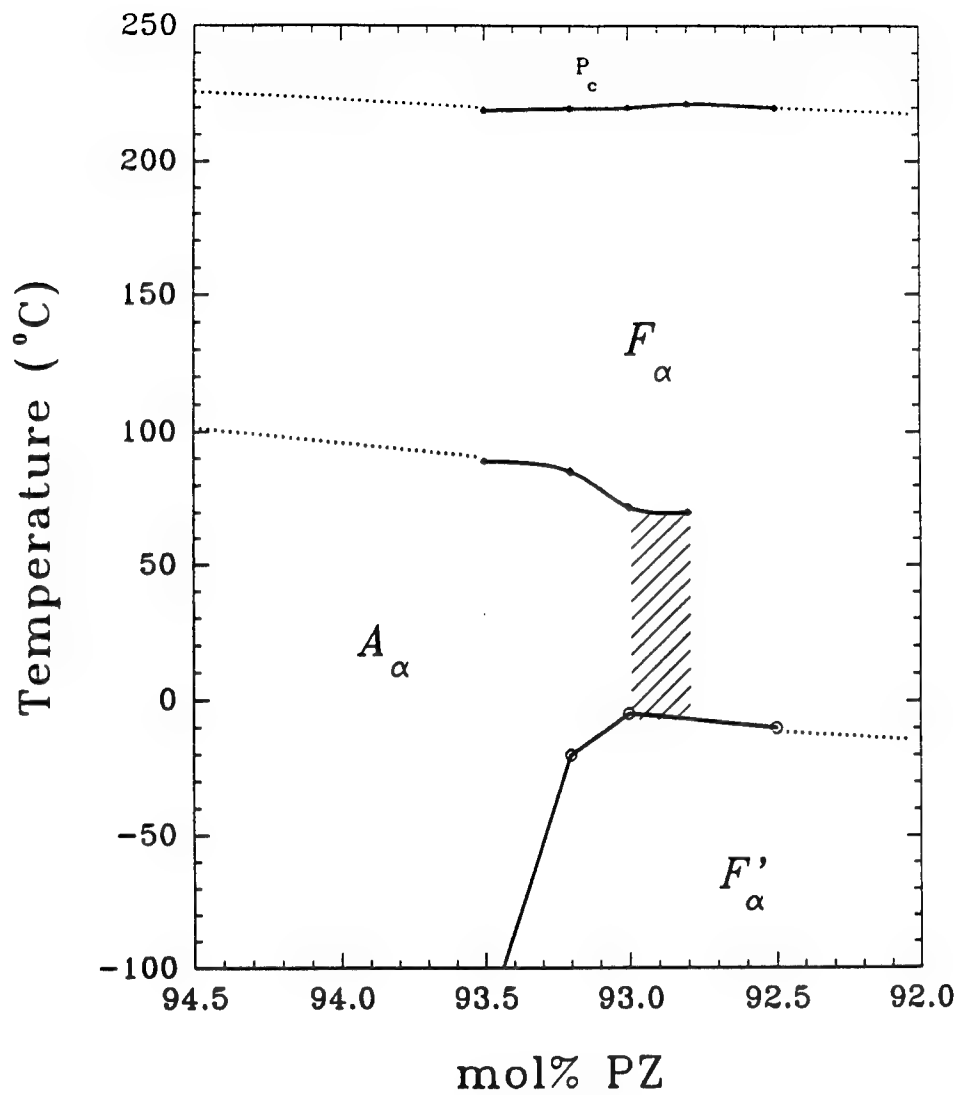


Figure 2: Binary phase diagram of the PZN-PZ system showing the antiferroelectric - antiferroelectric morphotropic phase boundary.

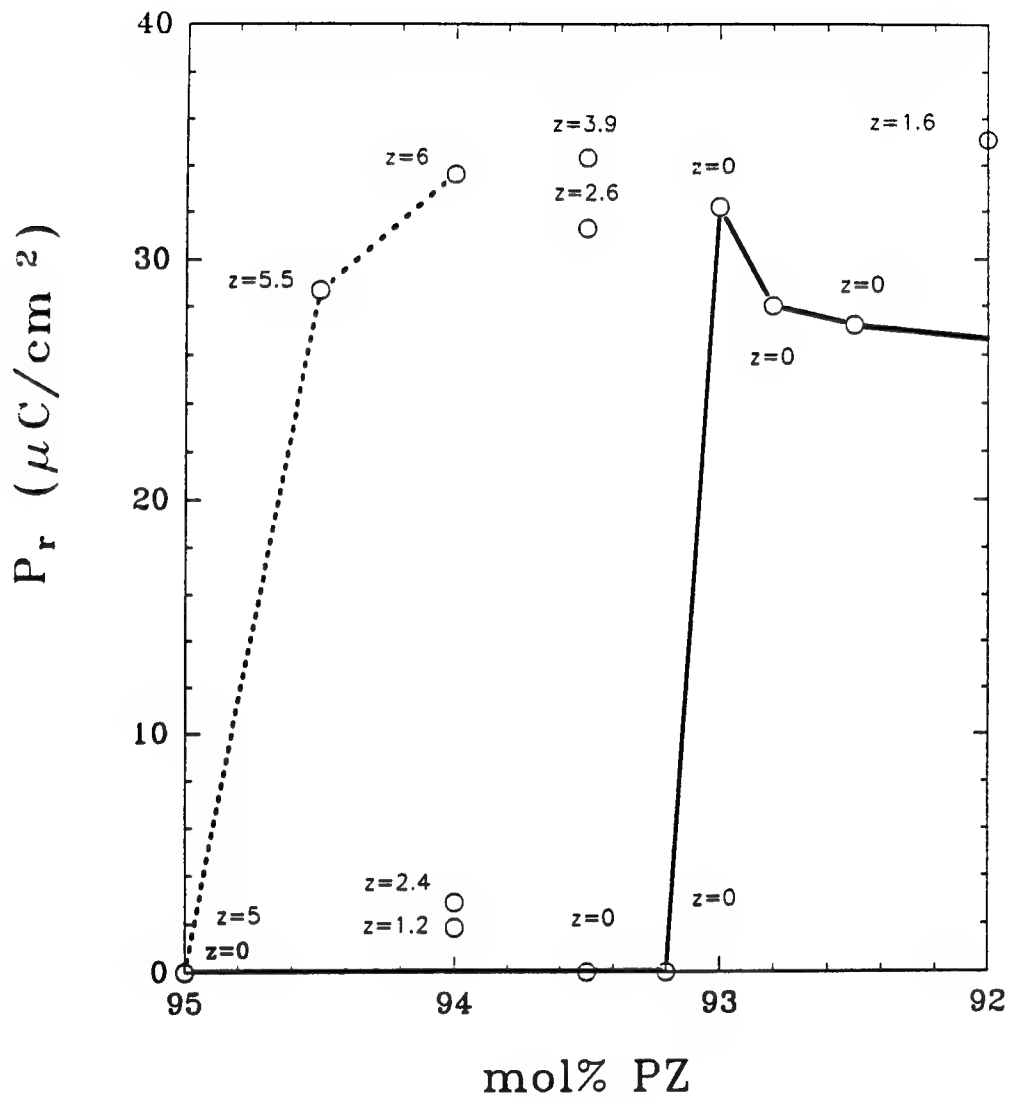


Figure 3: Summary of remanent polarization data as a function of composition measured at room temperature. Solid line indicates the data for PZZN. Dashed line indicates the data for PZT. Subscripts indicate the concentration of PT (i.e. $z=\text{mol\% PT}$).

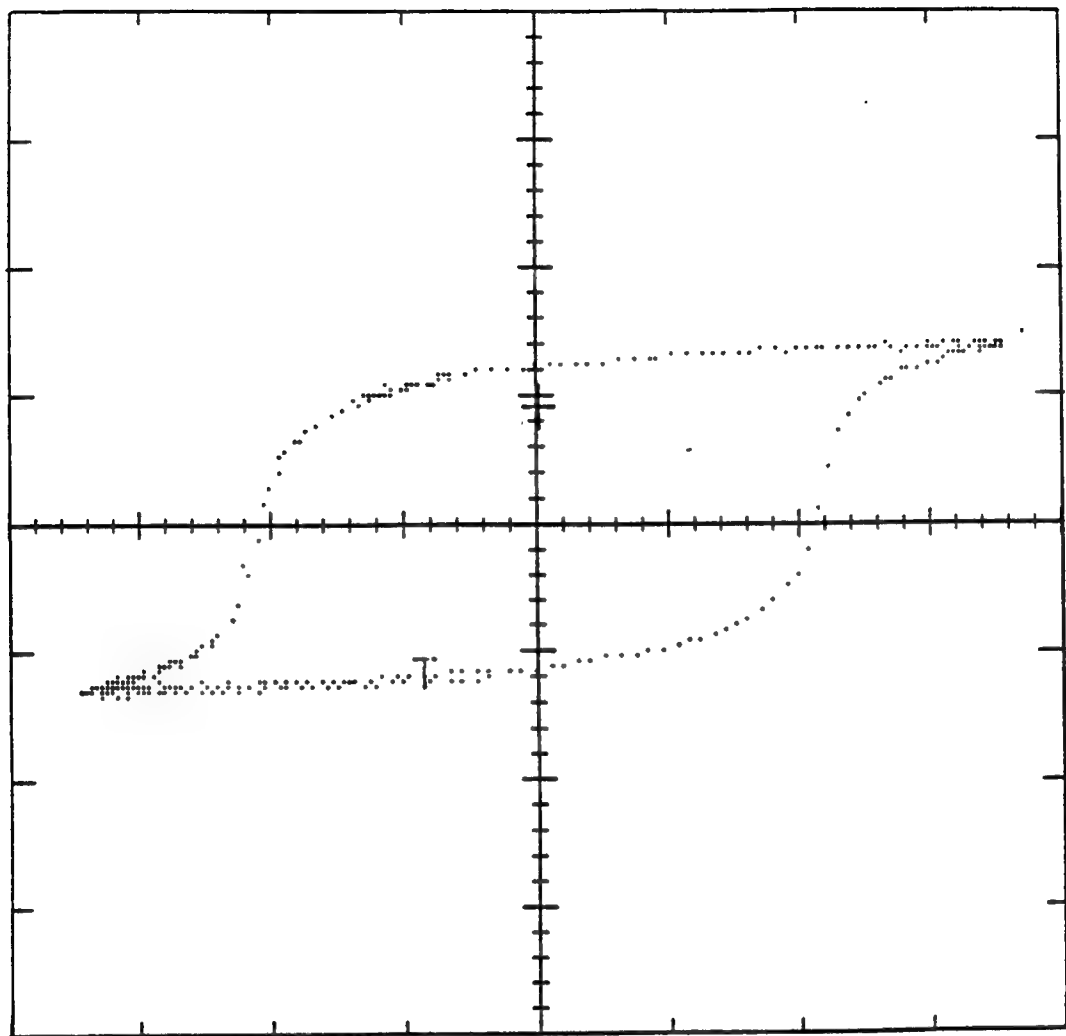


Figure 4: Ferroelectric hysteresis loop for PZZN (92.5) measured at a frequency of 0.10 Hz at 25 °C. $E_c=15.55$ kV/cm and $P_r=27.2$ μ C/cm 2 .

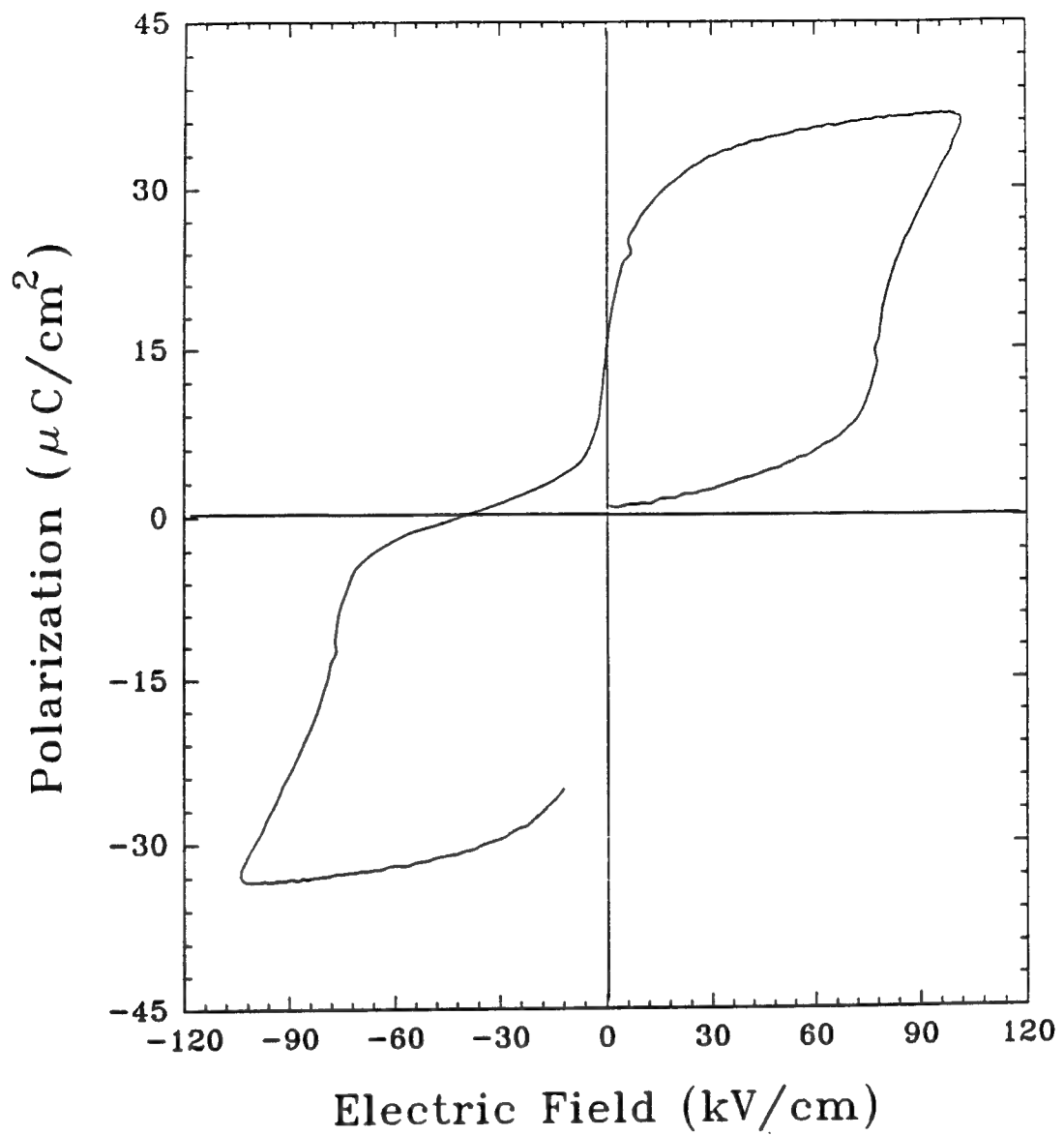


Figure 5: Antiferroelectric hysteresis loop for PZNT (95/5) measured at a frequency of 0.10 Hz at 25 °C.

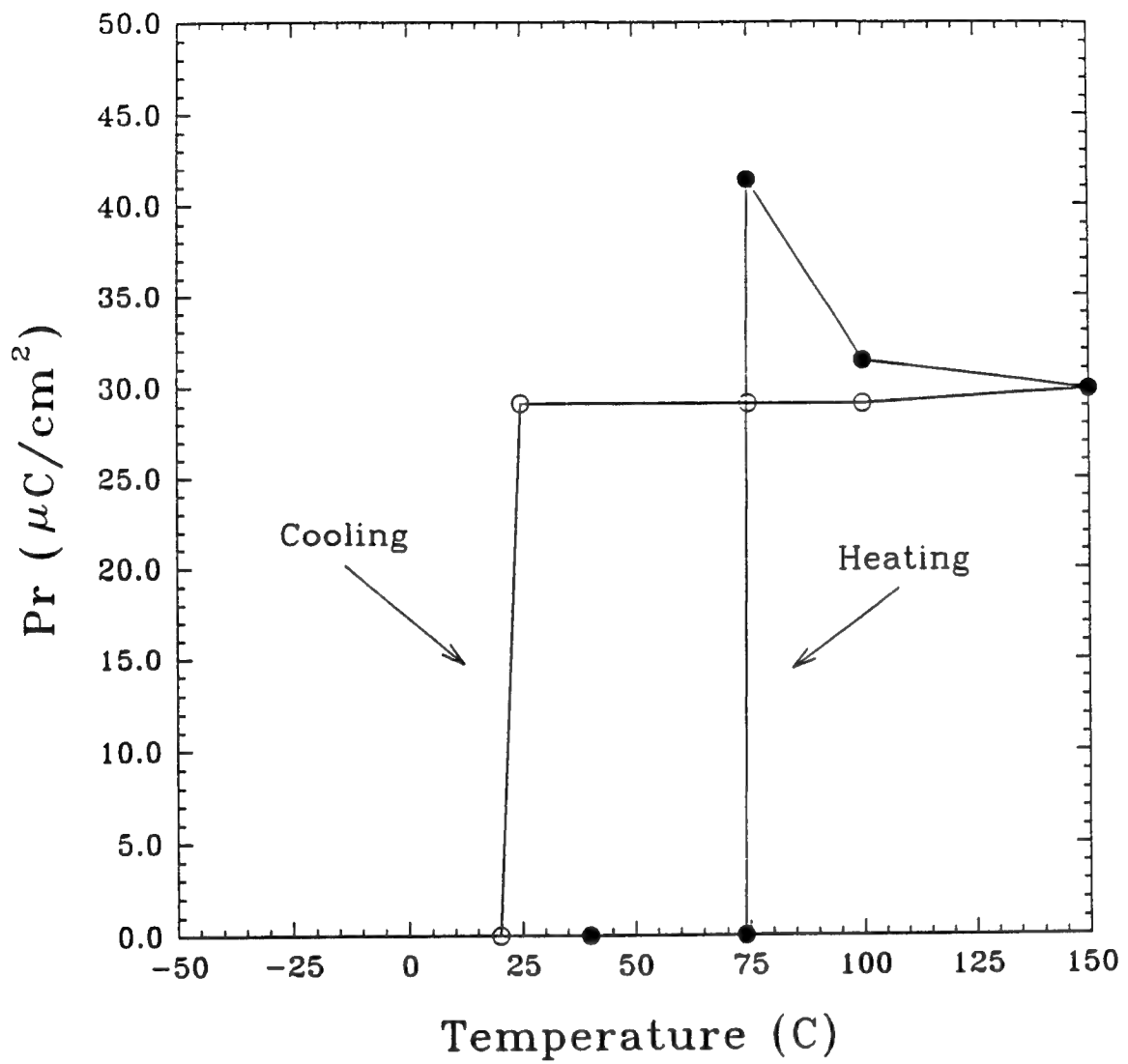


Figure 6: Remanent polarization, P_r , and coercive field, E_c , as a function of temperature for PZZN (93.5).

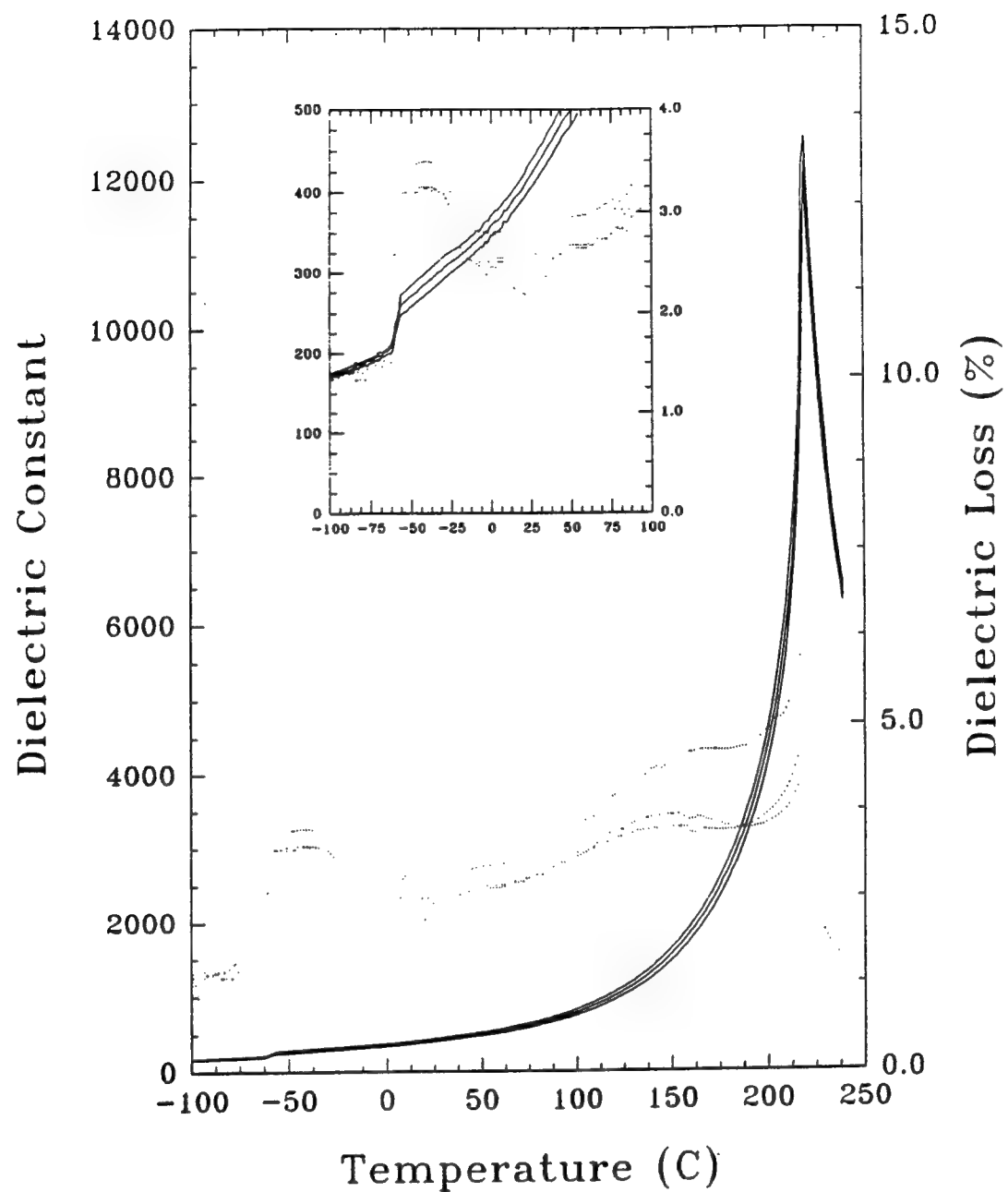


Figure 7: Frequency dependence of the dielectric constant and dielectric loss during cooling at 4 °C/min for PZZN (92.5).

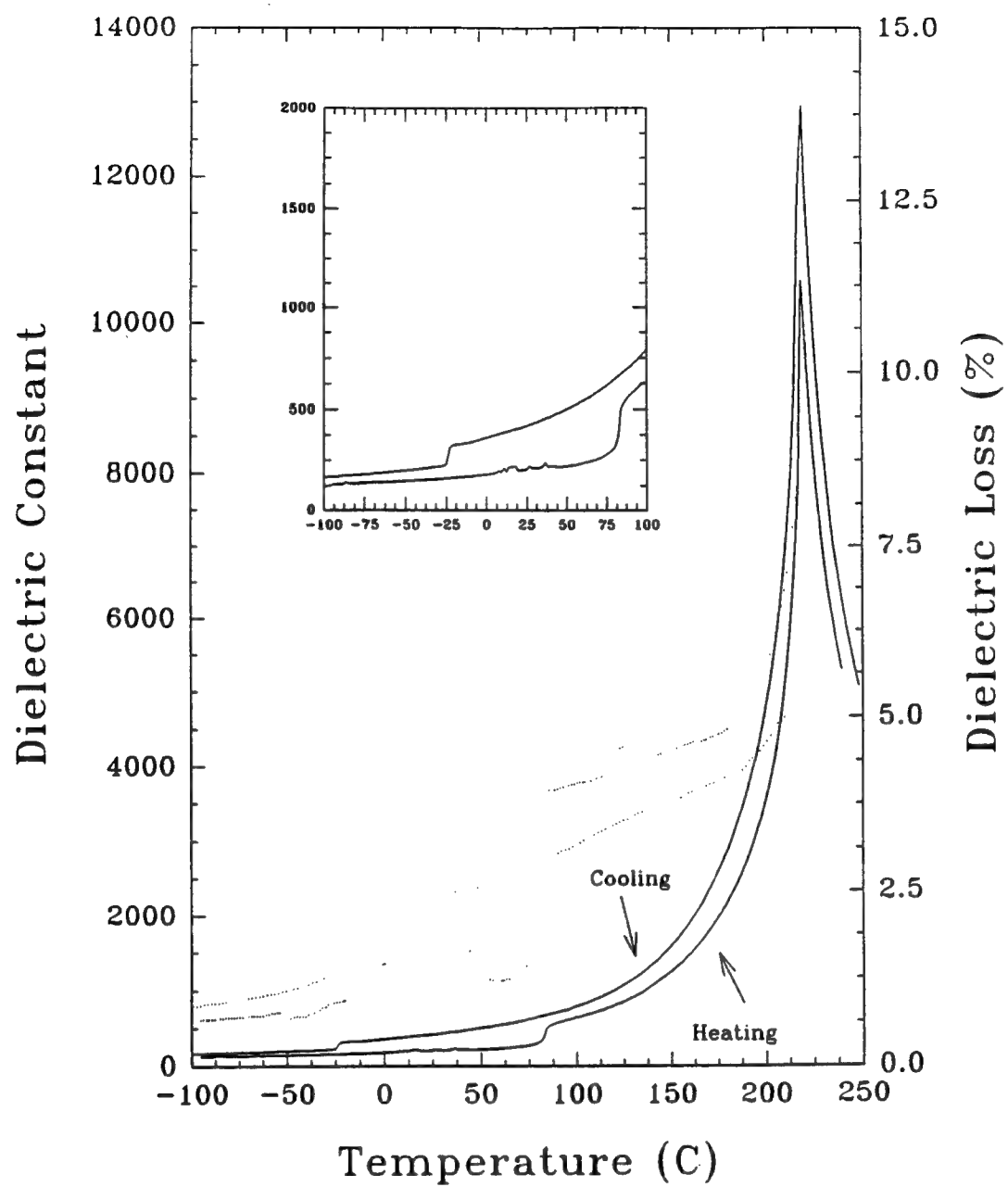


Figure 8: Dielectric constant and dielectric loss for PZZN (93.5) as a function of temperature (data taken at ± 4 °C/min with no applied bias).

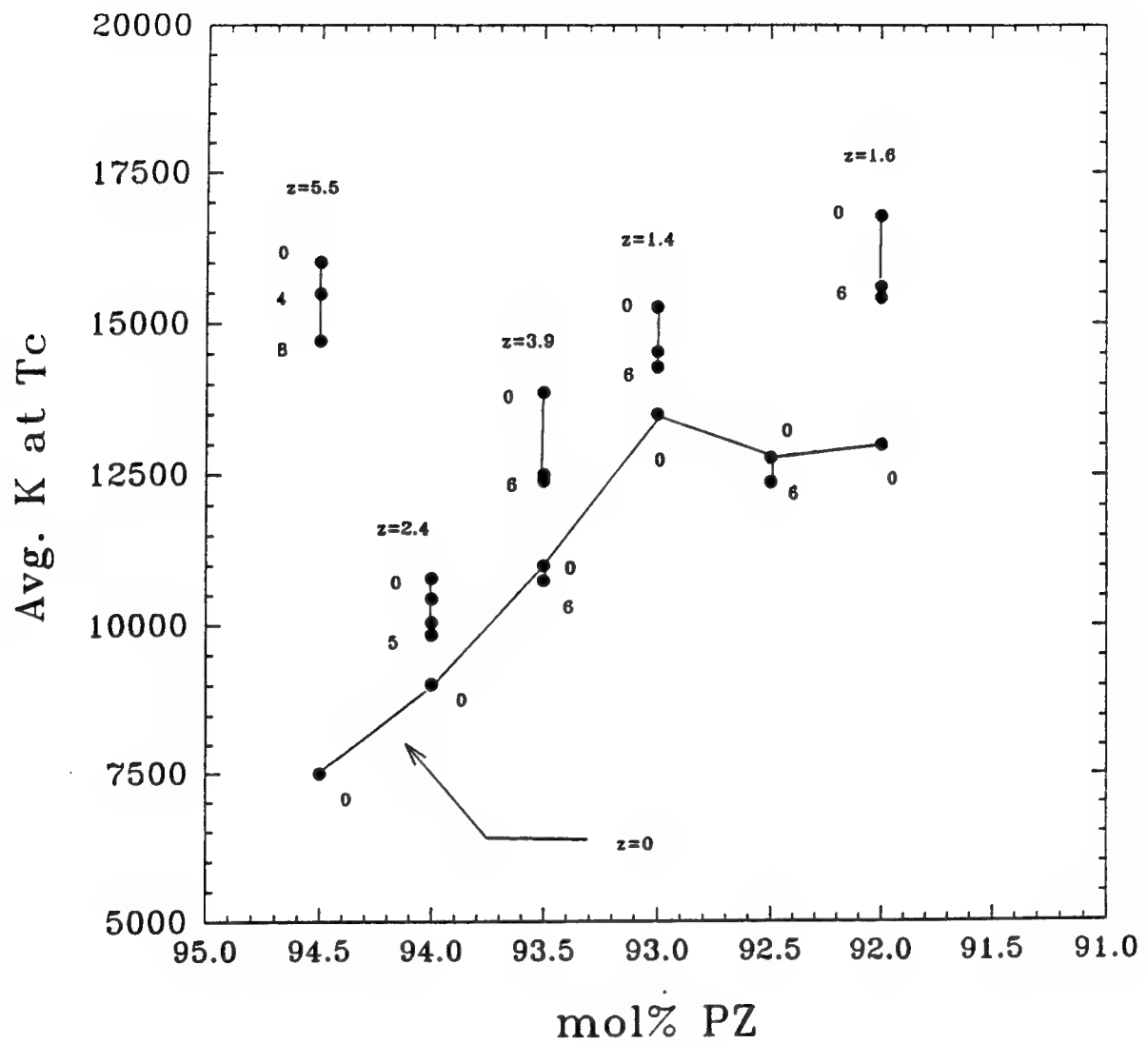


Figure 9: Maximum average dielectric constant at the Curie point measured at a frequency of 1 kHz. Superscripts indicate the applied bias in kV/cm. (z indicates the concentration of PT in mol%).

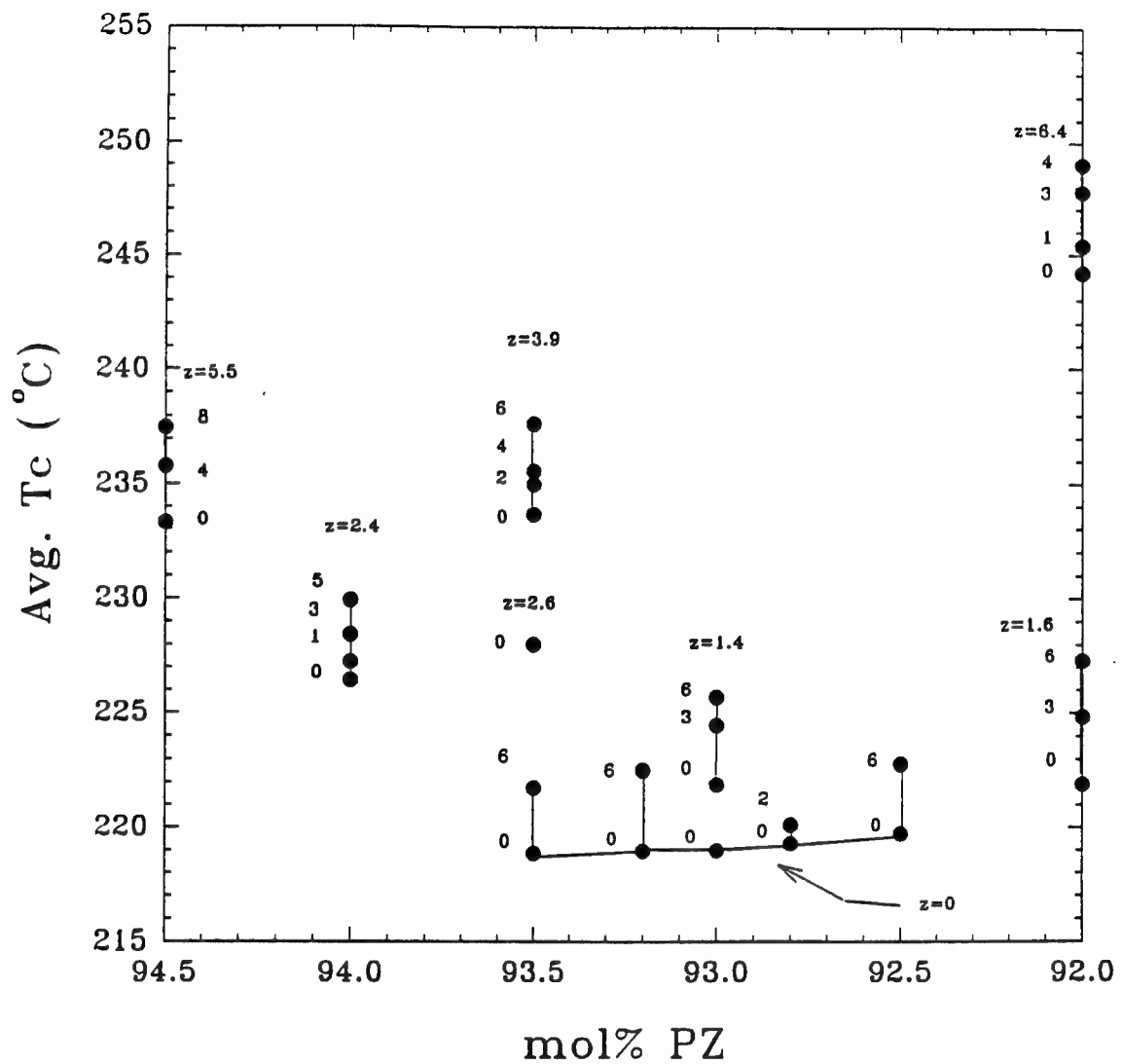


Figure 10: Average Curie point measured at 1 kHz. Superscripts indicate the applied bias in kV/cm. (z indicates the concentration of PT in mol%).

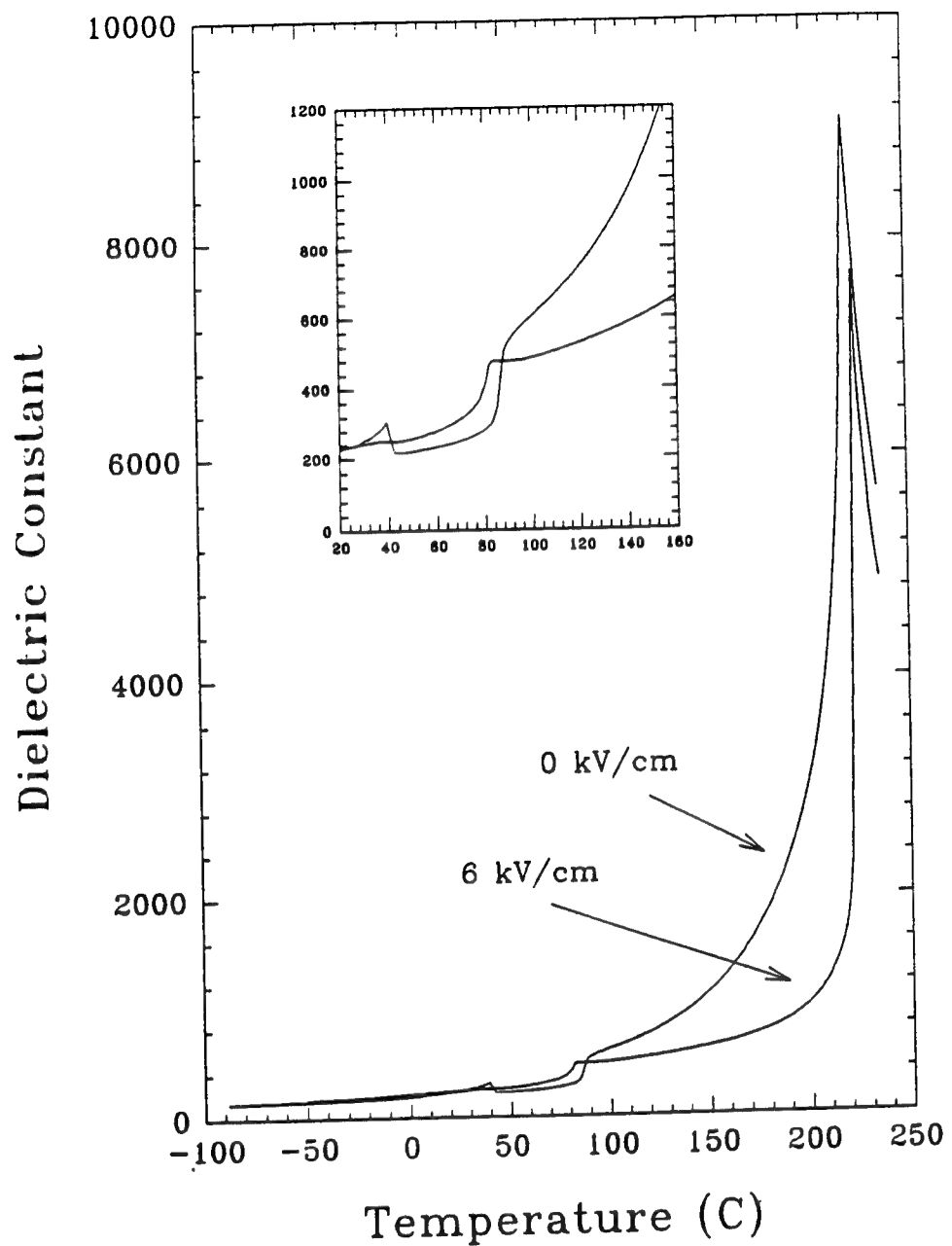


Figure 11: The effect of electric bias on the dielectric constant and dielectric loss for PZZN (93.2) (data taken on heating at +4 °C/min).

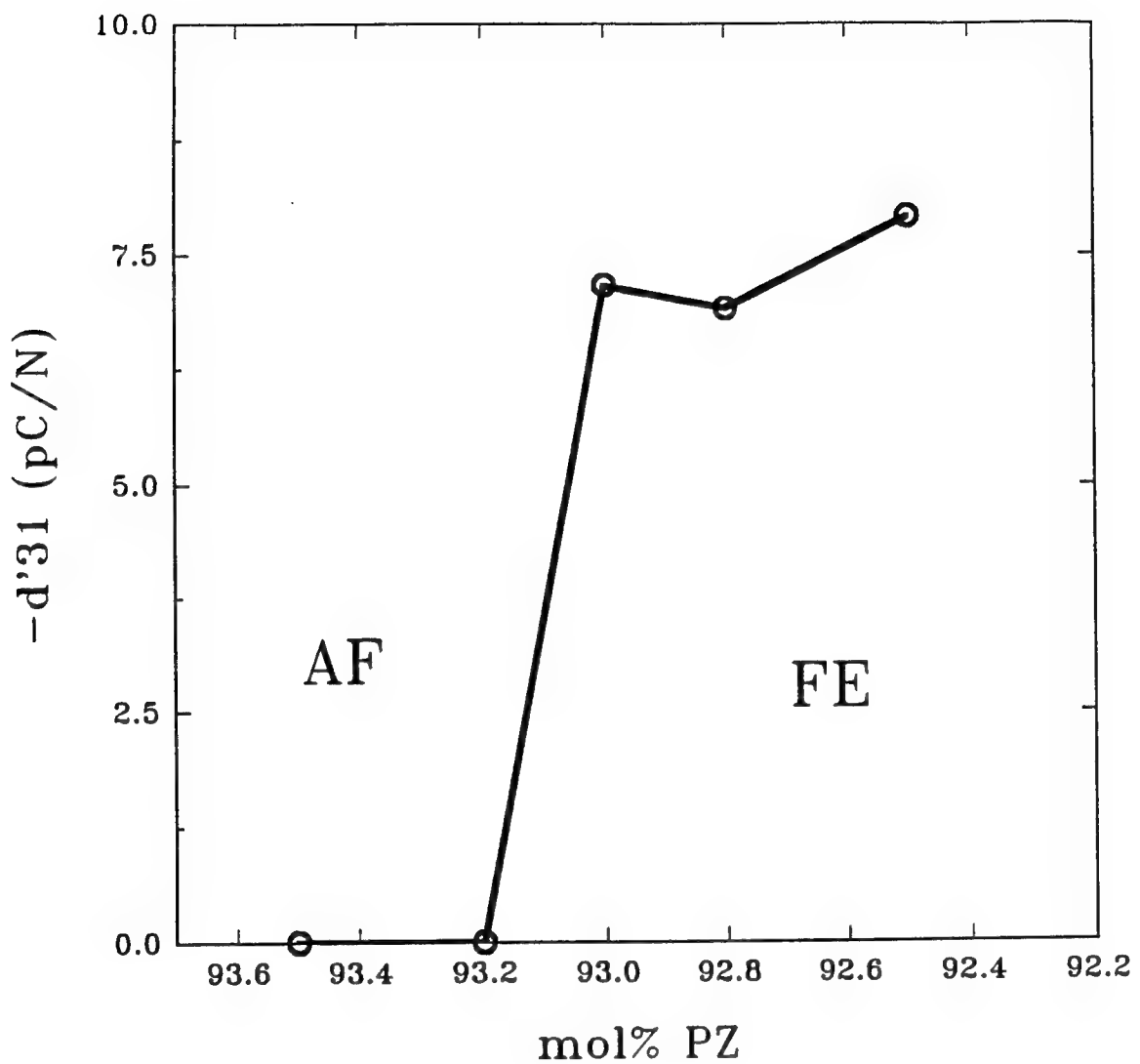


Figure 12: Variation in d'_{31} as a function of composition for PZZN ceramics measured at room temperature. The antiferroelectric - ferroelectric phase boundary is located between $x=93.0$ and 93.2 mol% PZ.

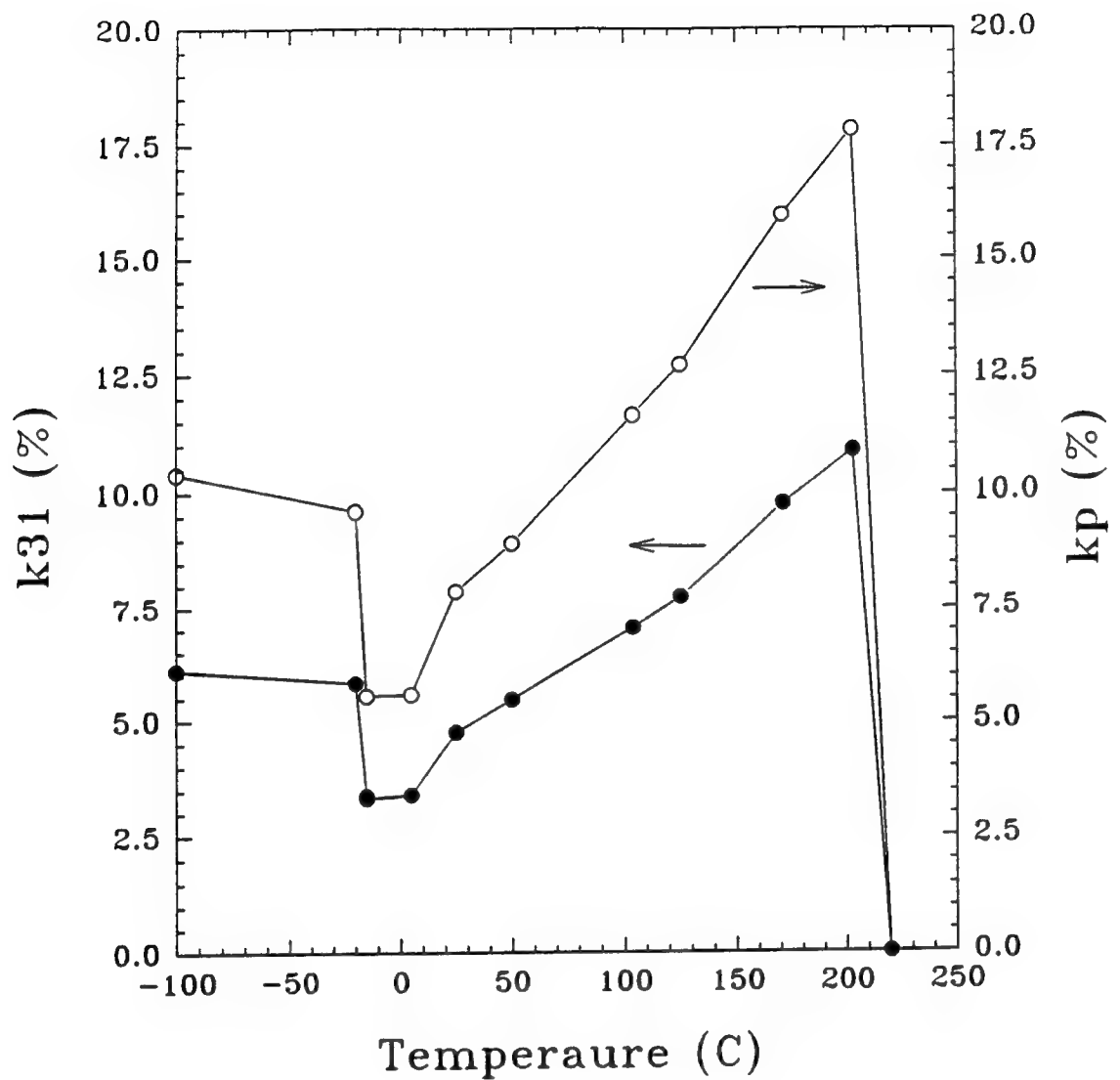


Figure 13: Temperature dependence of the piezoelectric coupling coefficients (k_{31} and k_p) for a PZZN (93.0) ceramic measured with no applied electrical bias.

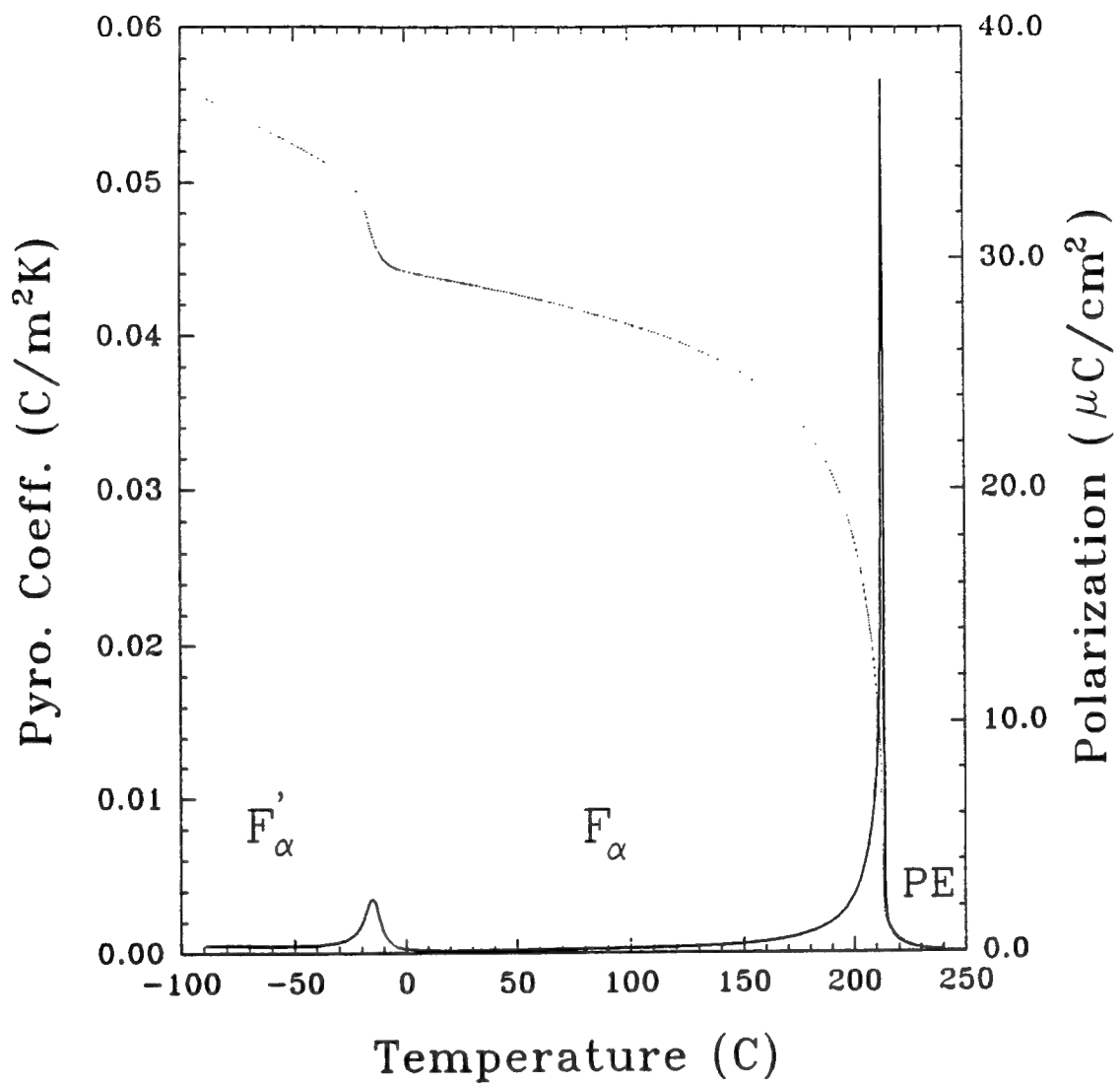


Figure 14: Pyroelectric coefficient and spontaneous polarization for a PZZN (92.5) ceramic measured while heating at $+4\text{ }^\circ\text{C/min}$. Sample poled during cooling from $100\text{ }^\circ\text{C}$.

Table 1: Hysteresis data for Various PZZN and PZNT compositions measured at room temperature and at a frequency of 0.10 Hz.

Composition: PZ / PZN / PT	After poling at 25 C:			After poling at 100 C:		
	Ps	Pr	Ec	Ps	Pr	Ec
95.0 / 5.0 / 0.0	APB	APB	APB	6.7	15.4	6.13
93.5 / 6.5 / 0.0	APB	APB	APB	30.7	29.1	16.36
93.0 / 7.0 / 0.0	36.0	32.2	15.25	36.0	32.2	15.25
92.8 / 7.2 / 0.0	33.6	28.0	15.90	33.6	28.0	15.90
92.5 / 7.5 / 0.0	27.2	27.2	15.55	27.2	27.2	15.55
94.5 / 0.0 / 5.5	31.9	28.7	12.15	---	---	---
93.5 / 2.6 / 3.9	37.7	34.3	11.78	---	---	---
92.0 / 1.6 / 6.4	26.8	25.0	9.20	---	---	---
92.0 / 6.4 / 1.6	40.2	35.1	15.05	---	---	---

Table II: Summary of the complex piezoelectric and elastic coefficients for selected PZNT Compositions. Measurements were made at room temperature with no applied bias after poling at 25 °C.

Composition:	d_{33} (pC/N)	$-d_{31}$ (pC/N)	$-d_{31}$ (pC/N)	s'_{11} ($\times 10^{-12}$ m/V/N)	s''_{11} ($\times 10^{-12}$ m ² /N)	k_{31} (%)	k_p (%)	Dielectric Mechanical	Dielectric Mechanical	Piezoelectric	Loss tangent (%)
PZ / PZN / PT											
95.0 / 5.0 / 0.0	0.0	0.00	0.00	0.00	0.00
93.5 / 6.5 / 0.0	0.0	0.00	0.00	0.00	0.00
93.5 / 6.5 / 0.0	52.0	5.20	0.26	7.30	0.014	4.00	...	1.90	1.92	5.01	...
	0.0	0.00	0.00	0.00	0.00
93.2 / 6.8 / 0.0	60.0	7.20	...	7.95	...	4.77	7.88
93.0 / 7.0 / 0.0	58.0	6.10	0.26	7.60	0.025	4.24	...	1.95	3.25	4.22	...
92.5 / 7.5 / 0.0	57.0	7.08	...	7.91	...	4.49	7.49
92.0 / 6.4 / 1.6	55.0	4.25	0.35	7.22	0.027	3.54	...	5.34	3.77	8.32	...
92.0 / 1.6 / 6.4	59.0	9.95	0.22	8.49	0.014	6.97
93.5 / 3.9 / 2.6	60.0	16.03	...	7.86	...	3.80	6.15

Note 1: Measurements made after poling at 100 °C.

APPENDIX 20

AN EVALUATION OF LEAD-ZIRCONATE BASED CERAMICS FOR USE IN NON-VOLATILE FERROELECTRIC MEMORY DEVICES.

E.F. Alberta and A.S. Bhalla

Materials Research Laboratory, The Pennsylvania State University, University Park, PA 16802, U.S.A.

ABSTRACT

This paper will present an initial evaluation of the lead zirconate - lead zinc niobate solid solution for use in non-volatile ferroelectric memory devices. Previous work has shown that the $(x)\text{PbZrO}_3 - (1-x)\text{Pb}(\text{Zn}_{1/3}\text{Nb}_{2/3})\text{O}_3$ [PZZN] system has "square" hysteresis loops accompanied by large remnant polarizations. In particular, compositions near the room temperature antiferroelectric to ferroelectric phase boundary will be investigated.

INTRODUCTION

Previous work within the PZZN system has shown that a pseudomorphotropic phase boundary exists at $x=93.0$ mol% PZ. This boundary separates the rhombohedral ferroelectric phase from the antiferroelectric orthorhombic phase at room temperature. Based on these works an investigation into the hysteresis behavior of PZZN has been undertaken. For the initial work hot pressed ceramic samples have been used. It is generally known that bulk and thin film properties can vary; however, this work is an indication that the thin film form of this material may be interesting from an applications point of view.

RESULTS

Compositions with less than 93.0 mol% PZ are found to be ferroelectric with bias independent piezoelectric coefficients. As an example of the ferroelectric phase, PZZN(92.5) will be used. The antiferroelectric phase will be represented by the composition PZZN(93.5). From dielectric data one can find two phase transformations in PZZN(92.5), one near -50°C (from cooling runs) and the second at 218°C . These anomalies correspond to the low- to high-temperature rhombohedral phase change and the high-temperature rhombohedral to cubic phase change, respectively. In PZZN(93.5), however, the phase transformations are from orthorhombic to high-temperature rhombohedral to cubic. At room temperature the dielectric constant is between 150 to 450 with losses of about 4% at 1kHz. Other work has also

shown that the dielectric constant of the ferroelectric phases are decreased with increasing bias fields and are decreased in the antiferroelectric phases. The typical effect of bias applied to a poled ferroelectric is shown in figure 1.

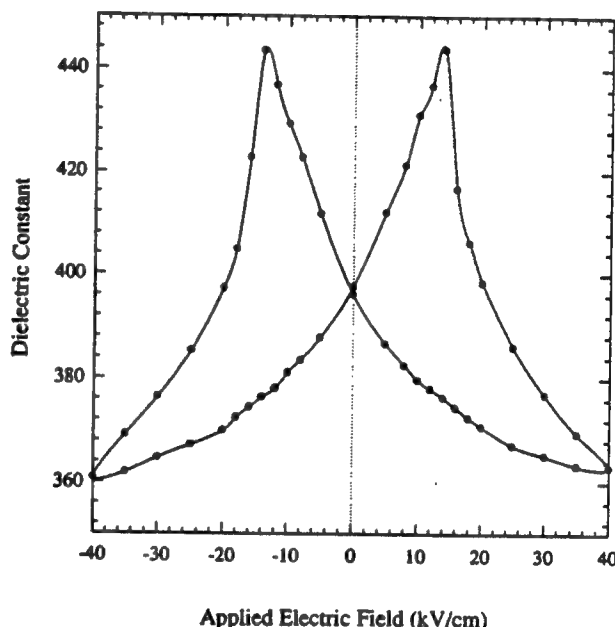


Figure 1. The effect of electrical bias on the dielectric constant of PZZN(92.5) at room temperature.

Hysteresis behavior can be found in the next few figures. Typical room temperature hysteresis curves can be found in Figure 3. PZZN(93.5) displays an interesting behavior. The antiferroelectric phase cannot be field-forced with field up to 70 kV/cm; however, the composition is easily poled near the antiferroelectric-ferroelectric phase transformation. Saturated values of d_{33} and P_s can be obtained after poling at 100°C with 8 kV/cm for 1 to 2 minutes. The effect of temperature on this field-and-temperature forced ferroelectric phase can be found in figure 4. This plot indicates the antiferroelectric phase becomes

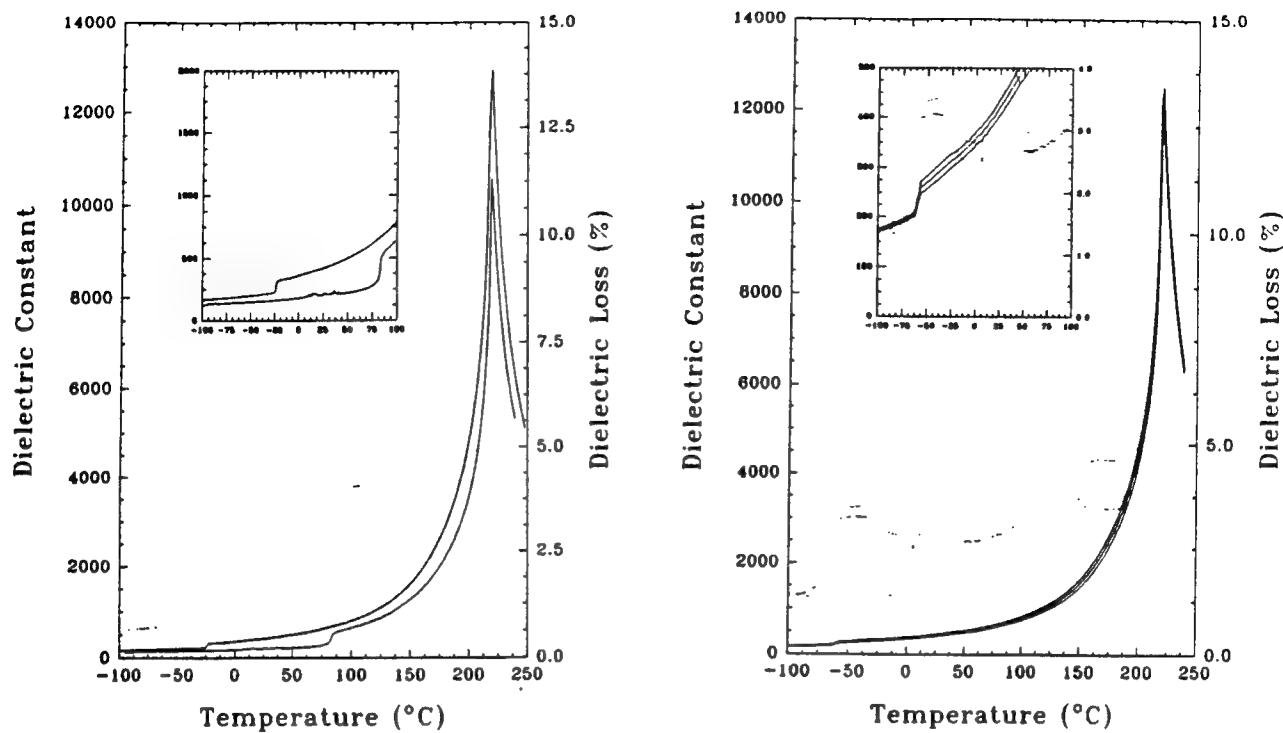


Figure 2. The dielectric constant and loss as a function of temperature for: (a) PZZN(92.5) heating and cooling and (b) PZZN(93.5) at 1 kHz, 10 kHz and 100 kHz.

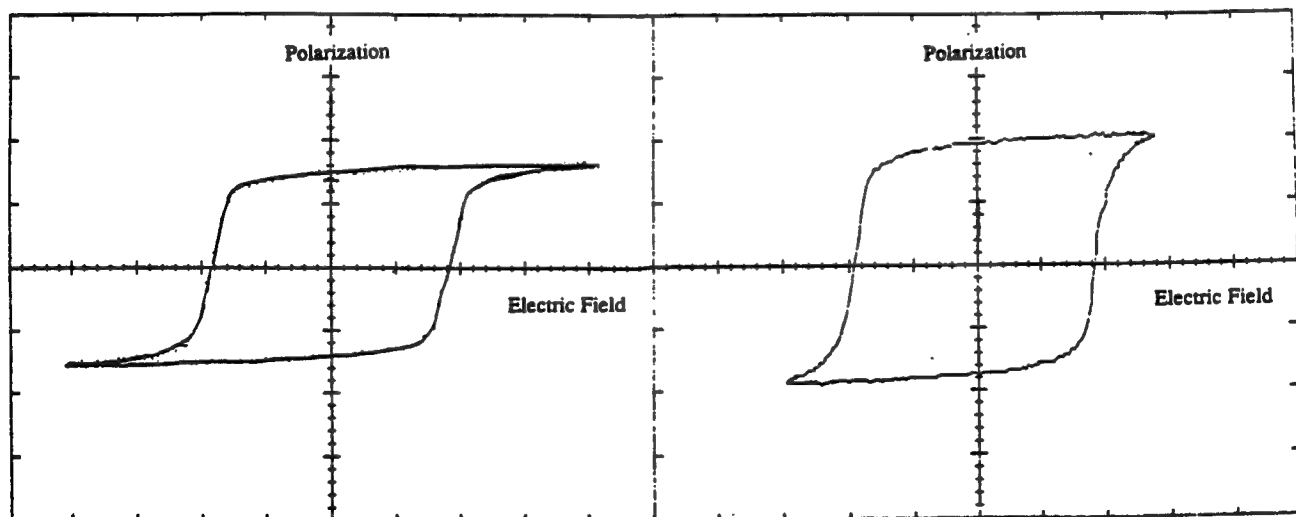


Figure 3. Typical hysteresis loops at room temperature for: (a) PZZN(92.5), $E_c=15.25 \text{ kV/cm}$ and $P_r=32.2 \mu\text{C}/\text{cm}^2$ and (b) PZZN(93.5) (poled at 100°C), $E_c=16.36 \text{ kV/cm}$ and $P_r=29.1 \mu\text{C}/\text{cm}^2$.

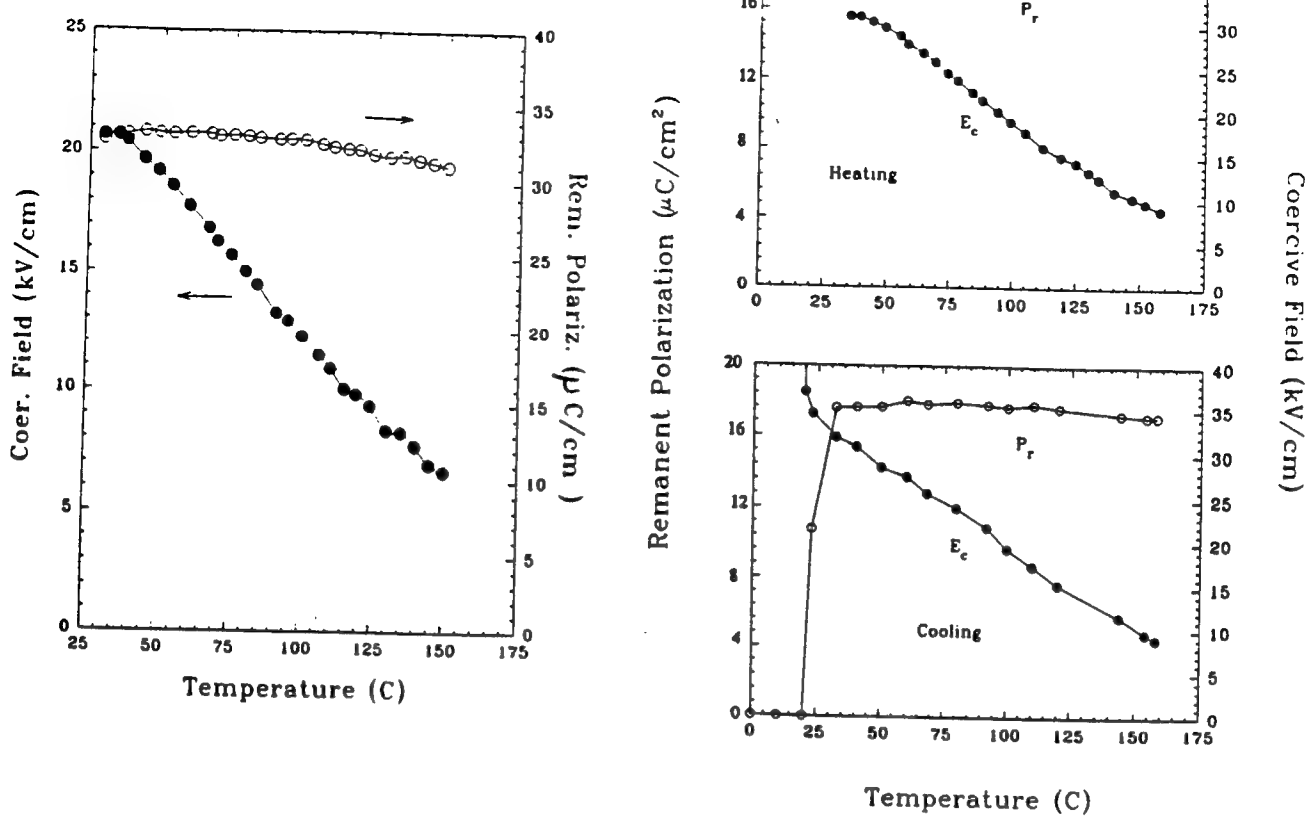


Figure 4. Polarization as a function of temperature (from hysteresis measurements) for: (a) PZZN(92.5) and (b) PZZN(93.5).

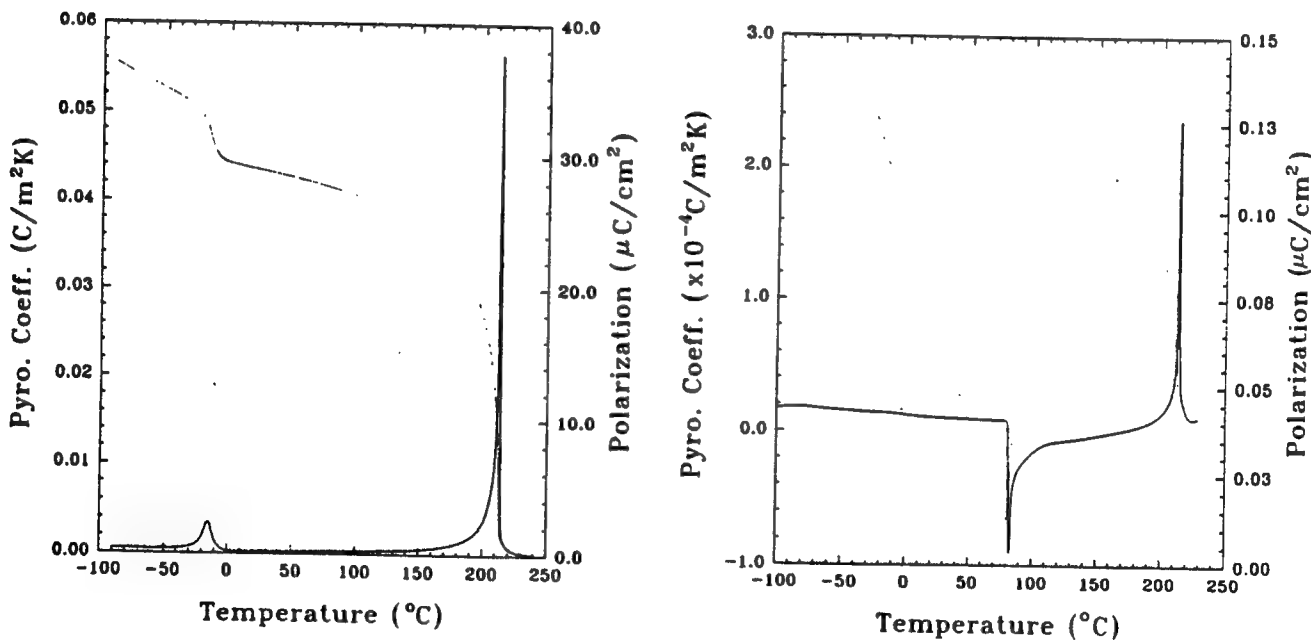


Figure 5. Pyroelectric response of PZZN ceramics (data taken during heating) for: (a) PZZN(92.5) and (b) PZZN(93.5).

stable at slightly less than room temperature which is approximately 50°C higher than indicated by the dielectric constant data. The ferroelectric composition, PZZN(92.5), displays a remnant polarization of 32.2 $\mu\text{C}/\text{cm}^2$ which is approximately equal to that for PZZN(93.5). However, this composition does not depole below room temperature and is easily poled at room temperature with 20 kV/cm for 1 to 2 minutes.

Typical pyroelectric responses of these materials are shown in figure 5. One can easily see the ferroelectric to ferroelectric phase change at -5°C for PZZN(92.5) and the resulting change in the polarization. For PZZN(93.5) the situation is slightly more complicated. Even when poled at 100°C the sample depoled in the process of cooling to the start temperature. Even with this loss of polarization, the plot is useful in determining the location of the antiferroelectric to ferroelectric phase transition which is at 83°C.

CONCLUSIONS

Using ceramic specimens, some important information has been obtained towards the use of PZZN in non-volatile memory applications. Most notable are the ease of poling, the large remnant polarizations, and the existence of square hysteresis loops. Clearly more work needs to be done with this material, especially in the area of thin films.

REFERENCES

- [1] Alberta, E.F., "The Dielectric, Piezoelectric, and Pyroelectric Properties of Lead Zirconate - Lead Zinc Niobate - Lead Titanate Ceramics," M.S. Thesis, The Pennsylvania State University, University Park PA (1994).
- [2] Lian, J., M. Adachi, E. Shiosake, and A. Kawabata, "Phase Transitions in the PbZr_3 - PbTiO_3 - $\text{Pb}(\text{Zn}_{1/3}\text{Nb}_{2/3})\text{O}_3$ System," *Ferroelectrics*, **96** 127 (1989).
- [3] Lian, J., and T. Shiosake, "Phase Transitions Characteristics in PbZrO_3 Based PZT-PZN Solid Solution Ceramics," *IEEE Trans. on Ultrasonics and Frequency Control*, **38** [6] (1991).
- [4] Takenaka, T., A.S. Bhalla, and L.E. Cross, "Dielectric, Piezoelectric and Pyroelectric Properties of Lead Zirconate-Lead Zinc Niobate Ceramics," *J Am. Ceram. Soc.*, **72** [6] 1016-23 (1989).
- [5] Takenaka, T., K. Komiya, and K. Sakata, "PbZrO₃-Based Composite Pyroelectric Ceramics," *IEEE Proc. International Symposium on the Applications of Ferroelectrics*, IEEE, Piscataway (1991).

APPENDIX 21

Dielectric and Piezoelectric Properties of Ceramics in The Lead Indium Niobate - Lead Scandium Tantalate Solid Solution.

E.F. Alberta and A.S. Bhalla

Materials Research Laboratory, The Pennsylvania State University, University Park, PA 16802, U.S.A.

ABSTRACT

The dielectric and piezoelectric properties of the solid solution: $(x)\cdot \text{Pb}(\text{In}_{1/2}\text{Nb}_{1/2})\text{O}_3 - (1-x)\cdot \text{Pb}(\text{Sc}_{1/2}\text{Ta}_{1/2})\text{O}_3$ [PIN/PST(x)] have been investigated. The two compositions that have been studied are $x=0.025$ and 0.975 . The degree of long range ordering in PIN/PST(92.5) was found to be 0.73 (i.e., 73% ordered.) Dielectric maximum was found to be at 10°C and the pyroelectric maximum was found to be at 0°C . The average dielectric constant from heating and cooling cycles was found to have a maximum of 1470 , and corresponds to a dielectric loss of 3% . The maximum pyroelectric response was found to be $0.002 \text{ C}/\text{K}\cdot\text{m}^2$. At room temperature d_{33} and d_{31} were found to be $0 \text{ pC}/\text{N}$ with poling fields of up to $45 \text{ kV}/\text{cm}$. Upon cooling to -30°C a ferroelectric hysteresis loop appears with $E_c = 9.86 \text{ kV}/\text{cm}$ and $P_r = 4.5 \text{ mC}/\text{cm}^2$.

INTRODUCTION

Earlier studies have shown that both $\text{Pb}(\text{In}_{1/2}\text{Nb}_{1/2})\text{O}_3$ [PIN] and $\text{Pb}(\text{Sc}_{1/2}\text{Ta}_{1/2})\text{O}_3$ [PST] are relaxor ferroics in which the degree of B-site cation ordering can be thermally controlled. Previous studies have mainly focused on solid solutions involving the normal ferroelectric PbTiO_3 [PT] with either PIN or PST. Recently, however, the system PIN-PST [PIN/PST(x)] has begun to be studied due to the unique combination both order-disorder behavior and antiferroelectric-ferroelectric phase transformations.

PIN has been found to have the rhombohedrally distorted perovskite structure (that is, either the space group $\text{R}3\text{m}$ or $\text{R}3$). Disordered PIN crystals are relaxor ferroelectrics and undergo a cell doubling phase transformation into an ordered antiferroelectric phase. PST has also been shown to be rhombohedral. However, Disordered PST crystals are relaxor ferroelectrics and undergo a cell doubling phase transformation into an

ordered ferroelectric phase. This combination of first-order (anti)ferroelectric behavior, relaxor behavior and the presents of variable order-disorder regions may prove to be interesting on both a theoretical and practical levels.

In this paper we will focus on the composition PIN/PST(0.025) and PIN/PST (0.975). The dielectric and piezoelectric properties of this as-fired PIN/PST ceramics will be described.

RESULTS

The degree of ordering in the as-fired ceramics has been determined by superstructure reflections in x-ray diffraction patterns. The long-range order parameter, S , has been determined by referring the intensity ratios of the superstructure/fundamental reflection pairs (111 and 200 in this case) and comparing them to those determined for an ordered structure. This relation is given as follows:

$$S^2 = \left[\frac{I_{\text{Superlattice}}}{I_{\text{Baseline}}} \right]_{\text{Obs}} \times \left[\frac{I_{\text{Superlattice}}}{I_{\text{Baseline}}} \right]_{S=1} \quad [1]$$

Stenger and Burggraaf have determined the ratio $[I_{111}/I_{200}]$ under perfect order ($S=1$) to be 1.33 . Before any electrical measurements were made the degree of ordering for as-fired PIN/PST(0.025) was determined to be 73% .

The temperature dependence of the dielectric constant was determined in the temperature range -100°C to 100°C . K was found to reach a maximum at 10°C of 1500 during heating of $4^\circ\text{C}/\text{min}$ and 1440 during cooling at $4^\circ\text{C}/\text{min}$. The dielectric loss at temperatures less than 10°C was found to be approximately 4% . The inverse dielectric constant follows the "Curie-Weiss Squared" law for both heating and cooling.

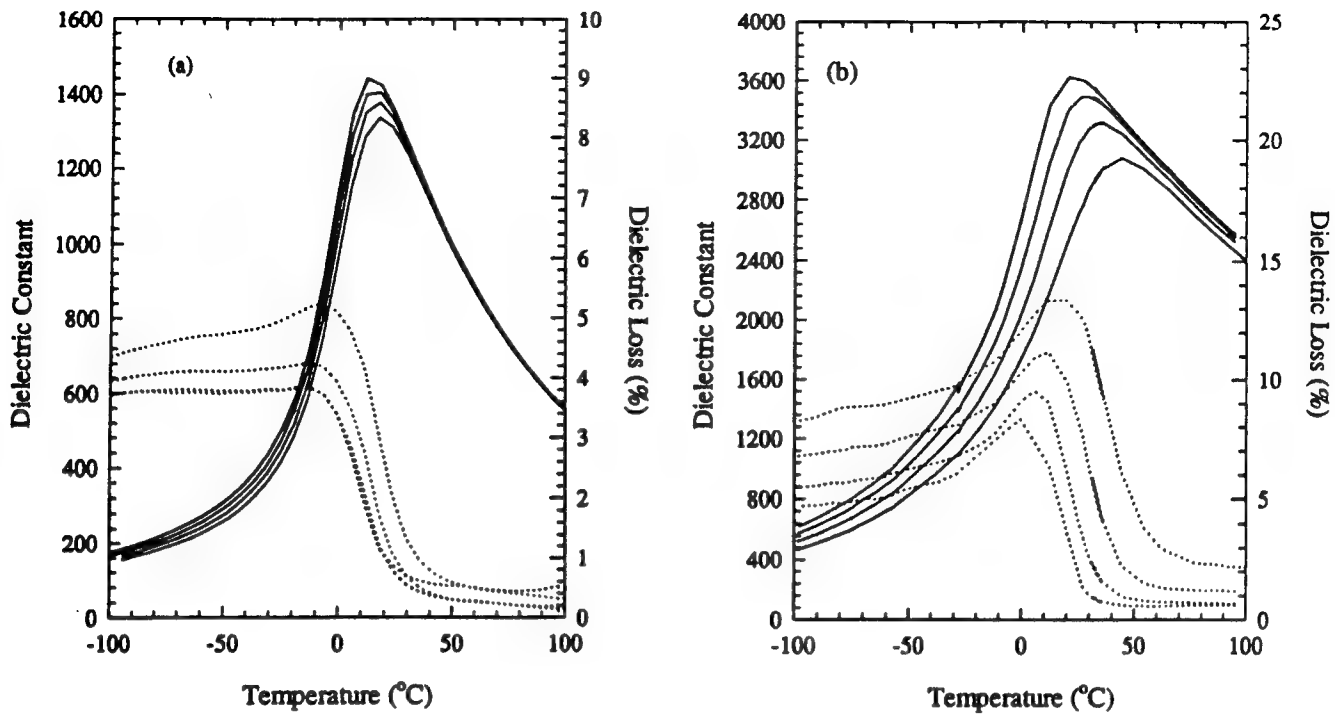


Figure 1. Dielectric Constant and Loss at 100 Hz, 1 kHz, 10 kHz, and 100 kHz for:
 (a) PIN/PST(0.025) and (b) PIN/PST (0.975).

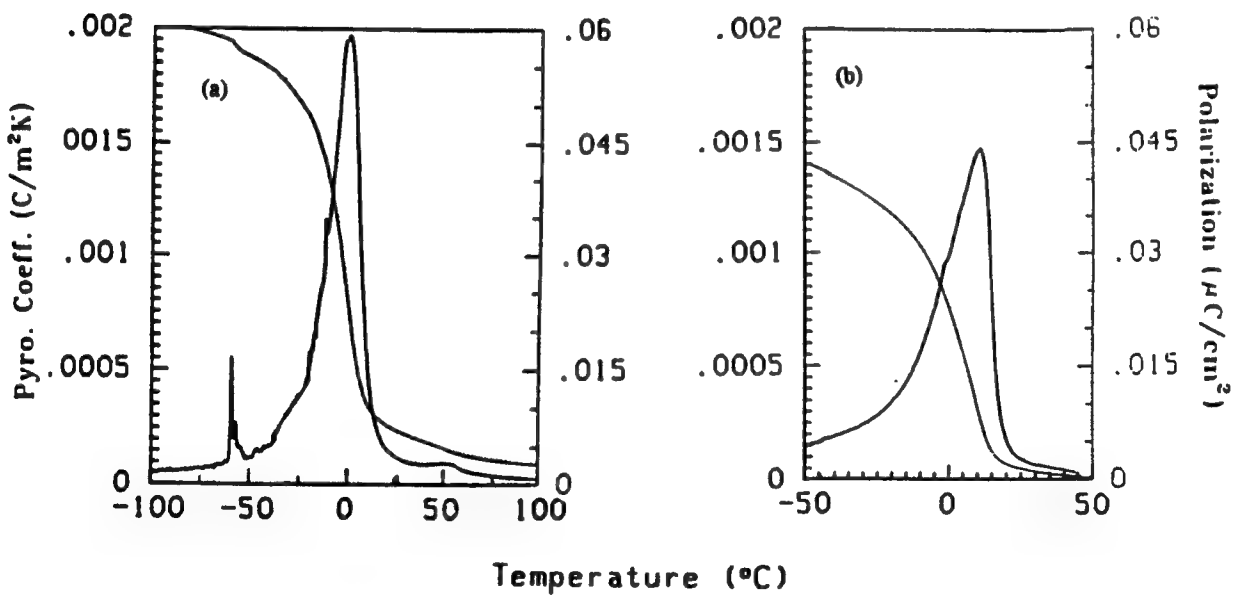


Figure 2. Pyroelectric coefficient and Polarization behavior of:
 (a) PIN/PST(0.025) and (b) PIN/PST(0.975).

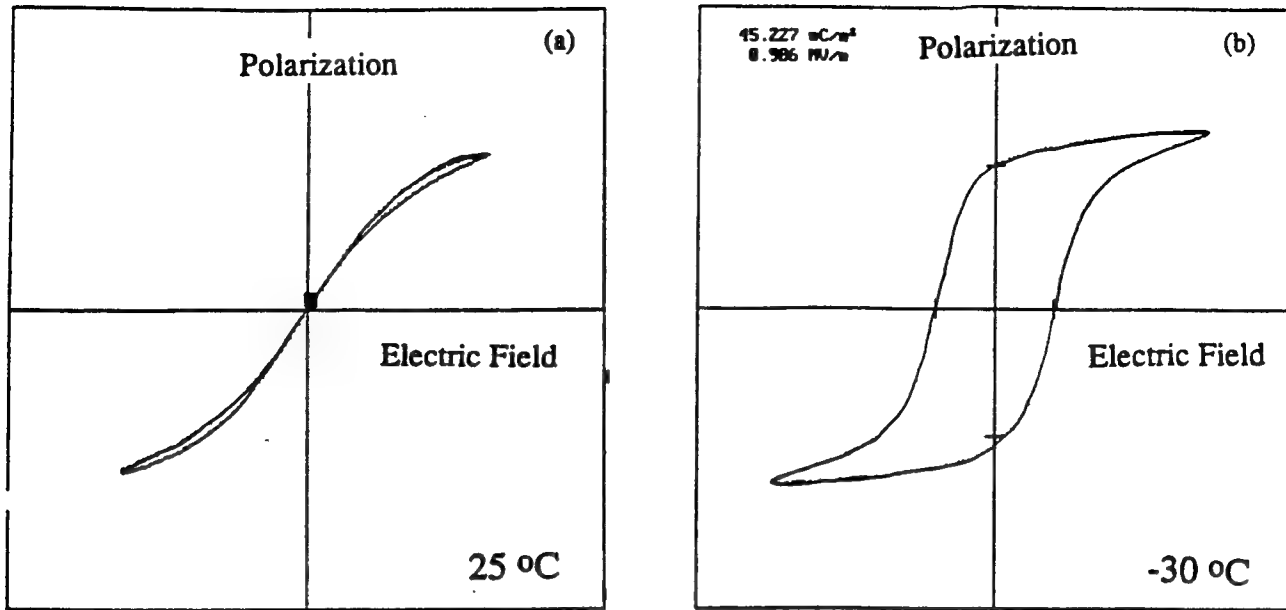


Figure 3. Dielectric hysteresis loops for PIN/PST(0.025) at: (a) 25°C and (b) -30°C ($P_f=4.52 \mu\text{C}/\text{cm}^2$ and $E_c=9.86 \text{ kV}/\text{cm}$).

Using the Byer-Roundy technique the pyroelectric coefficient, p_3 , was determined for the temperature range of -100°C to 100°C. The polarization was then calculated from the pyroelectric coefficient. The polarization behavior showed a relatively long tail between 10°C and 150°C. At room temperature the polarization was found to be 7 $\mu\text{C}/\text{cm}^2$. The polarization continues to increase with decreasing temperature to a saturated maximum value of 64 $\mu\text{C}/\text{cm}^2$ at 100°C. The pyroelectric response was found to reach a maximum value of 0.002 $\text{C}/\text{F}\cdot\text{K}\cdot\text{m}^2$ at 0°C.

Hysteresis measurements were also conducted in the temperature range -100°C to 100°C using a modified Sawyer-Tower circuit. Initially, at room temperature, the unpoled ceramics displayed "antiferroelectric" hysteresis loop. After cooling to -100°C and slowly heating to -30°C the samples showed typical ferroelectric behavior with $P_f=4.52 \mu\text{C}/\text{cm}^2$ and $E_c=9.86 \text{ kV}/\text{cm}$. Further heating to room temperature causes the loop to shrink. At room temperature the remnant polarization had decreased to 1.13 $\mu\text{C}/\text{cm}^2$ and the coercive field had decreased to 5.03 kV/cm . Upon further heating (to 45°C for example) the hysteresis loop slims dramatically and the remnant polarization slowly disappears. In addition, as illustrated in the pyroelectric measurement, the polarization curve has a tail extending to slightly over 150°C.

Following these experiments d_{33} was found to be 0 pC/N as determined by a Berlincourt d_{33} meter. Poling at or above room temperature with fields up to 45 kV/cm was found to have no effect on d_{33} . In addition, no d_{31} was detected even with applied electrical biases of up to $\pm 23 \text{ kV}/\text{cm}$. No attempt has yet been made to pole and/or measure the piezoelectric coefficients at lower temperatures.

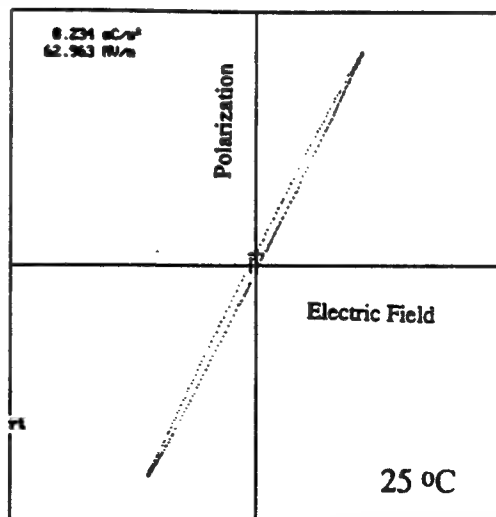


Figure 4. Dielectric hysteresis loop for PIN/PST(0.975) at room temperature.

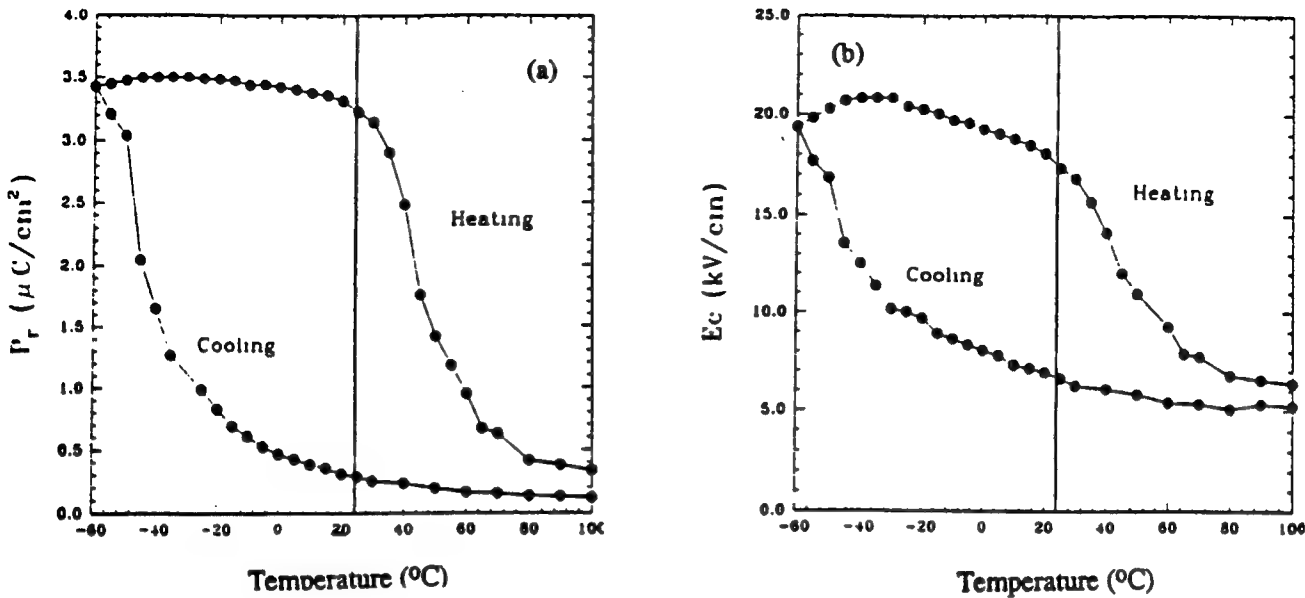


Figure 5. P_r and E_c as a function of temperature for PIN/PST(0.025). Determined from dielectric hysteresis loops.

CONCLUSIONS

To summarize the dielectric properties of PIN/PST(0.025) have been determined. The degree of long range ordering in these samples was found to be 0.73 (i.e., 73% ordered.) Dielectric maximum was found to be at 10 $^{\circ}\text{C}$ and the pyroelectric maximum was found to be at 0 $^{\circ}\text{C}$. At their maximum temperatures, the average dielectric constant, loss, and pyroelectric coefficient were determined to be 1470, 3%, and 0.002 $\text{C}/\text{K}\cdot\text{m}^2$, respectively. Finally, at or above room temperature d_{33} and d_{31} was found to be 0 pC/N with poling fields of up to 45 kV/cm .

REFERENCES

- [1] Giniewicz, J.R., A.S. Bhalla, and L.E. Cross, "Pyroelectric Response and Depolarization behavior of $(1-x)\text{Pb}(\text{Sc}_{1/2}\text{Ta}_{1/2})\text{O}_3 - (x)\text{Pb}(\text{Sc}_{1/2}\text{Ta}_{1/2})\text{O}_3$ Materials", *Ferroelectrics*, **118** 157-164 (1991).
- [2] Giniewicz, J.R., Ph.D. Thesis, The Pennsylvania State University, 1991.
- [3] Groves, P., "Fabrication and Characterisation of Ferroelectric Perovskite Lead Indium Niobate," *Ferroelectrics*, **65** 67-77 (1985).
- [4] Park, S.S., and W.K. Choo, "Pyroelectric and Dielectric Properties of Lead Indium Niobate Ceramics," *Ferroelectrics*, **118** 117-122 (1989).
- [5] Setter, N., Ph.D. Thesis, The Pennsylvania State University, 1980.
- [6] Setter, N., and L.E. Cross, "Flux Growth of Lead Scandium Tantalate and Lead magnesium Niobate Single Crystals," *J. Cryst. Growth*, **50** 555-556 (1980).
- [7] Zhili, C., Y. Xi, and L.E. Cross, "Reversible Pyroelectric effect in $\text{Pb}(\text{Sc}_{1/2}\text{Ta}_{1/2})\text{O}_3$ Ceramics Under DC Bias," *Ferroelectrics*, **44** 271-276 (1989).

APPENDIX 22

Dielectric response of $\text{Li}_{0.4}\text{K}_{0.6}\text{NbO}_3$ crystal in the frequency domain

BYUNG-MOON JIN, A. S. BHALLA

Material Research Laboratory, Pennsylvania State University, PA 16802, U.S.A

JUNG-BAE KIM, JUNG-NAM KIM

Department of Physics, Pusan National University, Pusan 609-735, Korea

Complex impedance and dielectric constants of ferroelectric crystals $\text{Li}_{0.4}\text{K}_{0.6}\text{NbO}_3$ have been studied in the frequency domain at several temperatures. A strong low-frequency dielectric dispersion below 1 kHz was revealed in the high temperature range. The normalized behaviour of the complex dielectric constants satisfies the universal dynamic response with its power exponent $n=0.04$. In the high frequency region, the complex impedance was described by a modified Cole-Cole arc. An equivalent circuit for the transport process of high frequency region has been examined. The temperature-dependent exponent has its minimum at the ferro- to para-electric phase transition point and relaxation frequencies do not satisfy the Arrhenius law in the ferroelectric region

1. Introduction

Ferroelectric crystal $\text{Li}_{0.4}\text{K}_{0.6}\text{NbO}_3$ (LKN) is an important non-linear optical material [1]. LKN has a tungsten-bronze structure and undergoes a diffuse phase transition at around 420°C from a ferroelectric phase (point group 4 mm) to a paraelectric phase (4 mm) on heating [2]. In the previous report on temperature-dependent dielectric measurements [3], we observed a strong low frequency dispersion from room temperature to 800°C , however, the electrical conductivity results did not satisfy the Arrhenius law. This implies that the conduction process of LKN is not fully based on ionic hopping. In the present work, the dielectric dispersion of LKN is studied in the frequency domain at several temperatures encompassing the ferroelectric phase transition. In addition, an a.c. impedance study is carried out and the equivalent circuit is proposed.

2. Experimental procedure

Dielectric constants were measured using the set-up as described previously [3]. Sample dimensions used for the capacitance measurements were 1.44 mm in thickness and 23.48 mm^2 in area. Fired-on platinum electrodes were applied on the plate surfaces perpendicular to the polar c -axis. Complex dielectric constants were measured in the frequency range from 5 Hz to 13 MHz using an HP 4192A Impedance Analyzer. The electrical furnace used in the temperature-dependent measurements was controlled within the accuracy of $\pm 0.5^\circ\text{C}$ at the measuring temperatures. Measured temperature range was from room temperature to 1000°C with temperature step of a 50°C . In order to avoid the effects of parasitic factors, which include stray capacitance and residual inductance of

lead wire, a standard calibration procedure was followed. Reference calibration frequencies were 1 MHz between 500 Hz and 1 MHz, 10 MHz between 1 MHz and 13 MHz and at calibration frequencies below 500 Hz, each frequency measured was calibrated.

3. Results and discussions

Fig. 1 shows the complex dielectric constants as a function of frequencies at various temperatures. Low temperature data have a little dispersive behaviour. Fig. 1a and b show the real dielectric constants and imaginary dielectric constants, respectively. Below 1 kHz, strong dispersions characteristics were noticed, whereas between 1 kHz and 100 kHz, linear frequency-dependent regions were observed; above 400 kHz saturated dielectric constants around the value of 2000 were observed. On the other hand, imaginary dielectric constants showed a similar tendency up to 400 kHz, but they do not have a saturated value above 400 kHz. Imaginary dielectric constants were calculated from real dielectric constants and dissipation factors using the relation of $\epsilon'' = \epsilon'D$. In the calculation of complex dielectric constants and impedances, there were no limiting values of the instruments.

Data obtained at different temperatures were normalized on the same scale [4, 5] to confirm the dynamical versatility of dielectric response of the sample. It is found that the frequency dependence does not change drastically with temperature, at least over the temperature ranges for which the material does not change its structure in any significant manner. The normalized data often provides a 'master curve' which gives a complete description of the dielectric behaviour when accompanied by the locus of the translation

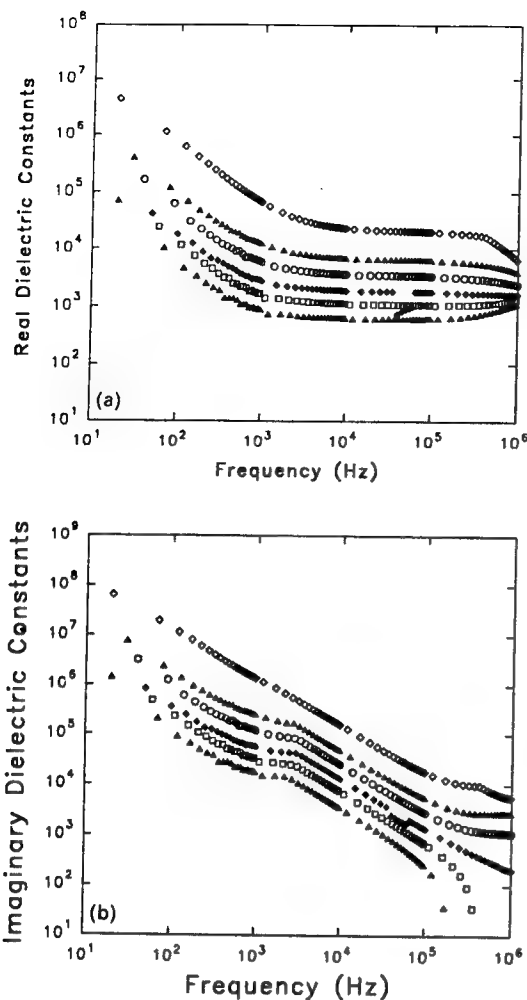


Figure 1 (a) Real dielectric constant as a function of frequency at several temperatures (in the heating cycle); (b) imaginary dielectric constant as a function of frequency at several temperatures (in the heating cycle) (\blacktriangle 750 °C; \square 801 °C; \blacklozenge 850 °C; \circ 901 °C; \blacktriangle 951 °C; \diamond 998 °C).

points [6]. The complex dielectric constants data is plotted on a log-log plot in order to investigate the nature of the frequency response, ω , of the dielectric properties. The expression used for the evaluation is [5]

$$\chi'(\omega) = \cot\left(\frac{n\pi}{2}\right)\chi'(\omega) \propto \omega^{n-1} \quad (1)$$

Fig. 2a and b show the normalized complex dielectric constants at several temperatures between 750 °C and 998 °C. Below 100 kHz, the universal Equation 1 is well satisfied and showed a clear tendency to a 'flat' frequency response of the real dielectric constants up to 400 kHz. Insets show the locus of the normalization for these temperatures. A flat locus indicates the unique relaxation mechanism and in this case, its impedance spectrum should have the same magnitude slope on either side of the peak frequency.

Fig. 3 shows the dynamic universal condition for Equation 1 with exponent $n = 0.04$. It implies that strong low frequency dispersion of LKN is caused by intrinsic point defects [7].

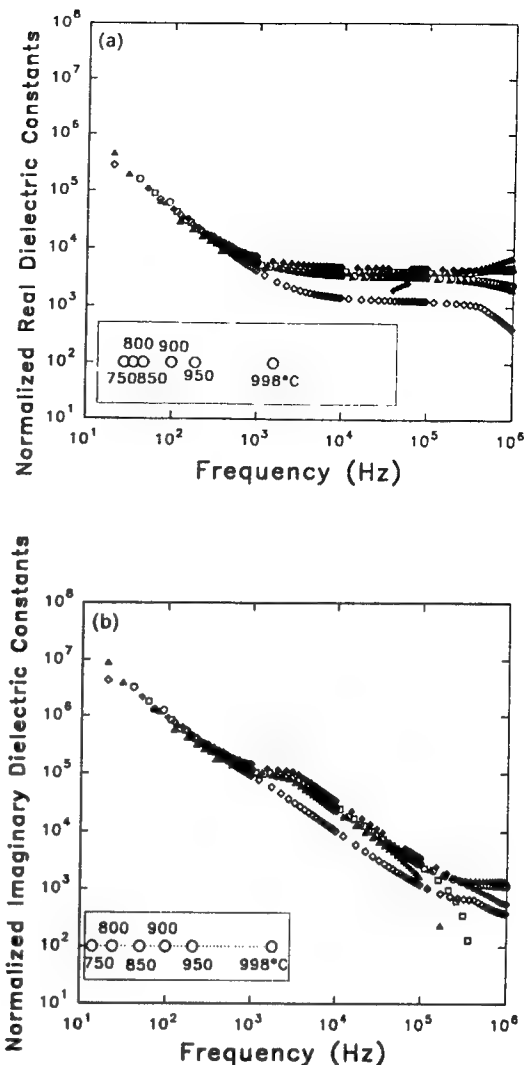


Figure 2 (a) Normalized real dielectric constant as a function of frequency at several temperatures (in the heating cycle); (b) normalized imaginary dielectric constant as a function of frequency at several temperatures (in heating cycle). Inset shows the locus of normalization at each temperature (\blacktriangle 750 °C; \square 801 °C; \blacklozenge 850 °C; \circ 901 °C; \blacktriangle 951 °C; \diamond 998 °C).

In order to investigate the equivalent circuit of LKN and its transport process, we studied the impedance spectra in the frequency domain. Impedance spectroscopy has been widely used for analysing the electrical relaxation in ionic conductors [8, 9] and conducting glasses [10, 11]. Among ferroelectric materials many a.c. complex impedance investigations have been carried out on semiconducting BaTiO₃ [12, 13] and ion conducting LiTaO₃ [14, 15].

Fig. 4 shows, for several temperatures including the ferroelectric phase transition temperature, the variation of the imaginary part of the impedance with frequency on a double logarithmic scale. The slopes of the curve below and above the peaks are the same in magnitude. This means that LKN has a unique relaxation mechanism, which is also supported by the flat nature of the locus of the normalized dielectric constants as shown in Fig. 2. Below 350 °C, the imaginary impedance does not have a peak value but it does show a down trend towards the low frequency limit.

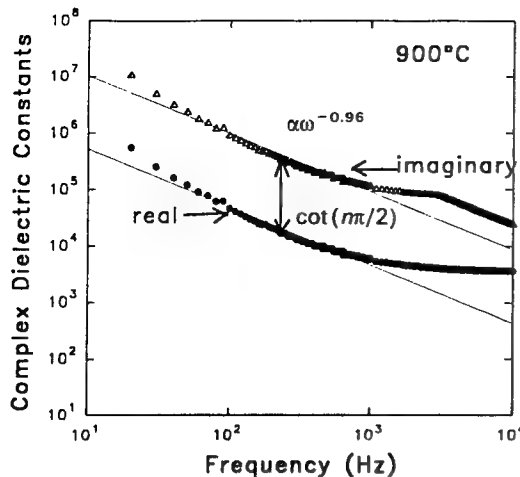


Figure 3 Plots of the universal dynamic response considering the exponent $n = 0.04$.

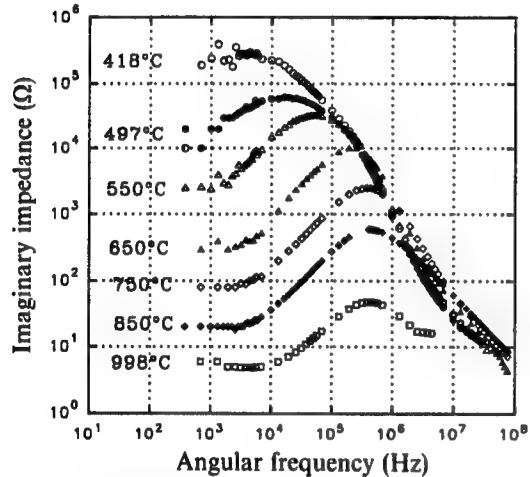


Figure 4 Imaginary part of the impedance versus frequency at various temperatures for the LKN crystal.

This suggests that LKN samples act as an equivalent circuit comprising a parallel combination of capacitance and resistance to the external fields. Thus in this case, impedance spectroscopy has much more importance than the dielectric study.

The impedance study can be ideally described by the Debye expression which may be established considering the material in a parallel circuit as a pure resistor (R_0) with an ideal capacitor (C_0) for the case of a unique relaxation mechanism:

$$Z^* = \frac{1}{\frac{1}{R_0} + i\omega C_0} = \frac{R_0}{1 + \frac{i\omega}{\omega_0}} \quad (2)$$

where $\omega_0 = 1/R_0 C_0$ is the characteristic angular frequency of the equivalent circuit and $\omega = 2\pi f$ is the angular frequency of the applied field. This expression is valid only when the origin of this impedance semi-circle is located on the real axis and has a single relaxation mechanism. But, in real dielectric materials, generally a non-ideal situation is observed. The impedance can be empirically expressed by introduc-

ing a temperature-dependent factor n into the Debye expression, Equation 2. This modification leads to the modified impedance Cole-Cole relation [16]:

$$Z^* = \frac{R_0}{1 + \left(i\frac{\omega}{\omega_0}\right)^{1-n}} \quad (3)$$

This expression gives a circular impedance arc with its centre located below the real axis. In addition, it is valid when the slope of high frequencies is $-(1-n)$ and the slope of low frequencies is $(1-n)$ [5].

The variation of the logarithmic peak frequency (relaxation frequency f_r) as a function of reciprocal temperature (from Fig. 4) is shown in Fig. 5. Minimum relaxation frequency is observed at the transition point ($T_C = 693$ K). This result does not satisfy the Arrhenius law in the ferroelectric phase but it does in the paraelectric phase region.

$$\frac{1}{\tau} = \omega_p = v \exp\left(-\frac{W}{kT}\right) \quad (4)$$

where ω is frequency and W is the activation energy.

Fig. 6 shows the impedance Cole-Cole plot for several selected temperatures in the paraelectric region. Circular behaviour of the plots was observed but the origin of these curves was located below the real axis. A tail in the low frequency region is illustrated by an equivalent circuit having a small capacitor connected in series with the parallel capacitor and resistor. The circular arc indicates that the slopes on the high

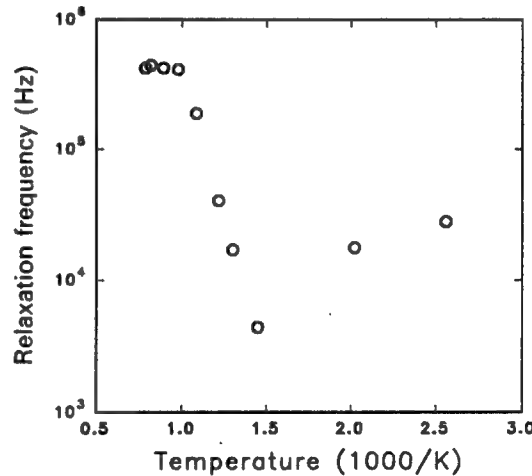


Figure 5 Arrhenius plot of the relaxation frequency for the LKN crystal.

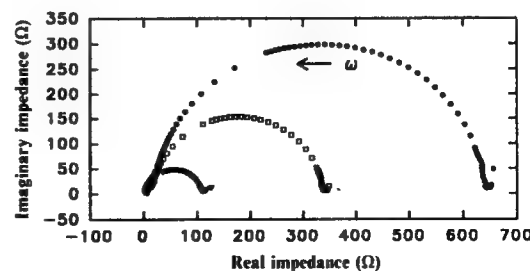


Figure 6 Impedance Cole-Cole plot for several selected temperatures (● 900°C; □ 950°C, △ 998°C).

frequency and low frequency sides are equal. This is also shown in Fig. 4. Thus we can consider the parallel equivalent circuit (capacitor in parallel with a resistor) satisfying the relation Equation 3. It is a very tedious procedure to fit Equation 3 to the experimental data. Instead, it is simpler to fit the data when it forms a circular arc, i.e.

$$(Z' - \alpha(T))^2 + (Z'' - \beta(T))^2 = R(T)^2 \quad (5)$$

where coordinate (α, β) indicate the origin of a circle in the complex impedance plane and R denotes its radius. An ideal Cole-Cole arc is constructed in the case $\beta = 0$ and $\alpha = R$: i.e. the case in Equation 2. If there is a temperature-dependent factor then it belongs to the case $\beta \neq 0$, namely with its origin below the real axis, i.e. the case in Equation 3. In this equation, β corresponds to n in Equation 3.

Thus we have fitted our experimental data using Equation 4. $R(T)$ is equivalent to the diameter of Cole-arc and is the reciprocal of a d.c. conductance in a parallel equivalent circuit. Our sample has a β -value from $-7.5 \times 10^4 \Omega$ to -3.14Ω over the temperature range 322°C to 998°C . $\alpha(T)$ decreases in proportion to the value of R as temperature increases. Rapid decrease of these values is observed at the transition temperature. Although, the mathematical relation is a little complex, we can imply that $\beta(T)$ has a physical meaning related to the exponent in Equation 3. Fig. 7 shows the curve fitting results using Equation 4. According to the lattice dynamic theory [17], one of the transverse optical modes (soft mode) is softened and the restoring force tends to zero at the paraelectric-ferroelectric phase transition. This implies that at T_C , it requires a higher energy loss and smaller energy storage. Thus β tends to be a minimum at the transition point.

4. Conclusion

The impedance behaviour of the ferroelectric $\text{Li}_{1-x}\text{K}_x\text{NbO}_3$ ($x = 0.6$) crystal is investigated be-

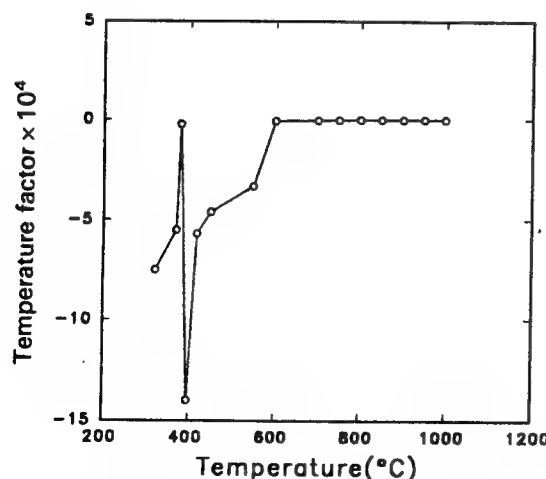


Figure 7 Curve fitting results using Equation 4.

tween room temperature and 998°C in the frequency range 5 Hz – 13 MHz . It satisfies the modified impedance Cole-Cole relation in the high frequency region. Normalized dielectric constants below 1 kHz obey the universal dynamic law with exponent $n = 0.04$ proposed by Joncher. In curve fitting procedures using the parallel equivalent circuit in the high frequency region, the exponent has a minimum at the transition point, thus suggesting that at the transition points the restoring force of the system is minimized.

Impedance Cole-Cole plots indicate that LKN has a hopping process and thus suggest a high density of point defects, as it constructs complete complex impedance circular arc. Although it is reported that LKN has a completely filled tungsten-bronze structure [2], the present results suggest that LKN has unfilled sites.

Acknowledgement

This work was supported in part by the Korea Science and Engineering Foundation (KOSEF) through the Science Research Centre (SRC) of Excellence Program.

References

1. J. E. GEUSIC, H. J. LEVINSTEIN, J. J. RUBIN, S. SINGH and L. G. VAN UITERT, *Appl. Phys. Lett.* **11** (1967) 269.
2. B. A. SCOTT, E. A. GIESS, B. L. OLSON, G. BURNS, A. W. SMITH and D. F. O'KANE, *Mater. Res. Bull.* **5** (1970) 47.
3. B. M. JIN, B. C. CHOI, J. B. KIM, H. R. JEONG, J. W. CHA, J. H. ROH and J. N. KIM, to be published in *J. Korea Physical Society*.
4. T. WIKTORCZYK, *Solid State Commun.* **67** (1988) 143.
5. A. K. JONSCHER, *Dielectric relaxation in solids* (Chelsea Dielectrics Press, London 1983) Chapter 3.
6. R. M. HILL and L. A. DISSADO, *J. Phys. C: Solid State Phys.* **15** (1982) 5171.
7. F. A. LOPEZ, C. R. A. CATLOW and P. D. TOWNSEND, *Point defects in materials* (Academic Press, 1988).
8. C. K. GUO and Y. M. YAN, *Solid State Ionics* **18/19** (1986) 236.
9. Y. T. TSAI and D. H. WHITEMORE, *ibid.* **7** (1982) 129.
10. P. B. MACEDO, C. T. MOYNIHAN and R. BOSE, *Phys. Chem. Glasses* **13** (1972) 171.
11. P. B. MACEDO, R. BOSE, V. PROVENZANO and T. A. LIVITZ, *Amorphous materials* (Wiley, New York, 1972) p. 251.
12. H. S. MAITI and R. N. BASU, *Mater. Res. Bull.* **21** (1986) 1107.
13. S. K. SUNDARAM, *Ferroelectrics* **102** (1990) 129.
14. A. HUANOSTA and A. R. WEST, *J. Appl. Phys.* **61** (1986) 5386.
15. D. C. SINCLAIR and A. R. WEST, *Phys. Rev. B* **39** (1989) 13486.
16. K. S. COLE and R. H. COLE, *J. Chem. Phys.* **9** (1941) 341.
17. T. MITSUI, I. TATSUZAKI and E. NAKAMURA, *An introduction to the physics of ferroelectrics* (Science Press, Peking, 1983).

Received 17 November 1992
and accepted 14 February 1993

APPENDIX 23

phys. stat. sol. (a) **140**, 239 (1993)

Subject classification: 77.80; 77.40; S11.1

Materials Research Laboratories, The Pennsylvania State University, University Park¹) (a) and Department of Physics, Pusan National University, Pusan²) (b)

Dielectric Anomalies in $\text{Li}_{0.4}\text{K}_{0.6}\text{NbO}_3$ Crystals

By

BYUNG-MOON JIN (a), A. S. BHALLA (a), BYUNG-CHUN CHOI (b),
and JUNG-NAM KIM (b)

$\text{Li}_{0.4}\text{K}_{0.6}\text{NbO}_3$ (LKN) belongs to the completely filled tungsten bronze-type ferroelectrics and undergoes a diffuse phase transition at around 420 °C. LKN has two thermal hystereses in the heating and cooling cycles, above and below the transition point. Hysteresis above T_c is wider than the one below T_c and the width of the hysteresis decreases as frequency increases. The Curie range of $\text{Li}_{0.4}\text{K}_{0.6}\text{NbO}_3$ is wider than that of $\text{Pb}(\text{Mg}_{1/3}\text{Nb}_{2/3})\text{O}_3$ (PMN) and $(\text{Sr},\text{Ba})\text{Nb}_2\text{O}_6$ (SBN) and it implies that $\text{Li}_{0.4}\text{K}_{0.6}\text{NbO}_3$ needs a wider temperature range to reach an equilibrium phase than PMN and SBN. In pyroelectric measurements using the current method, $P_s = 20 \mu\text{C}/\text{cm}^2$ in the ferroelectric phase, and the temperature of the pyroelectric current maximum is by 108 K higher than that of the dielectric constant maxima. Dielectric constants do not obey Devonshire's law (Curie-Weiss law) $1/\epsilon \propto (T_c - T)$ and in pyro-measurements, the mean field exponent ($n = 0.4$) is less than 1/2. These imply that $\text{Li}_{0.4}\text{K}_{0.6}\text{NbO}_3$ does not satisfy the single order parameter mechanism.

1. Introduction

Filled tungsten bronze-type ferroelectrics have gained much attention for electro-optic and non-linear optical applications. The crystals have a high stability to intense laser radiation, and have excellent linear and non-linear optical coefficients [1]. The useful non-linear coefficient d_{33} of $\text{Li}_{0.4}\text{K}_{0.6}\text{NbO}_3$ (LKN) is comparable to that of LiNbO_3 [2]. The tetragonal tungsten bronze structure has been discussed by Magnelli and Blomberg [3], Wadsley [4], and by Jamieson et al. [5]. LKN is the first typical tungsten bronze-type ferroelectric which is reported as having a "completely filled" tetragonal tungsten bronze-like structure. The relatively low crystal growth temperature of this material (≈ 1000 °C) and a tetragonal structure at room temperature make it particularly attractive for optical device applications. However, the lithium potassium niobate crystal may also display considerable property variations as a result of compositional fluctuations caused by unstable growth conditions [6 to 8]. Scott et al. [8] reported non-ferroelectric LKN which has orthorhombic structure at room temperature. They reported the non-ferroelectric phase, $\sqrt{10}c \neq a$, and the ferroelectric phase, $\sqrt{10}c = a$, as concluded from their X-ray powder diffraction study. The dielectric measurements showed the T_c broadening with compositional inhomogeneities (effects of excess niobium). Several members in the tungsten bronze family also undergo the diffuse phase transition related to the nanoscale compositional fluctuations (relaxor behavior).

¹) University Park, PA 16802, USA.

²) 609-735 Pusan, Korea.

Although non-linear optical properties of LKN have been studied by many investigators, its dielectric properties are not fully discussed in the frequency dependent measurements, especially. In this paper, we discussed the temperature dependence of the dielectric constants at several frequencies and the spontaneous polarization of an LKN crystal of well established composition.

2. Experiments

LKN mixed crystals were grown by the Czochralski method. The growth procedure was fully automatized with computer software [9]. The starting composition was prepared from the stoichiometric ratio of Li_2CO_3 , Nb_2O_5 , and K_2CO_3 of 99.99% purity. In the crystal growth procedure, there were some difficulties in using *c*-axis oriented seed. We could not get large single crystals due to the crystal cracking problem on cooling. Single crystals of excellent optical quality were grown on *b*-axis oriented seed. The crystals were pale yellow in color. Crystal pulling and rotation rates used in the typical growth runs were 0.2 to 0.4 mm/h and 20 to 30 r.p.m., respectively.

In mixed crystal systems, the real composition of the grown crystal is usually different from the starting composition of the melt. Therefore, it is necessary to investigate the real composition. We investigated the real composition of our samples using SEM-EDX (scanning electron microscopy with energy dispersive X-rays: EDAX 9100, Phillips Co.). Probe cross section area was fixed to about 30.0 nm.

Dielectric properties were measured by the method described previously [9]. Sample dimensions used in the dielectric constant measurements were typically 27.5 mm² in area and 0.37 mm in thickness and in the pyroelectric measurements 16.8 mm² in area and 0.9 mm in thickness, respectively. For the measurements, the sample was placed in the computer controlled furnace with a temperature accuracy of ± 0.2 K and heated with a constant heating rate of 1 K/min.

Dielectric constant versus temperature measurements were done using an LF impedance analyzer (Hewlett-Packard, 4192A) in the temperature range from room temperature to 800 °C at several frequencies. In pyroelectric current measurements, constant heating rate 1K/min was maintained throughout the experiment by using the programmable temperature controller. All measurements were automated with the help of computer software [9].

3. Results and Discussions

We investigated the real composition of the crystal used in this study, using SEM-EDX. To get accurate results, the composition was determined at six points on the same sample and an average value was calculated. In this paper, the sample used for study had the real composition of $x = 0.60$ (potassium content). We used the same sample through all the experiments to provide consistency.

Fig. 1 shows the dielectric constant ϵ_{33} versus temperature of LKN for several frequencies during the heating cycle. Dielectric constant maxima are observed around 693K except for the 1 kHz data. All these anomalies have a wide temperature range, but the position of the maxima is not shifted in the measured frequency range.

Fig. 2 shows the dielectric loss versus temperature. All loss factor plots have a peak temperature lower than that of the dielectric constant maxima. The abrupt increase in the loss apparently is due to the increase in conductivity on the high temperature side. Loss

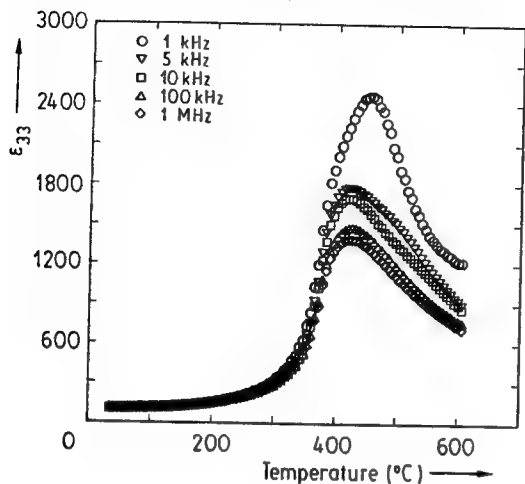


Fig. 1. Dielectric constant vs. temperature for LKN single crystal

peaks do not coincide with the temperature of the dielectric constant maxima, but coincide with the maximum slope of the dielectric constant versus temperature plot. These facts in general are characteristic of diffuse phase transition (DPT) materials [10, 11]. Scott et al. [8] by using optical and X-ray measurements reported that the ferroelectric phase of LKN has tetragonal symmetry with axial ratio $\sqrt{10} c = a$. Also, they reported that the non-ferroelectric phase has an orthorhombic structure and $\sqrt{10} c/a = 0.997$. The results on our sample suggested the tetragonal symmetry and showed a uniaxial optical conoscopic figure. X-ray powder diffraction analysis on LKN gave the value $\sqrt{10} c/a = 1$ [12]. Hysteresis loops could not be observed in LKN due to the fact that it has an extremely high coercive field strength, $\approx 900 \text{ kV/cm}$ [13] (comparing to 70 kV/cm in the case of LiNbO_3). Thus, we concluded that the ferroelectric phase exists at room temperature and the dielectric constant maxima represent the diffuse phase transition [14].

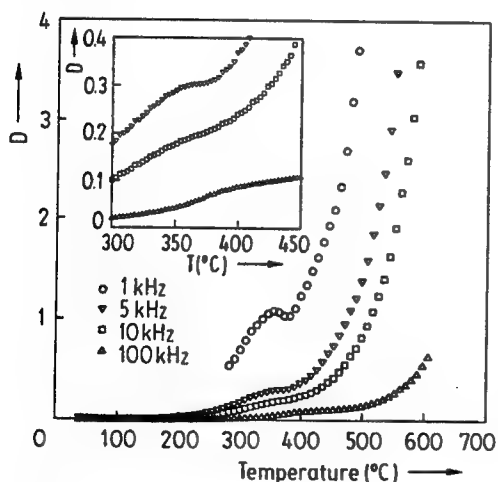


Fig. 2. Dielectric loss vs. temperature for LKN single crystal

Two characteristic features are seen in Fig. 1. There is no frequency dependent dispersion below the transition temperature range, and above the transition point there is a large dispersion in dielectric constant with frequency. This feature is in contrast with the usual diffuse phase transition materials. In the case of $\text{Sr}_x\text{Ba}_{1-x}\text{Nb}_2\text{O}_6$ (SBN) [15] and $\text{Pb}_3\text{MgNb}_2\text{O}_9$ (PMN) [16] and materials of the relaxor family, large dispersion occurs below the dielectric constant maxima and the transition temperature shifts to the higher temperature side and the dielectric constant maxima value decreases as frequency increases. On the other hand, in the case of LKN, larger dispersions were observed above the transition point, and the transition maxima decreased and the range of dielectric constant maxima decreased as the frequency increased. LKN has a large Curie range [17] at 5 kHz and runs over 205 K at around dielectric maxima.

Around the dielectric constant maxima, there is a large thermal hysteresis between heating and cooling cycles. Fig. 3a shows this thermal hysteresis of dielectric constant versus temperature at 1 kHz. In this figure, two hysteresis regions were observed around the transition temperature; a larger hysteresis above the transition temperature and a smaller hysteresis below the transition point due to the external field induced transition and no thermal hysteresis has been observed above the transition point [18]. While the area of lower hysteresis remains constant, as frequency is increased, the width of the upper hysteresis is suppressed. These properties are closely related with the low frequency dielectric dispersion already mentioned.

A relatively large anomaly was found in the 1 kHz data and the temperature of its dielectric constant maxima is quite different from the data at higher frequencies. It implies that LKN has large dielectric relaxation in the lower frequency regions.

Dielectric properties of ferroelectric materials are described by the ionic conductivity at radio frequency, associated with the electric field induced ion transport [19]. In LKN, the transition mechanism can also be explained by the transition entropy and ionic conductivity. The ac conductivities at several frequencies derived from $\sigma = \epsilon_0 \epsilon'' \omega$ are shown in Fig. 4. A broad and anomalous change of conductivity σ_{33} related to the phase transition is observed

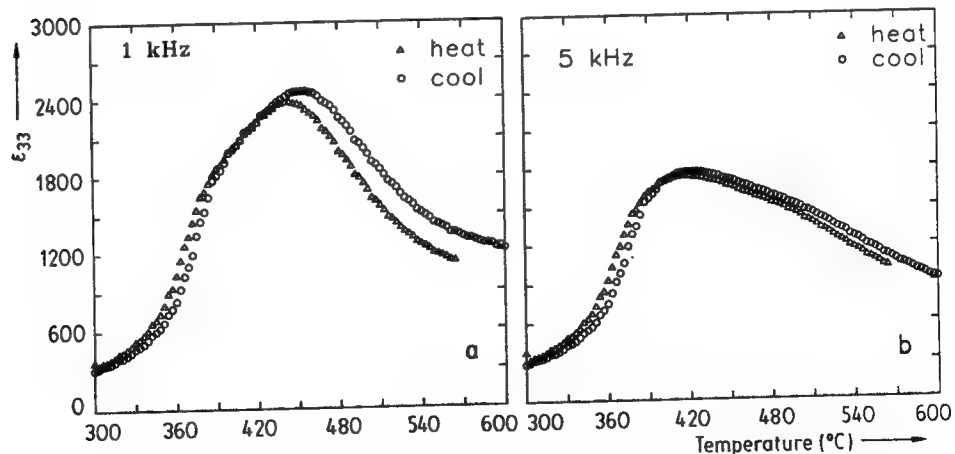


Fig. 3. Thermal hysteresis between the heating and cooling runs at a) 1 and b) 5 kHz

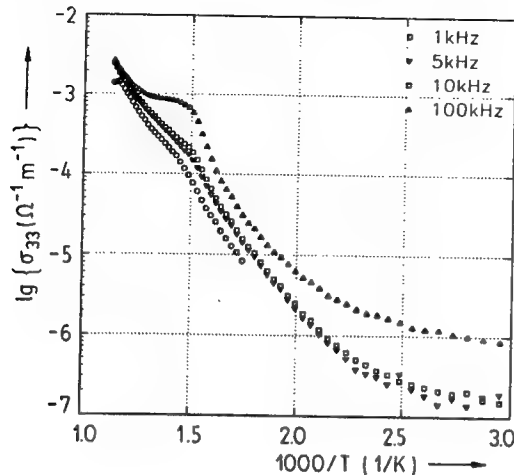


Fig. 4. Arrhenius plot of ac conductivities of LKN

near T_c . Two distinct slopes are shown in the figure. Below 418 K, extremely low activation energy and deviation from an Arrhenius plot are mainly due to the low frequency dielectric relaxation and clustering or precipitation [20] which is not yet clear. Above 418 K, the Arrhenius relation is satisfied over the whole temperature range and its activation energy as determined from the slope of the Arrhenius plot is 0.3 eV in average.

A relatively large anomaly in the activation energy plots is found in 100 kHz data. It implies that the stronger the increase in the frequency, the larger is the required activation energy. Although there is a little splitting at each frequency on the high temperature side, the low temperature side has large splitting as the frequency decreased. If we assume that the high temperature conductivity disturbs the ionic conductivity splitting (Fig. 2), we can imply that LKN has hopping conductivity. If so either LKN should have unfilled tungsten bronze sites or have high density of point defects. We can imply that LKN has a high point defect density which is reflected in the low frequency region of the dielectric response of LKN [21].

We then suppose that, although LKN has a completely filled tungsten bronze structure, compositional inhomogeneity and excess niobium play a role in the hopping process and are the main reason causing the dielectric dispersion.

Fig. 5 shows the spontaneous polarization of LKN as calculated from the pyroelectric data. Below 400 °C, the pyrocurrent does not show a remarkable anomaly, it increases gradually and reaches its maximum at 528 °C. The half width of the pyrocurrent peak is ≈ 40 K.

Abrahams et al. [13] reported that the pyroelectric current has a maximum which differs from the peak in dielectric constant by as much as 100 K. On the other hand, Nagai and Ikeda [22] reported the peak temperature in pyroelectric and dielectric measurements both almost at the same temperature. Spontaneous polarization calculated from the data in the ferroelectric phase is $20 \mu\text{C}/\text{cm}^2$ and it compares well with the value of $22 \mu\text{C}/\text{cm}^2$ reported by Nagai and Ikeda. LKN showed a second-order-like phase transition in dielectric constant measurements. The Curie constant calculated from the inverse dielectric constant data is in the order of 10^5 indicating the typical displacive phase transition [10]. But the slopes of

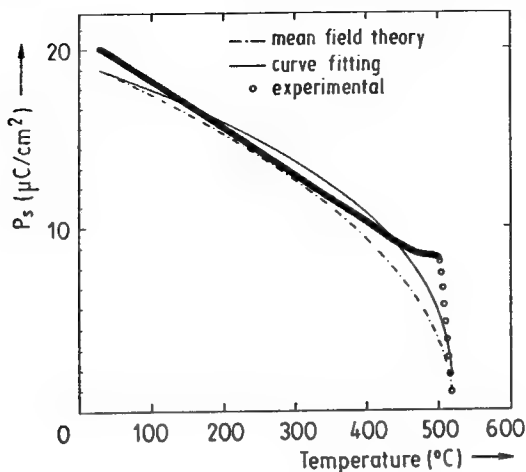


Fig. 5. Spontaneous polarization of LKN as calculated from the pyroelectric data

the inverse dielectric constant above and below T_c do not satisfy the Devonshire thermodynamic relation $1/\varepsilon \propto (T_c - T)$ except for the very narrow region around the phase transition point and in the pyroelectric measurements, it also has not the exponent of the mean field theory of 1/2. We have fitted the pyroelectric results in the equation $P_s \propto (T_c - T)^n$ and from this fitting get the value $n = 0.4$.

4. Conclusion

Based on the dielectric measurements, it is concluded that LKN undergoes a diffuse phase transition and dielectric constant maximum occurs at 420 °C for 5 kHz. LKN has low frequency dielectric dispersion which could be explained by assuming a high density of point defects. LKN has two thermal hystereses between the cooling and heating cycles: one above the transition temperature which was suppressed rapidly as the frequency increased and can be explained qualitatively by the fact that LKN has frequency dependent compositional fluctuations resulting in the low frequency relaxation.

The spontaneous polarization in the ferroelectric phase is $20 \mu\text{C}/\text{cm}^2$ and is comparable to the result of Nagai and Ikeda. The pyroelectric current maximum differs by 108 K from that of the dielectric constant result. Pyroelectric results do not satisfy the mean field theory value.

These results indicate that though LKN has a completely filled tungsten bronze structure, compositional inhomogeneity and excess niobium trigger the hopping process which could be the main reason for the dielectric dispersion.

Dielectric constants do not follow the Curie-Weiss behavior $1/\varepsilon \propto (T_c - T)$ and in the pyroelectric measurements, mean field exponent ($n = 0.4$) is smaller than the expected value 0.5.

Acknowledgement

This work was supported in part by the Korea Science and Engineering Foundation (KOSEF) through the Science Research Center (SRC) of Excellence Program.

References

- [1] J. E. GEUSIC, H. J. LEVINSTEIN, J. J. RUBIN, S. SINGH, and L. G. VAN UITERT, *Appl. Phys. Letters* **11**, 269 (1967).
- [2] L. G. VAN UITERT, H. J. LEVINSTEIN, J. J. RUBIN, C. D. CAPIO, E. F. DEARBORN, and W. A. BONNER, *Mater. Res. Bull.* **3**, 47 (1969).
- [3] A. MAGNELL and B. BLOMBERG, *Acta chem. Scand.* **5**, 372 (1951).
- [4] A. D. WADSLEY, *Rev. pure appl. Chem.* **5**, 165 (1955).
- [5] P. B. JAMIESON, S. C. ABRAHAMS, and J. L. BERNSTEIN, *J. chem. Phys.* **50**, 4352 (1969).
- [6] L. G. VAN UITERT, S. SINGH, H. J. LEVINSTEIN, J. E. GEUSIC, and W. A. BONNER, *Appl. Phys. Letters* **11**, 161 (1967).
- [7] T. FUKUDA, *Japan. J. appl. Phys.* **8**, 122 (1969).
- [8] B. A. SCOTT, E. A. GIESS, B. L. OLSON, G. BURNS, A. W. SMITH, and D. F. O'KANE, *Mater. Res. Bull.* **5**, 47 (1970).
- [9] J. B. KIM, B. C. CHOI, B. M. JIN, J. N. KIM, K. S. LEE, and J. H. KIM, *J. Korean Phys. Soc.* **25**, 368 (1992).
- [10] M. E. LINES and A. M. GLASS, *Principles and Applications of Ferroelectrics and Related Materials*, Oxford University Press, London 1982 (p. 286).
- [11] K. MAEDA, S. TASAKA, and N. INAGAKI, *Japan. J. appl. Phys.* **30**, L2107 (1991).
- [12] BYUNG-MOON JIN, Thesis, Pusan National Univ., 1991.
- [13] S. C. ABRAHAMS, P. B. JAMIESON, and J. L. BERNSTEIN, *J. chem. Phys.* **54**, 2355 (1971).
- [14] F. W. AINGER, J. A. BESWICK, W. P. BICKLEY, R. CLARKE, and G. V. SMITH, *Ferroelectrics* **2**, 183 (1971).
- [15] G. SCHMIDT and H. ARNOT, *Proc. 3rd Internat. Conf. Phonon Phys. and 6th Internat. Conf. Phonon Scatt. in Condensed Matter*, Heidelberg, August 21 to 25, 1989, Vol. 2, (p. 301).
- [16] G. A. SMOLENSKII, V. A. ISUPOV, A. A. AGRANOVSKAYA, and S. N. POPOV, *Fiz. tverd. Tela* **2**, 2906 (1960).
- [17] G. A. SMOLENSKII and V. A. ISUPOV, *Dokl. Akad. Nauk. SSSR* **97**, 653 (1954).
- [18] G. H. JONKER, *Mater. Res. Bull.* **18**, 301 (1983).
- [19] F. A. LOPEZ, C. R. A. CATLOW, and P. D. TOWNSEND, *Point Defects in Materials*, Academic Press, 1988 (p. 238).
- [20] F. A. LOPEZ, C. R. A. CATLOW, and P. D. TOWNSEND, *ibid.* (p. 240).
- [21] B. M. JIN, A. S. BHALLA, J. B. KIM, and J. N. KIM, *J. Mater. Sci.* (1993), in press.
- [22] T. NAGAI and T. IKEDA, *Japan. J. appl. Phys.* **12**, 199 (1973).

(Received December 9, 1992; in revised form April 8, 1993)

APPENDIX 24

Optical Study of Domains in $\text{Ba}(\text{Ti}_{1-x}\text{Sn}_x)\text{O}_3$ Ceramics

Ki-Young Oh,* Kenji Uchino,* and L. Eric Cross*

International Center for Actuators and Transducers, Materials Research Laboratory,
The Pennsylvania State University, University Park, Pennsylvania 16802

Domain structures of $\text{Ba}(\text{Ti}_{1-x}\text{Sn}_x)\text{O}_3$ ($x = 0, 0.05, 0.1, 0.13$) ceramics were observed dynamically under an electric field at various temperatures using a high-resolution charge-coupled-device (CCD) microscope system. The $\text{Ba}(\text{Ti}_{1-x}\text{Sn}_x)\text{O}_3$ ceramics showed a significant difference in domain structure and motion with changing composition: the domain structure became tiny and complex with increasing x , and the domain reorientation was easily induced with increasing and decreasing electric field. The results of the domain observations coincided well with electrical measurement data.

I. Introduction

OBSERVATION of domain structures and domain motion is very useful for understanding the physical properties of ferroelectric materials because domains are fundamentally associated with ferroelectricity. For the past few years we have been reporting on the dynamic domain motion in single crystals such as barium titanate and lead zinc niobate based compositions.^{1,2}

This paper concerns the domains in $\text{Ba}(\text{Ti},\text{Sn})\text{O}_3$ ceramics. $\text{Ba}(\text{Ti},\text{Sn})\text{O}_3$ solid solutions are known as typical relaxor ferroelectric materials, and they exhibit electrical and electromechanical characteristics associated with relaxor ferroelectrics such as very small hysteresis in the field-induced polarization and strain.^{3,4} These materials may provide a new category of useful actuator ceramics. Our investigation is focused on the

domain motion in these materials as a means of analyzing the electrical characteristics.

II. Experimental Procedure

Samples of BaTiO_3 (BT), $\text{Ba}(\text{Ti}_{0.95}\text{Sn}_{0.05})\text{O}_3$ (BTS-5), $\text{Ba}(\text{Ti}_{0.9}\text{Sn}_{0.1})\text{O}_3$ (BTS-10), and $\text{Ba}(\text{Ti}_{0.87}\text{Sn}_{0.13})\text{O}_3$ (BTS-13) were prepared by a conventional mixed-oxide method. Starting raw materials were BaCO_3 , TiO_2 , and SnO_2 . Powders were mixed with ethyl alcohol and zirconia grinding media and ground for 48 h. The slurry was dried and calcined at 1100°C for 2 h. The powders were ball-milled for 48 h, then dried, and 3 wt% of binder was mixed with the powder. Disks 13 mm in diameter were pressed and sintered at 1350°C for 10–50 h in air. Sintered disks were sliced and polished 100 μm in thickness. One side of each sample was finished with 0.25- μm diamond paste and attached to a glass plate using resin; then the other side was polished and finished with 0.25- μm diamond paste so that the sample thickness was less than 30 μm . Gold electrodes were

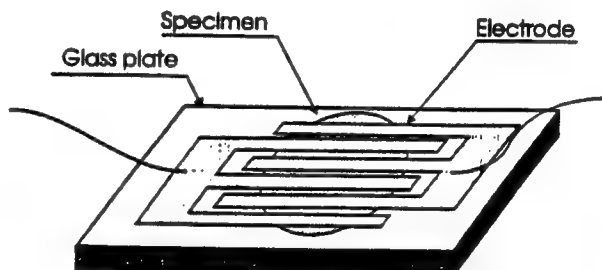


Fig. 1. Configuration of sample.

D. Clarke—contributing editor

Manuscript No. 194044. Received November 16, 1993; approved July 27, 1994.
Supported by the Office of Naval Research under Contract No. N00014-91-J-4145.

*Member, American Ceramic Society.

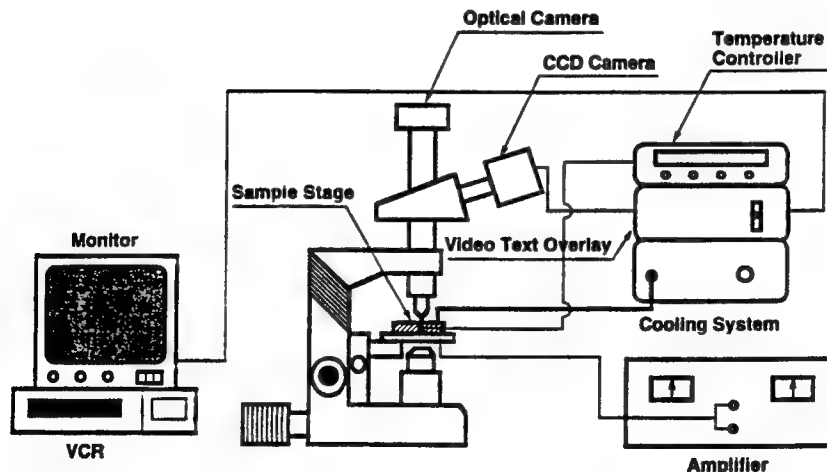


Fig. 2. Configuration of CCD microscope system.

sputtered on the sample surface, and then silver wires were attached to the electrode as shown in Fig. 1.

Domain motions of samples were observed with a high-resolution (480 000 pixels) CCD microscope (Japan Hightech Co.) at various temperatures with an electric field applied parallel to the surface. Figure 2 shows the CCD microscope system. This system consists of an optical microscope with a CCD camera, a temperature control unit, and a display. The maximum magnification of this microscope is $\times 1000$, and the controllable temperature range of the sample holder is from -190° to 600°C . The reasons for using a CCD microscope are as follows: (1) SEM or TEM has higher magnification but it is difficult to apply an electric field to samples and (2) ordinary optical microscopy cannot record the domain motion.

The dielectric constant versus temperature was measured in the temperature range from -100° to 200°C using an automated Hewlett-Packard system. Polarization versus electric field (P - E) curves were measured with a Sawyer-Tower circuit.

Strain-field characteristics were measured using a linear differential transformer.

III. Results and Discussion

Figure 3 shows the temperature dependence of permittivity for BT, BTS-5, BTS-10, and BTS-13. The Curie temperature shifts to lower values, and the shape of the peak becomes remarkably broader with increasing Sn content. The Curie temperatures of BT, BTS-5, BTS-10, and BTS-13 are 121.4° , 85.7° , 46.1° , and 25.3°C , respectively.

Electrical and electromechanical properties such as the P - E and field-induced strain characteristics were measured at room temperature, and the results are shown in Figs. 4 and 5. Compared with the BT samples, the BTS samples show smaller remanent polarization and less hysteresis. This is due to the Curie temperature shift to lower temperatures and the change of the phase transition characteristic from sharp to diffuse with increasing Sn content. The crystal structure of both BTS-10 and BTS-13 at room temperature was found to be pseudocubic. The field-induced strain curves show a trend similar to the P - E curves (Fig. 5). With increasing Sn content, the hysteresis becomes smaller.

Figure 6 shows the typical domain structures of BT, BTS-5, BTS-10, and BTS-13 samples at room temperature. The domain walls of BT are very clear straight lines, and the width of the domain is rather thick. On the other hand, the domains of BTS-5 are tiny and less well-defined. With increasing Sn content, these domain walls became more tiny and less well-defined, and finally, could not even be found in large grains (BTS-13). Variation of the domain structure with temperature was also observed, and the results are shown in Figs. 7–10. With increasing temperature, the domain walls became unclear and disappeared completely above the Curie temperature. BTS-5 showed clear and simple domain structure at 55°C because it has a tetragonal phase at this temperature. When the temperature was decreased, the BT and BTS samples showed different results.

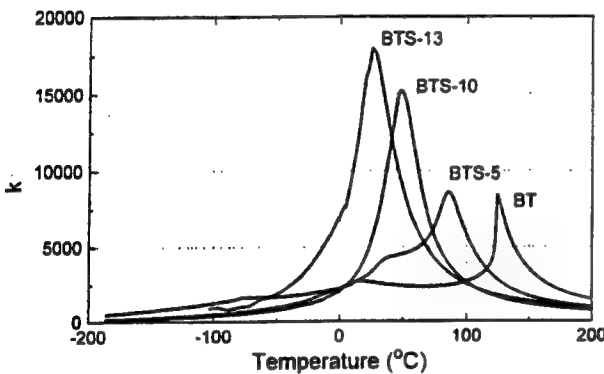


Fig. 3. Permittivity vs temperature characteristics.

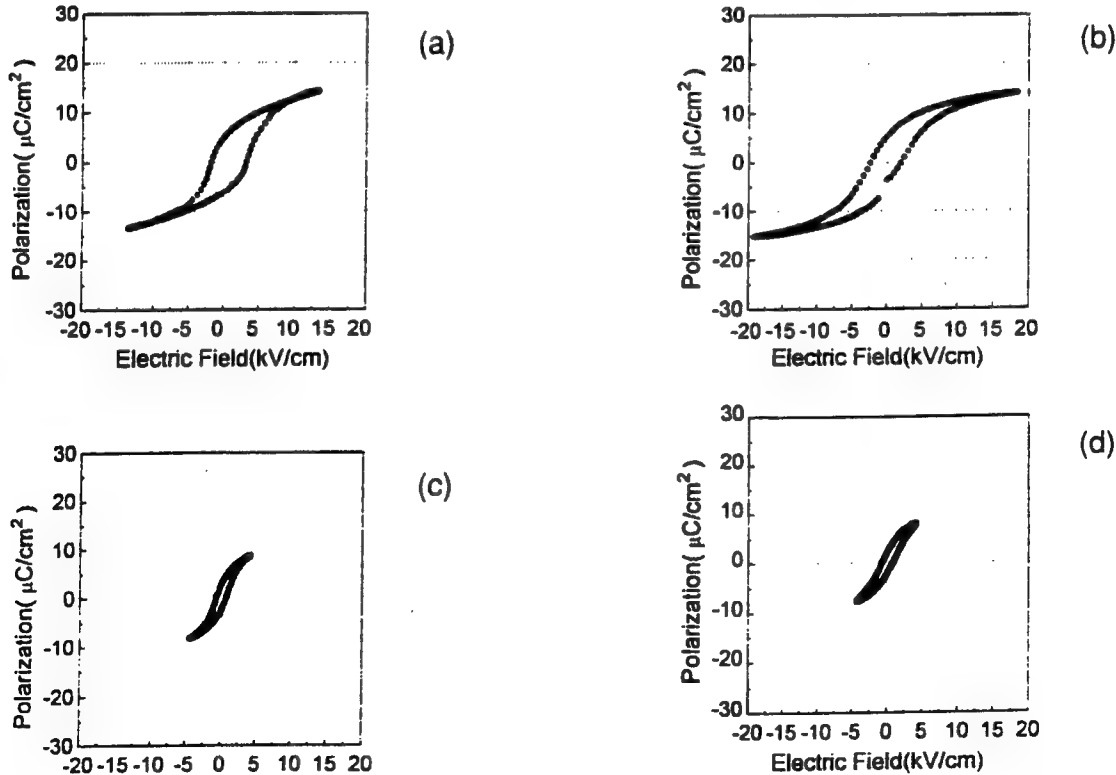


Fig. 4. P - E characteristics of (a) BT, (b) BTS-5, (c) BTS-10, and (d) BTS-13 samples.

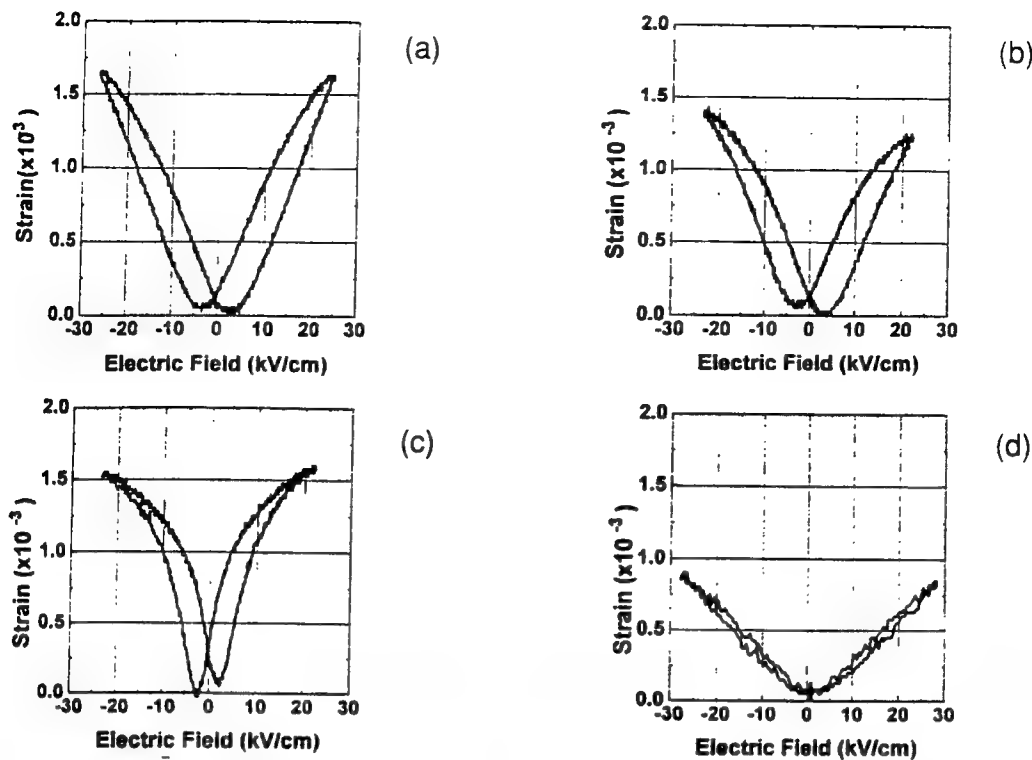


Fig. 5. Field-induced strain characteristics of (a) BT, (b) BTS-5, (c) BTS-10, and (d) BTS-13 samples.

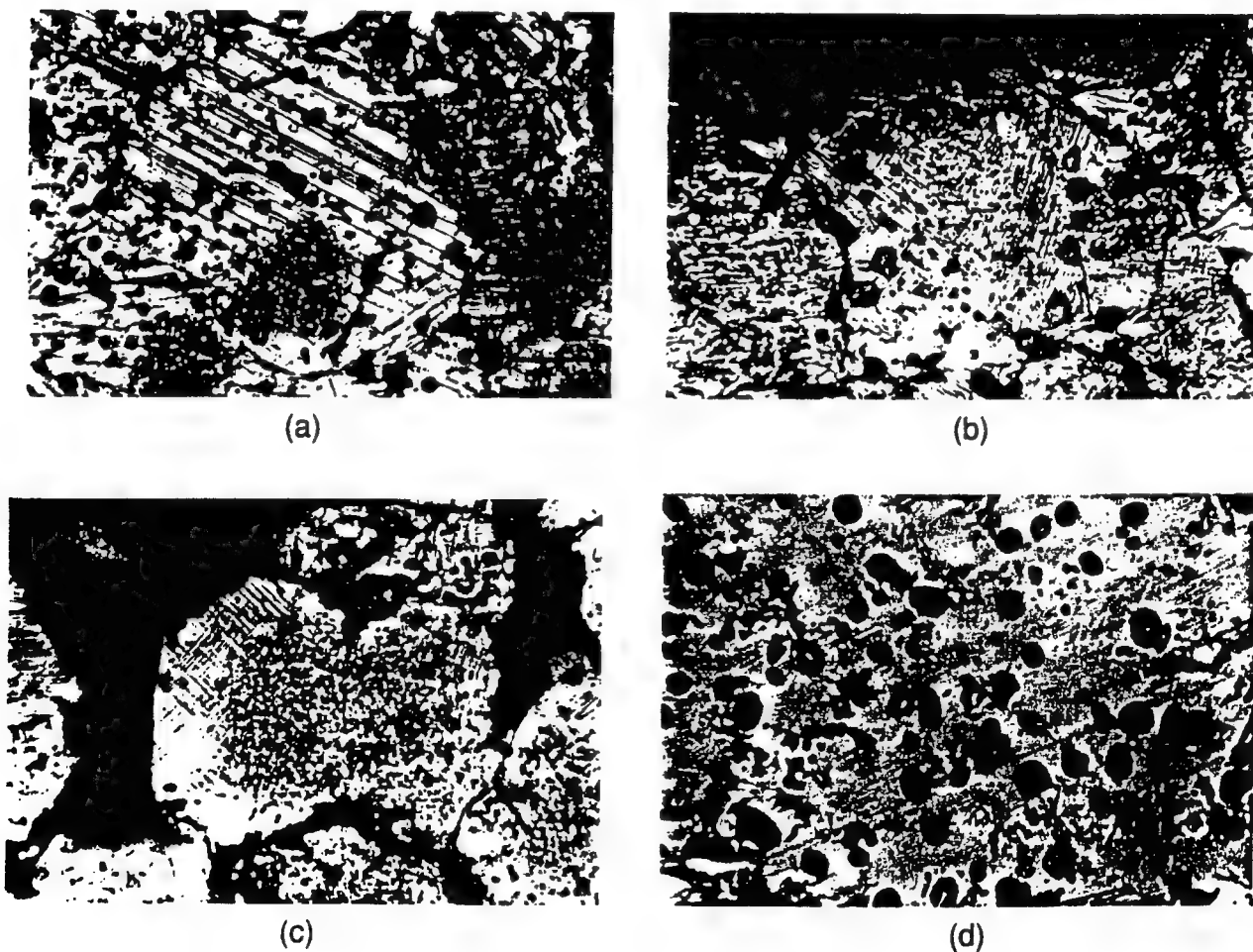


Fig. 6. Domain structures of (a) BT, (b) BTS-5, (c) BTS-10, and (d) BTS-13 (5 kV/cm) samples.

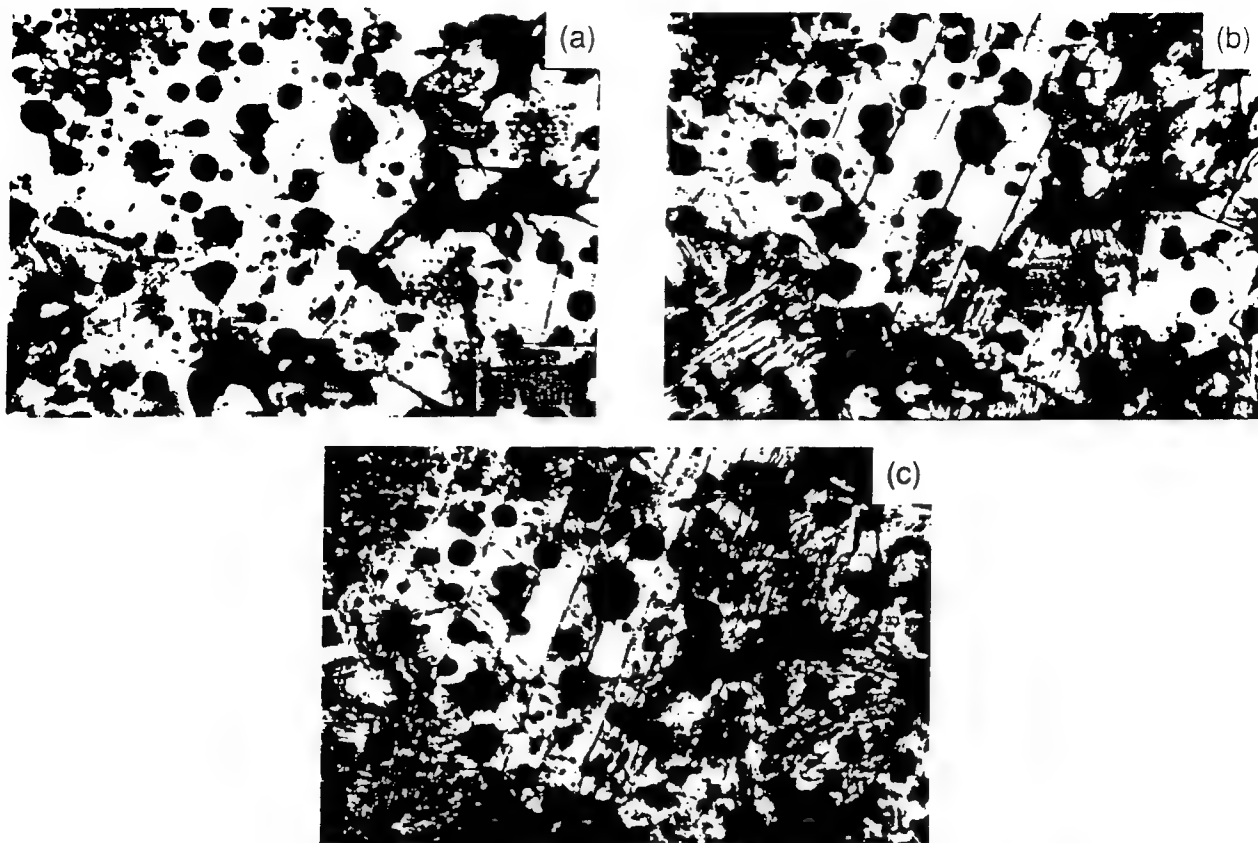


Fig. 7. Domain structures of BT samples as a function of temperature: (a) 143°, (b) 24°, and (c) 0°C.

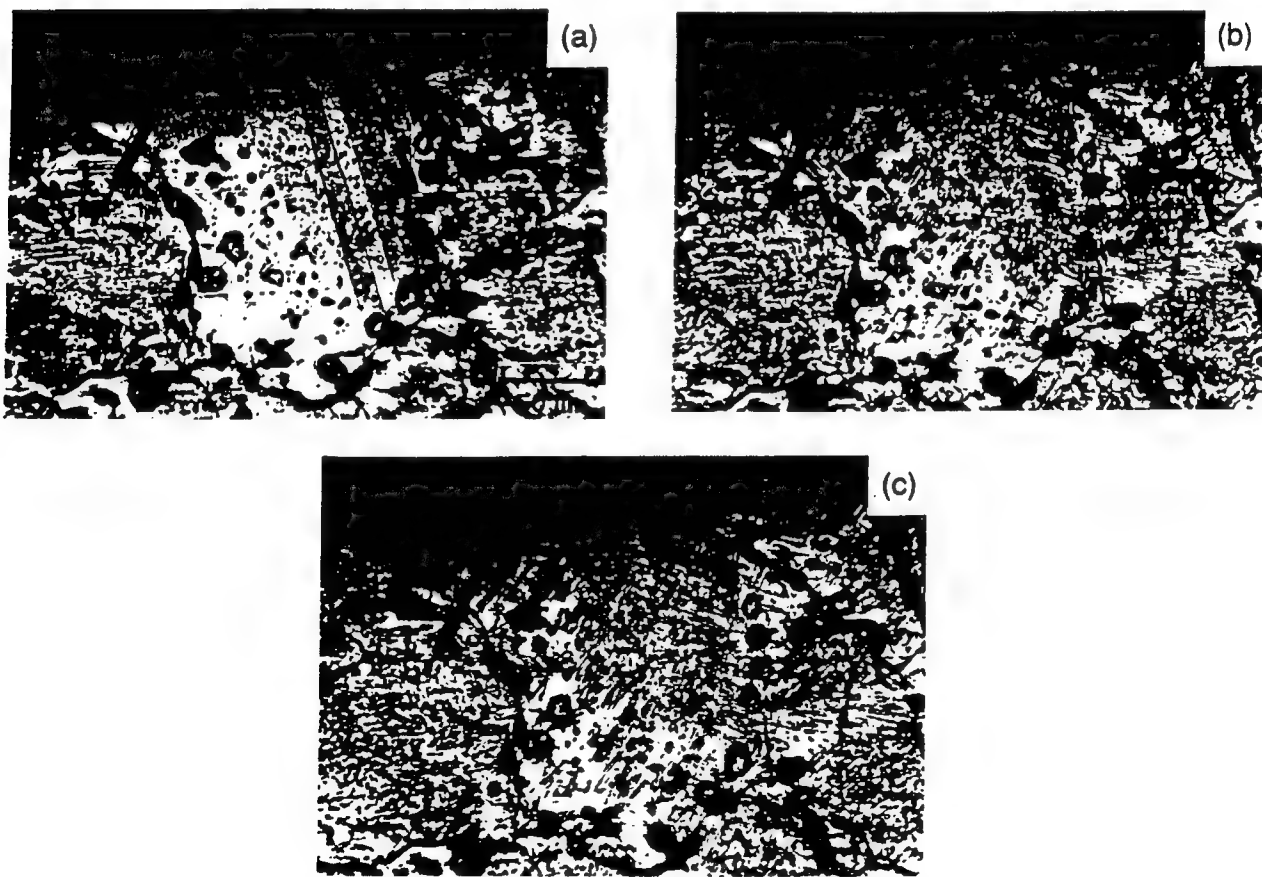


Fig. 8. Domain structures of BTS-5 samples as a function of temperature: (a) 55°, (b) 0°, and (c) -50°C.

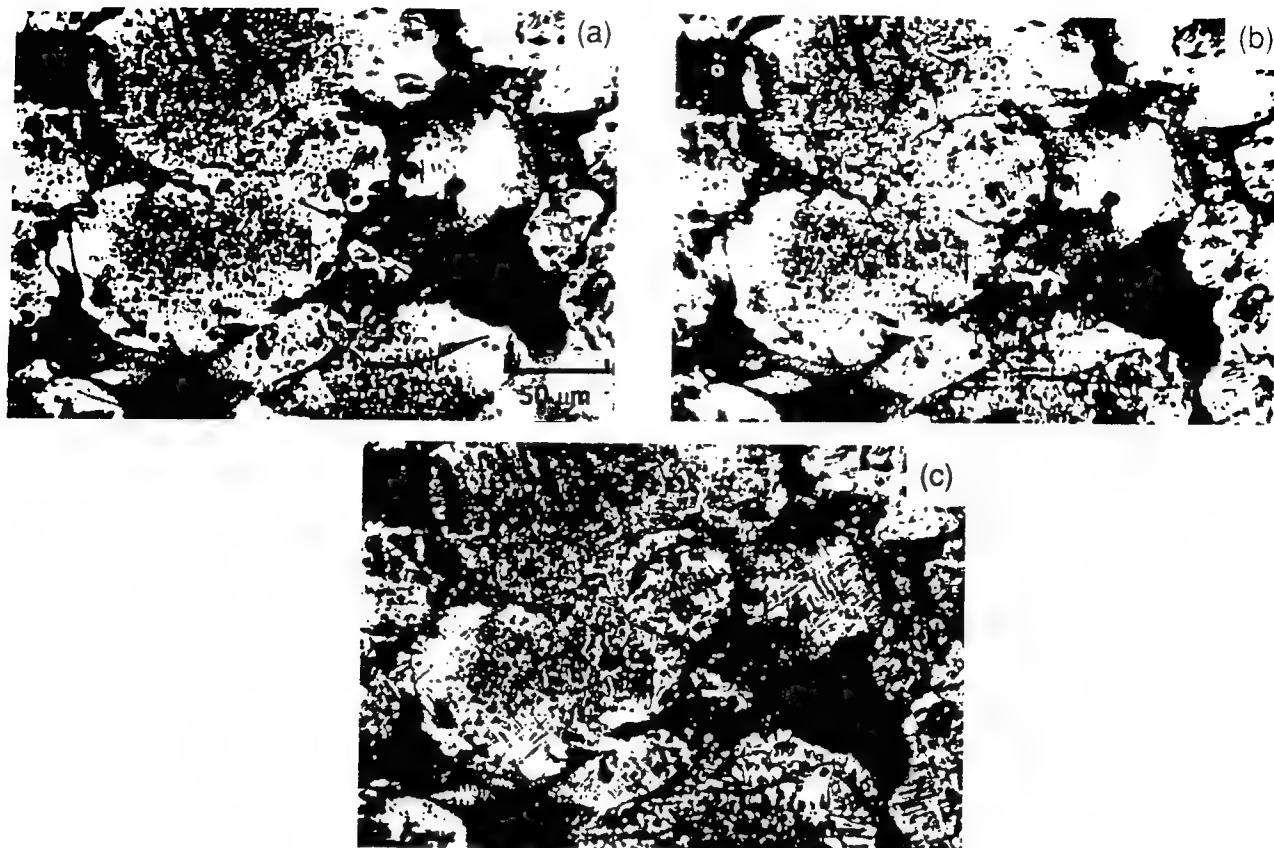


Fig. 9. Domain structures of BTS-10 samples as a function of temperature: (a) 70°, (b) 24°, and (c) -90°C.

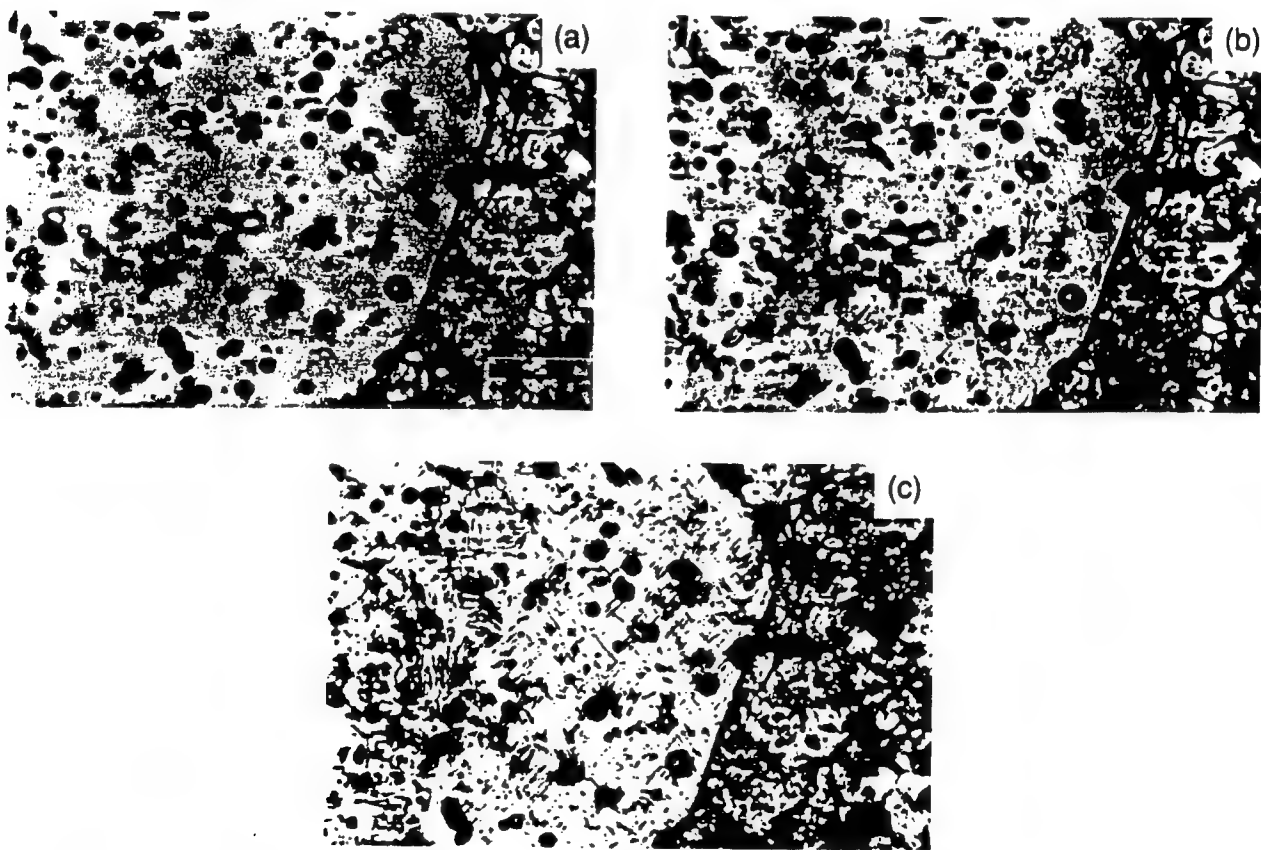


Fig. 10. Domain structures of BTS-13 samples as a function of temperature: (a) 45°, (b) 24°, and (c) -60°C.

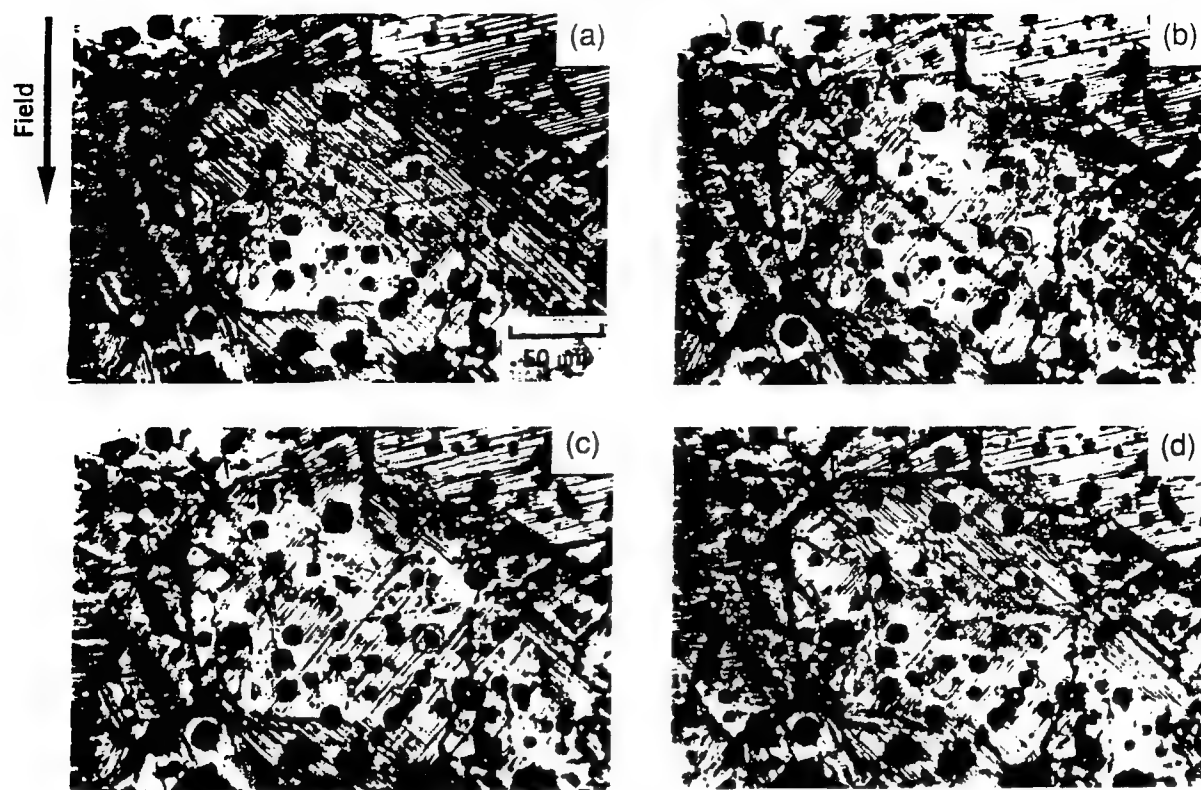


Fig. 11. Variation of domain structures of BT samples under an electric field: (a) initial state, and (b) 10, (c) 0, and (d) -6 kV/cm.

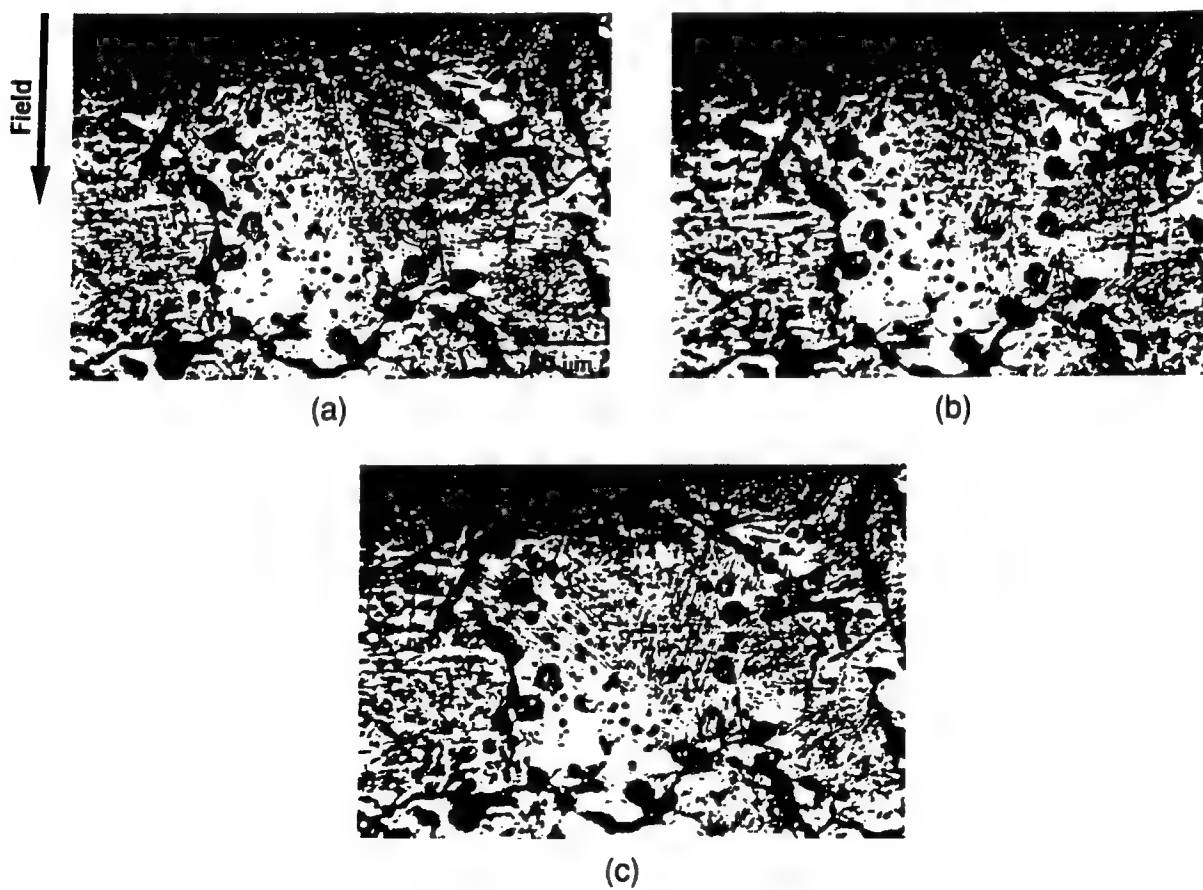


Fig. 12. Variation of domain structures of BTS-5 samples under an electric field: (a) initial state, and (b) 10 and (c) 0 kV/cm.

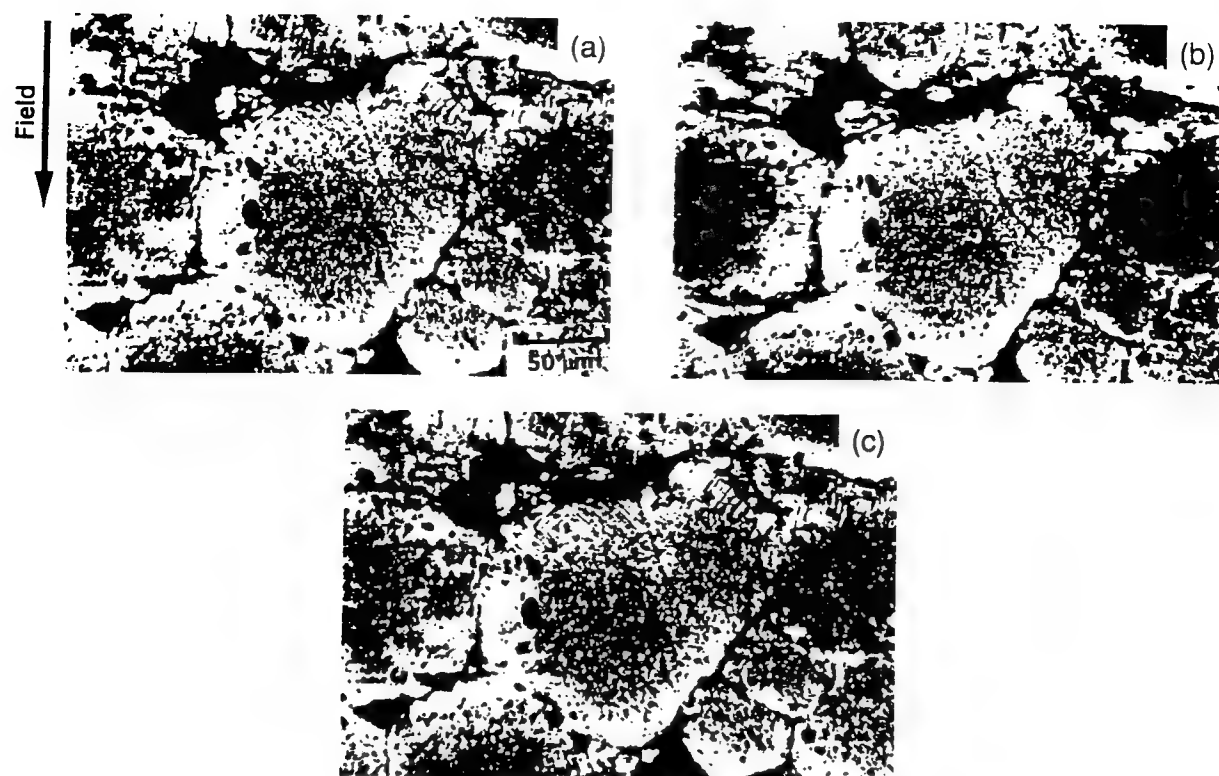


Fig. 13. Variation of domain structures of BTS-10 samples under an electric field: (a) initial state, and (b) 10 and (c) 0 kV/cm.

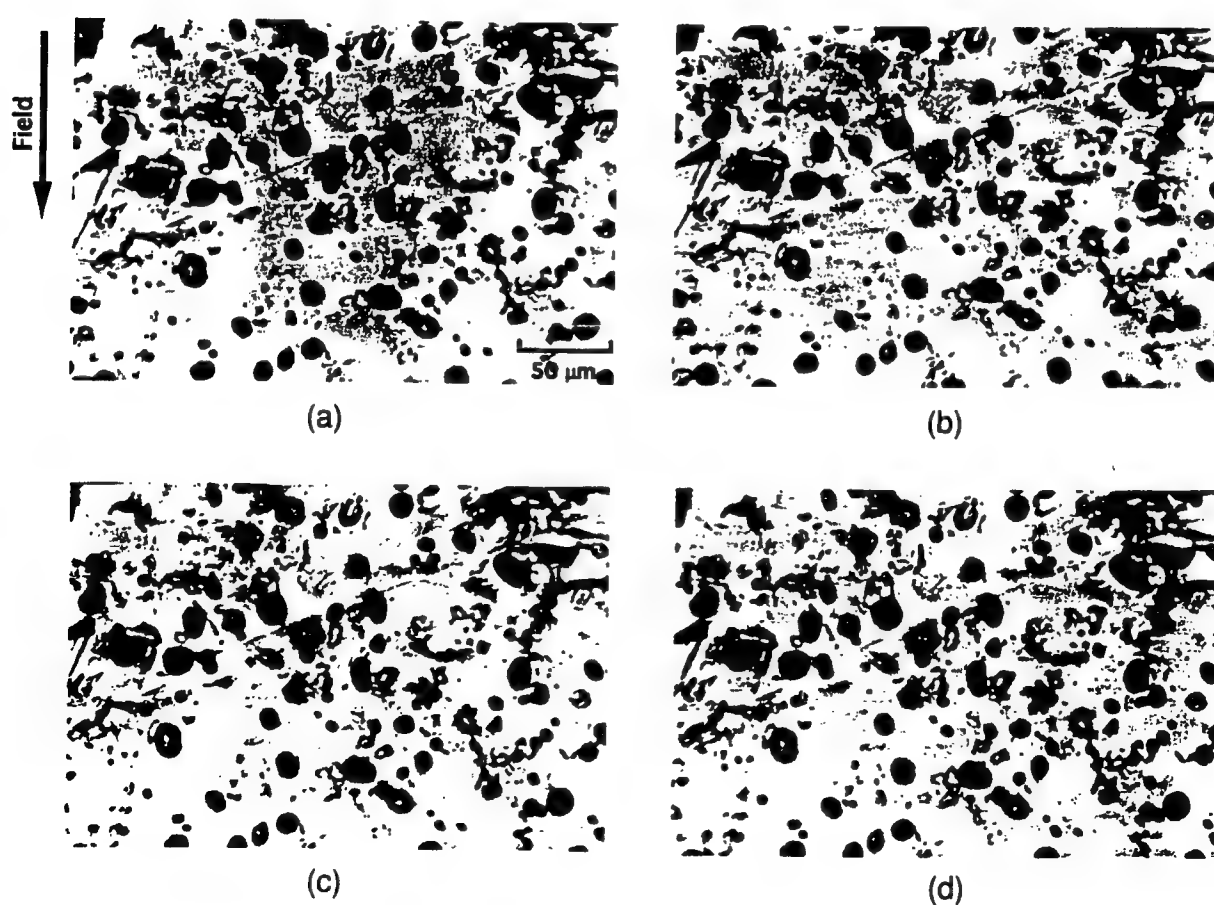


Fig. 14. Variation of domain structures of BTS-13 samples under an electric field: (a) initial state, and (b) 5, (c) 10, and (d) 0 kV/cm.

For the BT samples, the domain structures became difficult to define and some parts of the large domains were divided into small spindle shape domains suddenly at 0°C. We attribute this to the phase transition from tetragonal to orthorhombic at this temperature. The difference between the domain shapes in the tetragonal and orthorhombic phases is very clear; however, the difference between domain shapes in the orthorhombic and rhombohedral phases is not significant. The BTS-5 samples showed clear phase transitions from tetragonal to orthorhombic as shown in Fig. 3 but they did not show any sudden change of domain shape due to the phase transition as the BT samples did. It was reported that BTS-10 shows successive phase transitions from a tetragonal to an orthorhombic and finally to a rhombohedral phase in a small temperature range with decreasing temperature.³ We could not, however, distinguish obvious phase transitions in the dielectric measurements and domain shapes. The BTS samples showed a gradual change of domain structures with decreasing temperature. The domain walls became clear, in general, at lower temperatures. It is noteworthy that the BTS-13, which does not show any domain walls at room temperature, shows obvious domain walls at low temperature (Fig. 10). The domain size at this temperature is tiny and the domain walls are rather difficult to distinguish.

Figures 11–14 show domain motion of the BT and BTS samples as a function of electric field at room temperature. A field of ± 10 kV/cm was applied to the samples. The BT samples showed 90° and 180° domain switching with application of the electric field. When ± 10 kV/cm was applied to the BT sample, the domain walls were reoriented by 90° (Fig. 11(b)). The reoriented domain walls remained even after removing the electric field (Fig. 11(c)). The reoriented domain walls returned to their initial orientation when a small negative bias was applied (Fig. 11(d)). The hysteresis of the domain motion is associated with the hysteresis in the P – E and field-induced strain characteristics. The BTS-5 samples also showed small hysteresis of domain motion (Fig. 12). The poled domain shape was different from both the initial state (Fig. 12(a)) and the field state

(Fig. 12(b)). On the other hand, the BTS-10 and BTS-13 samples did not show any hysteresis of domain motion, as shown in Figs. 13 and 14. Applying an electric field up to ± 10 kV/cm to the BTS-10 sample induced domain growth from tiny and complex domains to large and simple domains, and the domain structure returned to its initial state as the electric field was removed. In the case of the BTS-13 sample, the domain walls were observed only when an electric field of ± 5 kV/cm was applied, and these domain walls disappeared above ± 5 kV/cm as well as zero field. The domain dynamics of the BTS-13 sample were associated with the small hysteresis of P – E and field-induced strain characteristics.

IV. Conclusions

Domain structures of $\text{Ba}(\text{Sn},\text{Ti})\text{O}_3$ become drastically small, less well-defined, and complex with increasing Sn content. These microdomain configurations are rather similar to those of the relaxor ferroelectric $\text{Pb}(\text{Zn}_{1/3}\text{Nb}_{2/3})\text{O}_3$.¹

The domain motion of BaTiO_3 and $\text{Ba}(\text{Ti}_{0.9}\text{Sn}_{0.05})\text{O}_3$ show hysteresis under an electric field, while the $\text{Ba}(\text{Ti}_{0.9}\text{Sn}_{0.1})\text{O}_3$ and $\text{Ba}(\text{Ti}_{0.87}\text{Sn}_{0.13})\text{O}_3$ samples do not exhibit hysteresis; this explains reasonably the superior nonhysteretic characteristics in the induced strain curve of $\text{Ba}(\text{Ti},\text{Sn})\text{O}_3$.

References

- K. Kato, K. Suzuki, and K. Uchino, "Observation of Domain Motion in Ferroelectric Single Crystals with a Diffuse Phase Transition," *J. Ceram. Soc. Jpn.*, **98** (5) 840–45 (1990).
- K. Uchino, "Relaxor Ferroelectrics," *J. Ceram. Soc. Jpn.*, **99** (10) 829–35 (1991).
- J. Von Cieminski, H. Th. Langhammer, and H. P. Abicht, "Peculiar Electromechanical Properties of Some $\text{Ba}(\text{Ti},\text{Sn})\text{O}_3$ Ceramics," *Phys. Status Solidi A*, **120**, 285–93 (1990).
- J. Von Cieminski and H. Beige, "High-Signal Electrostriction in Ferroelectric Materials," *J. Phys. D*, **24**, 1182–86 (1991). □

APPENDIX 25

(Received 11 February 1994; accepted for publication 22 April 1994)

An anomalous line narrowing along with the appearance of several new lines on cooling Bi₄Ti₃O₁₂ ceramics, indicates a subtle phase transition in the 150–200 K region. In the same temperature range, anomalies in dielectric properties (dielectric constant, coercive field, and spontaneous polarization) of single-crystal Bi₄Ti₃O₁₂ were reported. A possible subtle monoclinic-orthorhombic phase change, combined with a continuous ordering of dipoles associated with Bi³⁺ lone pair electrons and TiO₆ octahedra, may be responsible for these results.

I. INTRODUCTION

Bismuth titanate, Bi₄Ti₃O₁₂, is a well-known ferroelectric with a Curie temperature of 675 °C.^{1,2} It is a member of the family of layer-type compounds first reported by Aurivillius^{3,4} who established the crystal structure to consist of three perovskite-like units of nominal composition BiTiO_x (=Bi₂Ti₃O₁₀)²⁻ sandwiched between two (Bi₂O₂)²⁺ layers along the tetragonal *c* axis (Fig. 1). The detailed crystal structure was derived by Dorrian *et al.*,⁵ using x-ray and neutron diffraction methods. The room-temperature diffraction data can be accounted for by orthorhombic symmetry but careful optical studies by Cummins and Cross⁶ demonstrated that the true symmetry at room temperature is monoclinic with $\beta=90^\circ 1' \pm 1'$. Recently Rae *et al.*⁷ refined the structure and confirmed the monoclinic symmetry. Thus it appears that, at room temperature, Bi₄Ti₃O₁₂ is slightly monoclinic optically, but is essentially orthorhombic by diffraction studies.

Dielectric studies of single crystals^{1,8,9} and ceramics^{2,10} of Bi₄Ti₃O₁₂ over a wide temperature range showed only one dielectric constant peak at the Curie temperature. On the other hand, layer compounds with an even number of perovskite-like units between two Bi₂O₂ layers, e.g., Bi₃TiNbO₉ (*n* = 2) and Bi₅Ti₃FeO₁₅ (*n* = 4) exhibit two phase transitions about 200 °C apart, whereas compounds with an odd number of perovskite-type units in the unit cell display only one phase change.¹¹ However, dielectric measurements on single-crystal Bi₄Ti₃O₁₂ along the *c* axis below room temperature by Sawaguchi and Cross¹² showed a number of unusual features, which are summarized in Fig. 2. For example, with decreasing temperature, the dielectric constant (ϵ_r) generally decreases except for a broad hump around 150 K, the spontaneous polarization (P_s) changes little but for a gradual decrease in the 250–100 K range with some thermal hysteresis and the coercive field (E_c) gradually decreases to a minimum at 100 K except for the broad hump around 200 K. This contrasts with the behavior of ferroelectrics which exhibit a relatively constant P_s and increasing E_c with decreasing temperature. The fact that the P_s vector of Bi₄Ti₃O₁₂ is tilted in the monoclinic *ac* plane with the major component

along the *a* axis and that the switching of P_s may be to the energetically closer orthorhombic state and not to the tetragonal state, was suggested as the possible reason for the unusual dielectric behavior.¹² Thermodynamic arguments indicate that the energy separation of the orthorhombic and monoclinic states decreases with decreasing temperature.^{13,14} A frequency dependent anomaly in the dielectric constant of ceramic Bi₄Ti₃O₁₂ has recently been reported at about 220 K.¹⁵

Two earlier studies of Raman spectra of bismuth titanate exist. In one, the frequency of the soft mode decreased (but not to zero) at about 200 °C, indicative of a phase change.¹⁶ In the other, changes in Raman modes under the influence of pressure suggested two phase transitions at 3 and 11 GPa.¹⁷

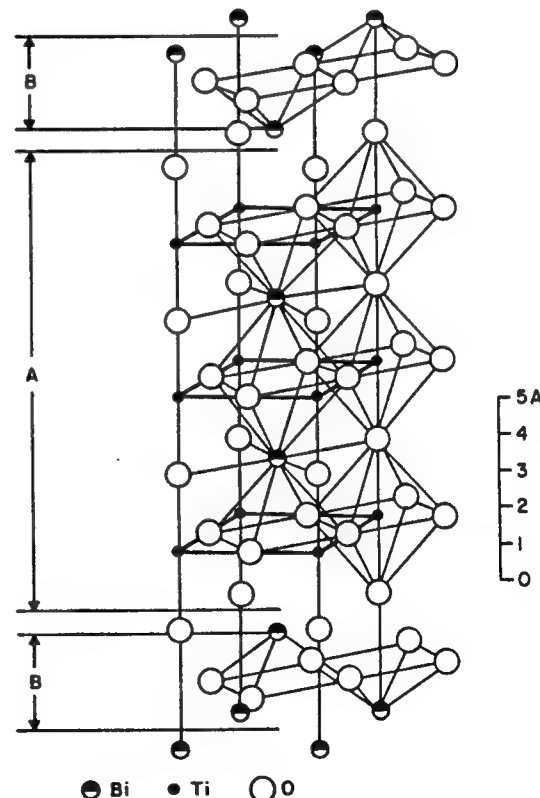


FIG. 1. Crystal structure of Bi₄Ti₃O₁₂ adapted from Ref. 3.

^{a)}Permanent address: Tata Research Development and Design Centre, 1 Mangaldas Road, Punc 411001, India.

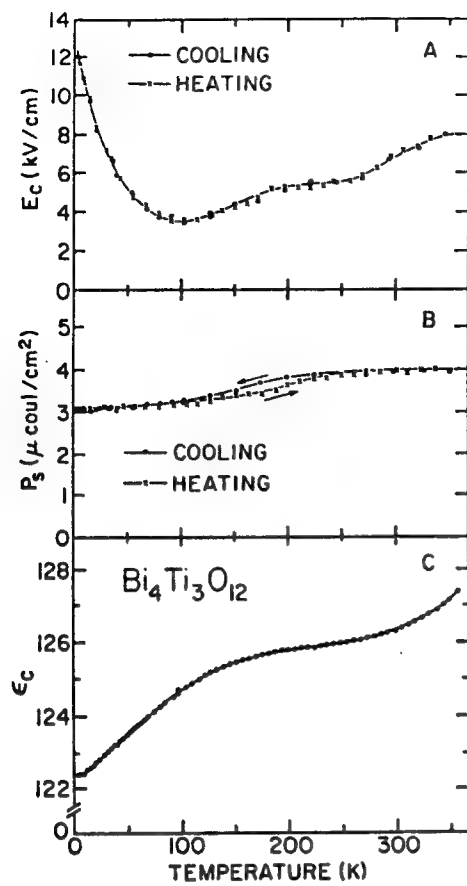


FIG. 2. Variation of dielectric properties of $\text{Bi}_4\text{Ti}_3\text{O}_{12}$ single crystal with temperature below 300 K (adapted from Ref. 12).

It thus appears that subtle phase transitions in $\text{Bi}_4\text{Ti}_3\text{O}_{12}$ can be studied by Raman spectroscopy.

The present work reports a study of Raman spectra of $\text{Bi}_4\text{Ti}_3\text{O}_{12}$ ceramics from room temperature to 70 K in order to elucidate low-temperature structural transitions.

II. EXPERIMENT

Ceramic discs of $\text{Bi}_4\text{Ti}_3\text{O}_{12}$ were prepared by conventional mixed oxide methods. X-ray diffraction methods were used to confirm compound formation.

The Raman spectra were obtained on an Instruments SA Ramanor U-1000 spectrometer with the 514.32 nm line of an Ar^+ laser as an excitation source. Laser power was set at 200 mW with a spectral slit width of 3 cm^{-1} . The instrument was equipped with a microscope attachment with a focal spot size of the order of a few microns. Optical losses were such that about 10% of the laser power was focused on the sample surface.

For measuring the temperature dependence of the Raman spectra, the sample was mounted on a cold stage of an MMR Joule-Thompson refrigerator equipped with the MMRK20 programmable temperature controller and capable of cooling from room temperature to 65 K. Thermally conducting grease was used to obtain the best contact between the cold stage and the sample. The sample was 0.5 mm thick in order to reduce the temperature gradient.

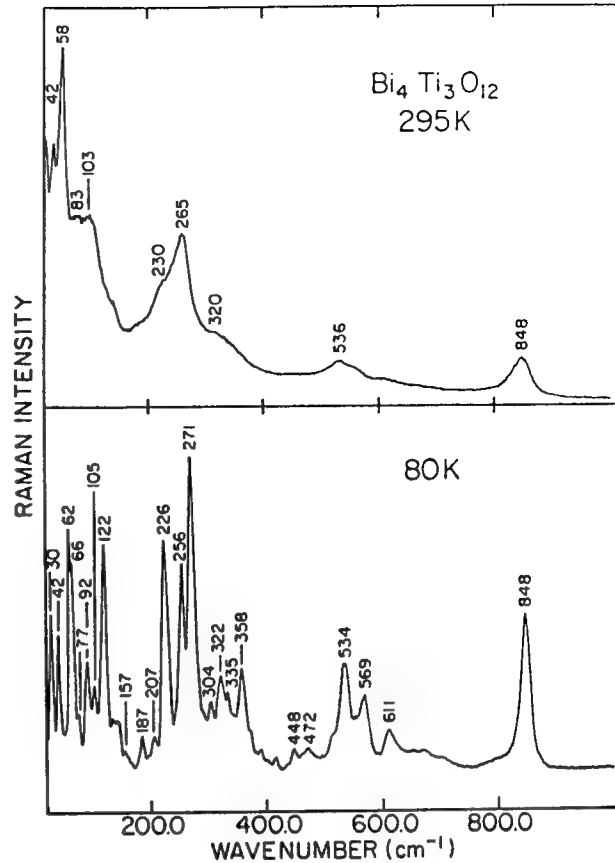


FIG. 3. Raman spectra of $\text{Bi}_4\text{Ti}_3\text{O}_{12}$ taken at 80 and 295 K.

III. RESULTS

Complete Raman spectra at 295 and 80 K are shown in Fig. 3. There is a dramatic narrowing of the Raman lines between room temperature and 80 K with much additional detail resolved at low temperature. At 295 K the spectrum consists of only five broad bands and two sharp bands at a very low wave number. At low temperatures, only the band near 850 cm^{-1} simply becomes sharper and more intense. The other broad features break up into clusters of sharp bands so that at 80 K, 32 distinct bands have been resolved.

Expanded spectra of selected regions collected at various intermediate temperatures (Fig. 4) show that the sharpening of the Raman bands is a continuous function of temperature; there is no abrupt change from broad to narrow Raman bands although much of the sharpening seems to take place near 150 K. Careful quantitative line-shape measurements show that the low wave number group of bands and the intense high wave number mode at 850 cm^{-1} are of most interest.

The wave number of the 850 cm^{-1} band is nearly independent of temperature (Fig. 5) and it broadens continuously from about 20 cm^{-1} at 80 K to 40 cm^{-1} at room temperature. The intensity, however, decreases markedly with increasing temperature up to about 150 K. At higher temperatures the intensity is low but constant.

The cluster of sharp, low wave number bands are likely to result from bending and torsional modes of the titanium and bismuth polyhedra, those aspects of the structure which are most involved with ferroelectric ordering and phase tran-

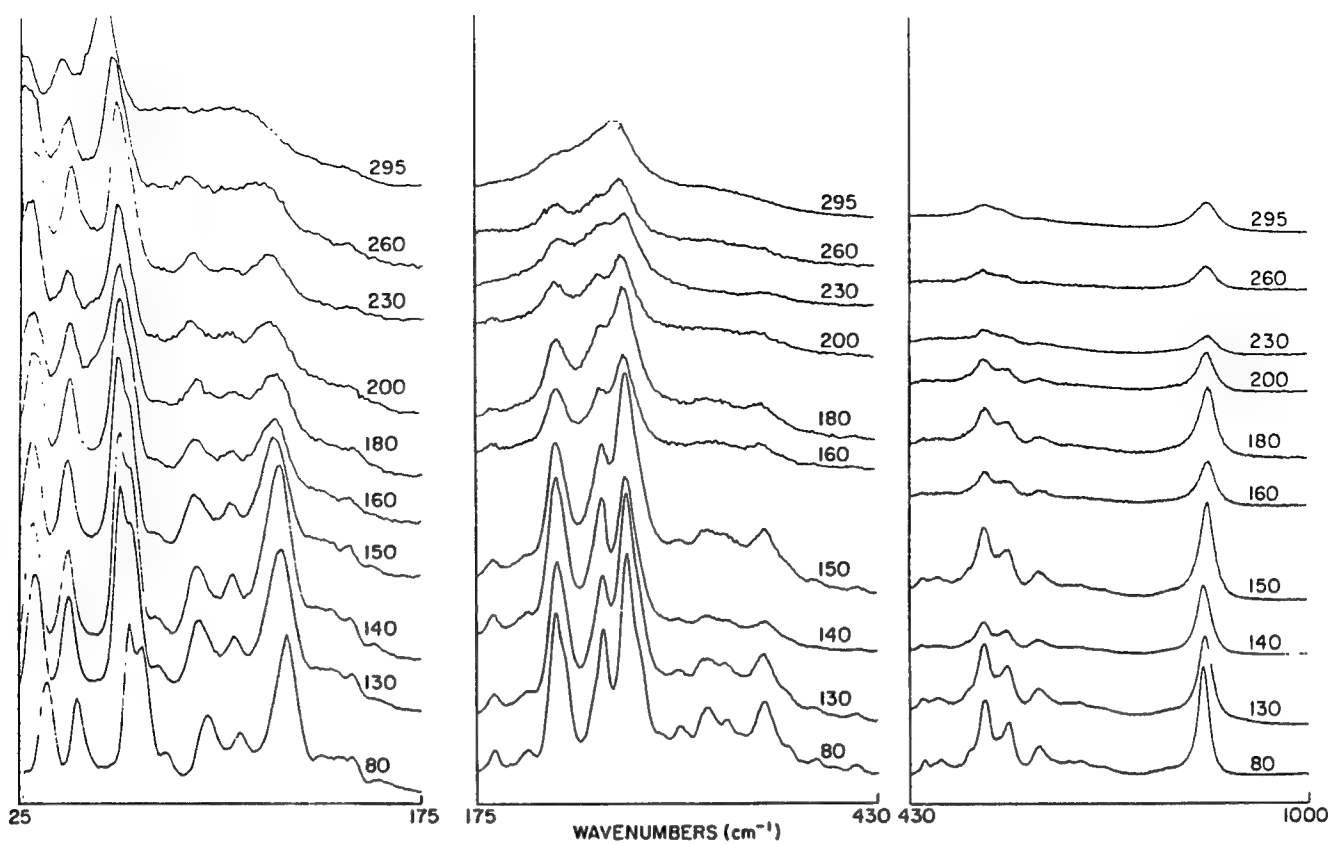


FIG. 4. The evolution of the shape of $\text{Bi}_4\text{Ti}_3\text{O}_{12}$ Raman bands with temperature.

sitions. The wave number of these bands does not change much with temperature (Fig. 6). The weak band at 75 cm^{-1} disappears as the temperature rises, being lost in the background at about 150 K. An intense doublet with components at 62 and 66 cm^{-1} is a major feature of the spectrum at 80 K. As the temperature rises, the 66 cm^{-1} component loses in-

tensity and merges into the shoulder of the 61 cm^{-1} band above 150 K.

The low-temperature bands are narrow, widths in the range of $8\text{--}10\text{ cm}^{-1}$ at 80 K. Some remain sharp or broaden only slightly as the temperature rises while the 92 cm^{-1} band broadens from 6 to 24 cm^{-1} over a relatively restricted temperature interval between 150 and 250 K (Fig. 7). The most pronounced effect occurs in the plots of integrated intensity (Fig. 8). Intensities decrease abruptly near 150 K in the three

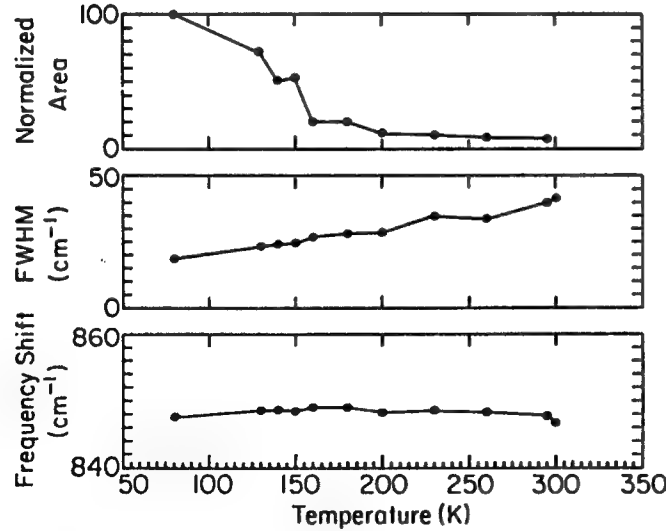


FIG. 5. Dependence on temperature of the integrated intensity, bandwidth, and wave number of the 850 cm^{-1} Raman band.

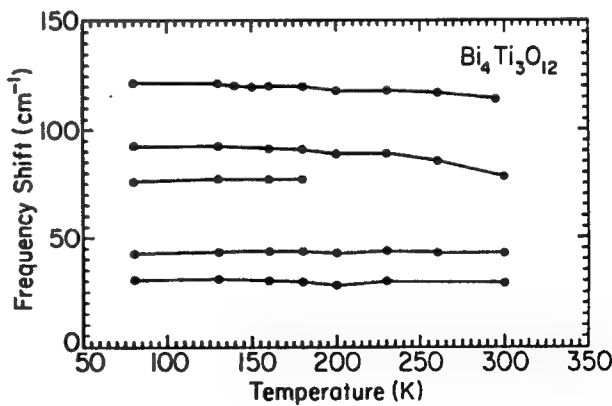


FIG. 6. Variation of wave number with temperature for low wave number set of $\text{Bi}_4\text{Ti}_3\text{O}_{12}$ Raman bands.

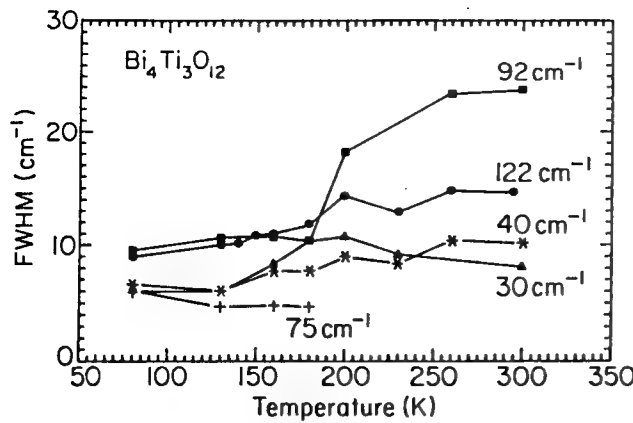


FIG. 7. Variation of line widths with temperature for low wave number set of $\text{Bi}_4\text{Ti}_3\text{O}_{12}$ Raman bands.

bands shown in Fig. 8 but it is apparent from Fig. 4 that the intensities of most other bands also decrease greatly in this temperature range.

IV. DISCUSSION

The large number of sharp bands seen in the low-temperature spectra lend themselves to the use of symmetry arguments to put some constraints on the possible low-temperature structures. Classification of the normal modes of the prototype tetragonal structure (Table I) predicts a maximum of 16 Raman active modes which is about twice the number of Raman bands observed at room temperature although these bands are too broad for accurate counting. Bismuth titanate is known to undergo a distortion from the high symmetry prototype to an orthorhombic structure which is referred to by Withers, Thompson, and Rae¹⁸ as the “parent structure” from which different ferroelectric orderings can be derived by modulation along various wave vectors. The parent structure, with space group Fmmm, is predicted to have 24 Raman active modes (Table II), very close to the actual number observed. Mode counting in the Raman spectra of ceramics is never quite exact because of the possibility of overlapping bands, bands formally allowed but too weak to

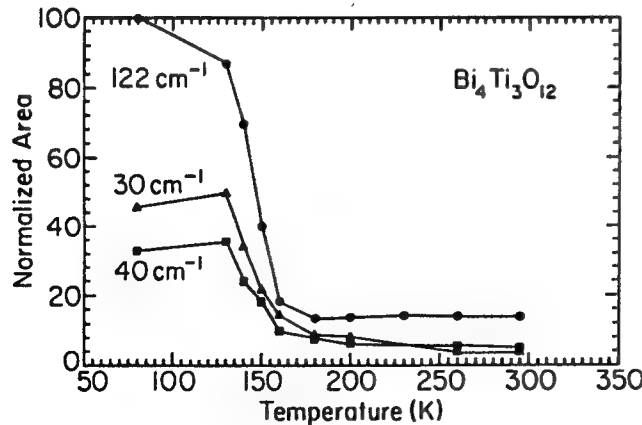


FIG. 8. Variation of integrated intensity with temperature for low wave number set of $\text{Bi}_4\text{Ti}_3\text{O}_{12}$ Raman bands.

TABLE I. Classification and selection rules for $\text{Bi}_4\text{Ti}_3\text{O}_{12}$ with tetragonal structure (space group I4/nmm).

D_{4h}	N_{vib}	Acoustic modes	Selection rules
A_{1g}	6		Raman: $(xx + yy), zz$
A_{2g}	0		...
B_{1g}	2		Raman: $(xx - yy)$
B_{2g}	0		...
E_g	8		Raman: (xz, yz)
A_{1u}	0		...
A_{2u}	8	$1(z)$	IR: $E \parallel c$
B_{1u}	0		...
B_{2u}	2		Inactive
E_u	10	$1(x, y)$	IR: $E \perp c$

observe, and bands that may be multiphonon features. There are 28 bands in the 80 K spectrum of which two disappear at the 150 K anomaly leaving exactly the predicted number in the intermediate temperature spectra.

All symmetric modes of vibration are Raman active in the centrosymmetric orthorhombic structure. A monoclinic distortion that would break the center of symmetry would allow additional modes from the antisymmetric set to possibly appear in the Raman spectrum.

The substantial amount of line broadening that occurs with increasing temperature requires a different explanation. Although the large increase in line width takes place over a small temperature range in certain modes is a feature of a phase transition, the overall broadening is also observed in the component oxides, TiO_2 (Ref. 19) and Bi_2O_3 ,²⁰ as well as in many other polar materials. The temperature dependent line narrowing is interpreted as arising from a positional disorder of the nonbonding lone-pair electrons on Bi^{3+} and from the dipole associated with the off-center Ti^{4+} atom in the perovskite layer TiO_6 octahedra. However, diffraction studies by Withers (personal communication) at liquid nitrogen temperature did not provide any evidence for a phase transition, at least not a phase transition that alters the space group.

V. CONCLUSIONS

Detailed examination of the temperature dependence of Raman line shapes in $\text{Bi}_4\text{Ti}_3\text{O}_{12}$ reveals an anomaly in the range of 150–200 K which correlates with anomalies in the dielectric properties. The anomaly can be interpreted as a

TABLE II. Classification and selection rules for $\text{Bi}_4\text{Ti}_3\text{O}_{12}$ with orthorhombic structure (space group Fmmm).

D_{2h}	N_{vib}	Acoustic modes	Selection rules
A_g	6		Raman: x^2, y^2, z^2
B_{1g}	2		Raman: xy
B_{2g}	8		Raman: xz
B_{3g}	8		Raman: yz
A_u	2		Inactive
B_{1u}	8	$1(z)$	IR: $E \parallel c$
B_{2u}	10	$1(y)$	IR: $E \parallel b$
B_{3u}	10	$1(x)$	IR: $E \parallel a$

ture. Superimposed on changes assigned to the phase transition is a temperature-dependent line broadening related to positional ordering of dipoles within the structure.

ACKNOWLEDGMENTS

This work was supported by the Office of Naval Research. We are grateful to Professor Roy Withers of the Australian National University for providing unpublished details of the crystal structure.

- ¹L. G. Van Uitert and L. Egerton, *J. Appl. Phys.* **32**, 959 (1961).
- ²E. C. Subbarao, *Phys. Rev.* **122**, 804 (1961).
- ³B. Aurivillius, *Arkiv Kemi* **1**, 494 (1949).
- ⁴B. Aurivillius, *Arkiv. Kemi* **2**, 519 (1950).
- ⁵J. F. Dorrian, R. E. Newnham, D. K. Smith, and M. I. Kay, *Ferroelectrics* **3**, 17 (1971).
- ⁶S. E. Cummins and L. E. Cross, *J. Appl. Phys.* **39**, 2268 (1968).

tallogr. B **46**, 474 (1990).

- ⁸A. Fauskova and L. E. Cross, *J. Appl. Phys.* **41**, 2834 (1970).
- ⁹N. N. Krainik, E. E. Mydinkova, and S. F. Kolesmican, *Fiz. Tverd. Tela* **10**, 260 (1968).
- ¹⁰E. C. Subbarao, *J. Phys. Chem. Solids* **23**, 665 (1962).
- ¹¹R. E. Newnham, R. W. Wolfe, and J. F. Dorrian, *Mater. Res. Bull.* **6**, 1029 (1971).
- ¹²E. Sawaguchi and L. E. Cross, *Mater. Res. Bull.* **5**, 147 (1970).
- ¹³L. E. Cross and R. C. Pohanka, *Mater. Res. Bull.* **6**, 939 (1971).
- ¹⁴R. C. Pohanka and L. E. Cross, *J. Appl. Phys.* **39**, 3992 (1968).
- ¹⁵W. Xiaoli and Y. Xi, *Ferroelectrics Lett.* **13**, 47 (1991).
- ¹⁶K. Hisano and K. Toda, *Solid State Commun.* **18**, 585 (1976).
- ¹⁷G. A. Kourouklis, A. Jayaraman, and L. G. Van Uitert, *Mater. Lett.* **5**, 116 (1987).
- ¹⁸R. L. Withers, J. G. Thompson, and A. D. Rae, *J. Solid State Chem.* **94**, 404 (1991).
- ¹⁹R. J. Betsch, H. L. Park, and W. B. White, *Mater. Res. Bull.* **26**, 613 (1991).
- ²⁰R. J. Betsch and W. B. White, *Spectrochim. Acta* **34A**, 505 (1978).

COMPOSITE SENSORS

APPENDIX 26

COMPOSITE SENSORS AND ACTUATORS

Robert E. NEWNHAM and Kelley A. MARKOWSKI

Intercollege Materials Research Laboratory, Pennsylvania State University,
University Park, PA 16802 USA

1. INTRODUCTION

Composite materials have found a number of structural applications but their use in the electronics industry has been relatively limited. As the advantages and disadvantages of electroceramic composites are better understood, we can expect this picture to change.

In this paper we review some of the composite sensor and actuator studies carried out in our laboratory during the past decade. These functional composites make use of a number of underlying ideas including connectivity patterns leading to field and force concentration; the use of periodicity and scale in resonant structures; the symmetry of composite structures and its influence on physical properties; polychromatic percolation and coupled conduction paths; varistor action and other interfacial effects; sum, combination, and product properties; coupled phase transformation phenomena; and the important role that porosity and inner composites play in composite materials. These ideas provide a basic understanding of functional composites and have been discussed previously.¹ In the present paper, we describe several composite piezoelectrics and thermistors which utilize some of these principles.

2. Composite Transducers

Early investigators concentrated on polymer-ceramic composites for use as hydrophones.² Several interesting connectivity patterns³ were developed including 3-3 structures made by the replamine process⁴ and by fugitive phase technique^{5,6}. Then came the more useful 1-3 composites consisting of parallel PZT fibers embedded in a polymer matrix. These structures were made by extrusion⁷, by dicing⁸, and more recently by injection molding⁹ and lithographic lost-wax techniques.¹⁰ The coupling between the ceramic fibers and the polymer matrix is important.¹¹ In optimizing hydrophone performance, the d_{high} product was

chosen as a figure of merit. The 1-3 composite increases d_h and g_h by reducing the d_{31} piezoelectric coefficient and the dielectric constant while maintaining the large d_{33} coefficient.

The usefulness of the 1-3 composite in high frequency applications for non-destructive testing and medical diagnostics was recognized later.^{12,13,14} Biomedical transducers require resonant frequencies in the 1-10 MHz range, high electromechanical coupling coefficients, low acoustic impedance, and broad bandwidth. The 1-3 transducers manufactured by Siemens¹⁰ have thickness resonances of 5-10 MHz, coupling coefficients $k_t=0.67$, $K=600$, $\tan \delta < 0.025$, and a mechanical Q about 10.

Poling is sometimes difficult for the long, slender PZT fibers used in 1-3 composites. Electric breakdown often occurs before poling is complete, and the transducer is ruined. Lower poling and driving fields are obtained when the spaghetti-like PZT fibers are replaced with macaroni-like PZT tubules. When electroded inside and out, the thin-walled tubes are poled and driven radially at relatively modest voltages. Radial motions are coupled to length-wise displacements through the d_{31} coefficient. Effective piezoelectric constants of about 8000 pC/N and large d_{hgh} products are achieved with these composites.¹⁵ Other variants on the basic 1-3 structure include the 1-2-3 composite with transverse load bearing fibers¹⁶, and the 1-3-0 composite with a foamed polymer matrix¹⁷, and the interesting woven fiber composites devised by Safari and co-workers.¹⁸

Perhaps the simplest piezoelectric composite is the 0-3 transducer made by dispersing ceramic particles in a polymer matrix.¹⁹ The NTK Piezo-Rubber films and cables are used as flexible hydrophones, keyboards, blood pressure cuffs, and musical instruments. They are made by hot-rolling $PbTiO_3$ particles into a chloroprene rubber matrix.²⁰

As mentioned earlier PZT is widely used as a transducer material because of its high piezoelectric coefficients. However, for hydrophones applications, PZT is a poor material for several reasons. The hydrostatic piezoelectric coefficient, d_h ($=d_{33} + 2d_{31}$), is very low. The piezoelectric voltage coefficients, g_{33} and g_h , are low because of the high dielectric constant of PZT (1800). The acoustic matching of PZT with water is poor because of its high density (7.9 g/cm^3). Moreover, it is a brittle, non-flexible ceramic.

In the last decade, several investigators have tried to fabricate composites of PZT and polymers to overcome the above problems of PZT. It has been shown that it is possible to improve upon the piezoelectric properties of homogeneous PZT by the composite approach. The concept that the connectivity of the individual phases control the resulting properties has been demonstrated in a number of composites with different geometry and different connectivity of the individual phases. The

hydrostatic piezoelectric properties of these composites are superior to single-phase PZT. However, some of the earlier composites suffer from disadvantages due to difficulty in preparation or reduction in hydrostatic sensitivity with increasing pressure. Thus, there still exists a need to further improve the piezoelectric properties of these composites. It is especially desirable to have the composites prepared without any problems in processing and fabrication and also show high figures of merit for hydrophone applications with little or no variation in static pressure sensitivity under hydrostatic loading.

It was demonstrated by Safari¹⁸ that based on the theory of connectivity new composites with different connectivity patterns could be fabricated with enhanced performance. Most of the work involved composites with 1-3 and 2-3 connectivity, shown below in figure 1. These composites were prepared by drilling either circular or square holes in prepoled PZT blocks, in a direction perpendicular to the poled axis and by filling the drilled holes with epoxy. On the samples optimized for hydrophone performance, the g_h and d_{hgh} coefficients were about 4 and 40 times greater, respectively, for the 1-3 composites; and 25 and 150 times greater for the 2-3 composites compared to those of solid PZT. For 1-3 composites, there was practically no variation of g_h with pressure up to 8.4 MPa. In the case of 2-3 composites, there was a slight variation of g_h with pressure.

2.1. BB Transducers

BB's are hollow spherical transducers a few millimeters in diameter, about the same size as the metallic pellets used in air rifles (BB guns). PZT BB's are mass produced, by a patented forming process in which air is blown through a PZT slurry of carefully controlled viscosity. The hollow spheres are 1-6 mm in diameter with wall thickness of 0.1 mm. Densities are about 1.3 g/cm³ giving the BB a low acoustic impedance close to that of water and human tissue.

When embedded in a polymer matrix to form a 0-3 composite the BB spheres are surprisingly strong, and able to withstand large hydrostatic pressure without collapse. Close-packed transducer arrays are easily assembled.

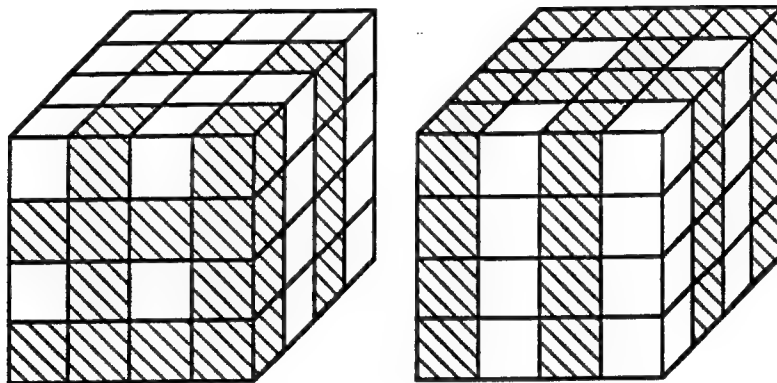
When electrode inside and out, and poled radially the BB becomes an omnidirectional transducer²¹ suitable for underwater or biomedical applications. For spheres 2.6 mm is diameter with 90 μ m thick walls, the resonant frequencies are 700 kHz for the breathing mode (d_{31}) and 10 MHz for the wall thickness mode (d_{33}). BB's are small enough to be used in catheters for non-invasive surgery to act as beacons, sensors, and actuators. More than a million such procedures are now carried out annually.

2.2. Zig-Zags and Smarties

Zig-zag actuators are split bimorphs in which two ceramic legs are driven independently to generate synchronized horizontal and vertical displacements.

The legs are joined in a teepee-like configuration which imparts a rolling motion to the load. Typical motions are in the 1- 30 μm range and look to be useful in piezomotor and conveyor belt applications.²²

Smarties are a family of composite transducers which combine two or more active elements to provide the sensing and actuating functions characteristic of a smart material. There are four solid-state actuator materials currently in use throughout the world²³: Piezoelectric PZT, electrostrictive PMN, magnetostrictive TbFe_2 , and NiTi shape memory alloy. We have begun to look at ways in which these materials can be joined to take advantage of the best features of each. Preliminary results on the first of these composite actuators - NiTi strips coated with sol-gel layers of PZT have been reported.²⁴



2-3 CONNECTIVITY 1-3 CONNECTIVITY

FIGURE 1

Two connectivity patterns utilized in composite transducers.

3. FLEXTENSIONAL TRANSDUCERS "MOONIES"

In recent years, piezoelectric and electrostrictive ceramics have been used in many actuator applications. To meet these needs a new type of composite actuator based on a flexextensional transducer has been developed.²⁷⁻³⁰ This ceramic-metal composite actuator, or "moonie" consists of either a piezoelectric ceramic disc or a multilayer stack, sandwiched between two specially designed metal end caps. This design provides a sizable displacement, as well as a large generative force. In other words, it bridges the gap between the two most common types of actuators, the multilayer and the bimorph.³¹ The shallow spaces under the end caps produce a substantial increase in strain by combining the d_{33} and the d_{31} contributions to the ceramic. It is attractive for hydrophone, transceiver and actuator applications, and is especially advantageous for use as a non-resonant, low frequency projector in deep water.

The basic configuration of the moonie is shown in figure 2. The metal end caps serve as mechanical transformers for converting and amplifying the lateral motion of the ceramic into a large axial displacement normal to the end caps. Both the d_{31} ($=d_{32}$) and d_{33} coefficients of the piezoelectric ceramic contribute to the axial displacement of the composite. Figure 3 below shows the enhanced displacement of the moonie actuator as a function of applied electric field compared to PZT ceramic.

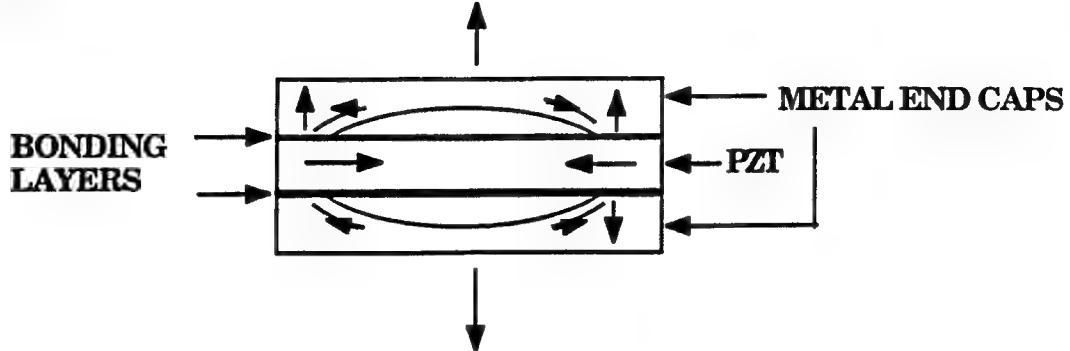


FIGURE 2

The geometry of the ceramic-metal composite actuator "Moonie". The arrows describe the direction of displacement.

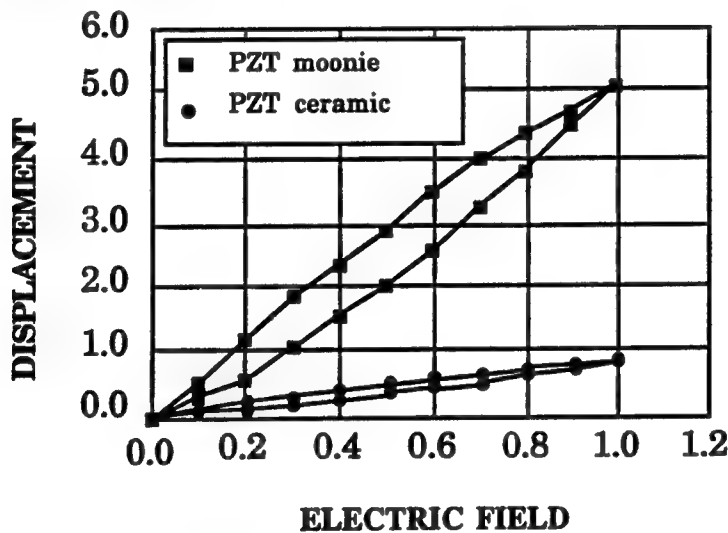


FIGURE 3

Typical static displacement of the moonie actuator as a function of the applied \vec{E} field.

3.1. Applications of the moonie

Three applications for this type of flexextensional transducer, the moonie, have been explored³²: Hydrophone sensors, transceivers for fish finders, and positional actuators. Geometry and bonding effects on the resonance characteristics and

displacement of the moonie transducer were investigated using finite element analysis (FEA).

3.1.1. Hydrophone applications of the moonie

Hydrophone sensitivity depends on d_h , the hydrostatic piezoelectric charge coefficient, and g_h , the hydrostatic piezoelectric voltage coefficient. The moonie transducer was introduced as a hydrophone having the highest figure of merit, $d_h \times g_h = 50,000 \times 10^{15} \text{ m}^2/\text{N}$, which is about 500 times larger than the PZT ceramic, as well as maintaining high capacitance and pressure tolerance. The stress distribution of the moonie hydrophone under a hydrostatic pressure was determined using FEA. FEA showed that extensional stresses along the radial and tangential directions were generated under a hydrostatic pressure, and contributed significantly to the very high figure of merit of the moonie.

In addition to this, the effect on prestresses caused by thermal treatment of the moonie were also estimated. The maximum stress concentration reached several hundred MPa. The maximum compressive stress concentration reaches about 300 MPa along the radial direction at the inner bonding edge, and 400 MPa extensive stress concentration occurs at the cavity top of the cap.

The combined effect of high hydrostatic pressure (7 MPa corresponding to a 700 m water depth), and thermal processes were also estimated. Even 7 MPa hydrostatic pressure causes little deformation to the moonie hydrophone because the effect of relatively large prestress pressures exceed those of the hydrostatic environment. This is one of the reasons that the moonie hydrophone has high pressure tolerance.

3.1.2. Transceiver for fishfinder

Using FEA to design the moonie fish finder made it possible to predict the flexextensional resonant frequency. The effect of the following five geometrical parameters: PZT diameter, PZT thickness, cap thickness, cavity size, and bonding layer thickness on the resonant frequency were carefully investigated. Among these parameters, the resonant frequency is sensitive to the diameter, cap thickness and cavity size. The bonding layer thickness, however, has little effect on the resonant frequency. It was found that the lowest flexextensional frequencies are proportional to the square root of the cap thickness and inversely proportional to the square of the diameter. These results are demonstrated below in figures 4 and 5.

From the results obtained by Onitsuka⁹ the moonie fish finders showed high response sensitivity but poor transmission. The high impedance of the moonie fish finder makes it difficult for practical for usage, but additional inductance will help to reduce the impedance.

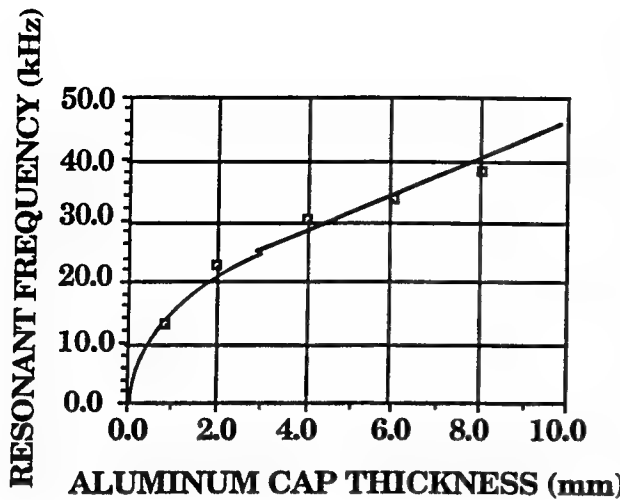


FIGURE 4

First resonant frequencies as a function of the aluminum cap thickness. Dimensions: $dp=35$ mm, $dm=35$ mm, $dc=28$ mm, $tp=2$ mm, $h=0.2$ mm where dp =PZT diameter, dm =metal cap diameter, dc =cavity diameter, h =cavity depth, tp =PZT thickness, and tm =metal cap thickness.

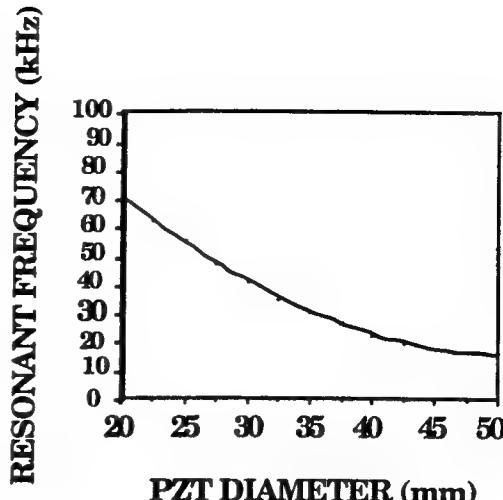


FIGURE 5

First resonant frequencies calculated by finite element analysis plotted as a function of PZT diameter. (Calculated curve for $dc/dp=0.8$, $tp=3$, $tm=6$)

3.1.3. Actuator

Moonie actuators have very high effective d_{33} coefficients depending on the geometry. Effective d_{33} coefficients as large as 4,000 pC/N were obtained with brass caps 0.3 mm thick, but the value decreased rapidly toward the edge of the transducer. This is approximately ten times higher than the d_{33} of a PZT-5 ceramic. The characteristics of the moonie actuator depend markedly on the geometry and material combination. Among the geometric parameters, cavity diameter, cavity depth, and cap thickness are the main contributors to the displacement of a moonie actuator. An applied 1 kV/mm electric field produces a displacement of 22 μ m at the center of a carefully designed brass capped moonie actuator. By stacking two identical single moonies with these dimensions, the double stacked moonie actuator produced 40 μ m displacement. It was confirmed that the incorporation of a multilayer ceramic actuator as a moonie driver reduced the applied voltage to a practical range.

The load carrying capability of the moonie was measured experimentally and calculated by FEA. The calculated maximum load (300 gf.) at the effective working area of 3 mm^2 agrees with that obtained by the extrapolation of the experimental data.

By choosing the appropriate position on the caps, their desired displacement and generative force can be obtained. The moonie actuator has a great potential for many applications because of its unique characteristics.

4. CONDUCTOR FILLED COMPOSITES

Composites consisting of a highly conductive filler powder dispersed in a flexible, insulating polymer matrix are commonly used in electronic applications for die attach³³, solderless connectors³⁴, thermistors^{35,36}, and pressure sensing elements.³⁷ Other uses of such composites include electromagnetic shielding and antistatic devices³⁸ as well as chemical sensors.³⁹

The electrical properties of these materials are described by conventional percolation theory.⁴⁰ When a sufficient amount of conductive filer is loaded into an insulating matrix, the composite transforms from an insulator to a conductor, arising through the continuous linkages of particles, figure 6. As the volume fraction of filler is increased, the probability of continuity increases until the critical volume fraction is reached, beyond which the electrical conductivity is high, comparable to the filler material.

Once percolation is "complete", i.e. a significant number of percolated linkages has formed, the difference in conductivity between samples with the same degree of self connectivity and the same volume fraction of filler but with different filler materials can be unpredictably large. All particle-filled composites have resistivities several orders of magnitude higher than the resistivities of the pure filler materials.

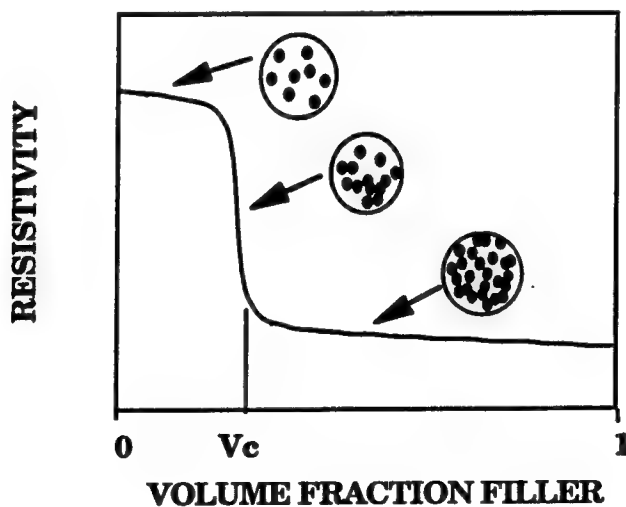


FIGURE 6

Percolation theory as applied to conductive composites, showing the development of conductive pathways with an increase in volume fraction of filler.⁴⁰

Thermistors or temperature dependent resistors, are typically made from doped ceramics (BaTiO₃). The desire for improved properties and ease of processing has spurred the development of composite thermistors.⁴¹ This type of composite combined a low resistivity filler powder, such as carbon black, vanadium sesquioxide, or nickel with a high resistivity polymer matrix such as polyethylene or polystyrene. In the dormant room temperature state the thermistor has a resistivity similar to the filler. On being activated by heating, however, the resistivity increases to a value close to the polymer matrix resistivity, often an increase of eight orders of magnitude.

5. CHEMICAL SENSORS

Conductive composites exposed to a solvent, in order to produce chemical sensing capabilities, have also been shown to take advantage of percolation phenomena.⁴² A conductive composite which shows some sensitivity to chemical vapors undergoes a four-step resistance change during exposure to the solvent. First, adsorption of solvent onto the surface of the composite results in a small, quick increase in resistance. Secondly, as the solvent diffuses through the sensor sample, the number of percolated chains decreases and the remaining chains become less conductive; a gradual increase in resistance occurs during this step. Third, when the last remaining percolated linkage is disrupted, there is a large increase in resistivity, usually several orders of magnitude; this conductor-to-insulator switch is the most important step for application purposes. Finally, as more solvent diffuses into the composite, the resistivity saturates at a level determined primarily by the conductivity of the solvent/polymer solution, although some effects from the filler are evident.

The maximum sensor response occurs when the maximum swelling in the polymer occurs. Maximum swelling occurs when the solubility parameters for the solvent equal those of the solvent, although this interpretation is only valid in the absence of strong intermolecular forces. The variations in swelling and in solvent resistivity help to improve the selectivity of the sensors. From polymer to polymer, the maximum possible swelling varies as a function of flexibility of the polymer; the higher the flexibility, the greater the swelling. Swelling does not appear to be a continuous function of solvent vapor pressure.

The response time of the composite is determined by three factors: the diffusivity of the solvent in the polymer, the thickness of the sensor film, and the maximum possible swelling in the polymer. For sensor applications, a high diffusivity, high maximum swelling, and small film thickness are desired.

The greatest sensitivity can be obtained by choosing composite samples close to V_c and with the hardest possible filler material. The sample must be thin enough to promote a quick response but thick enough to promote low initial resistivity. A hysteretic curve is seen upon repeated exposure of a sensor to a solvent, with the total recovery time dependent on the exposure time.

6. SMART MATERIALS

Smart materials⁴³ have the ability to perform both sensing and actuating functions. Passively smart materials respond to external change in a useful manner without assistance, whereas actively smart materials have a feedback loop which allows them to both recognize the change through an actuator circuit. Many smart materials are analogous to biological systems: piezoelectric hydrophones mentioned earlier are similar in mechanism to the "ears" by which a fish senses vibrations. Piezoelectrics with electromechanical coupling, shape memory materials that can "remember" their original shape, electrorheological fluids with adjustable viscosities, and chemical sensors which act as synthetic equivalents to the human nose are examples of smart electroceramics. "Very smart" materials, in addition to sensing and actuating, have the ability to "learn" by altering their property coefficients in response to the environment. Integration of these different technologies into compact, multifunction packages is the ultimate goal of research in the area of smart materials. We expect big changes to occur in this field during the coming decades.

REFERENCES

- 1) R. E. Newnham, *J. Mat. Educ.* 7(1985)601
- 2) R.E. Newnham, Q.C. Xu and S. Yoshikawa, Transformed stress direction-acoustic transducer, U.S. Patent # 4,999,819, March 12, 1992
- 3) Q.C. Xu, S. Yoshikawa, J. Belsick, R.E. Newnham, *IEEE Transactions on Ultrasonics, Ferroelectrics and Frequency Control* 38(1991)634
- 4) Y. Sugawara, K. Onitsuka, S. Yoshikawa, Q. Xu, R.E. Newnham, and K. Uchino, *J. Am. Ceram. Soc.* 75(1992)996
- 5) Q.C. Xu, A. Dogan, J. Tressler, S. Yoshikawa and R.E. Newnham, "Ceramic-Metal Composite Actuator", *IEEE Ultrasonic Symposium Proceedings* (Florida, 1991)
- 6) A. Dogan, Q.C. Xu, K. Onitsuka, S. Yoshikawa, K. Uchino and R.E. Newnham, "High Displacement Ceramic-Metal Composite Actuators (Moonie)", *Ferroelectric Special Issue for IMF8* (in press)

- 7) K. Onitsuka, A. Dogan, Q.C. Xu, J. Tressler, S. Yoshikawa, and R.E. Newnham, "Design Optimization for Ceramic-Metal Compostie Actuators (Moonie)", Ferroelectric Special Issues for IMF8 (in press)
- 8) K. Uchino, Piezoelectric and Electrostrictive Actuators (Morikita Publication, Tokyo, Japan)
- 9) K. Onitsuka, "Effects of Bonding and Geometry on the Flexensional Transducer, "Moonie", Ph.D. Thesis, The Pennsylvania State University, University Park, PA (1993)
- 10) T.R. Gururaja, R.E. Newnham, K.A. Klicker, S.Y. Lynn, W.A. Schulze, T.R. Shrout nad L.J. Bowen, Proc. IEEE Ultrasonics Symposium 2(1980)576
- 11) R.E. Newnham, D.P. Skinner and L.E. Cross, Mat. Res. Bull. 13(1978)525
- 12) D.P. Skinner, R.E. Newnham and L.E. Cross, Mat. Res. Bull. 13(1978)599
- 13) T.R. Shrout, W.A. Schulze, and J.V. Biggers, Mat. Res. Bull. 14(1979)1553
- 14) K. Rittenmyer, T. Shrout, W.A. Schulze, and R.E. Newnham, Ferroelectrics 41 (1982)189
- 15) K.A. Klicker, J.V. Biggers and R.E. Newnham, J. Am. Ceram. Soc. 64(1981)5
- 16) H.P. Savakus, K.A. Klicker and R.E. Newnham, Mat. Res. Bull. 16(1981)677
- 17) L. Bowen, Proceedings IMF (1993 Gaithersburg, MD), Ferroelectrics (in press)
- 18) G. Preu, A. Wolff, D. Crames, U. Bast Euro-Ceramics II 3(1991) 2005
- 19) C. Richard, P. Eyraud, L. Eyraud, A. Pelourson, M. Richard Euro-Ceramics II 3 (1991)2001
- 20) T.R. Gururaja, W.A. Schulze, L.E. Cross, R.E. Newnham, B.A. Auld and Y.J. Wang, IEEE Transactions on Ultrasonics 32(1985)481
- 21) T.R. Gururaja, W.A. Schulze, L.E. Cross, R.E. Newnham, B.A. Auld and Y.J. Wang, IEEE Transactions on Ultrasonics 32(1985)499
- 22) W. Smith, IEEE Ultrasonics Symposium (1989) p. 755
- 23) W. Pan, Q.M. Zhang, A. Bhalla and L.E. Cross, J. Am. Ceram. Soc. 72(1989)571
- 24) M.J. Haun, R.E. Newnham and W.E. Schulze, Adv. Ceram. Mat. 1(1986)361
- 25) M.J. Haun and R.E. Newnham, Ferroelectrics 68(1986)123
- 26) A. Safari, "Preforated PZT-Polymer Composites with 3-1 and 3-2 Connectivity for Hydrophone Applications," Ph.D. Thesis, The Pennsylvania State University, University Park, PA (1983)

- 27) J. Giniewicz, R.E. Newnham and A. Safari, *Ferroelectrics* **73**(1987)38
- 28) H. Banno, *Ferroelectrics* **50**(1983)329
- 29) S. Li, R.E. Newnham and L.E. Cross, The Effective Masses in Domain Walls in Ferroelectric Polycrystalline Materials (in press)
- 30) M.G. Matsko, Q.C. Xu and R. E. Newnham, Zig-Zag Piezoelectric Actuators: Geometrical Control of Displacement and Resonance, *J. of Intelligent Mat. Systems and Structures* (in press)
- 31) R.E. Newnham, *Mat. Res. Bull.* **18**(1993)24
- 32) J. Chen, Q.C. Xu, M. Blaszkiewicz, R. Meyer and R.E. Newnham, *J. Am. Ceram. Soc.* **75**(1992)2891
- 33) R.L. Opila and J.D. Sinclair, *Ann. Proc. Reliab. Phys. Symp.* **23**(1985)164
- 34) G.E. Pike, Sandia National Laboratory Technical Report 81-0263, 1981
- 35) K.A. Hu, D. Moffatt, J. Runt, A. Safari, and R.E. Newnham, *J. Am. Ceram. Soc.* **70**(1987)583
- 36) L.L. Rohlfing, R.E. Newnham, S.M. Pilgrim, and J. Runt, *J. Wave Mat. Int.* **3**(1988)273
- 37) S. Yoshikawa, T. Ota, and R.E. Newnham, *J. Am. Ceram. Soc.* **73**(1990)263
- 38) K. Bhattacharya, *Metal-Filled Polymers* (Marcel-Dekker, New York)
- 39) G.R. Ruschau, R.E. Newnham, J. Runt, and B.E. Smith, *Sens. Act.* **20**(1989)269
- 40) G.R. Ruschau, S. Yoshikawa, and R. E. Newnham, "Percolation Constraints in the Use of Conductor-Filled Polymers for Interconnects", Proceedings Electronic Components and Technology Conference San Diego, CA (1992)
- 41) R.J. Sullivan and R.E. Newnham, *Composite Thermistors, Chemistry of Advanced Materials* (Blackwell Scientific Publications)
- 42) G. Ruschau, "Conductive Composites as Chemical Sensors," Ph.D. Thesis, The Pennsylvania State University, University Park, PA (1991)
- 43) R.E. Newnham and G. Ruschau, *J. Am. Ceram. Soc.* **74**(1991)463

APPENDIX 27

THE EFFECT OF GEOMETRY ON THE CHARACTERISTICS OF THE MOONIE TRANSDUCER AND RELIABILITY ISSUE

A. Dogan, S. Yoshikawa K. Uchino, and R.E. Newnham
International Center for Actuators and Transducers
Materials Research Laboratory
The Pennsylvania State University
University Park, PA 16802

Abstract: The moonie actuator is a versatile performer that fills the gap between the multilayer actuator and the bimorph actuator. This paper describes the effect of geometrical changes in the endcap on the moonie's actuator characteristics. The reliability of multilayer moonie actuators were tested for long term usage and a wide range of temperatures. The effect of cavity dimensions, which are the key parameters for transformation and amplification of lateral motion into axial motion, on the characteristics of the moonie actuator were investigated. Fatigue tests of multilayer moonie actuator were performed under a cyclic electric field of 1 kV/mm with triangular wave form at 100 Hz, up to 10^7 cycles, at room temperature. Deviations less than $\pm 0.1\%$ from the original displacement value were observed. Temperature dependence experiments were performed in the range of -20 to +70 °C. Maximum $\pm 15\%$ nonpermanent deviations in the displacement from the room temperature value were observed.

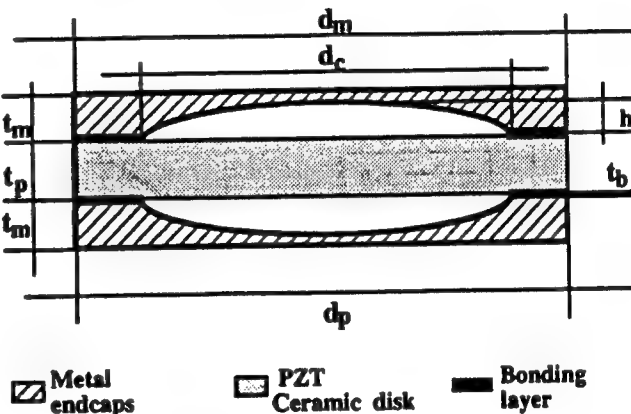
INTRODUCTION

The unique design of the ceramic-metal composite "moonie" transducer, makes it a candidate for several transducer applications including hydrophones, transceivers (e.g. fish finder), actuators, and active vibration controllers (smart systems)[1-5]. The objective of this study is to evaluate the actuator characteristics of the moonie. Desirable actuator properties such as displacement, generative force, and response time (resonant frequency) were the parameters used to evaluate the characteristics of the moonie actuator. The cross sectional view of the moonie actuator is shown in Figure 1. The dimensions of the cavity are key parameters for transformation and amplification of lateral motion into axial motion. The effect of cavity dimensions on the characteristics of the moonie were studied systematically altering the cavity diameter and cavity depth while keeping the endcap thickness constant. Concerns over long term reliability arose because of the bonding layer between the ceramic driving element and the metal endcaps. Multilayer moonie actuator, were fabricated with epoxy bonding agent (Emerson & Cuming, Eccobond 45LV) and tested for long term usage under a range of temperature conditions.

SAMPLE PREPARATION AND MEASUREMENT TECHNIQUES

The composite actuators were made from electrode PZT-5A or multilayer ceramic disks (11-12.7 mm in diameter and 1 mm thick) and endcaps (11-12.7 mm in diameter with thickness ranging from 0.3 to 3.0 mm). The endcaps were machined from brass with composition 30% Zn-70% Cu. The ceramic disk and the endcaps were bonded together around the circumference with Emerson & Cuming epoxy (Eccobond 45).

taking care not to fill the cavity or short circuit the electrodes. The displacement of a composite actuator at 0.01 Hz was measured with a Linear Voltage Differential Transducer (LVDT) having a resolution of approximately 0.05 μm . Resonant frequencies were obtained with a Hewlett-Packard Impedance / Gain-Phase Analyzer HP-4194A or Network Analyzer HP-3577A. Mechanical resonant characteristics were studied with a double beam laser interferometer[6]. Fatigue tests of the multilayer moonie actuator were performed under a cyclic electric field of 1 kV/mm with triangular wave form at 100 Hz, up to 10^7 cycles, at room temperature. Temperature dependence experiments were performed in the range of -20 to +70 °C.



Dimensions: (all in mm) Endcap diameter, $d_m = 12.7$ mm
PZT diameter, $d_p = 12.7$ mm Cavity diameter, $d_c = \text{variable}$: 3.0, 5.0, 7.0, 9.0 Cavity depth, $h = \text{variable}$: 0.3, 0.5, 0.7, 0.9
Metal cap thickness, $t_m = 1.0$ PZT thickness, $t_p = 1.0$
Bonding layer thickness, $t_b = 0.020$

Figure 1 The cross sectional view of the moonie actuator

EVALUATION OF THE EFFECT OF GEOMETRY ON THE CHARACTERISTICS OF THE MOONIE TRANSDUCER

Effect of Cavity Depth and Diameter

Brass endcaps with 3, 5, 7, and 9 mm cavity diameters and 0.3, 0.5, 0.7, and 0.9 mm crescent shaped cavity depths were fabricated by matrix combination while keeping the thickness constant at 1.0 mm, and diameter fixed at 12.7 mm. Figures 2 and 3 shows the relation between displacement-cavity diameter and cavity depth. The displacement amplification is exponentially related to the cavity diameter of the endcaps (at

constant cavity depth) and linearly related to the cavity depth (at constant cavity diameter).

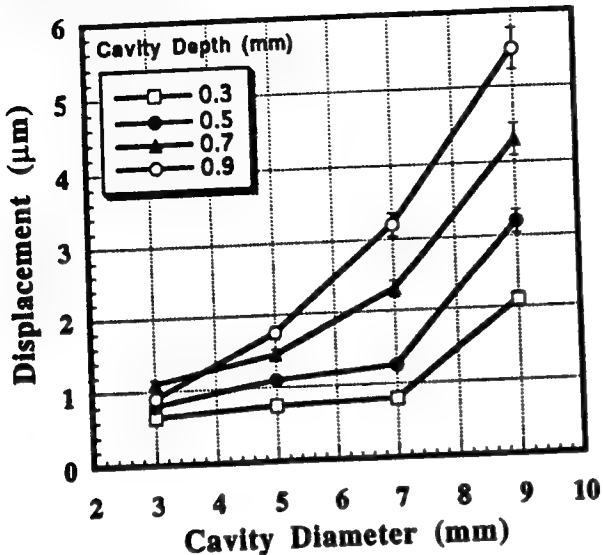


Figure 2. The displacement-cavity diameter relation of the moonie actuator

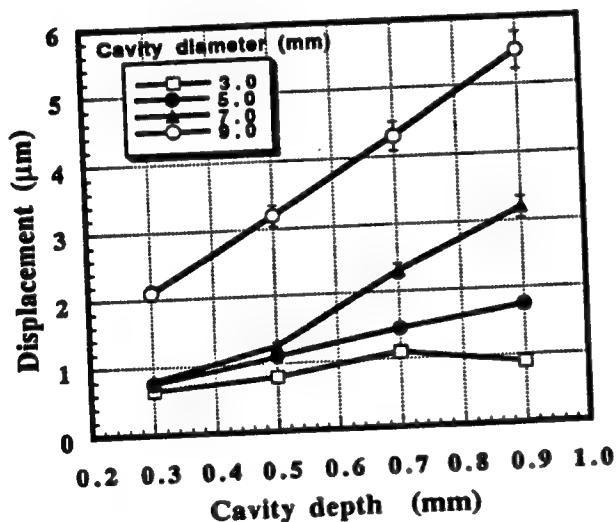


Figure 3. The displacement-cavity depth relation of the moonie actuator

Effect of Endcap Thickness

In later experiments, the cavity diameter ratio was fixed at 80% which is the ratio of the inner diameter of the endcap to the outer diameter. This allows room for a reliable bonding layer that can transfer motion from the ceramic to the endcap without failure during high displacement. The experimental results for the effect of cap thickness on the displacement of the moonie actuator is shown in Figure 4. The displacement of the moonie actuator increases with decreasing thickness, because of the increased flexibility of the endcaps. The displacement

shows an inverse relation with endcap thickness. A moonie actuator with 0.3 mm thick brass endcap exhibits a 22 μm displacement under an applied field of 1.0 kV/mm. After a certain value an abrupt increase in displacement is observed with decreasing brass thickness. A possible reason for this behavior is that the center of the endcap, which is approximately 100 μm thick, may no longer act as a rigid solid, but as a membrane. A membrane is more flexible than a rigid solid because of the large surface area. The FEA (Finite Element Analysis) of moonie actuators was also investigated^[7]. The calculated displacement values are plotted as a function of the endcap thickness in Figure 4. The FEA results are in fairly good agreement with experimental. A membrane element, unfortunately, was not available in the SAP90 program. A rigid solid element, for which bending or other large deformations was not allowed, was used in the FEA. This may be the reason for the deviations from the experimental results.

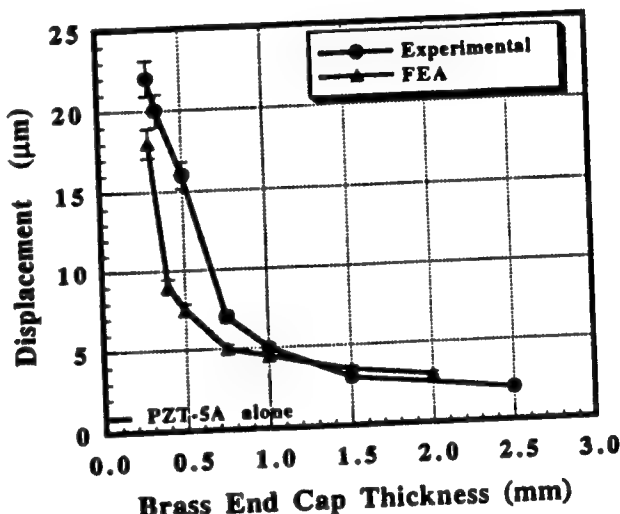


Figure 4. The displacement-endcap thickness relation of the moonie actuator

Fastest Response Time of the Moonie Actuator

Double Beam Laser Interferometer and Hewlett Packard impedance and gain-phase analyzer (HP-4194A) were used to determine the mechanical and electromechanical resonant characteristics of the moonie transducers. Consistent results with 5% accuracy are obtained with both methods. Because of easy handling, the HP Impedance Analyzer was used for the remainder of the characterization. Fastest response time-cavity diameter relations at various constant cavity depths of the moonie actuators are shown in Figure 5. Response time increases rapidly with increasing cavity diameter and decreases slightly with increasing cavity depth.

Figure 6 shows the relation between the fastest response time and endcap thickness. The calculated fastest response time (from first resonance frequencies) by FEA are also plotted for comparison with those obtained with experimentally. There is a very good agreement between the calculated and experimentally obtained values. Response time is approximately inversely proportional to brass endcap thickness.

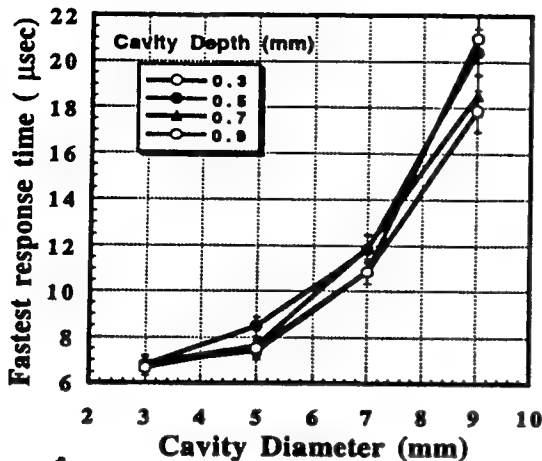


Figure 5. Fastest response time-cavity diameter relation of the moonie actuator

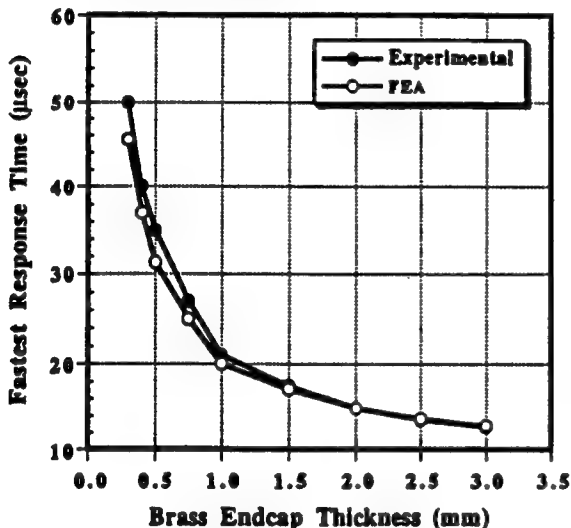


Figure 6 Fastest response time-endcap thickness relation of the moonie actuator

The Effective Coupling Factor of Moonie Transducer at First Flextensional Mode

The effective coupling factor, k_{eff} , can be derived from the series (resonant) and parallel (antiresonant) resonant frequencies of the transducer by using following equations.

$$k_{eff}^2 = \frac{f_p^2 - f_s^2}{f_p^2} \quad (1)$$

The effective coupling factor for the first resonance mode of moonie actuators with varying cavity depth and cavity diameters were calculated from their admittance spectra. Figure 7 shows the calculated effective coupling factor of the moonie actuator as a function of the cavity diameter at various cavity depths. The planar coupling factor of PZT-5A disc with 12.7 mm diameter and 1.0 mm thickness is around 0.65. The coupling factor decreases to 0.54 because of the load effect when the PZT-5A ceramic disc is sandwiched between brass endcaps

which have no cavities. The moonie actuator with a cavity diameter of 3.0 mm, and a cavity depth of 0.9 mm has the highest effective coupling factor of 0.42. As the cavity diameter increased, the effective coupling factor decreased linearly down to 0.11 for a cavity diameter of 9.0 mm with a cavity depth of 0.3 mm. Effective coupling factor depends heavily on the cavity diameter and depend a much lesser extent on the cavity depth.

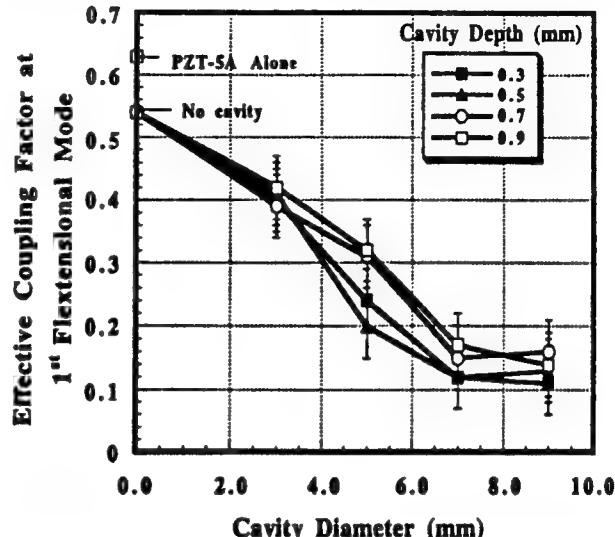


Figure 7 Effect of cavity diameter on the effective coupling factor of the moonie transducer at various cavity depths.

Maximum Generative Force of the Moonie Actuator

Although the flexural motion and displacement are largest at the center of the endcaps, the generative force is low. The position dependence of displacement is shown in Figure 8 for the moonie actuator with 0.30 mm thick brass endcaps. A displacement of about 22 μ m was obtained at the center of the moonie. Displacement decreases dramatically when moving from the center to the edge. Conversely, generative force increases when moving from the center to the edge, where it approaches that of PZT ceramic. Therefore, it becomes possible to tailor the desired actuator properties by changing the contact area over the brass endcaps.

RELIABILITY OF THE MOONIE ACTUATOR

The bonding layer between the PZT disk and metal endcaps plays an important role in the performance of the moonie transducers. The reliability of the moonie transducers depends strongly on the chemical, electrical and mechanical stability of the bonding layer. Strong bonding will assure efficient mechanical impedance transformation and long term reliability. To investigate the characteristics of the bonding layer, peel-up test, fatigue test, temperature dependence test were performed.

Peel-up test

When an electric field is applied to the moonie in the z-direction, i.e. the polarization direction of the PZT ceramic disk, there are two stresses on the bonding layer. One is a shear stress along the planar direction, the other is a tensile stress located at the tip of the metal-ceramic joining point, inside the cavity of the moonie. A modified peel up test was used to provide a quantitative measure of the tensile strength components of the

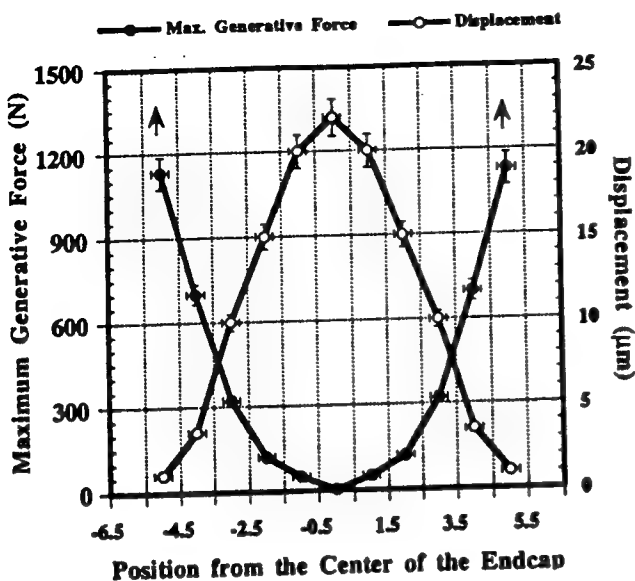


Figure 8 Trade-off between maximum generative force and displacement.

various bonding materials used in the moonie structure. The peel-up test was performed in order to simulate mechanical failure that begins at the stress concentration tip at the boundary of the moonie cavity.

The three bonding materials used in destructive testing were Emerson & Cuming epoxy (black epoxy), Acme conductive epoxy No. 3021 (conductive silver epoxy), and Indalloy No. 8 (or indium solder). Figure 9 shows the specimen geometry used for the modified peel up test. An Instron mechanical tester with suitable sensitivity and specimen clamping ability was used for the modified peel-up tests.

Figure 10 shows the applied force at which failure occurred for silver epoxy, black epoxy, and indium solder specimens. In this study force term is used to give a sense of the strength of the bonding layer. Maximum strength was observed for the samples fabricated with indalloy. The reason of this is the partial dissolution of silver electrode and penetration of the indium alloy into the grain boundaries into the PZT with optimum wettability. The wettability of the indium alloy was increased by using soldering resin. The indium solder was then able to establish a good contact between the brass and silver coated surface of PZT. The insulator and conductive epoxies did not dissolve the silver electrode. They create physical bonding between brass end caps and silver coated surface of PZT. Silver epoxy showed the lowest strength. The reason for this behavior is most likely due to the silver particles (approximately 5 μm in diameter) in the conductive epoxy which cause stress concentrations in certain regions and so lead to failure.

Fatigue Characteristics

The fatigue characteristics of a moonie actuator with different endcap thicknesses under a high cyclic electric field are shown in Figure 11. An electric field of 1 kV/mm at 100 Hz was applied to the actuators. Experiments were performed at room temperature ($25^\circ\text{C} \pm 2$). During Cycling test, a deviation in displacement of only $\pm 0.8\%$ was observed. Fatigue tests were continued for 10^7 cycles. The reason for the deviation is probably due to the effect of environmental temperature change on the bonding layer. Before and after the cyclic test, the admittance spectra of the actuators were recorded. The

admittance spectrum is extremely sensitive to any destruction in the bonding layer and to sample imperfections. For this reason, it is used as a nondestructive test method. After the fatigue tests, no significant changes were observed. The resonant and antiresonant frequencies as well as their peak amplitudes were the same as the original values.

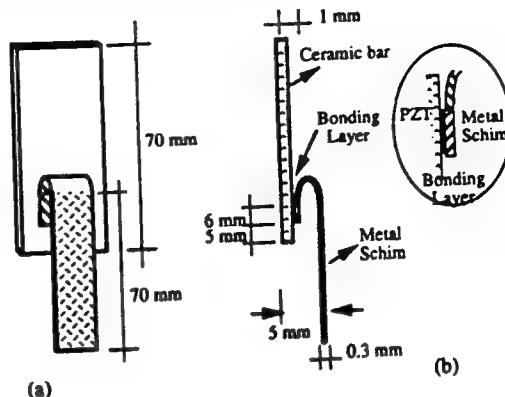


Figure 9 Sample geometry of modified peel-up test

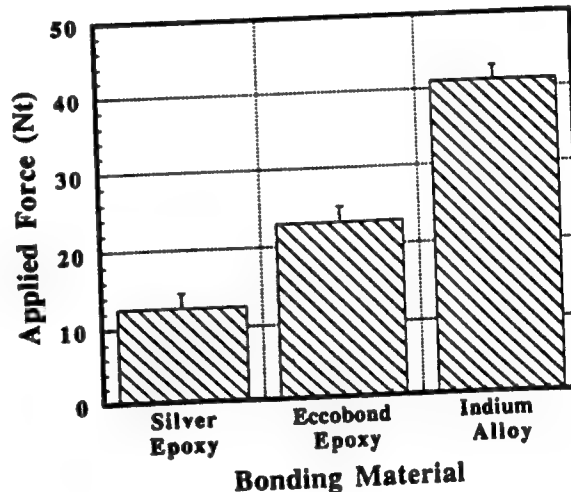


Figure 10 Peel-up strength of bonding materials

Temperature Dependence Of Multilayer Moonie Actuator

A multilayer piezoelectric ceramic can also be used as the driving element in the moonie design (referred to as a multilayer moonie), making it possible to decrease the applied voltage without sacrificing high displacement. Even higher displacement values can be obtained by stacking multilayer moonies together^[2]. Multilayer piezoelectric ceramics (NEPEC-10, Tokin Co.) with 100 μm layer thickness and 1.0 mm total thickness were used as driving element in the multilayer moonie actuator. The effect of temperature on the displacement of a multilayer moonie actuator is shown in Figure 12. The displacement appears to be approximately constant from 10 to 45°C . There is a 7-8% deviation in this range. Between -20 and $+10^\circ\text{C}$ significant temperature dependent behavior is observed. The main reason for this temperature dependence is the multilayer piezoelectric ceramic

itself. The temperature characteristic of a multilayer ceramic was measured and it shows similar behavior to the multilayer moonie actuator fabricated with the same multilayer ceramic element. A secondary reason is the bonding layer between the ceramic and the metal end caps. The thermal expansion coefficient difference between the brass end caps (Cu 70%, Zn 30%: $18 \times 10^{-6} /^{\circ}\text{C}$) [8] and ceramic (PZT = $4 \times 10^{-6} /^{\circ}\text{C}$) causes thermally induced flexensional displacement. By choosing a low thermal expansion material, e.g. titanium, titanium alloys, stainless steel or some special epoxy compositions, this problem can be overcome.

thickness) can be summarized as: displacement ~22 μm , maximum generative force ~3 N, response speed ~50 μsec . Moreover, there is a trade off among these criteria. The moonie actuator can give displacements of 20 to greater than 100 μm , maximum generative force of 3 N to several N's, and response time of 20 to 100 μsec . By altering some of the dimensions on the moonie design, it is easy to tailor an actuator with desired properties. Multilayer moonie shows high reliability for long term usage; less than 0.1% deviation was observed after 10^7 cycles. Modest temperature dependent behavior was observed with a maximum deviation of $\pm 15\%$ when cycled between -20 and $+70^{\circ}\text{C}$.

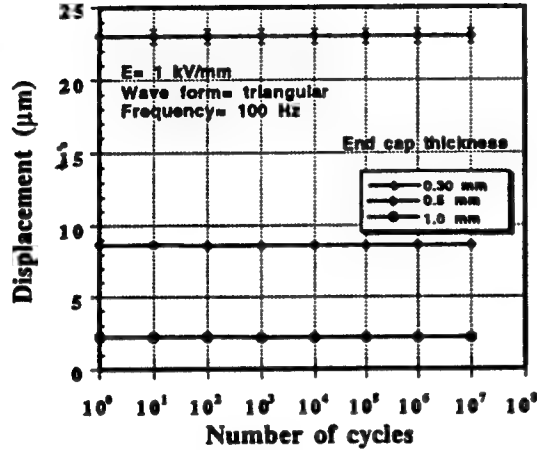


Figure 11 Fatigue characteristic of the moonie actuator

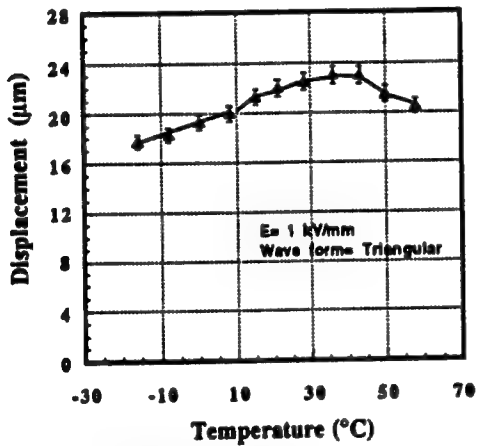


Figure 12 Temperature dependence of the multilayer moonie actuator

SUMMARY

Displacement of the moonie actuator is approximately inversely proportional to endcap thickness, exponentially proportional to the cavity diameter, and linearly proportional to the cavity depth. Response time of the moonie actuator increases with increasing cavity diameter. Moonie shows position dependent behavior with maximum displacement at the center and maximum force at the perimeter. Desired actuator properties can be easily tailored by changing the contact area over the endcaps. The properties of the moonie actuator (12.7 mm in diameter with 0.3 mm thick end caps, ~1.7 mm in total

REFERENCES

- [1] R.E.Newnham, Q.C.Xu and S. Yoshikawa, *U.S Patent # 4,999,819* (March 12, 1992).
- [2] A.Dogan, Q.C. Xu, K.Onitsuka, S.Yoshikawa, K.Uchino and R.E.Newnham, *Ferroelectrics*, vol. 156, pp. 1-6, (1994)
- [3] Y.Sugawara, K.Onitsuka, S.Yoshikawa, Q.Xu, R.E.Newnham, and K.Uchino, *J.Am.Ceram.Soc.*, vol. 75, no.4, pp. 996-999, (1992).
- [4] R.E.Newnham, A.Dogan, Q.C. Xu, K.Onitsuka, S.Yoshikawa, K.Uchino IEEE - UFFC , Baltimore 1993
- [5] Q.C.Xu, S.Yoshikawa, J.Belsick, and R.E.Newnham, *IEEE Transactions on Ultrasonics, Ferroelectrics and Frequency Control*, vol. 38, no. 6, pp. 634-639, (1991).
- [6] W.Y. Pan, and L.E. Cross, *Rev.Sci.Instrum.* 60 (8) August 1989
- [7] K.Onitsuka, A.Dogan, J.Tressler, Q.C.Xu, S.Yoshikawa, and R.E.Newnham, *J. Intell. Mater. Syst. and Struct.* (accepted for press).
- [8] C.R.Tuttle, "An Encyclopaedia of Metallurgy and Materials," Great Britain, Macdonald and Evans, 1984.

APPENDIX 28

CERAMIC-METAL COMPOSITE ACTUATOR

Q.C. Xu, A. Dogan, J. Tressler,
S. Yoshikawa, and R. E. Newnham
Materials Research Laboratory
The Pennsylvania State University
University Park, PA 16802

ABSTRACT

The main objective of this work was to develop a new type of actuator. It consists of a piezoelectric ceramic disk or multilayer stack and two metal end plates with a crescent-shaped cavity on the inner surface. The plates are used as mechanical transformers for converting and amplifying the lateral displacement of the ceramic into a large axial motion in the plates. Both d_{31} and d_{33} contribute to the axial displacement. Sizeable strains were obtained with both PZT-metal and PMN-metal actuators. Displacement amplification principle, fabrication, and measurement results are presented.

INTRODUCTION

In recent years, piezoelectric and electrostrictive ceramics have been used in many actuator applications. The two most common types of actuator are a multilayer ceramic actuator with internal electrodes and a cantilevered bimorph actuator^[1]. A frame structure for displacement amplifier in impact printer head has also been developed using piezoelectric multilayer actuators^[2].

This paper describes a new type of ceramic-metal composite actuator which is based on the concept of a flexextensional transducer^[3]. The ceramic is excited in an extensional mode and the metal plates in a flexure mode. The metal plates are used as a mechanical transformer for transforming the high mechanical impedance of the ceramic to the low mechanical impedance of the load. Therefore, a large effective piezoelectric coefficient, d_{33} , exceeding 4000 pC/N as well as a hydrostatic piezoelectric coefficient d_h , exceeding 800 pC/N can be obtained from a single PZT disk-metal (brass) composite^[4].

PRINCIPLE

The extensional mode of the piezoelectric ceramic element is characterized by a large generated force, a high electromechanical coupling, a high resonant frequency, and a small displacement. Often it is desirable to use a compact structure to magnify the displacement of the ceramic element. Figure 1 shows the basic configuration of the ceramic-metal composite

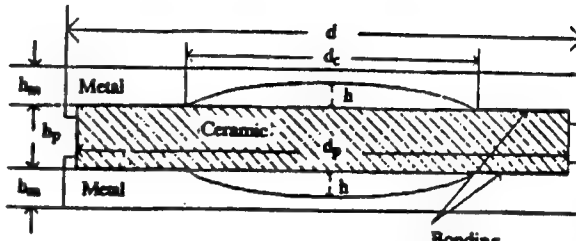


Figure 1. The geometry of composite.

actuator. The ceramic element can either be a piezoelectric ceramic or an electrostrictive ceramic with single layer or multilayer. Low driving voltages can be used for the multilayer ceramic element. The electrostrictive ceramic is expected to reduce hysteresis as well as exhibit a nonlinear relationship between the voltage and the displacement.

The "Moonie" metal plates are used as displacement magnifiers. The relationship between the displacement of the metals and the geometry of the metals and the ceramic is explained below. For simplicity, consider a curved beam with small curvature bonded to a ceramic bar (Figure 2). According to elastic theory [5], the bending moment M under an electroactive force from the ceramic is as eq. (1):

$$M = \frac{-T_d \left(b^2 - a^2 \right) - 4ab \left(\ln \frac{b}{a} \right)^2}{a} \quad (1)$$
$$4 \left[\frac{a^2 b^2}{r} \ln \frac{b}{a} + b^2 \ln \frac{r}{b} + a^2 \ln \frac{a}{r} + b^2 a^2 \right]$$

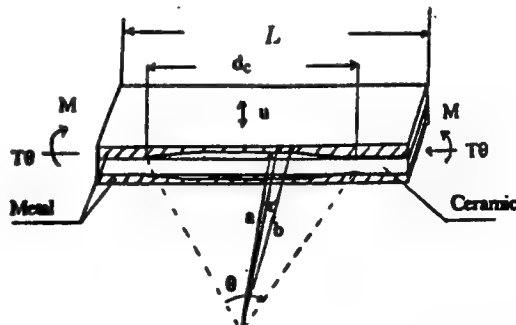


Figure 2. Simplified model for displacement magnification.

The electroactive force will be transmitted to the Moonic metal. The stress in the metal is:

$$T_\theta = \frac{dE_3 Y_c A_c}{A_m} \quad (2)$$

where d = piezoelectric strain coefficient of the ceramic,
 E_3 = electric field in the ceramic,
 Y_c = Young's modulus of the ceramic,
 A_c, A_m = cross sectional area of the ceramic and metal, respectively,

and $r \sim a \sim b$.

The normal displacement of the metal produced by the piezoelectric effect of the ceramic is:

$$U_{pi} = \frac{-M \left(\frac{h_m}{2} \right)^2}{2 Y_m I_m} \sim \frac{3}{4} \frac{d Y_c d_c}{h_m Y_m \theta} V \quad (3)$$

h_m = thickness of the metal
 Y_m = Young's modulus of the metal
 V = applied voltage
 I_m = moment of inertia of the metal

$$d_{33} \Big|_{eff} = \frac{U_{pi}}{V} = \frac{3}{4} \frac{d Y_c d_c}{h_m Y_m \theta} \quad (4)$$

For the electrostrictive effect:

$$T_\theta = \frac{Q \epsilon E^2 Y_c A_c}{A_m} \quad (5)$$

Q = electrostrictive coefficient of the ceramic
 ϵ = permittivity

The displacement of the metal by the electrostrictive effect is then:

$$U_{el} = \frac{3}{4} \frac{Q \epsilon^2 Y_c d_c}{h_m h_c Y_m \theta} V^2 \quad (6)$$

The transverse displacement at the end of the ceramic bar is:

$$\delta = \frac{dV}{h_c} L$$

and the displacement conversion ratio is:

$$\frac{U}{\delta} = \frac{3}{4} \frac{d_c Y_c h_c}{L \theta Y_m h_m} \quad (7)$$

Equations (3) and (6) explain how the normal displacement U of the metal is related to the transverse piezoelectric or electrostrictive effect of the ceramic. The total displacement is the sum of the displacement described above and the displacement due to longitudinal effects.

The lowest resonant frequency of the actuator is a flextensional mode which is determined mainly by the stiffness of the ceramic in a planar mode and the equivalent mass of the metal plate. The equivalent mass is much larger than the real mass of the metal plate because the vibration velocity of the metal part is much larger than the reference velocity of the PZT. The equivalent mass is

$$M_e = \frac{\int_0^L \frac{1}{2} \rho_m b h_m U^2 \omega^2 dX}{\frac{1}{2} \delta^2 \omega^2} \sim M_m \frac{d_c^2 Y_c^2 h_c^2}{L^2 \theta^2 Y_m^2 h_m^2}$$

$$M_m = \rho_m V_m = \rho_m b h_m L$$

When the h_c/h_m ratio is high and $k_m \ll k_c$, the resonant frequency of the lowest flextensional mode is:

$$f_R = \frac{1}{2\pi \sqrt{(M_e + M_c)(k_c + k_m)^{-1}}} \sim \frac{f_c}{\sqrt{1 + (2\pi f_c)^2 M_c k_c^{-1}}} \\ = [1 + (2\pi f_c)^2 \frac{M_m k_c^{-1} Y_c^2 h_c^2 d_c^{-1}}{L^2 \theta^2 Y_m^2 h_m^2}]^{1/2} f_c \quad (8)$$

The M_e is much larger than the real mass of the metal.

Here k_c =stiffness of ceramic
 k_m =stiffness of metal plate
 f_c =resonant frequency of planar mode of the ceramic itself.

$$f_c = \frac{1}{2\pi \sqrt{M_c k_c^{-1}}}$$

From equation (8) the lowest flextensional frequency f_R is proportional to $\sqrt{h_m}$.

SAMPLE PREPARATION

The composite actuators were made from electroded PZT5A or PMN-PT ceramic disks (11 mm in diameter and 1 mm thick) and brass end caps (from 11 mm to 13 mm in diameter with thicknesses ranging from 0.2 to 3 mm). Shallow cavities from 6 mm to 8.5 mm in diameter and about 150 μm center depth were machined into the inner surface of each brass cap. The ceramic disk and the end caps were bonded around the circumference, taking care not to fill the cavity or short circuit the ceramic electrodes. Three kinds of bonding materials have been utilized:

1. Silver foil (25 μm thickness) and silver paste bonding.

This composite was heated to 600°C under stress to solidify the bond. After cooling, the actuator was encapsulated using Spurr's epoxy resin, followed by curing at 70°C for 12 hours. Electrodes were attached to the brass end caps and the PZT ceramic was poled at 2.5 MV/m for 15 minutes in an oil bath held at 120°C.

2. Pb-Sn-Ag Solder Bonding.

The PMN-PT or poled PZT and the brass end caps with the Pb-Sn-Ag solder ring (thickness 50 μm) were heated to 190°C under pressure. After cooling, the composite was encapsulated using epoxy resin.

3. Epoxy Resin Bonding.

The brass end caps and the ceramic were bonded by Emerson & Cuming epoxy resin around the rim at room temperature.

An electrostrictive actuator was made from a multilayer ceramic stack and a brass beam and bonded to the Moonie inner surface with an epoxy (Figure 3). This composite demonstrates that a sizeable displacement can be produced under low driving voltage using a multilayer ceramic stack.

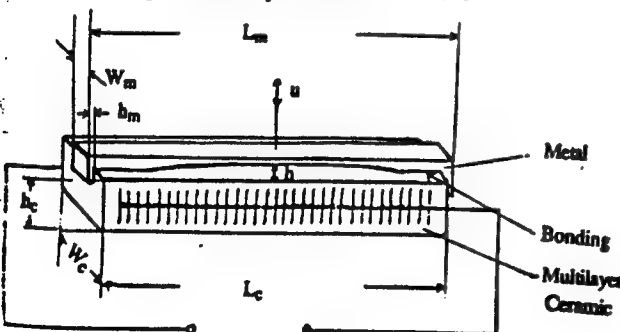


Figure 3. Another type of ceramic-metal composite actuator with multilayered ceramic part.

EXPERIMENT RESULTS

The displacement of the composite actuator in the low frequency range was measured with a Linear Voltage Differential Transducer (LVDT) having a resolution of approximately 0.05 μm . The direct piezoelectric coefficient d_{33} was measured at a frequency of 100 Hz using a Berlincourt d_{33} meter. The displacement-frequency dependence was measured with a double beam laser interferometer. Resonant frequencies were obtained with a Hewlett-Packard Spectrum Analyzer (HP-3585A) or Network Analyzer (HP-3577A).

1. Displacement Measurement

Figure 4 shows the displacements versus electric field curves for composite actuators driven by PZT and PMN ceramics. Displacements for the uncapped ceramics are shown for comparison. PMN does not need to be poled because it utilizes the electrostrictive effect rather than piezoelectricity. Dimensions of the PMN composite sample in Figure 4 are as follows: $d=13$ mm, $d_p=11$ mm, $h=150 \mu\text{m}$, $d_c=6$ mm, $h_p=1 \text{ mm}$, and $h_m=0.4 \text{ mm}$. The dimensions of the PZT composite-1 sample are: $d=d_p=11$ mm, $h=50 \mu\text{m}$, $d_c=7$ mm, $h_p=1 \text{ mm}$, and $h_m=0.5 \text{ mm}$. Both of the uncapped PZT and PMN ceramics have the same size, $d_p=11$ mm and $h_p=1 \text{ mm}$. The experimental results show that the composites produce a strain amplification of about 10 times. A displacement of about 10 μm can be obtained under a field of 1 kV/mm. By loading these actuators with weights, it is capable of exerting forces in excess of 2 kgf.

As shown in Equation 3 and Equation 6, the displacement amplification is dependent on the thickness of metal h_m and cavity diameter d_c . The sample PZT composite-2 with dimensions $d=d_p=11$ mm, $h_p=1 \text{ mm}$, $h=200 \mu\text{m}$, $h_m=0.3 \text{ mm}$, and $d_c=8.5$

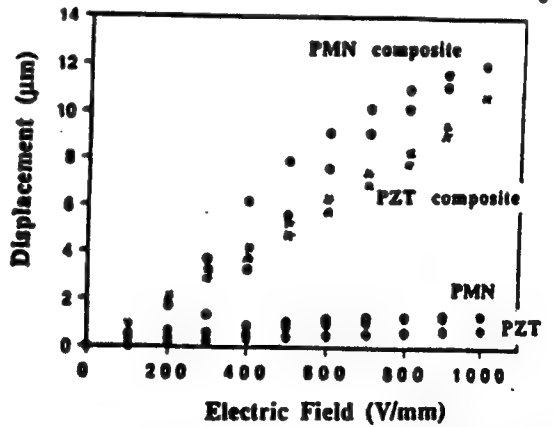


Figure 4. Displacements measured for composite actuators driven by PZT and PMN ceramics. Displacement for the uncapped ceramics are shown for comparison.

mm exhibits sizeable displacements - as large as 20 μm with a force capability of 0.15 kgf (see Figure 5).

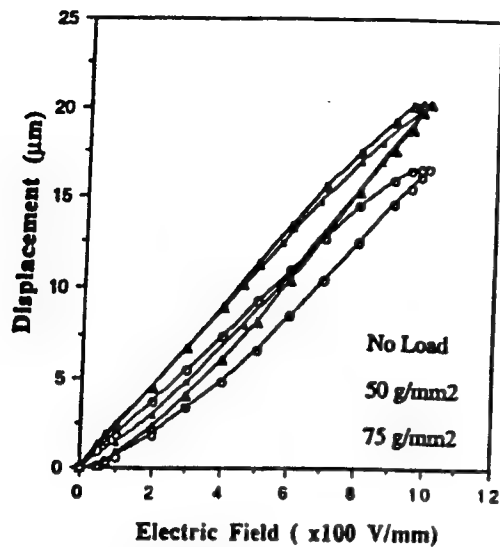


Figure 5. Displacement vs. field curves under different exert forces for the sample PZT composite-2.

The 124 layer electrostrictive composite actuator shown in Figure 3 gave the displacement exhibited in Figure 6. More than 15 μm displacement can be obtained under an applied voltage of 150V. Notice that this experimental result is obtained with only one metal end-cap on the ceramic stack. If the convex or concave metal end-caps are placed on both sides of the ceramic stack, more than 30 μm displacement will be obtained under the applied voltage of 150V. Displacements for the uncapped multilayer ceramic in the same direction are shown for comparison. The lowest flextensional resonant frequency for the composite is 6.4 kHz.

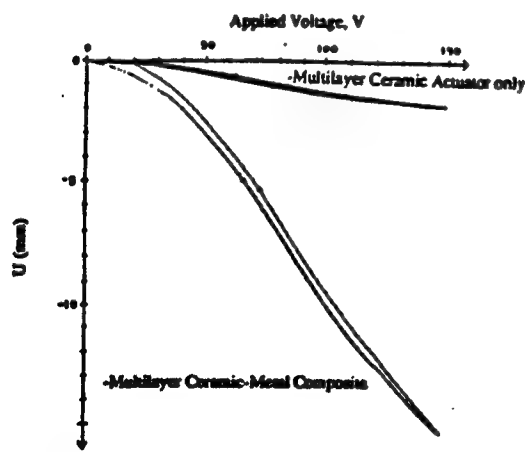


Figure 6. Displacement with increase in applied voltage of the multilayer ceramic-metal composite actuator using no electrostrictive ceramic stack and a brass end cap.

2. Thickness Dependence

Figure 7 shows the effective d_{33} coefficient and resonant frequency plotted as a function of the brass thickness. As expected in Eq. (4) and Eq. (8), the effective d_{33} is proportional to $1/h_m$ and the lowest resonant frequency is proportional to $\sqrt{h_m}$. The d_{33} values were measured at the center of the brass end caps using a Berlincourt d_{33} meter. Values as high as 4000 pC/N, approximately 10 times that of PZT5A, were obtained with the Moonie actuator.

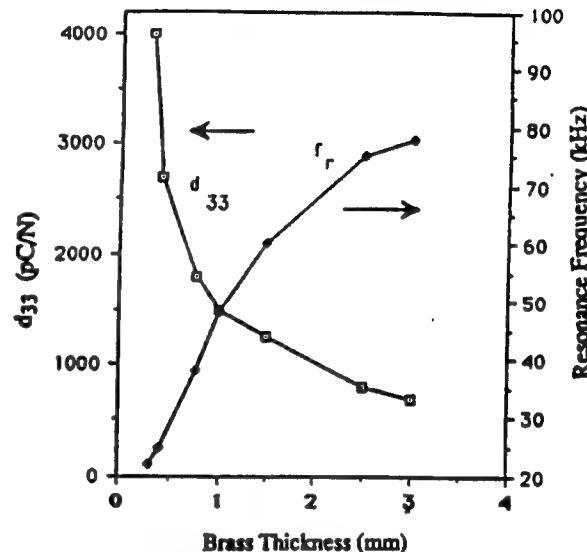


Figure 7. Resonance frequency f_r and d_{33} coefficient plotted as a function of the thickness of the brass endcaps.

Piezoelectric effects are largest near the center of the transducer where the flexural motion is largest. The effective values measured as a function of position with a Berlincourt meter are shown in Figure 8. Plots are shown for two brass thicknesses of 0.4 and 3.0 mm. Ample working areas of several mm^2 are obtained with the actuators.

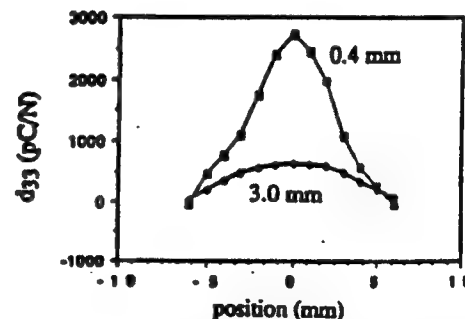


Figure 8. Positional dependence of the d_{33} coefficient for two actuators with brass thickness of 0.4 mm and 3.0 mm.

3. Resonant Frequency-Temperature Dependence

The lowest flextensional frequency of the PZT-brass composite with Pb-Sn-Ag solder bond and without epoxy encapsulation decreases with temperature as shown in Figure 9. This is probably due to the high stress in the PZT ceramic arising from thermal stresses set up by the metal.

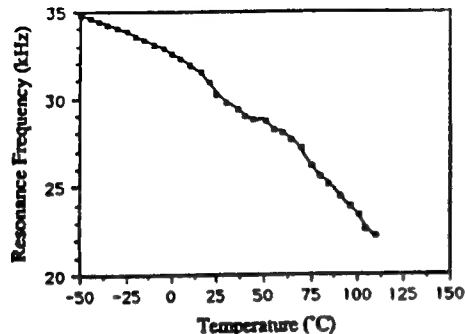


Figure 9. Resonance Frequency vs. Temperature

4. Electrode Effect

Figure 10 shows the effective piezoelectric d_{33} coefficient of the composite increases with electrode area of PZT. This means that all the PZT is contributing uniformly to the displacement.

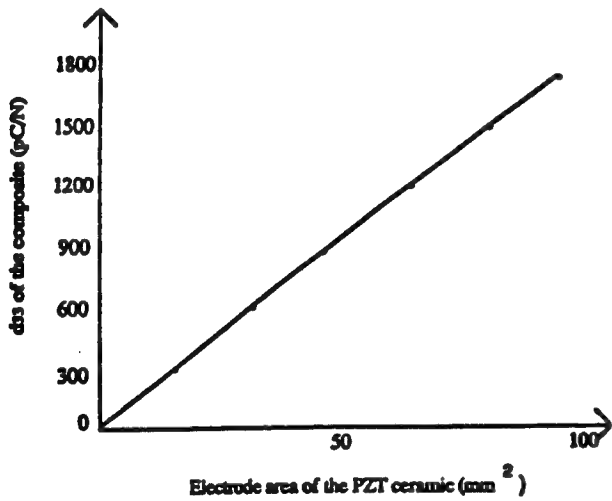


Figure 10. Effective d_{33} vs. electrode area of the ceramic.

5. Creep

Keeping a field of 1 kV/mm on the composite sample with epoxy bonding for two hours, no displacement change was observed by LVDT measurement (see Figure 11) after one hour.

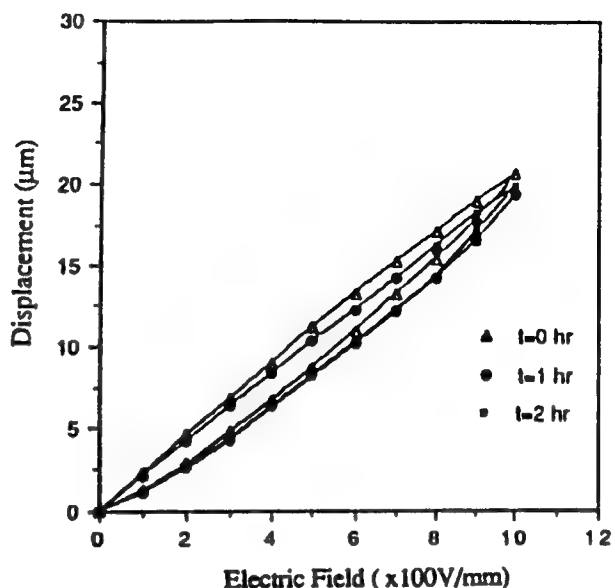


Figure 11. Creep under field 1KV/mm.

CONCLUSIONS

A new type of actuator has been constructed from piezoelectric PZT ceramics bonded to metal end caps. Shallow spaces under the end caps produce substantial increases in strain by combining the d_{33} and d_{31} contributions of the ceramic. Even larger displacements were obtained using PMN electrostrictive ceramics.

The displacement is inversely proportional to the metal thickness.

The lowest resonant frequency is proportional to the square root of the metal thickness.

The displacement is proportional to the area of the driving ceramic.

The creep under 1 kV/mm is very small after one hour.

Further improvements in actuator performance are expected using improved materials and design. Driving voltages can be reduced using multilayer ceramics, and larger displacements can be obtained using multimoenie stacks (Figure 12).

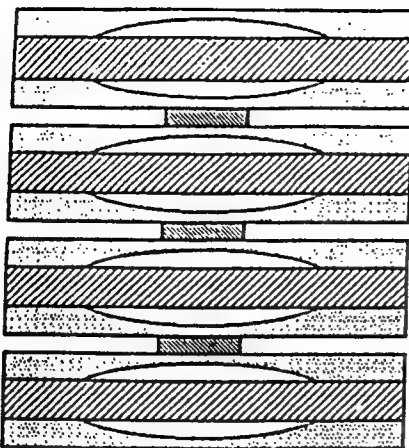


Figure 12. Illustration of Stacked Composite.

ACKNOWLEDGEMENTS

The authors wish to thank Dr. W. Smith, Professor L.E. Cross, Dr. K. Uchino, and Dr. J. Dougherty for their advice, as well as Y. Sugawara, K. Onitsuka, and J. Belsick for work reported in earlier papers [3,6].

REFERENCES

1. K. Uchino, "Piezoelectric/Electrostrictive Actuator," Morikita Publishers, Tokyo, Japan(1986)
2. K. Yoda , H. Morita, T. Mori, T. Shibuya, "Frame Structure for Impact Print Head," Spring Meeting of IECE of Japan, 7-96 (1990) (in Japanese).
3. Q.C. Xu, J. Belsick, S. Yoshikawa, and R. E. Newnham, "Piezoelectric Composites with High Sensitivity and High Capacitance for Use at High Pressure," IEEE Transactions on UFFC (in press).
4. R.E. Newnham, Q.C. Xu, and S. Yoshikawa, (patent) "Transformed Stress Direction-Acoustic Transducer (to the Pennsylvania Research Corporation) U.S. 4,999,819 (March 12, 1991).
5. S. Timoshenko and J. N. Goodier, "Theory of Elasticity," Chapters 4 and 10, 2d ed., New York, McGraw-Hill, 1951.
6. Y. Sugawara, K. Onitsuka, S. Yoshikawa, Q.C. Xu, R.E. Newnham, and K. Uchino, "Piezoelectric and Electrostrictive Composite Actuators," Proceedings of the 1991 International Symposium on Active Materials and Adaptive Structures, Alexandria, VA (in press).

APPENDIX 29

DESIGN OPTIMIZATION FOR METAL-CERAMIC COMPOSITE ACTUATOR, "MOONIE"

KATSUHIKO ONITSUKA, AYDIN DOGAN, QICHANG XU,
SHOKO YOSHIKAWA, AND ROBERT E. NEWNHAM
Intercollege Materials Research Laboratory, The Pennsylvania State University
University Park, PA 16802 USA

(Received August 9, 1993)

Abstract A piezoelectric ceramic-metal composite actuator has been developed to amplify the displacement of the piezoelectric ceramic. In this structure, the PZT ceramic is sandwiched between end caps with shallow cavities. This paper describes the design optimization of the flexextensional transducer using finite element analysis (FEA). By using FEA, shape, material, and geometrical contributions to the displacement of the actuator were calculated. The effect of load on the displacement was also estimated. It was found that the displacement of the actuator increases with cavity diameter and depth, and that introducing a ring-shaped groove on the metal end caps of the actuator greatly enhances the displacement.

INTRODUCTION

A piezoelectric ceramic-metal composite actuator has been developed to amplify the displacement of a piezoelectric ceramic. The cross section of the moonie actuator is illustrated in the previous paper by Dogan et al. In this structure, the PZT ceramic is sandwiched between end caps with shallow cavities. Typical dimensions of these actuators are 11 mm in diameter and 2 mm in total thickness. The depth of the cavity is about 0.1 to 0.2 mm. The PZT and metal end caps are bonded together tightly using epoxy. By applying an electric field to the moonie actuator, the radial motion of PZT ceramic can be converted into flexextensional motion creating a large displacement.

This paper describes the design optimization of the flexextensional transducer using finite element analysis (FEA). The principal factors controlling the performance of the actuator were found to be the design of metal end caps and the bonding. Using FEA, the material and geometrical contributions to the displacement and generative force of the actuator were calculated. Load effects on the displacement were also estimated. Based on the modeling, changes in cap thickness and cavity size produced large effects on the displacement. It was also found that the displacement of the actuator increases with cavity diameter and depth, and that introducing a ring-shaped groove on the metal end caps of

the actuator greatly enhances the displacement. Finally, the displacement and generative force obtained experimentally were fitted to those calculated by FEA.

FEA Modeling

Two commercially available FEA programs (ANSYS and SAP90) were used for this study. For frequency response analysis, the relationship between admittance and frequency was calculated using 3-D axisymmetric piezoelectric elements in ANSYS. In the displacement analysis, the relationship between displacement and applied electric field was calculated using 2-D axisymmetric elements in SAP90. Each model was divided into three parts: the end cap, the PZT ceramic, and the bonding layer. Material parameters used in this analysis were Young's modulus, density, Poissons' ratio, piezoelectric constants, and dielectric constants.

CALCULATED AND EXPERIMENTAL RESULTS

(1) Frequency response of a moonie actuator

From the frequency response analysis, the lowest three resonant frequencies were calculated. Figure 1 shows admittance spectrum of the moonie plotted as a function of the frequency from 10 to 300 kHz. Three resonance peaks appear at 50, 187, and 210 kHz, corresponding the lowest three flexensional vibration modes. The first flexensional mode can be effectively utilized up to nearly 50 kHz. Based on these results, the coupling coefficient of the first mode was calculated as 20%.

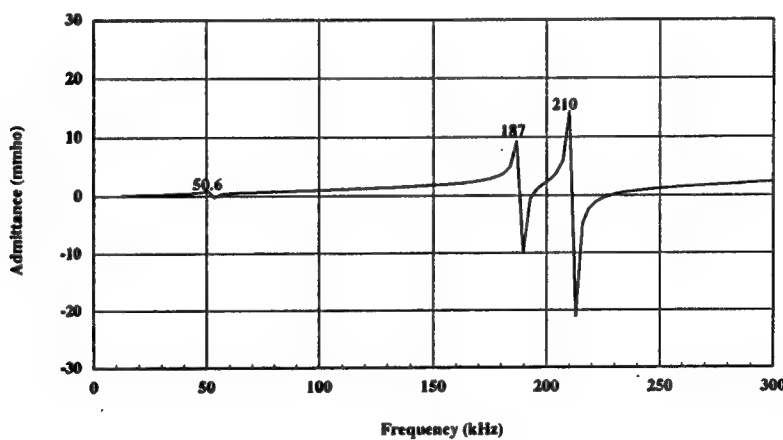


FIGURE 1 Calculated admittance curve of the 11 mm moonie actuator

Figure 2 compares the first resonant frequencies calculated by FEA with those obtained experimentally, for a range of brass cap thicknesses. Excellent agreement was obtained. The first resonant frequency is approximately proportional to the square root of the brass cap thickness.

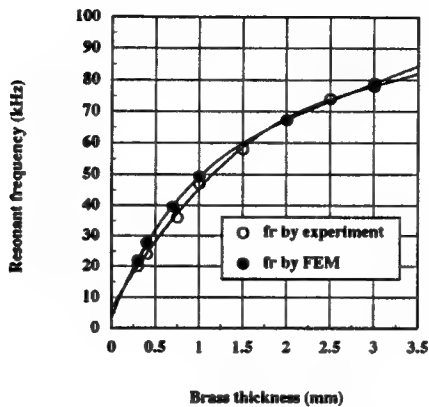


FIGURE 2 Calculated and measured first resonant frequencies of the moonie actuator

(2) Geometrical control of displacement for a moonie actuator

Figure 3 shows calculated displacement contour of the upper cap of a moonie actuator under an applied electric field of 1 kV/mm. The maximum displacement of 4.5 μ m appears at the center of the moonie cap and gradually decreases toward the edge. The displacement profile of the moonie actuator corresponds to the effective d_{33} profile measured.

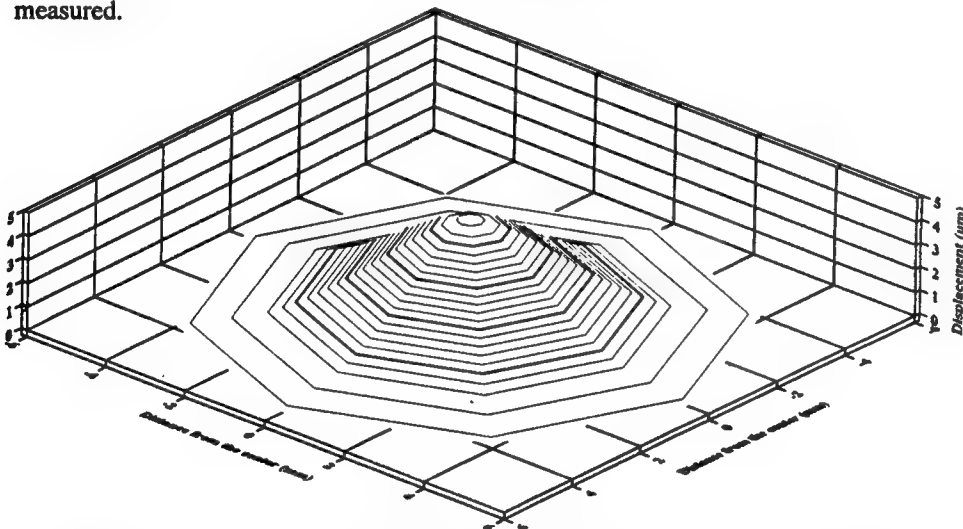


FIGURE 3 Calculated displacement contour of the upper cap of a moonie actuator

Figures 4 show the effect of geometry on displacement. The four variables are cap thickness, cavity size, cavity depth, and bonding thickness. Displacement decreases markedly with cap thickness and is inversely proportional to the brass cap thickness (Figure 5). Cavity diameter and cavity depth also affect the displacement. By increasing cavity size and cavity depth, displacement increases almost linearly. On the other hand, the thickness of the bonding layer has very little effect on the displacement in the range from 5 to 100 μm . In practice, the moonie has about 10 to 20 μm thick bonding layer.

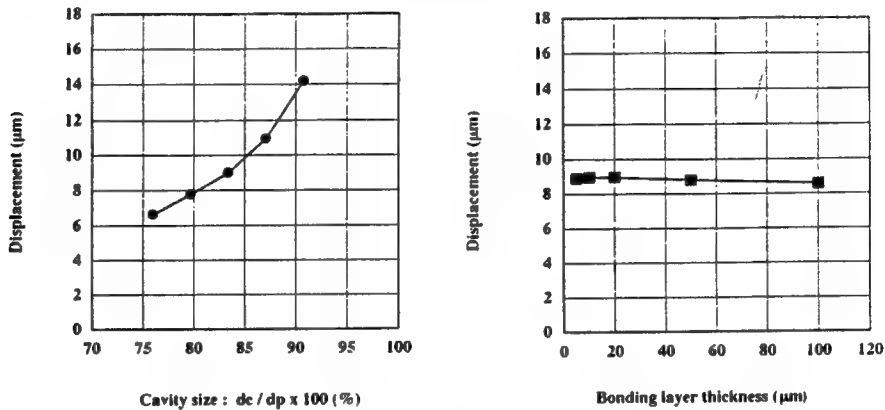


FIGURE 4 Effect of cavity diameter (left) and bonding layer thickness (right) on the displacement of the moonie actuator

Figure 5 compares the displacement calculated by FEA with those obtained by experiment, and plotted as a function of the brass thickness. This actuator is made of PZT-5, brass caps, and epoxy bonding with 20 μm thickness. There is very good agreement in displacement between the calculated and experimental values.

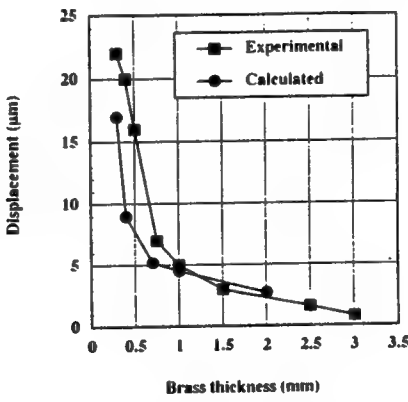


FIGURE 5 Calculated and measured displacements of the moonie actuator

In order to enhance the displacement of the moonie actuator, some modifications of the cap design were considered. It was found that introduction of a groove on the caps enhanced the displacement markedly. To determine the effect of the groove on displacement, the locations and dimensions of the groove were altered. Figure 6 compares the effect of groove position on the displacement (the maximum displacement is shown at the left side of each deformed shape) where g_p , g_d , and g_w are the groove position, groove depth, and groove width, respectively.

The most effective position of the groove is just above the edge of the inner cavity. In this case, a doubling of displacement (8.86 μm) was observed.

Also the depth of the groove is important in enhancing the displacement. The deeper the groove, the higher the displacement. A displacement (12 μm) three times higher than the original is observed on the deepest grooved moonie.

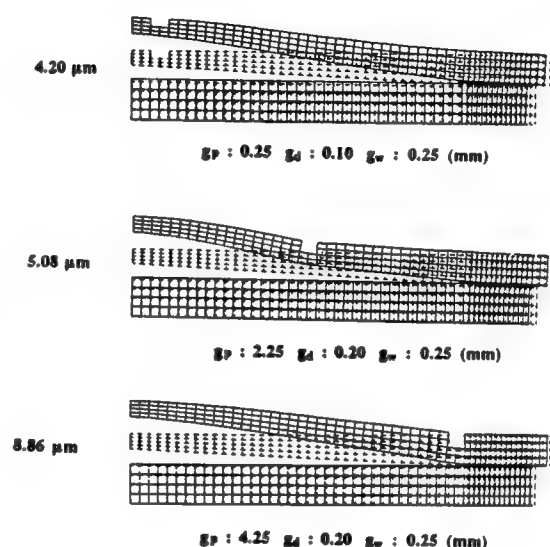


FIGURE 6 Groove positional effect on the displacement of the moonie actuator

(3) Effect of cap material effect on the displacement of a moonie actuator

Cap material partially controls the displacement of a moonie actuator. Four different cap materials stainless steel, brass, bronze, and plastic were selected for modeling. It was found that the higher the elastic stiffness, the lower the displacement. A plastic capped moonie actuator produces about 30 μm at a cap thickness of 0.3 mm.

(4) Load effect on displacements of a moonie actuator.

Normally the displacement decreases when a load is applied to the actuator. A moonie actuator also decreases under load, but shows rather peculiar behavior. Figure 7 compares the displacement profiles of the exterior surface of the moonie when four

different loads are applied over an area of 3 mm^2 under an applied E-field of 1 kV/mm . By increasing the load, the center displacement is suppressed gradually, and the center is no longer the maximum displacement point. The calculated load carrying capability of the moonie is 300 gf. for the effective working area of 3 mm^2 which corresponds to stress level of 10 kg/cm^2 .

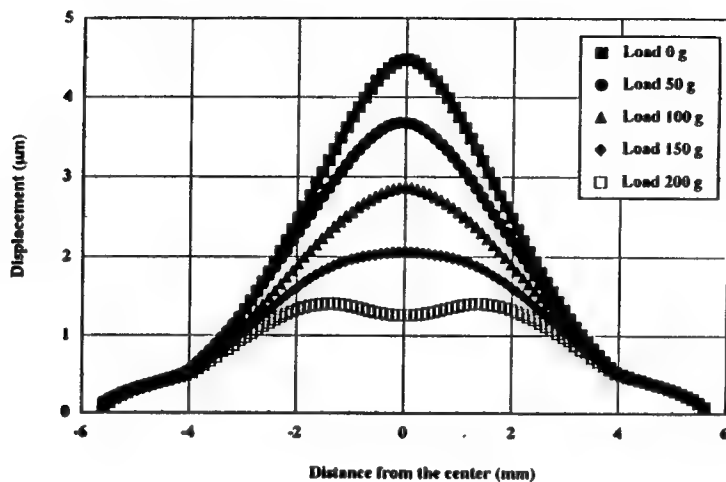


FIGURE 7 Calculated displacement profile on the exterior surface of the moonie actuator under the application of four different load

SUMMARY

1. Based on the frequency response analysis on the moonie actuator :
 - (1) calculated resonant frequencies agreed well with the experimental results.
 - (2) a coupling coefficient of the first mode was calculated as 0.2.
2. Based on the displacement analysis of the moonie actuator :
 - (1) Among changeable geometrical parameters of the moonie actuator,
 - (a) larger cavity diameter and higher cavity height lead to higher displacement.
 - (b) thinner cap lead to higher displacement.
 - (c) thickness of the epoxy bonding layer had little effect on the displacement.
 - (d) Introduction of a groove on the caps above the bond edge enhanced the displacement.
 - (2) The higher the stiffness of the cap material, the lower the displacement of the moonie.
 - (3) The calculated maximum load (300 gf.) at the effective working area of 3 mm^2 agreed with that obtained by extrapolation of the experimental curve.

APPENDIX 30

COMPOSITE FLEXTENSIONAL TRANSDUCERS FOR SENSING AND ACTUATING

JAMES F. TRESSLER, Q.C.XU, SHOKO YOSHIKAWA, KENJI UCHINO, and ROBERT E. NEWNHAM

The Pennsylvania State University, Intercollege Materials Research Laboratory, University Park, PA 16802 USA

(Received August 9, 1993)

Abstract A ceramic-metal composite flexextensional transducer has been developed which integrates both sensing and actuating functions into a single device for the purpose of suppressing low-level vibration noise. This prototype sensor/actuator composite is capable of detecting and completely suppressing in real time, small ($<1\mu\text{m}$) vibration displacements with low ($<100\text{gf}$) forces. The dynamic frequency range of the device spans from 100Hz to at least 2500Hz. The actuator portion of the composite consists of a standard (11mm diameter, 3mm thick) "moonie" transducer. The sensor is a separate piece of piezoceramic, 0.1mm thick, imbedded within the surface of the actuator. Vibrations are detected by the sensor; then, via a feedback loop, the vibration noise is suppressed by the actuator. Potential applications for this device include active optical systems, rotor suspension systems, and other low-level vibration suppression devices.

INTRODUCTION

The elimination of vibration noise has achieved considerable attention in recent years, both on the macroscopic (smart shock absorbers) and microscopic (active optic systems) scale. The fundamental parameters that must be considered for a vibration control device are its response time, as well as the force and vibration displacement amplitude that it must be able to cancel. Once these criteria have been met for a particular application, it then becomes advantageous to reduce costs by miniaturizing and/or reducing the power delivered to the device.

Multilayer piezoelectric actuators have seen extensive use as vibration control

devices because of their large generative forces, high precision, and quick response time. Unfortunately, large driving voltages are necessary to achieve displacements of several microns. By sandwiching a multilayer actuator between two moonie endcaps, the displacement is amplified,^{1,2} thereby making it possible to reduce the driving voltage³ or reduce the size of the device. The response time is only slightly slower.

Using this information, it became our objective to fabricate a vibration control device based on the moonie actuator. In order to produce the most efficient device, the sensing and actuating functions were integrated into a single composite. The design is shown in Figure 1. The actuator portion of the prototype device consists of the standard moonie, 11mm in diameter and 3mm thick. The sensor is a separate piece of piezoceramic (PZT), 0.1mm thick, which was imbedded within the upper endcap. The sensor detects sinusoidal vibrations, as shown in the Figure 1, then via a feedback loop, sends a signal of appropriate amplitude and phase back to the actuator so that the latter effectively cancels the external vibration.

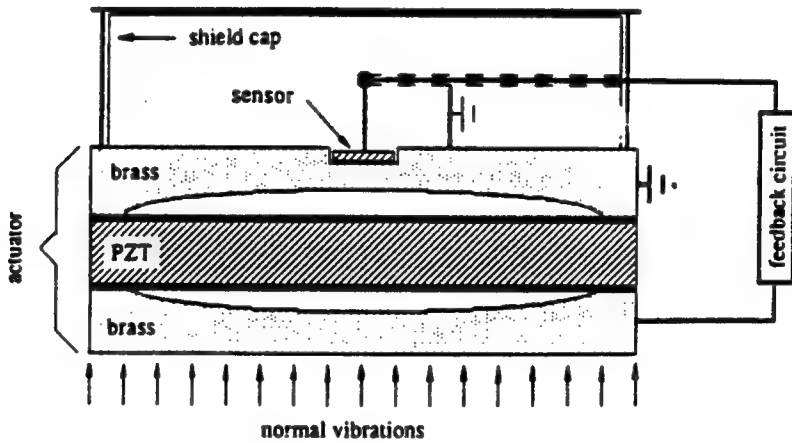


FIGURE 1 Integrated sensor and actuator

VIBRATION CONTROL RESULTS

The ability of the moonie actuator to actively control external vibrations was determined by adhering the device atop a vibrating multilayer actuator of known frequency and displacement amplitude. The dynamic frequency range of the sensor was found by applying a sinusoidal AC field to the moonie actuator and observing the resulting vibration

signal on an oscilloscope. The response remained relatively flat between 100 and 6000Hz.

The data in Figure 2 show that the integrated sensor/actuator device can indeed be used to cancel external vibrations. The horizontal axis shows the 1kHz electric field applied to the moonie actuator when the field applied (at 1kHz) to the multilayer vibration source was either 75V/mm, 125V/mm, or 250V/mm. The vertical axis shows the corresponding net vibration signal amplitude, which comes from the sum of the multilayer and moonie vibrations. The results show that whenever the applied field and phase shift into the moonie are adjusted to the appropriate magnitude, the net vibration signal goes to zero, indicating that the integrated sensor/actuator device has effectively cancelled the external vibration. The reason the phase shift is 1° rather than the expected 180° was due to the polarization direction of the sensor being opposite that of the actuator.

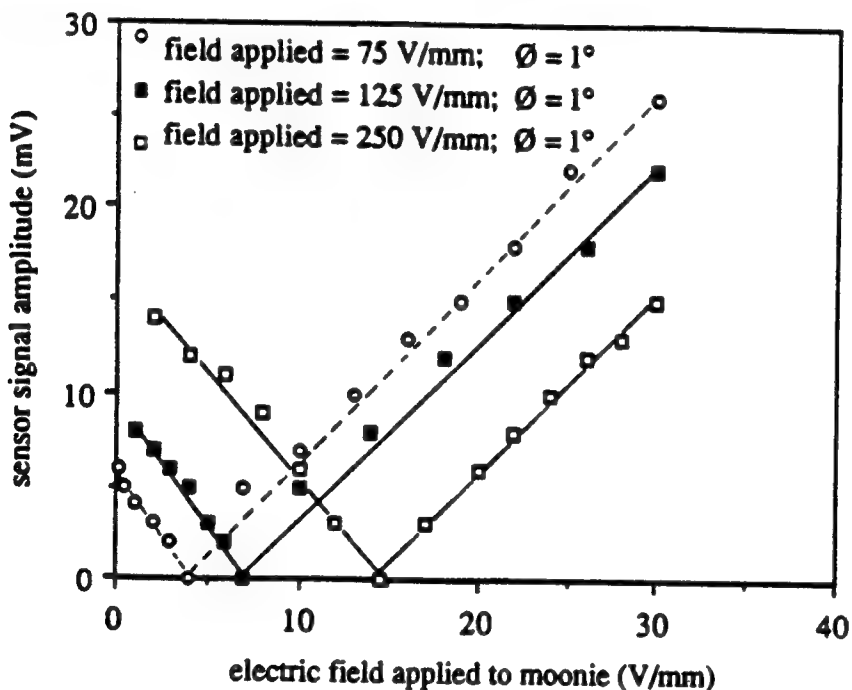


FIGURE 2 Net sensor signal response as a function of electric field applied to the multilayer vibration source at a frequency of 1kHz

Figure 3 shows how the net vibration signal amplitude changes with phase shift when the applied field to the multilayer is 125V/mm and the field applied to the moonie is 7.05V/mm. These data show that when the phase shift between the two fields is slightly greater than 0° , the moonie and multilayer vibrations have the same displacement amplitude

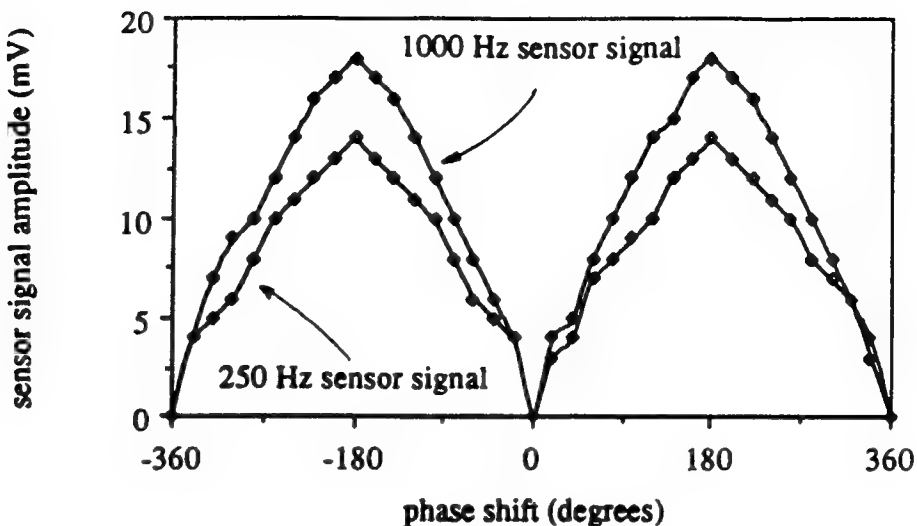


FIGURE 3 Sensor signal response as a function of phase shift of the electric field applied to the moonie

and are exactly 180° out-of-phase, resulting in no net vibration signal.

Figure 4 shows the applied electric field and phase shift (feedback signal) needed to be supplied to the moonie actuator in order to cancel the external vibration over the shown frequency range when the field applied to the multilayer was 75V/mm. Figure 5 superimposes the subsequent sensor signal amplitude detected from the multilayer vibration source both with and without the feedback signal activated. These data show that when the feedback field given in Figure 4 is activated, the multilayer vibration signal can be completely suppressed over this entire frequency range. The reason 2500Hz was chosen as the cut-off frequency was the inability to prevent "ultrasonic floating" (which arose from incomplete coupling) by the moonie atop the multilayer at higher frequencies.

The minimum and maximum electric fields into the moonie actuator for which the sensor signal remained sinusoidal were 200mV/mm and 370V/mm, respectively, and were independent of frequency. These fields thus define the dynamic displacement range that the sensor is capable of detecting as being between 0.35nm and 0.65 μ m (as calculated by finite element analysis).²

The external force that the integrated sensor/actuator could detect was estimated from the output voltage of the sensor (Equation 1). Since the sensor was bonded to the actuator, it was assumed that g_{31} and g_{32} provided the major contribution to the output voltage. Also, since the sensor was square in shape, it was further assumed that $g_{31}=g_{32}$.

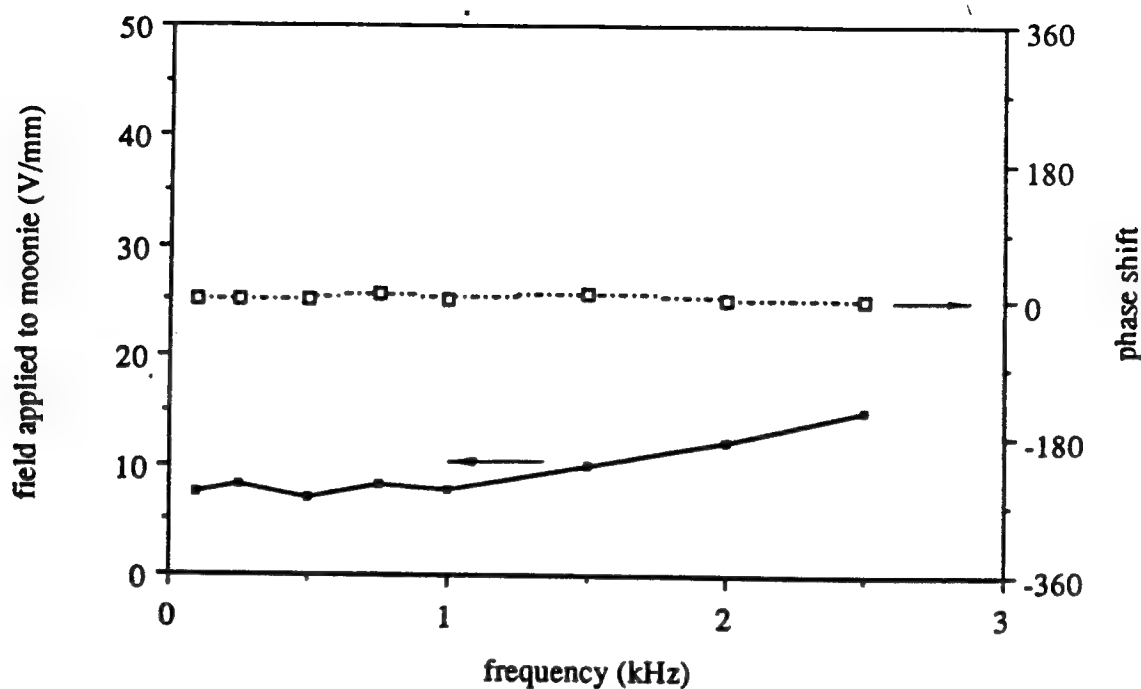


FIGURE 4 Field and phase shift applied to the moonie actuator needed to cancel the external vibration when the field applied to the multilayer vibration source is 75V/mm

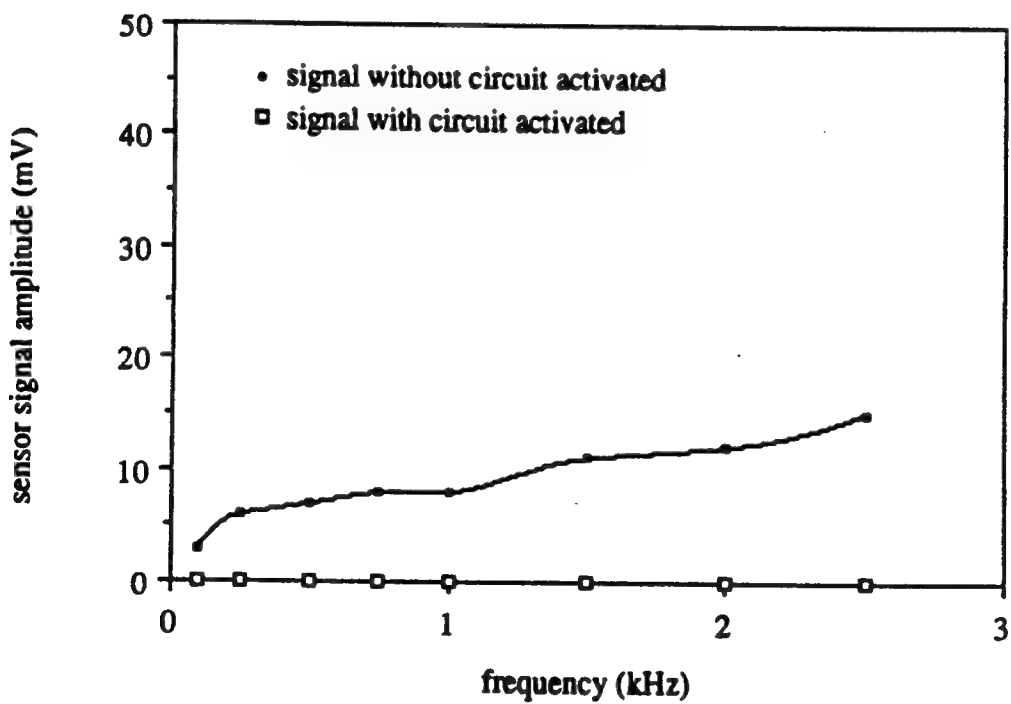


FIGURE 5 Sensor signal response both with and without the feedback circuit activated

$$F = \frac{A V_{out}}{2t |g_{31}|} \quad (1)$$

where F = force detected by the sensor
 t = thickness of the sensor
 A = area of the sensor

V_{out} = output voltage from the sensor
 g_{31} = piezoelectric charge coefficient

It was further assumed that the maximum and minimum force detected arose from the maximum and minimum electric fields reported previously. Table I provides a list of the values used for these calculations.

TABLE I Values used to calculate force detected by the sensor at a frequency of 1kHz

sensor area = $6.25 \times 10^{-6} \text{ m}^2$

sensor thickness = $1 \times 10^{-4} \text{ m}$

$g_{31} = -12.4 \times 10^{-3} \text{ Vm/N}$

$(V_{out})_{max} = 340 \text{ mV}$

$(V_{out})_{min} = 0.2 \text{ mV}$

Therefore $F_{max} = 0.85 \text{ N} \approx 85 \text{ gf}$ and $F_{min} = 0.5 \text{ mN} \approx 0.05 \text{ gf}$. The reason for these rather small values is due to the sensor being located over the center of the cavity, which is the region of minimum generative force for the device.²

Lastly, the response time of the device, $20 \mu\text{sec}$, was estimated from the resonance frequency of the actuator, 50kHz.

REFERENCES

1. Y. Sugawara, K. Onitsuka, S. Yoshikawa, Q.C. Xu, R.E. Newnham, and K. Uchino, J. Am. Ceram. Soc., 75, 996-998 (1992).
2. K. Onitsuka, Ph.D. thesis, Effects of Bonding and Geometry on the Flexionional Transducer, "Moonie", The Pennsylvania State University (1993).
3. K. Imanaka, Proceedings of the SPIE, 1751, (1992).

APPENDIX 31

Lead Zirconate Titanate Hollow-Sphere Transducers

Richard Meyer, Jr.,* Holger Weitzing, Qichang Xu, Qiming Zhang,* and Robert E. Newnham*

Materials Research Laboratory, The Pennsylvania State University, University Park, Pennsylvania 16802

Joe K. Cochran*

School of Materials Engineering, Georgia Institute of Technology, Atlanta, Georgia 30332

Millimeter-sized, hollow spheres of lead zirconate titanate were fabricated by blowing gas through a fine-grained slurry of PZT-5. After they were sintered, the spheres were poled in two ways: radially between inside and outside electrodes, and tangentially between two outside electrodes. The capacitance and vibration modes were modeled and measured for these two poling configurations. The two principal modes of vibration were a breathing mode near 700 kHz and a wall thickness mode near 10 MHz. These spheres have potential uses in medical ultrasound, nondestructive testing, and low-density transducer arrays.

I. Introduction

LEAD ZIRCONATE TITANATE (PZT) has been a standard piezoelectric material for the past 40 years.¹ PZT and its doped derivatives are widely used because of their large electromechanical coupling coefficients, temperature stability, and high resistance to depolarization from mechanical stress and high driving voltages. During the past few years, a number of development programs have been initiated on polymer-ceramic and metal-ceramic composites, fibers, multilayer actuators, and flexextensional transducers based on the solid solutions of PZT.

Current research on piezoelectric sensors and actuators is moving toward miniaturization to achieve better resolution and high power densities. High resolution and small sizes are needed in applications such as biomedical ultrasound, probes for invasive procedures, flow noise studies, and nondestructive evaluation of composites.

Higher frequencies and better acoustical impedance matches are advantageous in underwater transducers and biomedical ultrasonics. Tiny hollow spheres meet both of these criteria. In this paper, we describe a way of making and poling piezoelectric hollow spheres, with preliminary results on their dielectric and piezoelectric properties.

II. Preparation of PZT Hollow Spheres

Thin-wall piezoelectric hollow spheres are produced using a process developed in the Materials Science and Engineering Department at the Georgia Institute of Technology² based on the Torobin patent.³ Slurries containing PZT-501-A (Ultrasonic Powders, Inc.) powder are injected through a coaxial nozzle with air passing through the center. The slurry exits the nozzle in a hollow cylindrical form that closes from surface tension and hydrostatic forces. The inner air pressure inflates the bubble

until the inner sphere pressure equals the hollow cylinder pressure. At this critical pressure, the bubble closes and breaks free. A fluid dynamic model for this process has recently been developed.⁴

The process is highly adaptable in composition because of slurry processing and produces large quantities of monosized hollow spheres with relatively uniform wall thickness. The uniformity in the process results in diameter variations of less than $\pm 5\%$, spherodity of $\pm 4\%$, and bulk density variations of $\pm 6\%$. Diameters can be uniformly varied from 1 to 6 mm, and wall thickness typically varies from 30 to 100 μm .⁵ Bonded spheres of alumina and mullite have found applications in refractories, burners, vacuum insulation, and low-density castables.⁶ Metal spheres and foams have also been fabricated and characterized,⁷ but hollow piezoelectric spheres are described here for the first time.

PZT-5 spheres, produced from a slurry, had a diameter of 3.1 mm in the green state. The firing process consisted of binder burnout at 600°C, followed by sintering at 1285°C for 4 h. A 16% radial shrinkage was observed during firing. The effective density of the fired sphere was 1.33 g/cm³, including the hollow center. The wall had a dense microstructure, shown in Fig. 1(A), with an average grain size of 2.5 μm . The wall thickness of the fired ceramic, measured using environmental scanning electron microscopy (SEM), as shown in Fig. 1(B), ranged from 45 to 100 μm .

Two poling configurations were investigated: radial poling and external top-to-bottom poling. Electroding the inside of the sphere was necessary to pole in the radial direction. A 350- μm circular hole was drilled in the wall such that silver electrodes could be injected into the sphere. The outside surface was also coated, using air-dry silver paint, leaving a small, uncoated region around the hole, as shown in Fig. 2(A). The spheres were poled radially using an electric field of 25 kV/cm. Volatile insulating oil was used to fill the sphere through the 350- μm hole. Therefore, radial poling was conducted at room temperature to reduce oil loss. The two principal vibration modes associated with this configuration were a volumetric expansion or breathing mode and a wall thickness mode at a much higher frequency.

Top-to-bottom poling was accomplished using silver caps on opposite sides of the sphere, as shown in Fig. 2(B). The caps were separated by an unelectroded region. This gap was varied in size from 0.5 to 2.0 mm. Approximately 25 kV/cm at an elevated temperature of 110°C was used for poling in this configuration, depending on the size of the electrode caps. The principal mode under investigation here was the distortion of the sphere to an ellipsoidal shape.

III. Results and Discussion

The capacitance and resonance frequencies were modeled and measured for radial poled spheres. A typical capacitance of 900 pF was measured on an impedance analyzer (Model HP 4192a, Hewlett-Packard Co., Palo Alto, CA) at 10 kHz and 0.10 V. The following spherical capacitor model was used:

J. W. Stevenson—contributing editor

Manuscript No. 194149. Received October 4, 1993; approved March 23, 1994.
Supported by the Army Research Office, Electronics Technology and Devices Laboratory, under Contract No. DAAL03-91-C-0034, and the Office of Naval Research, under URI Contract No. N00014-92-J-1510.

*Member, American Ceramic Society.

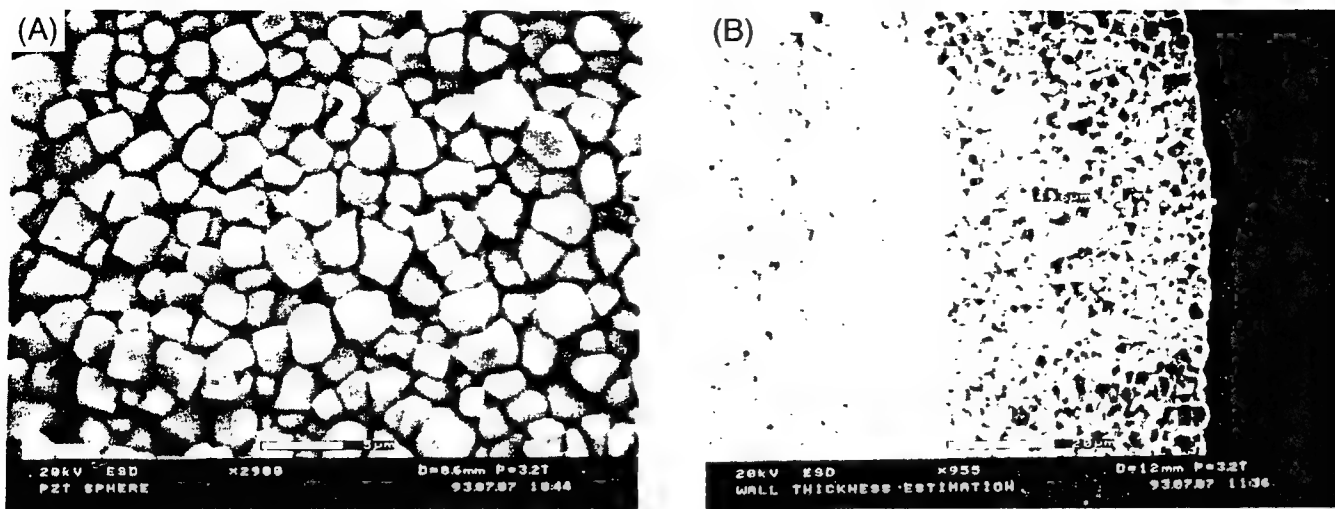


Fig. 1. SEM micrographs depicting (A) the dense microstructure of the sphere walls (bar = 5 μm) and (B) wall thickness approximation (bar = 20 μm , wall thickness = 49.6 μm). Grain sizes averaged 2.5 μm in diameter.

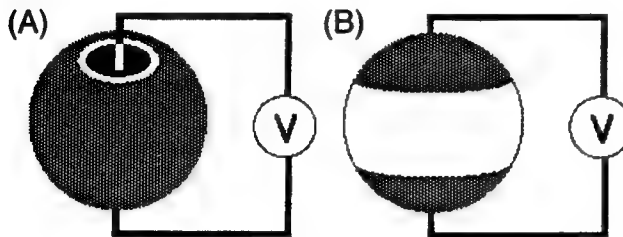


Fig. 2. Electrode design for (A) the radial poling configuration showing the small uncoated ring used to separate the inner and outer coating, and (B) the electrode configuration for top-to-bottom poling. Shaded areas represent the air-dry silver coating.

$$C = 4\pi\epsilon_r\epsilon_0 \left(\frac{r_1 r_2}{r_2 - r_1} \right) \quad (1)$$

where r_1 and r_2 are the inside radius and outside radius, respectively. The capacitance was calculated to be ~ 3000 pF.* The difference in the measured and calculated values was attributed to the hole, the size of the unelectroded ring, and the difficulty in electroding the interior surface of the sphere.

The fundamental mode for vibration in the sphere is the breathing mode, with a volumetric expansion and contraction. The resonance frequency of this mode is given by the relation⁸

$$f_r = \frac{1}{2\pi a} \left(\frac{2}{\rho(s_{11} + s_{12})} \right)^{1/2} \quad (2)$$

where a is the average radius, ρ the density, and s_{ij} the tensor components of compliance. This equation predicts the breathing mode resonance frequency to be ~ 600 kHz.*

In addition to the breathing mode, a wall thickness mode was also observed. This mode was described by the relation

$$f_r = \frac{1}{2t} \left(\frac{2}{\rho(s_{11} + s_{12})} \right)^{1/2} \quad (3)$$

where t is the thickness of the sphere wall.⁴ When an average thickness of 90 μm was used, the thickness mode was calculated to be 14.5 MHz.*

The resonance frequencies were observed, using a network analyzer (Model HP 3577A, Hewlett-Packard). The fundamental mode or breathing mode resonance and antiresonance frequencies for radial poling, shown in Fig. 3(A), were located at 675 kHz and 706 kHz, respectively. Using the relation⁸

$$k_p^2 = 1 - \frac{f_r^2}{f_a^2} \quad (4)$$

the planar coupling factor (k_p) was calculated to be 0.30. Because of electroding problems, this value was smaller than the bulk value of 0.60.⁸

The thickness mode resonance, depicted in Fig. 3(B), appears at ~ 12 MHz. This resonance peak is broadened due to nonuniformity in the thickness of the wall. Discrepancies between the calculated and measured values result from the electrode problems, the presence of a hole in the sphere, and deviations from a perfect shape. The breathing and thickness mode resonant frequencies are reproducible to within $\pm 5.0\%$ and can be shifted to higher or lower frequencies by changing the wall thickness or the diameter of the sphere.

The capacitance of the top-to-bottom poling configuration is modeled using a cylindrical tube approximation:

$$C = \epsilon_r\epsilon_0 \frac{\pi t(r_2 + r_1)}{d} \quad (5)$$

where t is the wall thickness and d the distance between the top and bottom electrodes. The calculated values, 9 to 11 pF, are in fair agreement with the measured values of 5 to 8 pF.* These values are highly dependent upon electrode size and uniformity.

After the samples were poled, the effective d coefficient was measured on a Berlincourt d_{33} meter. Typical values range from 500 to 600 pC/N. These values are larger than either d_{33} or d_{31} for PZT-5. The geometry of the sphere accounts for this difference by providing a mix of d_{31} and d_{33} . The admittance spectrum for these samples measured from 100 kHz to 2.2 MHz (Fig. 4(A)) shows an active material with resonances of approximately 200 kHz, 290 kHz, 650 kHz, 700 kHz, 1 MHz, and 2 MHz. The nature of the modes at 200 and 290 kHz is believed to be the ellipsoidal distortion, with the 1-MHz peak being the third harmonic. This ellipsoidal mode, centered at ~ 245 kHz, has a split peak, resulting from a nonuniform diameter. An oval-shaped sample, with differences associated with the major axis and minor axis dimensions, results in the splitting of the resonance peaks to two resonances. The first of the two peaks represents the larger diameter. A more uniform sphere shows a single resonance at 247 kHz, demonstrating the disappearance of the splitting phenomena. The resonances at 650 and 700 kHz

*Values used in these calculations are available in Ref. 8 and are as follows: $\epsilon_r = 1700$, $\rho = 7.7 \text{ g/cm}^3$, $s_{11} = 16.4 \times 10^{-12} \text{ m}^2/\text{N}$, $s_{12} = -5.72 \times 10^{-12} \text{ m}^2/\text{N}$. The dimensions of the sphere are as follows: $r_2 = 1.30 \text{ mm}$, $r_1 = 1.21 \text{ mm}$, and $t = 90 \mu\text{m}$.

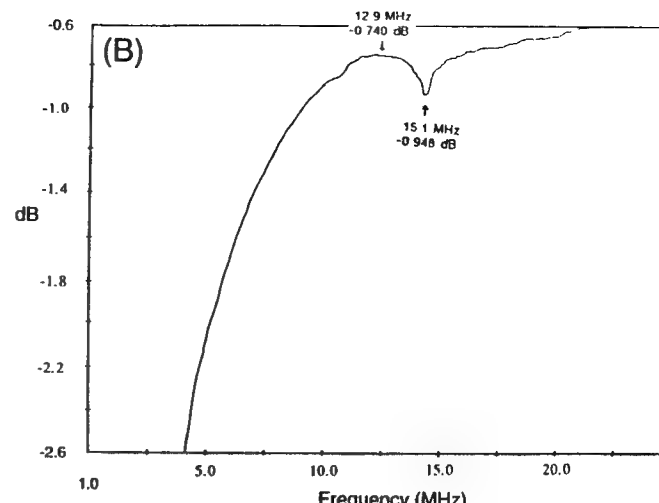
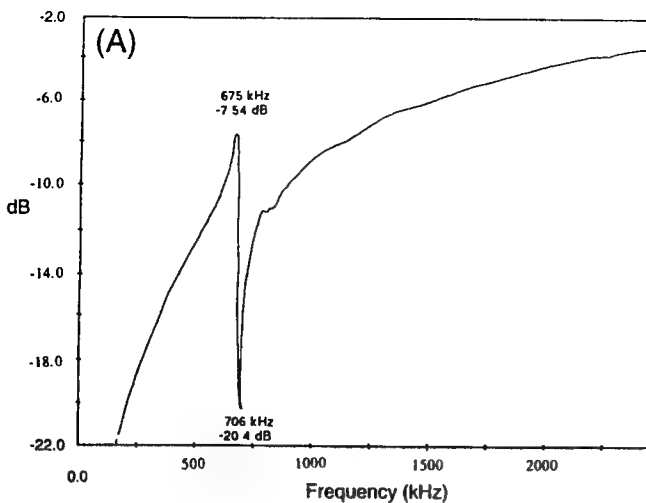


Fig. 3. Admittance spectra showing (A) the fundamental or breathing mode resonance for a radially poled sphere and (B) the thickness mode resonance observed for a radially poled sphere having an average wall thickness of 75 μm and a diameter of 2.6 mm.

are believed to be the same breathing mode or volumetric expansion observed in the radial poling configuration. A wall thickness mode also appears at a frequency of 9 MHz, as shown in Fig. 4(B). The resonant characteristics for the top-to-bottom poling are highly dependent on the uniformity of sample shape and the size of the electrodes. Each sample tested shows the same resonance characteristics with only slight differences in amplitude (less than 10%) and position (less than 6%).

IV. Potential Applications

The hollow spheres of PZT have good dielectric and piezoelectric properties, which suggests a number of possible applications. If an array or stack of spheres is close-packed and embedded in epoxy, as shown in Fig. 5, a low-density transducer can be developed. The effective density of this type of composite is approximately that of water and the human body. This provides for good acoustical coupling between the composite and water in hydrophone applications and with human tissue in biomedical ultrasonic systems. This type of composite, similar to the series type-F42 omnidirectional underwater transducer developed at the Naval Research Laboratory,⁹ is small in size, which allows it to be used as a flow noise sensor and to measure acoustic pressure¹⁰ in narrow openings and adj-

acent to complex surface shapes. The low density of the spheres is advantageous in sonar arrays, where buoyancy is a problem.

Other applications involving the piezoelectric properties of the spheres involve the use of the high-frequency thickness modes. High-frequency devices have found numerous applications in medical ultrasound. The geometry of the spheres allows them to be used as sensors that are independent of receiving direction. This omnidirectional characteristic, the small size, and the low processing costs of the sphere fulfill the necessary requirements needed for small invasive devices used in medical ultrasonic guidance systems.¹¹ The omnidirectional characteristic of the sphere also allows it to be used as a transducer in non-destructive testing and in monitoring flow noise in engineering systems. The tiny spheres can easily be embedded in polymer-based composites and cement. Polymer coatings dramatically improve the mechanical strength of the hollow spheres.

V. Conclusions

The processing technique designed for making thin-walled, hollow spheres provides an inexpensive and adaptable way to manufacture large quantities of piezoelectric spheres. Two poling configurations have been demonstrated which generate reproducible resonance characteristics. These resonances can be

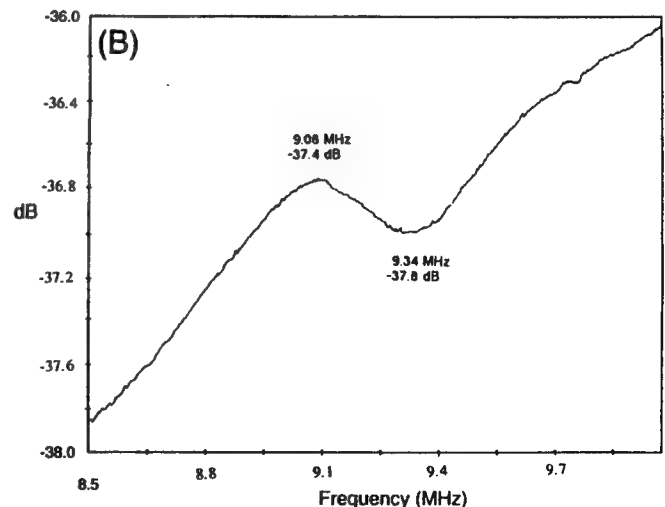
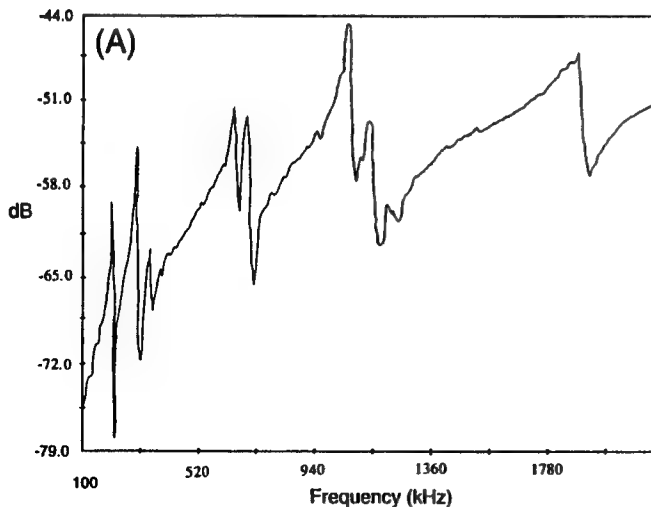


Fig. 4. Admittance spectra for (A) a typical sphere electroded on the top and bottom with a ~1.5-mm gap between the electrodes and (B) the thickness mode resonance observed for a sphere 2.6 mm in diameter electroded on the top and bottom with a 1.5-mm gap between the electrodes.

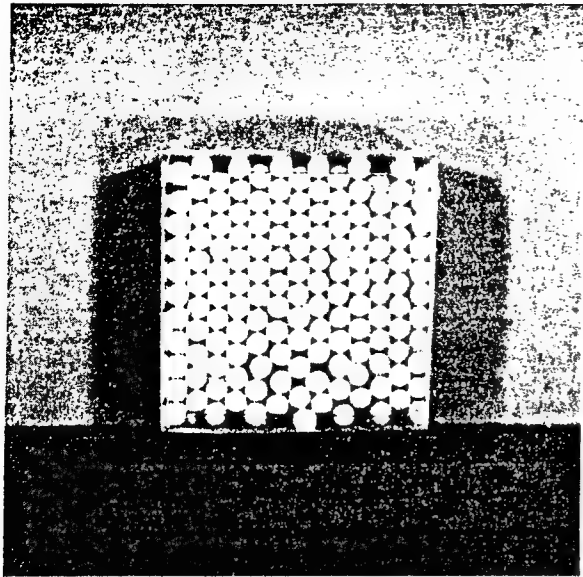


Fig. 5. Array of spheres embedded in a polymer to form a low-density transducer.

tailored by changing electrode areas or the wall thickness and diameter of the spheres. The good dielectric and piezoelectric properties of the PZT-5 hollow spheres suggest several interesting applications in medical ultrasonics and underwater transducers.

Acknowledgments: We thank Shoko Yoshikawa for her helpful discussions and supplies used for this research, and Joe Kearns for his efforts. Coaxial-

nozzle hollow-sphere technology is owned by Microcel Technology, Edison, NJ, for these applications, and their cooperation is appreciated.

References

- ¹B. Jaffe, W. R. Cook, Jr., and H. Jaffe, *Piezoelectric Ceramics*, pp. 135-83, R.A.N. Publishers, Marietta, OH, 1971.
- ²A. T. Chapman, J. K. Cochran, J. M. Britt, and T. J. Hwang, "Thin-Wall Hollow Spheres, from Slurries," DOE-ECUT Program, ORNL Subcontent 86X-22043C, Annual Reports, 1987, 1988, 1989, Department of Energy, Washington, DC.
- ³L. B. Torobin, "Methods of Making Hollow, Porous Microspheres," U.S. Pat. No. 4,671,909, 1987.
- ⁴P. R. Chu and J. K. Cochran, "Coaxial Nozzle Formation of Hollow Spheres from Liquids I: Model"; unpublished work.
- ⁵A. T. Chapman, J. K. Cochran, M. K. Adicks, G. E. Carlson, P. R. Chu, J. H. Chung, R. B. Clancy, T. R. Ford, S. D. Furlong, T. J. Hwang, C. M. Moore, and M. J. Shapiro, "Thin-Wall Hollow Spheres from Slurries," Materials Engineering Department, Georgia Institute of Technology, Poster Presentation for Advanced Industrial Concepts Materials Program, Department of Energy, Albuquerque, NM, 1991.
- ⁶J. K. Cochran, G. E. Carlson, P. R. Chu, J. H. Chung, R. P. Gonzales, T. J. Hwang, A. S. Jensen, and L. A. Touryan, "Thin-Wall Hollow Spheres from Slurries," Materials Engineering Department, Georgia Institute of Technology, Poster Presentation for Advanced Industrial Concepts Materials Program, Department of Energy, Pleasanton, CA, 1992.
- ⁷R. B. Clancy, T. H. Sanders, and J. K. Cochran, "Fabrication of Thin-Walled Hollow Nickel Spheres and Low-Density Syntactic Foams"; pp. 477-85 in *Light Weight Alloys for Aerospaces Applications II*, Edited by E. W. Lee and N. J. Kim. The Minerals, Metals, and Materials Society, Warrendale, PA, 1991.
- ⁸D. A. Berlincourt, D. R. Curran, and H. Jaffe, "Piezoelectric and Piezomagnetic Materials and Their Function in Transducers"; pp. 169-257 in *Physical Acoustics*, Vol. 1, Part A. Edited by W. P. Mason. Academic Press, New York, 1964.
- ⁹L. E. Ivey, "NRL-USRD Series F42 Omnidirectional Standard Transducers," Underwater Sound Reference Detachment, Naval Research Laboratory, Orlando, FL, 1979.
- ¹⁰E. V. Romanenko, "Miniature Piezoelectric Ultrasonic Receivers," *Sov. Phys. Acoust. (Engl. Transl.)*, 3, 364-70 (1957).
- ¹¹D. Vilkomerson, B. Gardineer, and H. Hojeibane, "Quasi-Omnidirectional Transducers for Ultrasonic Electro-Beacon Guidance of Invasive Devices," *Proc. SPIE*, 1733, 154-65 (1992). □

APPENDIX 32

Piezoelectric, dielectric, and elastic properties of poly(vinylidene fluoride/trifluoroethylene)

H. Wang, Q. M. Zhang, and L. E. Cross

Materials Research Laboratory, The Pennsylvania State University, University Park, Pennsylvania 16802

A. O. Sykes

Acoustical Research and Applications, Vienna, Virginia 22180

(Received 21 September 1992; accepted for publication 18 May 1993)

The symmetry-predicted nonzero components of the piezoelectric coefficient, dielectric constant, and elastic compliance matrices have been determined on poly(vinylidene fluoride/trifluoroethylene) (75/25) copolymer at room temperature and a frequency of 500 Hz. The temperature dependence of each of the complex piezoelectric coefficients and complex dielectric constants has been measured in the temperature range of -100 to 65 °C. The frequency dependence of these coefficients has also been measured at room temperature. It is found that the relaxation observed in the tensile piezoelectric coefficients of this material is different from that of the dielectric constants, whereas the relaxation of the piezoelectric shear constants shows behavior similar to that of the dielectric constants.

I. INTRODUCTION

Polyvinylidene fluoride (PVDF) and its copolymers with trifluoroethylene (TrFE) or tetrafluoroethylene (TFE) have become important piezoelectric materials for transducer applications. Compared with inorganic piezoelectric materials, these materials have high mechanical flexibility, low acoustic impedance, and can be easily molded into desirable forms. The piezoelectric coefficients of the materials are higher compared with other piezoelectric polymeric materials. In the past two decades, a large number of investigations have been conducted to improve the performance and to explore the physical bases of piezoelectricity and ferroelectricity of these materials.¹⁻⁴

Like other piezoelectric materials, the linear coupling of mechanical and electrical effects of PVDF and its copolymers is described by the constitutive equations. These equations contain the piezoelectric, dielectric, and elastic coefficients, which are all important material parameters for both device design and fundamental understanding of the materials. For a stretched and poled PVDF-type polymer, its symmetry properties belong to point group mm2. The piezoelectric coefficient, dielectric constant, and elastic compliance matrices have the forms of

$$\begin{pmatrix} 0 & 0 & 0 & 0 & d_{15} & 0 \\ 0 & 0 & 0 & d_{24} & 0 & 0 \\ d_{31} & d_{32} & d_{33} & 0 & 0 & 0 \end{pmatrix},$$

$$\begin{pmatrix} K_{11} & 0 & 0 \\ 0 & K_{22} & 0 \\ 0 & 0 & K_{33} \end{pmatrix},$$

and

$$\begin{pmatrix} s_{11} & s_{12} & s_{13} & 0 & 0 & 0 \\ s_{12} & s_{22} & s_{23} & 0 & 0 & 0 \\ s_{13} & s_{23} & s_{33} & 0 & 0 & 0 \\ 0 & 0 & 0 & s_{44} & 0 & 0 \\ 0 & 0 & 0 & 0 & s_{55} & 0 \\ 0 & 0 & 0 & 0 & 0 & s_{66} \end{pmatrix},$$

where the coordinate axis 1 refers to the polymer chain direction (stretch direction), 3 the poling direction, and 2 the axis orthogonal to 1 and 3 axes. Experimental evidence has shown that these coefficients vary with polymer processing methods even for samples with the same composition and the same measuring conditions. For the purpose of application and fundamental understanding of these materials, it is desirable to establish a complete data base to characterize all these properties on samples with similar processing conditions. However, as can be seen in Table I, which presents the typical experimental results for piezoelectric, dielectric, and compliance coefficients of PVDF materials available in the literature, in spite of extensive investigations in the past, the characterization of the materials, especially copolymers, is far from being complete. For example, although the piezoelectric tensile coefficients, especially d_{31} , have been studied extensively using quasistatic methods, there is little information about the imaginary part of these coefficients. Furthermore, few measurements of the shear coefficients have been made. The experiment results from various groups differ significantly and they cannot be used to consistently describe the physical properties of the materials.

In this paper, the experimental results from recent studies on a P(VDF-TrFE) (75/25) copolymer are presented. The matrix elements of the piezoelectric, dielectric, and elastic compliance coefficients have been measured at room temperature (22 °C) and a frequency of 500 Hz. Both real and imaginary parts of the piezoelectric and di-

TABLE I. The piezoelectric, dielectric, and elastic coefficients of PVDF-type materials (unit: d is in pC/V , ϵ is in D/cm^2 , K is in N/m^2).

Properties	P(VDF-TrFE) (75/25)	Drawn PVDF	P(VDF-TrFE)	P(VDF-TFE)
d_{31}'	10.7	12.5, ^b 21, ^{c,h,k} 28, ^{c,f} 16.8, ^a 9.8 ^a	11.6 ^d	
d_{31}''	0.18	0.4 ^b		
d_{32}'	10.1	2.3, ^{h,k} 1.5, ^c 2, ^c 4.8, ^f 2.2 ^a		
d_{32}''	0.19			
d_{33}'	-33.5	-26, ^h -32.5, ^c -17.4, ^f -28, ⁱ -14.8, ^h	-30 to -44 ^h	
d_{33}''	-0.65			
d_{15}'	-36.3	-27 ^c		
d_{15}''	-0.32			
d_{24}'	-40.6	-23 ^c		
d_{24}''	-0.35			
K_{11}'	7.40	6.9 ^l		
K_{11}''	0.07			
K_{22}'	7.95	8.6 ^l		
K_{22}''	0.09			
K_{33}'	7.90	13, ^m 7.6, ^b 6.2, ^d 16, ^h 15.1, ^b	19, ^g 10.4 to 15.4 ^h	10 ^l
K_{33}''	0.09	0.24 ^b		1.5 ^l
s_{11}'	3.32	3.65, ^p 3.3, ^a 5.9, ^a 2.5 ^f		
s_{11}''	0.10			
s_{22}'	3.24	4.24, ^p 2.3 ^f		
s_{22}''	0.07			
s_{33}'	3.00	4.72 ^p		
s_{33}''	0.07			
s_{12}'	-1.44	-1.10 ^p		
s_{13}'	-0.89	-2.09 ^p		
s_{23}'	-0.86	-1.92 ^p		
s_{44}'	94.0			
s_{44}''	2.50			
s_{55}'	96.3			
s_{55}''	2.33			
s_{66}'	14.4			

^aReference 1.^bReference 10.^cR. Hahn, J. Appl. Phys. 57, 1294 (1985).^dK. Koga and H. Ohigashi, J. Appl. Phys. 59, 2142 (1986).^eE. L. Nix and I. M. Ward, Ferroelectrics 67, 137 (1986).^fH. Ohigashi, J. Appl. Phys. 47, 949 (1976).^gT. Furukawa *et al.*, Ferroelectrics 32, 61 (1981).^hR. G. Kepler, Ann. Rev. Phys. Chem. 29, 497 (1978).ⁱQ. C. Xu *et al.*, IEEE 1987 Ultrasonics Symp. 663 (1987).^jS. Tasaka and S. Miyata, J. Appl. Phys. 57, 906 (1985).^kR. Al-Jishi and P. L. Taylor, J. Appl. Phys. 57, 902 (1985).^lV. V. Varadan *et al.*, IEEE 1989 Ultrasonics Symp. 727 (1989).^mH. Sussner, IEEE 1979 Ultrasonics Symp. 49 (1979).ⁿT. Furukawa and N. Seo, Jpn. J. Appl. Phys. 29, 675 (1990).^oM. Tamura, K. Ogasawara, N. Ono, and S. Hagiwara, J. Appl. Phys. 45, 3768 (1974).^pH. Schewe, IEEE 1982 Ultrasonics Symp. Proc. 1, 519 (1982).

electric constants were measured over wide frequency and temperature ranges.

II. EXPERIMENTAL WORK

A. Sample preparing

Unoriented poled P(VDF-TrFE) (75/25) copolymer plates purchased from Atochem North America Inc. (Part No. A002335-00) were in two thicknesses of 0.5 and 10 mm. From these plates, test samples were cut into suitable shapes and sizes for measuring the dielectric, piezoelectric,

elastic compliance constants. Samples for the measurements of the tensile piezoelectric coefficients d_{3i} ($i=1, 2$, and 3) and dielectric constant K_{33} were cut from 0.5 mm

thick plate while samples for the measurements of the shear piezoelectric coefficients d_{15} and d_{24} and dielectric constants K_{11} and K_{22} were cut from a 10 mm thick plate. For tensile elastic compliance measurements, samples were made into square rods from the 10 mm thick plate with their length along the direction in which the measurement was made. For shear compliance measurements, samples were made of twenty layers of 0.5 mm plate by gluing them together.

B. Measurement details

Complex piezoelectric coefficient, dielectric constant, and elastic compliance are defined as follows:⁵

$$\begin{aligned} d_{ij} &= d'_{ij} - j d''_{ij}, \\ K_{ii} &= K'_{ii} - j K''_{ii}, \end{aligned} \quad (1)$$

$$s_{jk} = s'_{jk} - j s''_{jk},$$

where $i = 1, 2, 3$, and $j, k = 1, 2, \dots, 6$.

The piezoelectric coefficients were measured by utilizing a laser ultradilatometer.⁶ Making use of the converse piezoelectric effect, strain x_i induced by an alternating electric field E_i was measured and the piezoelectric coefficients were determined by

$$d_{ij} = \left. \frac{\partial x_i}{\partial E_j} \right|_{T=0}. \quad (2)$$

Depending on the coefficient to be measured, either the single beam or double beam laser dilatometer was used.⁷ As demonstrated previously,⁸ the system is capable of detecting both the amplitude and phase angle of the field induced strain, thus yielding the real and imaginary part of the piezoelectric strain coefficients.

It should be pointed out that in general, for piezoelectric constant measurement, the quantity determined from the direct piezoelectric effect is $\partial Q_i / A_i \partial T_j$, where A_i is the area of the electrodes in the unstrained sample with its normal along the i direction, Q_i the charges on the electrodes, and T_j the stress applied on the sample. It can be shown that

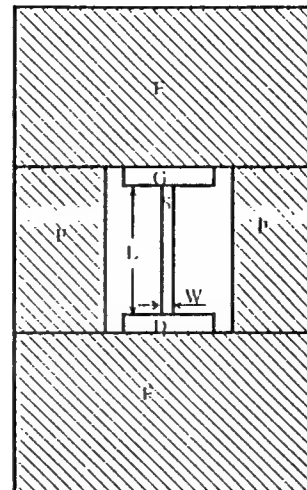
$$\left. \frac{\partial Q_i}{\partial T_j} \right|_E = \left. \frac{\partial D_i}{\partial T_j} \right|_E + \left. \frac{D_i \partial A_i}{A_i \partial T_j} \right|_E, \quad (3)$$

where D_i is the electric displacement. The first term on the right hand side of the equation is the d_{ij} defined in the IEEE standard.⁹ For conventional piezoelectric ceramics, the second term on the right hand side is much smaller than the first term and therefore the quantity measured from the direct piezoelectric effect is practically equal to d_{ij} . However, for polymeric piezoelectric materials, the second term is not negligible. It can also be shown that the piezoelectric strain coefficients d_{ij} determined from the converse effect [Eq. (2)] is equal to the right hand side of Eq. (3).³ Hence, the direct effect and converse effect yield the same piezoelectric constants, and in practice, they are the physical parameters of interest.

A capacitance bridge (General Radio) was used to measure the dielectric constants. For K_{33} , an impedance analyzer (HP) was used to carry out the measurement at higher frequencies.

In the piezoelectric and dielectric constant measurements, temperature was regulated by a microminiature refrigerator system (MMR Technologies Inc.). The temperature variation throughout the measurement was less than 0.1 K.

The principal diagonal components of the elastic compliance matrix were measured by a dynamic compliance-measuring apparatus (DCA), developed at Acoustical Research and Applications. The off-diagonal components were measured by using the DCA in conjunction with the double beam laser interferometer. The DCA, shown in Fig.



F: Frame
G: Force Gage
D: Displacement Generator
S: Test Sample
L: Length of the Sample
W: Width of the Sample

FIG. 1. Schematic drawing of the dynamic compliance apparatus.

1, consisted of a massive stiff frame, a calibrated piezoelectric displacement generator, and a force gage. Both the generator and the force gage were attached rigidly to the frame; between the generator and force gage, a sample of the material to be tested can be inserted.

III. RESULTS AND DISCUSSION

The results of the complex piezoelectric, dielectric, and elastic constants on P(VDF-TrFE) (75/25) samples acquired at room temperature and a frequency of 500 Hz are presented in the column 1 of Table I for comparison with those from the literature. To our knowledge, this set of piezoelectric, dielectric, and compliance coefficient data is the most complete currently available for any PVDF copolymeric materials.

To avoid the possible clamping effect of the two ends of the sample rods inserted in the DCA on the measured elastic compliance, samples with length to width ratio (aspect ratio) of 10 were used. All the measurements were repeated several times and the data can be reproduced within 5%. To further confirm that the end clamping effect is negligible here, we also performed the measurement with samples of aspect ratio of 5 and the results were basically the same as those acquired from the samples with aspect ratio of 10. For a piezoelectric material, its elastic compliance can also be measured by the piezoelectric resonance technique.¹⁰ For the copolymer samples, s_{31}^E was also measured by utilizing the resonance technique and the result was consistent with that from the DCA. The uncertainty of the shear compliance data is greater than that of tensile compliances.

Shown in Figs. 2 and 3, respectively, are the temperature dependencies of the piezoelectric and dielectric constants at a frequency of 500 Hz. The measured Curie temperature of this material is 115 °C. These results reveal several interesting features. In contrast to drawn PVDF, which is very anisotropic piezoelectrically in the plane perpendicular to the poling direction, and for which d_{31} and d_{32} exhibit very different magnitudes and temperature de-

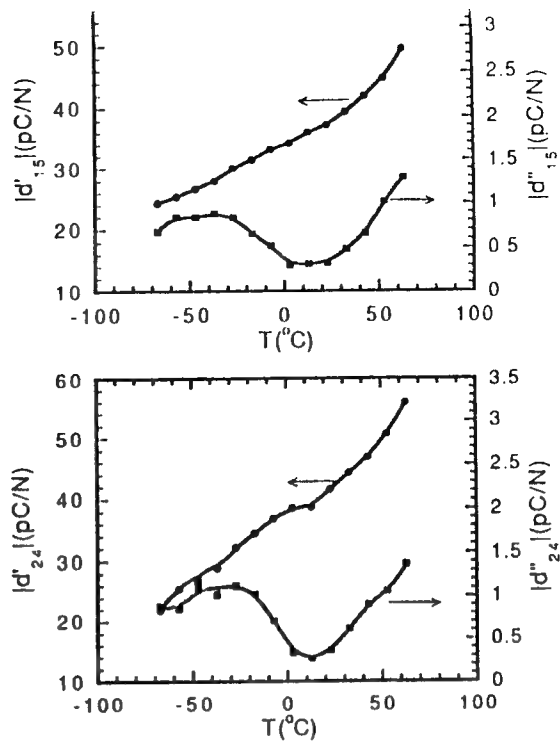
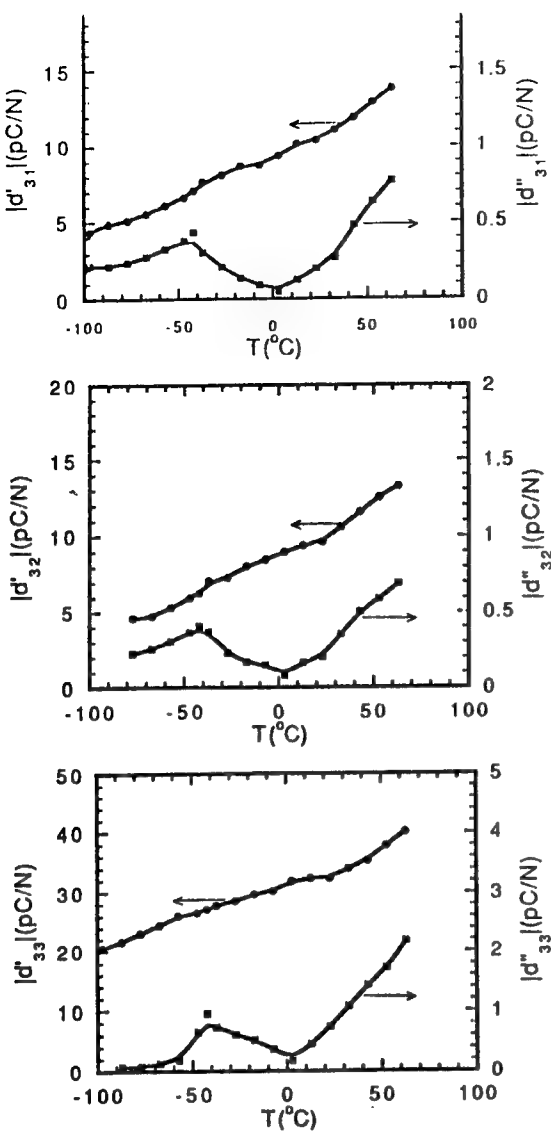


FIG. 2. Piezoelectric strain coefficients as functions of temperature.

pendencies, a very small difference in magnitude and in temperature dependence were observed between d_{31} and d_{32} for this copolymer. The piezoelectric constants d_{31} and d_{32} increase with temperature much faster than d_{33} , d_{15} , and d_{24} . Additionally, higher losses were measured. On the other hand, the dielectric constants along three axes exhibit nearly identical temperature dependencies.

For PVDF and its copolymers, experimental evidence has shown that the mesoscopic morphology is that crystalline lamellae are embedded in an amorphous region of disordered polymer chains. Hence, the piezoelectric response is governed by the mechanically induced change of the mechanical and electrical field distribution within the amorphous and crystalline regions. It has been proposed that there are two major contributions to the piezoelectric response in these materials: the intrinsic change of polarization (biased electrostriction effect), and the change of the sample dimensions while electric moments are fixed (dimensional effect). The dimensional effect contribution calculated by using a model of dipoles dispersed in an amorphous medium.⁴ For example, the dimensional contribution to d_{33} from this model is $-P_r s_{33}$, where P_r is the

remanent polarization and s_{33} is the elastic compliance. P_r measured for this sample is $5.4 \mu\text{C}/\text{cm}^2$, hence, the dimensional effect contribution to d_{33} is $-16.2 \text{ pC}/\text{N}$, which is about 50% of the total d_{33} . However, for the shear components, this contribution is extremely large when calculated using this model. For example, the dimensional effect contribution to d_{15} is $-520 \text{ pC}/\text{N}$. If the model is correct, the contributions from the intrinsic and dimensional effects are in opposite signs in shear constants and they almost cancel each other out, resulting in a small total coefficient.

For PVDF homopolymer there exist three relaxation processes associated with different types of segment motion in the material. The α relaxation occurs at temperatures above 55°C , β near -40°C , and γ near -70°C . Previous studies have shown that α relaxation is associated with molecular motion in crystalline regions of α phase, the β relaxation with the segment motion in the amorphous regions and hence signifies the glass transition, and the γ relaxation with local motion in the amorphous regions. For this P(VDF-TrFE) (75/25) copolymer, only β relaxation was observed at temperatures around -30°C . This together with the x-ray diffraction data¹¹ indicate that the

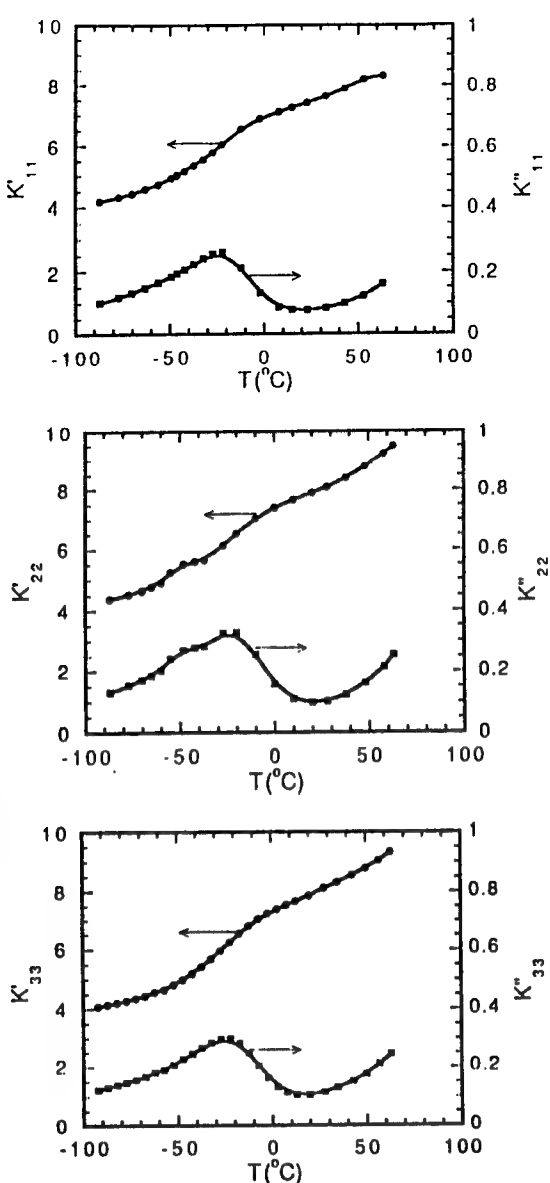


FIG. 3. Dielectric constants as functions of temperature.

crystalline phase in this copolymer is β phase. The interesting feature is that the loss peaks related to the β relaxation in the dielectric curves are about 20 °C higher than those in the tensile piezoelectric coefficient curves, i.e., the dielectric loss peaks are at about -20 °C while the loss peaks in the tensile piezoelectric coefficients are at -40 °C. More interestingly, the loss peaks in the shear piezoelectric coefficient curves are almost at the same temperature as those of the dielectrics.

Figure 4 shows the frequency dependence of the dielectric constant K_{33} . The relaxation observed near 1 MHz in

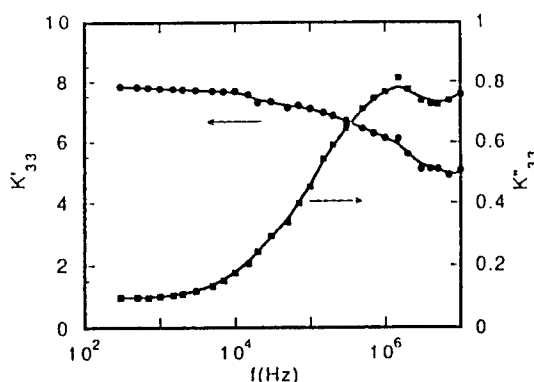


FIG. 4. Dielectric constant K_{33} as function of frequency.

the K_{33} spectrum is associated with β relaxation, as has been identified from the earlier studies on the PVDF homopolymer.¹² K_{11} and K_{22} were measured in the frequency range from 100 Hz to 100 kHz and their dependencies on frequency are similar to that of K_{33} . No frequency dispersion was observed for piezoelectric d constants in the range of 100 Hz-5 kHz.

In conclusion, the complete piezoelectric coefficient, dielectric constant, and elastic compliance matrices have been determined on P(VDF-TrFE) (75/25) copolymer at room temperature and a frequency of 500 Hz. The frequency and temperature dependencies of all five complex piezoelectric coefficients as well as three complex dielectric constants have been characterized.

ACKNOWLEDGMENTS

This work was supported by the Naval Undersea Warfare Center's Small Business Innovation Research (SBIR) program under contract No. N66604-90-C1558 (Low Cost Acoustic Sensor Technology) and the Office of Naval Research.

- ¹G. M. Sessler, *J. Acoust. Soc. Am.* **70**, 1596 (1981).
- ²M. G. Broadhurst, G. T. Davis, and J. E. McKinney, *J. Appl. Phys.* **49**, 4992 (1978).
- ³R. G. Kepler and R. A. Anderson, *J. Appl. Phys.* **49**, 4490 (1978).
- ⁴T. Furukawa, J. X. Wen, K. Suzuki, Y. Takashina, and M. Date, *J. Appl. Phys.* **56**, 829 (1984).
- ⁵R. Holland and E. P. EerNisse, *Design of Resonant Piezoelectric Devices* (M.I.T., Cambridge, MA, 1969).
- ⁶Q. M. Zhang, S. J. Jang, and L. E. Cross, *J. Appl. Phys.* **65**, 2807 (1989).
- ⁷W. Y. Gu, W. Y. Pan, and L. E. Cross, *Mater. Lett.* **8**, 3 (1989).
- ⁸W. Y. Pan, H. Wang, and L. E. Cross, *Jpn. J. Appl. Phys.* **29**, 1570 (1990).
- ⁹IEEE Standard on Piezoelectricity, ANSI/IEEE Std. 176 (1987).
- ¹⁰J. G. Smiths, *IEEE Trans. Sonics Ultrason.* **SU-23**, 393 (1976).
- ¹¹H. Wang, Q. M. Zhang, L. E. Cross, and A. O. Sykes (unpublished).
- ¹²T. T. Wang, *The Application of Ferroelectric Polymers* (Chapman and Hall, New York, 1988).

APPENDIX 33

PIEZOELECTRIC RELAXATION OF P(VDF-TrFE) COPOLYMER

H. WANG, Q. M. ZHANG and L. E. CROSS
Materials Research Laboratory, The Pennsylvania State University, University Park,
PA 16802, USA

(Received August 9, 1993)

Abstract The dielectric and piezoelectric relaxations of poly(vinylidene fluoride-trifluoroethylene)(75/25) copolymer over the temperature interval of -100 to 60 °C are reported in this paper. A two-dimension model is proposed to explain the experimental results. The expressions of piezoelectric d constants from the direct and the converse effects, dielectric constant and the elastic compliances are derived as functions of the physical properties of crystalline and amorphous regions. The numerical calculations of the model are in good agreement with the experimental results.

INTRODUCTION

The studies of dielectric, mechanical and piezoelectric dispersion are important in describing the dissipation behavior of a piezoelectric material. In many applications, such as acoustic target location and multielement 360° scanning sonar transducer, the knowledge of complex piezoelectric coefficients is useful. The relaxation phenomenon is related to the microstructure of a material and, therefore, is important in understanding the structure-property relations of a material. Due to the nature of the mesoscopic morphology of semicrystalline polymers, which consist of crystalline and amorphous regions, the relationship among dielectric, elastic, and piezoelectric relaxations can be different from that of piezoelectric ceramics which has been studied relatively well.^{1,2} In typical piezoelectric polymers, several relaxation mechanisms can coexist due to local mode motion, side chain motion, and segment motion of main chains, and relaxation occurs in both crystalline and amorphous regions. Piezoelectric relaxation has been studied on a number of polymeric materials.^{3,4} However, for PVDF and its copolymers, the only commercialized piezoelectric polymers, information is very limited at present. Recently, we have carried out a systematic investigation of complex dielectric, elastic and piezoelectric coefficients of P(VDF-TrFE) copolymer.⁵ It is found that near the glass transition temperature, the piezoelectric properties also exhibit relaxation. However, the relaxation frequency of piezoelectric coefficients is different from that of dielectric constants. This is similar to previous experimental results of other piezoelectric polymers, in which dielectric, piezoelectric and elastic relaxations occurred at different frequencies. To explain this phenomenon, a two-dimension model is proposed to derive the piezoelectric, dielectric, and elastic compliance coefficients of polymeric materials. Numerical calculations show they are in good agreement with the experiment results.

COMPLEX PIEZOELECTRIC COEFFICIENTS

The constitutive equations for a piezoelectric material are:⁶

[3423]/281

$$D_m = d_{mj} T_j + \epsilon_0 K_{mn} E_n \quad (1a)$$

$$S_i = s_{ij} T_j + d_{ni} E_n, \quad (1b)$$

where stress T_j and electric field E_n are taken as the independent variables, and electric displacement D_m and strain S_i the dependent variables, respectively; K_{mn} , s_{ij} and d_{mj} are dielectric constant, elastic compliance and piezoelectric strain coefficient of the material, respectively; ϵ_0 is the free space permittivity. The complex material coefficients are defined by the following equations:⁷

$$K_m^* = K_m^* - j K_m^*, \quad s_{ij}^* = s_{ij}^* - j s_{ij}^*, \quad \text{and} \quad d_{mj}^* = d_{mj}^* - j d_{mj}^*. \quad (2)$$

For a homogeneous material, the piezoelectric strain coefficients d_{mj} , determined by the direct effect using Eq. (1a), is the same as that by the converse effect using Eq. (1b). However, for complex materials, such as piezoelectric polymers, this equality needs to be verified because of the complicated boundary conditions. For a material with complex coefficients, the response process of the material is not thermodynamically reversible. Although it has been shown, through the irreversible thermodynamics, that Eqs. (1) are still valid for a single phase material, it is not clear and is interesting to know whether or not, for multiphase materials, the complex piezoelectric constants measured through the direct effect and through the converse effect will be equal.

EXPERIMENTAL WORKS AND RESULTS

P(VDF-TrFE) (75/25) copolymer samples used in this study were purchased from Atochem North America Inc.. The complex piezoelectric coefficients d_{mj} of the copolymer through the converse effect were measured by a laser ultra-dilatometer.⁸

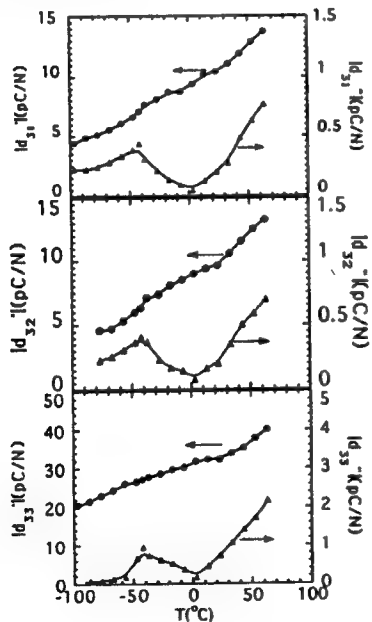


FIGURE 1 Complex piezoelectric coefficients as functions of temperature.

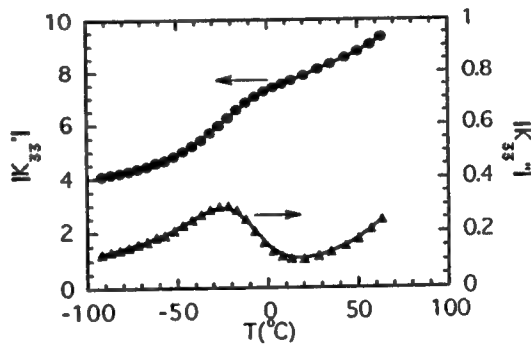


FIGURE 2 Complex dielectric constant as a function of temperature.

Shown in Fig. 1 are the tensile complex d coefficients thus determined as a function of temperature. For comparison, the complex dielectric constant K_{33} is shown in Fig. 2. Apparently the peak temperature of dielectric loss is different from that of imaginary part of piezoelectric constants. The complex d_{33} constant of the samples through the direct effect was measured by a high sensitivity, phase sensitive d_{33} meter that was developed recently in this laboratory.⁹ The room temperature results for the copolymer are: $|d_{33}|=31.0 \text{ pC/N}$ and $|d_{33}''|=0.62 \text{ pC/N}$, which are consistent with those measured from the converse effect within the data scattering. To our knowledge, these are the first experimental results of a complex piezoelectric coefficient from the direct and converse effects.

CALCULATION OF THE COMPLEX COEFFICIENTS

There has been a number of models to predict and explain the piezoelectric properties of PVDF type materials.^{10,11} However, the observed relaxation behaviors of the copolymer can not be explained by these models. In order to understand the experimental results and to explore the interactions between crystalline and amorphous regions involved in the piezoelectric responses, a model is proposed to derive the expressions of material coefficients as functions of the properties of crystalline and amorphous regions. For simplicity, only two dimension case is considered. The material is approximated as piezoelectric crystallites dispersed in nonpiezoelectric, isotropic amorphous matrix, as shown in Fig. 3, in which the 3-direction is the polar direction. The mechanical properties of the crystalline regions are also assumed to be isotropic. Because of the nonuniformity of the material and the interaction between crystalline and amorphous regions, the material is divided into four regions. For the crystalline region, the constitutive relations of the direct and the converse effects are:

$$S_3^c = s_{11}^c(T_3 + \frac{F_3^{II}}{\beta_c}) + s_{12}^c \frac{F_1^I}{\alpha_c}, \quad (3a)$$

$$S_1^c = s_{12}^c(T_3 + \frac{F_3^{II}}{\beta_c}) + s_{11}^c \frac{F_1^I}{\alpha_c}, \quad (3b)$$

$$S_3^c = d_{33}E_3^c + s_{11}^c \frac{F_3^{II}}{\beta_c} + s_{12}^c \frac{F_1^I}{\alpha_c}, \quad (3c)$$

$$S_1^c = d_{31}E_3^c + s_{12}^c \frac{F_3^{II}}{\beta_c} + s_{11}^c \frac{F_1^I}{\alpha_c}, \quad (3d)$$

respectively, where T_3 is the external stress in the direct effect and E_3^c is the electric field on the crystalline region in the converse effect; d_{33} and d_{31} are the intrinsic piezoelectric constants of crystalline regions; F^I and F^{II} are forces applied by the region A1 and AII to the crystalline region, respectively; superscript c stands for the crystalline region. Similar equations can be written for the other regions. Using the boundary conditions, which are based on the static force equilibrium and equal strains at boundaries, all these equations can be solved, and the piezoelectric constant from the direct effect $\overline{d_{33}^d}$ and from the converse effect $\overline{d_{33}^c}$, dielectric constant $\overline{K_{33}}$, and the elastic compliance $\overline{s_{11}}$ can be derived. For brevity, the detailed derivations are omitted here. The final results are:

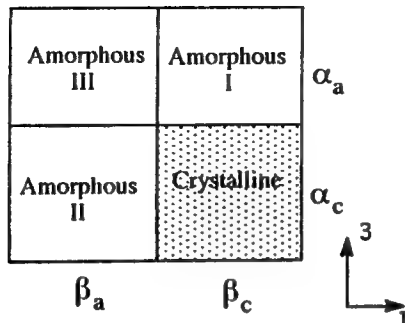
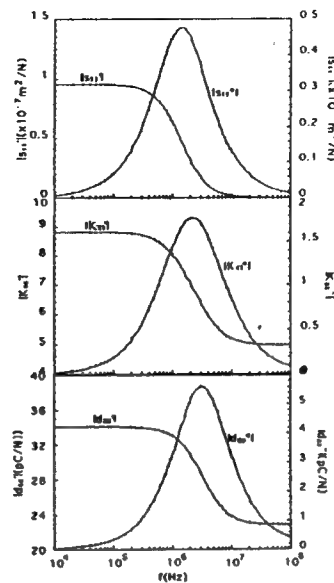


FIGURE 3 The two-dimension model.

FIGURE 4 Calculated s^* , K^* , and d^* as functions of frequency.

$$\overline{d_{33}^a} = \frac{K^c \alpha_a \beta_c}{K^a \alpha_c + K^c \alpha_a} \left\{ d_{33} \left\{ 1 + \frac{1}{AB - CD} \left[\frac{\beta_a}{\beta_c} \frac{1}{\sigma_a} \left(\frac{1}{\alpha_a} + \frac{1}{\alpha_c} \right) (\Delta s_{12} A - \Delta s_{11} D) \right. \right. \right. \\ \left. \left. \left. - \frac{1}{\beta_c} (\Delta s_{11} B - \Delta s_{12} C) \right] \right\} + d_{31} \frac{1}{AB - CD} \right. \\ \left. \left[\frac{\alpha_a}{\alpha_c} \frac{1}{\sigma_a} \left(\frac{1}{\alpha_a} + \frac{1}{\alpha_c} \right) (\Delta s_{11} B - \Delta s_{12} C) - \frac{1}{\alpha_c} (\Delta s_{12} A - \Delta s_{11} D) \right] \right\} \quad (4)$$

$$\overline{d_{33}^c} = \frac{K^a}{K^a \alpha_c + K^c \alpha_a} \frac{s_{11}^a}{\beta_a} \frac{1}{AB - CD} \left\{ (d_{31} C - d_{33} B) - \frac{\beta_a}{\sigma_a} \left(1 + \frac{\alpha_c}{\alpha_a} \right) (d_{33} D - d_{31} A) \right\} \quad (5)$$

$$\overline{K_{33}} = K^a \beta_a + \frac{\beta_c K^c K^a}{K^c \alpha_a + K^a \alpha_c} \quad (6)$$

$$\overline{s_{11}} = (\alpha_c s_{11}^c + \alpha_a s_{11}^a) + \frac{1}{AB - CD} \left\{ \left[\frac{\beta_a}{\beta_c} \frac{1}{\sigma_a} s_{11}^c \left(1 + \frac{\alpha_c}{\alpha_a} \right) + \Delta s_{12} \right] (\Delta s_{12} A - \Delta s_{11} D) \right. \\ \left. - \left[\frac{\alpha_a}{\sigma_a} \Delta s_{12} \left(\frac{1}{\alpha_a} + \frac{1}{\alpha_c} \right) + \frac{1}{\beta_c} (\alpha_a s_{11}^a - \alpha_c s_{11}^c) \right] (\Delta s_{11} B - \Delta s_{12} C) \right\} \quad (7)$$

Where K^c and K^a are dielectric constant of crystalline and amorphous regions, respectively; $\sigma^a = -s_{12}^a / s_{11}^a$ is the Poisson ratio of amorphous regions; Δs_{ij} ($= s_{ij}^a - s_{ij}^c$) is the elastic compliance difference of amorphous and crystalline regions; A, B, C, and D are quantities depending on the mechanical properties of both crystalline and amorphous regions:

$$A = \frac{\alpha_a}{\alpha_c} \frac{1}{\beta_c} \frac{1}{\sigma^a} s_{12}^c - \frac{s_{11}^c + s_{11}^a}{\beta_c \beta_a} \quad (8a)$$

$$B = \frac{\beta_a}{\beta_c} \frac{1}{\alpha_c} \frac{1}{\sigma^a} s_{12}^c - \frac{s_{11}^c + s_{11}^a}{\alpha_c \alpha_a} \quad (8b)$$

$$C = \frac{s_{11}^c + s_{11}^a}{\beta_c \beta_a} \left(\frac{1}{\alpha_c} + \frac{1}{\alpha_a} \right) \frac{\beta_a}{\sigma^a} + \frac{1}{\alpha_c} (s_{12}^a - s_{12}^c) \quad (8c)$$

$$D = \left(\frac{s_{11}^c + s_{11}^a}{\alpha_c \beta_c} \right) \left(\frac{1}{\beta_a} + \frac{1}{\sigma^a} \right) \frac{\alpha_a}{\beta_c} + \frac{1}{\beta_c} (s_{12}^a - s_{12}^c) \quad (8d)$$

Similarly, piezoelectric constant \bar{d}_{31} from both the direct and the converse effects and the elastic compliance \bar{s}_{12} can be derived. Apparently, Eqs. (4)-(7) are too complex to reveal the physical insight of the problem. To study the relaxation behaviors of these coefficients, numerical calculations of these equations were carried out. Compared with relaxation of the properties of amorphous regions, the relaxation frequencies of dielectric and piezoelectric constants of crystalline regions could be much higher. Hence, to study the effect of glass transition that occurs in amorphous regions, we assumed relaxation only occurs in amorphous regions with Debye type:

$$s_{ij}^a(\omega) = s_{ij}^a(\infty) + \frac{s_{ij}^a(0) - s_{ij}^a(\infty)}{1 + j \omega \tau}, \text{ and } K^a(\omega) = K^a(\infty) + \frac{K^a(0) - K^a(\infty)}{1 + j \omega \tau}, \quad (9)$$

where τ is the relaxation time. The parameters used in the calculation are listed in Table I. The typical results are shown in Fig. 4 with the volume fraction of crystalline regions of 0.56.

TABLE I Parameters used in the calculations

K^{c12}	8.5	s_{11}^{c13}	$5.0 \times 10^{-11} \text{ m}^2/\text{N}$
$K^a(0)^{12}$	10.2	s_{12}^{c13}	$-0.5 \times 10^{-11} \text{ m}^2/\text{N}$
$K^a(\infty)^{12}$	3.0	$s_{11}^a(0)$	$5.0 \times 10^{-7} \text{ m}^2/\text{N}$
d_{33}^5	-40 pC/N	$s_{11}^a(\infty)$	$5.0 \times 10^{-11} \text{ m}^2/\text{N}$
d_{31}^5	20 pC/N	$s_{12}^a(0)$	$-2.5 \times 10^{-7} \text{ m}^2/\text{N}$
τ^5	$1.13 \times 10^{-7} \text{ s}$	$s_{12}^a(\infty)$	$-0.5 \times 10^{-11} \text{ m}^2/\text{N}$

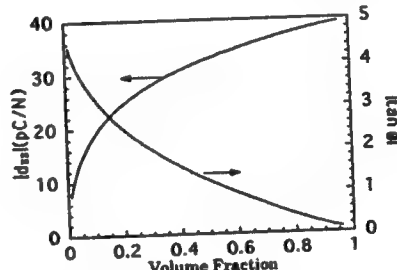


FIGURE 5 Complex d coefficient as functions of degree of crystallinity.

DISCUSSION

(1) As shown in Fig. 4, the model predicts that the relaxation peaks of dielectric, piezoelectric, and elastic coefficients can occur at different frequencies. The relaxation frequency of dielectric constant is lower than that of piezoelectric constant. Using the WLF relation, it can be deduced that in temperature domain, the relaxation peak of d

constants should occur at lower temperature compared with that of dielectric constant. This conclusion is consistent with the experimental results as shown in Figs. 1 and 2. The calculations also show the differences among three relaxation frequencies increase with the degree of crystallinity.

(2) The experimental results of dielectric constant indicate, in the temperature range of -80 to 60 °C, the only relaxation observed in this copolymer is β -relaxation, which is associated with the glass transition of non-crystalline molecules. On the other hand, for PVDF type polymeric materials, it is believed that the piezoelectricity only exists in the crystalline regions. Therefore, for the single crystal PVDF, there should be no relaxation at the glass transition temperature and frequency. The observed piezoelectric relaxation near the glass transition temperature clearly indicate that the piezoelectric response of the materials can be strongly affected by the properties of amorphous regions. Again, this confirms the results of the theoretical model in which no relaxation is assumed in crystalline regions, and relaxation behavior still occur in the piezoelectric properties of the material.

(3) Experimental evidence has shown that the piezoelectric response of polymeric materials strongly depends on the degree of crystallinity of the materials. The model predicts nonlinear relations between d_{33} constant and the volume fraction of the crystalline regions, as shown in Fig. 5. The decrease of the loss tangent is caused by the relaxation free assumption of the crystalline regions.

(4) For P(VDF-TrFE) (75/25) copolymer, the complex d_{33} coefficients measured through the direct and converse effect are equal. This result is consistent with the numerical calculations. Since this is the first and perhaps the only existing precise measurement of the complex piezoelectric coefficient, we do not intend to generalize the conclusion to other complex materials. Further theoretical and experimental studies are needed.

(5) When volume fraction of the crystalline regions is 90%, the calculated elastic compliance at low frequencies is $0.95 \times 10^{-7} \text{ m}^2/\text{N}$, which is much greater than the measured compliance of the copolymer ($s_{11}=3.32 \times 10^{-10} \text{ m}^2/\text{N}$). It is believed that this big difference is caused by the assumption that crystallite are isolated by amorphous medium. In fact, when the crystallinity is high, the model is not accurate because there must be some percolation of the crystalline regions which can significantly reduce the compliances of a material.

REFERENCES

1. G. Arlt and H. Dederichs, *Ferroelectrics*, **29**, 47 (1980).
2. P. Gerthsen, K. H. Hardtl and N. A. Schmidt, *J. Appl. Phys.*, **51**, 1131 (1980).
3. T. Furukawa and E. Fukada, *Nature*, **221**, 1235 (1969).
4. M. date, S. Takashita and E. Fukada, *J. Polymer Sci. A-2*, **8**, 61(1970).
5. H. Wang, Q. M. Zhang, L. E. Cross and A. O. Sykes, *J. Appl. Phys.*, (1993).
6. IEEE Standard on Piezoelectricity, 176-1987.
7. R. Holland, *IEEE Trans. Sonics and Ultraso.* **SU-14**, 18 (1967).
8. W. Y. Pan, H. Wang and L. E. Cross, *Jpn. J. Appl. Phys.*, **29**, 1570 (1990).
9. H. Wang, Q. M. Zhang and L. E. Cross, *Jpn. J. Appl. Phys.*, Accepted.
10. M. G. Broadhurst, G. T. Davis and J. E. McKinney, *J. Appl. Phys.*, **49**, 4992 (1978).
11. Y. Wada and R. Hayakawa, *Ferroelectrics*, **32**, 115(1981).
12. S. Ikeda and M. Kutani, *Jpn. J. Appl. Phys.*, **30**, 3456 (1991).
13. K. Tashiro, M. Kobayashi, H. Tadokoro and E. Fudaka, *Macromolecules*, **13**, 691 (1980).

APPENDIX 34

for low-frequency applications

Q. M. Zhang, Wenwu Cao, H. Wang, and L. E. Cross

Materials Research Laboratory, The Pennsylvania State University, University Park, Pennsylvania 16802

(Received 20 April 1992; accepted for publication 15 October 1992)

In general, the piezoelectric ceramic and polymer in a 1-3 type composite will have different deformations when subjected to an external field. How each component deforms, to a large extent, determines the performance of the composite. Based on the force equilibrium condition, an elastic model is introduced to analyze the strain profiles of these composites, and the theoretical results are in quantitative agreement with the strain profiles measured on several composites using a double beam ultradilatometer. The results obtained provide quantitative information on how various parameters in a composite affect the performance of the composite. Furthermore, a scheme is proposed for evaluating the strain profile of a 1-3 type composite under a hydrostatic pressure using a double beam dilatometer.

I. INTRODUCTION

A variety of piezoelectric composite materials can be formed by combining a piezoelectric ceramic with a polymer phase. Among them, the piezoelectric 1-3 composite has attracted a great deal of attention and been used widely.¹⁻³ A typical configuration of 1-3 type composites is illustrated in Fig. 1. In the composites, piezoelectric ceramics, usually lead zirconia titanate (PZT) ceramics, play the active role of energy conversion between the mechanical energy and electric energy, while the polymer phase acts as a passive medium, which transfers the mechanical energy between the piezoelectric ceramic and the surrounding with which the composite interacts. The disparity in the physical properties between the two constituent phases and different roles they play in a composite make it possible to fine tailor the material properties of a composite to meet different requirements of specific application.⁴⁻⁷

There are two major areas where 1-3 composites have been widely used: underwater hydrophone application and ultrasonic actuators and sensors for medical diagnostic devices.¹⁻⁴ The former is operated at frequencies below 40 kHz while the latter are operated at a MHz frequency range. As can be seen from Fig. 1, in making a 1-3 composite, several parameters can be varied: the elastic properties of the polymer phase, the shape, and the aspect ratio of the PZT rods, the spacing between the rods, the volume content, and the arrangement of the PZT rods in the composite. The intention of this paper is to provide some understanding of how these design parameters affect the performance of the composites for low-frequency applications. To achieve that, a new model is introduced that treats the composites beyond the earlier equal-strain model.^{2,8,9}

When a 1-3 composite is subjected to an electric field or a stress field, a strain field will be induced in the sample. Due to the large difference in the elastic and piezoelectric properties, in general, the two components will have different strain levels and the strain in each component will not be uniform. This strain profile is determined by the parameters listed in the preceding paragraph and determines how effectively the two components in a composite

couple to each other. The strain profile of a composite under an electric field can be mapped out using a double beam ultradilatometer, as will be shown in this paper.¹⁰ However, it may not be measured easily when the composite is subjected to a stress field. In this paper, we will show that the strain profile measured on a composite under an electric field can be used to describe the deformation of the composite under a uniaxial or a hydrostatic stress.

The basic elastic coupling mechanism between the two components in the 2-2 piezoelectric composite is similar to that of the 1-3 composite. Although this structure is not widely used, the mathematical analysis on the performance of the composite is much simpler and the results obtained can also be applied to the 1-3 composite. Hence, in this paper, we will first discuss the performance of 2-2 composites (Sec. II). In Sec. III, 1-3 composites will be analyzed in the dilute limit. In Sec. IV, the results obtained in Sec. III will be applied to 1-3 composites beyond the dilute limit.

II. 2-2 COMPOSITE

In a 2-2 composite, the PZT plates and polymer are arranged in a parallel manner, as schematically drawn in Fig. 2(a). Assuming the sample dimension in the y direction is much larger than the sample thickness L and the spacing d between the neighboring PZT plates, a 2-2 composite can be modeled as a one-dimensional system. When there is a strain change S_3 in PZT plates, for example, due to an electric field on the composite, there will be a corresponding change in the strain profile of the polymer phase. Denoting $u(x)$ the surface displacement of the polymer phase in the z direction, the longitudinal strain S_3 in the z direction of the polymer phase is $2u(x)/L$, where L is the sample thickness. As a result of the strain gradient $u(x)$, a shear force $\mu L \partial^2 u(x)/4 \partial x^2$ will be induced in the z direction, where μ is the shear modulus of the polymer. Under the static condition, this shear force will be balanced by the restoring force $2Yu(x)/L$ in the polymer, that is

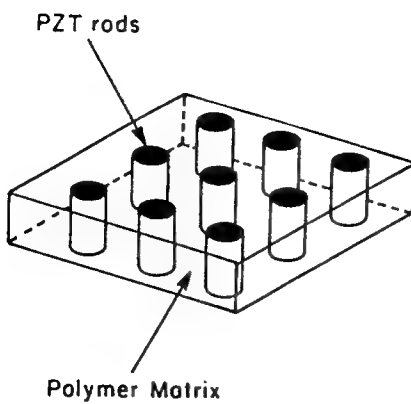


FIG. 1. Schematic drawing of a 1-3 PZT-polymer composite, where PZT rods are embedded in a polymer matrix.

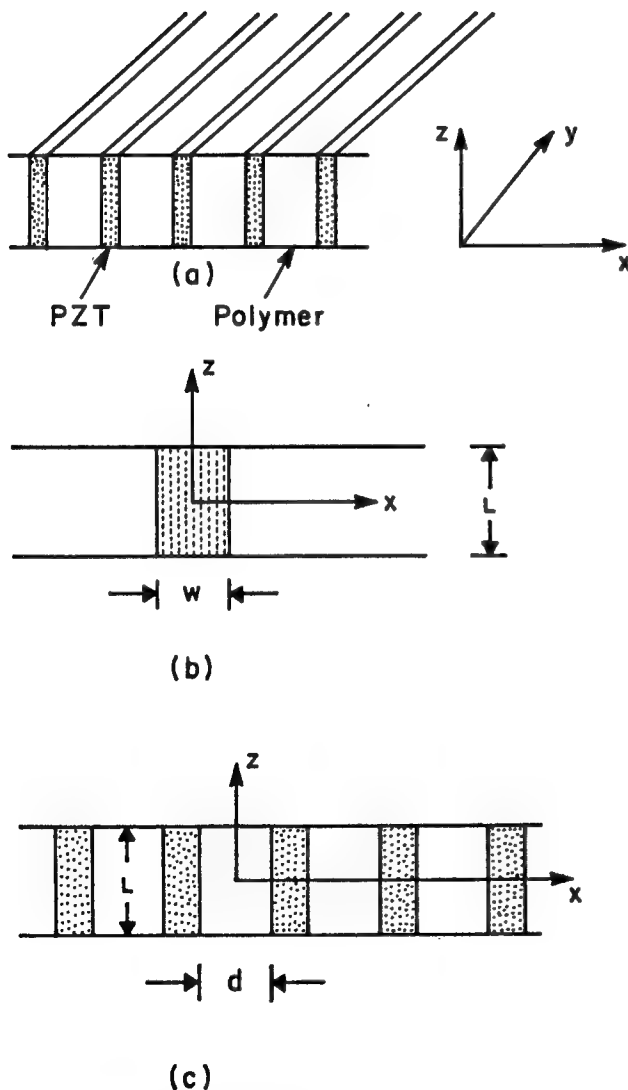


FIG. 2. (a) A schematic drawing of a 2-2 composite, where the hatched plates are PZT; (b) the coordinate system for a 2-2 composite with a single PZT plate; and (c) the coordinate system for Eq. (1.3).

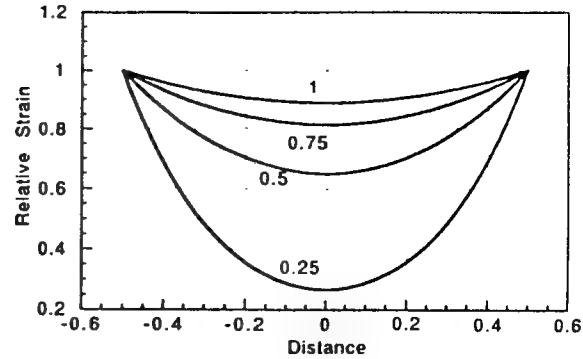


FIG. 3. The strain profile for the polymer between two PZT plates [from Eq. (1.3)]. The parameter shown in the figure for each curve is $\xi = L/(2\sqrt{2Y/\mu})$. In the figure, the gap width d is 1 mm.

$$\frac{\mu L \partial^2 u(x)}{4 \partial x^2} = \frac{2Y}{L} u(x), \quad (1.1)$$

where Y is the Young's modulus of the polymer. The details of the derivation of Eq. (1.1) will be presented in a separate paper.¹¹ The solution to Eq. (1.1) is

$$2u(x)/L = A \exp(2x\sqrt{2Y/\mu}/L) + B,$$

where A and B are integration constants. For the case when there is only one PZT plate in the composite, as shown in Fig. 2(b), the longitudinal strain S_3 of the polymer phase is

$$\left(\frac{2u}{L}\right) = \left(\frac{2u}{L}\right)_0 \exp\left[-\left(x - \frac{w}{2}\right) \frac{2\sqrt{2Y/\mu}}{L}\right] \quad \left(x > \frac{w}{2}\right) \quad (1.2)$$

and

$$\left(\frac{2u}{L}\right) = \left(\frac{2u}{L}\right)_0 \exp\left[\left(x + \frac{w}{2}\right) \frac{2\sqrt{2Y/\mu}}{L}\right] \quad (x < -w/2),$$

where w is the PZT plate width and $2(u/L)_0$ is the strain at the PZT-polymer interface. Equation (1.2) shows that the strain in the polymer phase decays exponentially with a characteristic length $\xi = L/(2\sqrt{2Y/\mu})$ as the polymer phase moves away from the PZT plate.

For a 2-2 composite as depicted in Fig. 2(c), the solution to Eq. (1.1) is

$$\left(\frac{2u}{L}\right) = \left(\frac{2u}{L}\right)_0 \cosh\left(\frac{2x\sqrt{2Y/\mu}}{L}\right) \operatorname{sech}\left(\frac{d\sqrt{2Y/\mu}}{L}\right), \quad (1.3)$$

where d is the gap width between the two PZT plates. Equation (1.3) describes the strain profile in the polymer between the two neighboring PZT plates. In Fig. 3, we plot the strain profile of the polymer phase calculated from Eq. (1.3) for $L=4.7$ mm ($\xi=1$), 3.5 mm ($\xi=0.75$), 2.3 mm ($\xi=0.5$), and 1.2 mm ($\xi=0.25$) for the gap width $d=1$ mm. In the calculation, $Y=4.7 \times 10^9$ N/m² and $\mu=1.7 \times 10^9$ N/m², the elastic constants for spurs epoxy were used. The figure shows a strong dependence of induced strain profile in the polymer phase on the sample thickness.

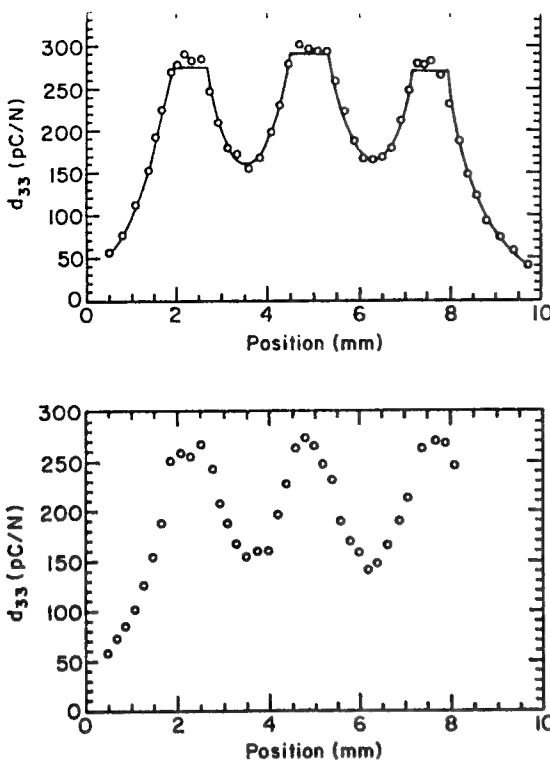


FIG. 4. (a) Strain profile for the 2-2 composite made of PZT-5A and spurs epoxy with thickness $L = 4.5$ mm. The sample is driven electrically at 200 Hz, circles are the data points and the solid line is the fitting. (b) Strain profile for the 2-2 composite measured at 40 kHz.

From the figure, one can make the following observations: in this one-dimensional structure, as the sample thickness approaches that of the gap width, induced strain in the gap center of the polymer phase approaches zero; On the other hand, for $L/d = 5$, the strain nonuniformity in the polymer phase is less than 10% and the equal-strain model can be used to calculate the effective material properties without introducing significant errors. Equations (1.2) and (1.3) also reveal that the elastic properties of the polymer phase have a significant effect on the strain profile. By reducing Y or increasing μ , one can greatly increase the elastic coupling between the two components.

To compare with the theoretical results, several 2-2 composites were made using PZT-5A (PZT-5A and PZT-5H are trademarks of Vernitro Corp. for their PZT products) plates and spurs epoxy. The strain profile of the sample was measured along a path parallel to the x axis using the double beam laser interferometer when the sample was driven electrically. Shown in Fig. 4(a) is the result of one of the scans thus obtained. The solid line in the figure is the theoretical fitting using Eq. (1.3) for the polymer regions between the PZT plates and Eq. (1.2) for the polymer regions at the two edges of the sample. Clearly, the theoretical curve describes the data quite well. The fitting yields the ratio of $Y/\mu = 3.35$ for spurs epoxy, which is larger than the true value of $Y/\mu (= 2.76)$. We believe that this is due to the fact that in Eq. (1.1), the effect of the stress in the x and y directions is not included. Further

effect in the constitutive equations.

Equation (1.1) can be modified to account for the situation when a composite is subjected to a low-frequency driving field (either a stress field or an electric field). By low frequency, we mean that the frequency is at least five times smaller than the first thickness resonance frequency. Under this circumstance, the longitudinal strain in the sample can be approximated as uniform and Eq. (1.1) can be rewritten as

$$\frac{\mu L \partial^2 u}{4 \partial x^2} = \frac{2Y}{L} u + \frac{\rho L \partial^2 u}{4 \partial t^2}, \quad (1.4)$$

to include the time-dependent effect. In Eq. (1.4), ρ is the polymer density. For a sinusoidal strain $u = u(x) \exp(i\omega t)$, where ω is the angular frequency of the driving field, Eq. (1.4) becomes

$$\frac{\mu L \partial^2 u}{4 \partial x^2} = \left(\frac{2Y}{L} - \frac{\rho L \omega^2}{4} \right) u. \quad (1.5)$$

It is easy to realize that as long as the quantity $(2Y/L^2 - \rho\omega^2/4) > 0$, the solution to Eq. (1.5) is the same as that of Eq. (1.1). The strain profile in the polymer region is still described by Eqs. (1.2) and (1.3), except the characteristic decay length ξ becomes $\xi = L/[2\sqrt{2(Y - \rho\omega^2 L^2/8)/\mu}]$. In all the practical cases, the change in ξ is very small. For instance, the change of ξ is about 2% when ω varies from 0 to 40 kHz for the 2-2 composite used here. To verify this, the strain profile of the 2-2 composite was measured at higher frequency (40 kHz) using the laser dilatometer. The data is shown in Fig. 4(b) and the strain profile is almost identical to that measured at 200 Hz [Fig. 4(a)]. The experimental as well as theoretical results both indicate that the polymer strain profile will not change significantly in this low-frequency region.

We now discuss the situation when the composite is subjected to a uniaxial stress T in the z direction. The force balance condition yields

$$T + \left(\frac{\mu L}{4} \right) \frac{\partial^2 u}{\partial x^2} = \frac{2Yu}{L}. \quad (1.6)$$

By making the variable substitution, $v = u - LT/(2Y)$, Eq. (1.6) becomes identical to Eq. (1.1). Hence the solution to Eq. (1.6) for the polymer strain profile between two PZT plates is

$$\left(\frac{2u}{L} \right) = A \cosh \left(\frac{-2x\sqrt{2Y/\mu}}{L} \right) + \frac{T}{Y}, \quad (1.7)$$

where $A = [(2u/L)_0 - T/Y] \operatorname{sech}(-d\sqrt{2Y/\mu}/L)$, $(2u/L)_0$ is the strain at the PZT-polymer interface, and d is the gap width of the polymer phase between the two PZT plates.

Comparison of Eq. (1.3), which is the polymer strain profile induced by the PZT plates when the composite is driven electrically, with Eq. (1.7), which is the strain profile of the polymer phase when a uniaxial stress is applied on the composite, yields that except for the prefactor and a constant term, the functional forms of the two cases are the

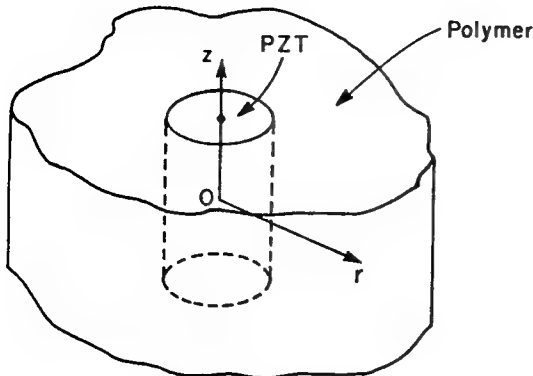


FIG. 5. 1-3 composite in the dilute limit.

same. As will be shown later in the paper, a similar conclusion is also true for the strain profile of a composite under a hydrostatic stress. This link between the two cases provides a convenient way for evaluating composites for hydrophone applications.

III. 1-3 COMPOSITE IN THE DILUTE LIMIT

In the dilute limit, the performance of a 1-3 composite can be modeled as that of a single PZT rod embedded in an infinitely extended polymer matrix, as schematically drawn in Fig. 5. From the symmetry of the problem, a cylindrical coordinate system is chosen with the z and r directions along the axis of the PZT rod and the radial direction, respectively. Similar to the situation for Eq. (1.1), the equation that describes the equilibrium condition of the polymer phase when the composite is driven electrically is

$$\frac{\mu L}{4} \left(\frac{\partial^2 u}{\partial r^2} + \frac{\partial u}{r \partial r} \right) = \frac{2Yu}{L}. \quad (2.1)$$

The meaning of each term in Eq. (2.1) is the same as that in Eq. (1.1). Equation (2.1) can be transformed to the zeroth-order Bessel equation of the imaginary argument. The solution that satisfies the boundary condition $r \rightarrow \infty$, $u/L \rightarrow 0$, is the imaginary argument zeroth-order Hankel function $K_0(\rho)$, where $\rho = 2r\sqrt{2Y/\mu}/L$. When the strain in the polymer phase is induced by the PZT rod, the solution to Eq. (2.1) is

$$(2u/L) = (2u/L)_0 K_0(\rho) / K_0(a/\xi), \quad (2.2)$$

where $(2u/L)_0$ is the strain at the PZT rod-polymer interface, a is the radius of the PZT rod, and $\xi = L/(2\sqrt{2Y/\mu})$.

It is interesting to compare the strain profile of the polymer phase in the 2-2 composite with that in the 1-3 composite. Shown in Fig. 6(a) are the strain profiles calculated from Eq. (2.2) (single PZT rod 1-3 composite) and from Eq. (1.2) (single PZT plate 2-2 composite). Apparently, the strain decay in the polymer phase in a 1-3 composite is much faster than that in a 2-2 composite. Besides that, there is an additional difference between the two cases: the decay in the polymer phase for a 1-3 composite also depends on the PZT rod diameter $2a$, while in

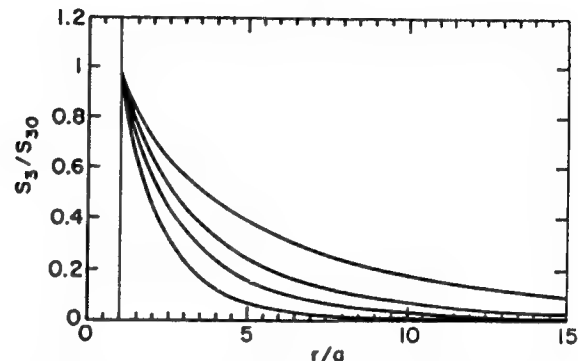
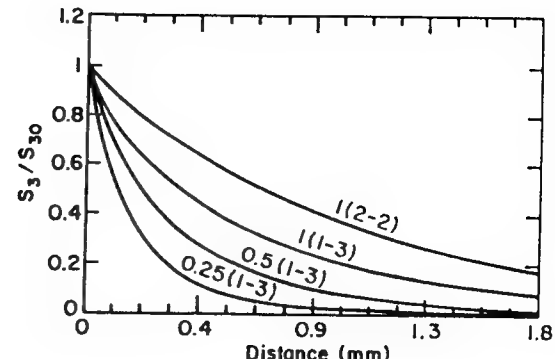


FIG. 6. (a) Decay of the strain in the polymer phase for (from the top to the bottom) a 2-2 composite [Eq. (1.2)] with $\xi=1$, a single rod 1-3 composite with $\xi=1$, $\xi=0.5$, and $\xi=0.25$, where $\xi = L/(2\sqrt{2Y/\mu})$. In the 1-3 composite, the PZT rod radius is 0.3 mm. The strain S_3 in the polymer phase is normalized to that of PZT rod S_{30} . The abscissa is the distance from the polymer-PZT interface. (b) The dependence of the strain in the polymer phase on the radius of a PZT rod in a 1-3 composite in the dilute limit. From the top to the bottom: $a=0.1, 0.2, 0.3, 0.5$ mm. In all the curves, $\xi=1$. r is distance defined in Fig. 5.

a 2-2 composite, it is independent of the PZT plate width. To illustrate this, in Fig. 6(b), the strain profiles in the polymer phase for PZT rod radius $a=0.1, 0.2, 0.3, 0.5$ mm are plotted, where $\xi=1$ and $(2u/L)_0=1$ are assumed for all the cases. Therefore, both the elastic properties of the polymer phase and the aspect ratio of the PZT rod are important parameters in determining the performance of 1-3 composites.^{8,12}

Shown in Fig. 7 is the strain profile measured on a 1-3 composite made of a single PZT tube embedded in spurs epoxy matrix. The strain profile was mapped out using the double beam ultradilatometer when the sample was driven electrically at 200 Hz. The solid line in the figure is $K_0(r/\xi)$, the strain profile predicted theoretically. The only adjustable parameter in the fitting is ξ , and the theoretically calculated curve agrees with the experimental data quite well. The fitting yields the ratio of $Y/\mu=3.35$ for the spurs epoxy used, which is the same as that measured in the 2-2 case. The consistency between the two measurements indicates that the model contains the essence of the elastic coupling between the two components in 1-3 type composites.

In what follows, the elastic coupling between the PZT rod and polymer will be analyzed using this model for the composite subjected to (a) an electric field E along the z

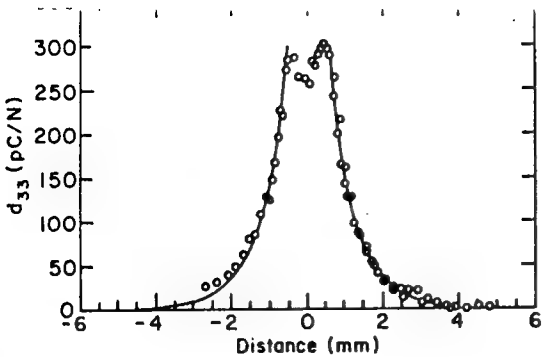


FIG. 7. The strain profile of a single tube 1-3 composite (tube o.d. = 1.2 mm) measured at 200 Hz using the double beam ultradilatometer. The composite is made of PZT-5H tube and spurs epoxy. Solid lines are the fittings using Eq. (2.2) with only one adjustable parameter ξ ($\xi = 1.15$ from the fitting). Sample thickness $L = 4.5$ mm.

direction; (b) a uniaxial stress T along the z direction; and (c) a hydrostatic pressure. In all the cases, the poling direction of the PZT rod is in the z direction.

(a) when an electric field E is applied to the composite, from the constitutive equation, one can obtain the z component of the strain in the PZT rod $S_0 = d_{33} E$ if there is no elastic coupling between the PZT rod and polymer. The effect of the polymer on the PZT rod is to add a mechanical load to it. In this situation, the strain in the polymer phase is described by Eq. (2.2). The stress transferred from the polymer to the PZT rod due to this strain field is

$$T = -Y(2u/L)_0 F(a, \xi), \quad (2.3)$$

where $(2u/L)_0$ is the strain in the PZT rod after the polymer loading and

$$F(a, \xi) = \frac{2\xi K_1(a/\xi)}{a}, \quad (2.4)$$

where $\xi = L/(2\sqrt{2Y/\mu})$, a is the radius of the PZT rod, and $K_1(x)$ is the first-order modified Bessel function. The strain of the PZT rod due to this additional polymer loading is

$$\left(\frac{2u}{L}\right)_0 = \frac{d_{33}E}{1 + 's_{33}Y F(a, \xi)}, \quad (2.5)$$

where $'s_{33}$ is the elastic compliance of PZT. Clearly, due to the polymer loading, the strain level of the PZT rod is smaller than $d_{33}E$. Using Eq. (2.5), one can calculate the strain reduction $(2u/L)_0/(d_{33}E)$ if $'s_{33}Y$ and ξ are known. For a thin PZT rod (small a), even when the elastic compliance of the polymer is much larger than that of PZT, the reduction in the strain of the PZT rod can still be substantial.

In general cases, $d_{33}E$ can be replaced by S_0 , the strain of the PZT rod without the polymer matrix. Hence the total stress on the PZT rod is

$$T = -\frac{YS_0 F(a, \xi)}{1 + 's_{33}Y F(a, \xi)}. \quad (2.6)$$

$Y S_0$	0.02	0.1
a (mm)	γ	γ
0.1	31.4	9.0
0.2	8.3	7.6
0.5	7.1	4.8
1.0	3.6	3.0

A large stress would arise during the poling of a 1-3 composite since S_0 is relatively large as the PZT rods are poled, and this stress acts as a depoling field on the PZT rods in composites. For example, considering a composite made of a PZT-5H rod and spurs epoxy, taking $a = 0.2$ mm, $L = 5.2$ mm, $S_0 = 0.1\%$, $\xi = 1$, $'s_{33}Y = 0.1$, and $Y = 4.7 \times 10^9$ N/m 2 , the stress on the PZT rod is 3.4×10^7 N/m 2 .

(b) From the result of the preceding section, the strain profile of the polymer phase under a uniaxial stress T in the z direction is

$$(2u/L) = AK_0(r/\xi) + T/Y, \quad (2.7)$$

where $A = [(2u/L)_0 - T/Y]/K_0(a/\xi)$, $(2u/L)_0$ is the strain of the PZT rod. When a composite is used in this situation, one major concern is how much the stress on the polymer will be transferred to the PZT rod. To calculate this quantity, we notice that without the elastic coupling to the PZT rod the strain in the polymer under the stress T is T/Y . By subtracting out this quantity from Eq. (2.7), one can obtain the change in the strain profile of the polymer phase due to the elastic coupling to the PZT rod. From this consideration, T_{tr} , the stress transferred from the polymer to the PZT rod is

$$T_{tr} = T \left[\frac{1 + F(a, \xi)}{1 + ('s_{33}Y) F(a, \xi)} - 1 \right], \quad (2.8)$$

or in a more familiar language, the stress amplification factor γ due to the composite

$$\gamma = T_{total}/T = [1 + F(a, \xi)]/[1 + ('s_{33}Y) F(a, \xi)], \quad (2.9)$$

where $T_{total} = T + T_{tr}$ is the total stress applied to the PZT rod. In Table I, γ is calculated for composites with a different radius of the PZT rod and different elastic properties of the constituent phases ($\xi = 1$). For a composite with a fixed volume percentage of PZT rods, the effective d_{33} of the composite is proportional to γ . Therefore, the result in Table I illustrates how the effective d_{33} of the composite changes as one varies the radius of PZT rods. Clearly, to increase the piezoelectric response of the composite, thin PZT rods should be used. The result in Table I also shows that the polymer self-loading (polymers with a large Young's modulus) will significantly reduce the amount of stress to be transferred to the PZT rod and result in a smaller γ .

In Eq. (2.9), as Y/μ approaches zero, $F(a, \xi)$ will approach the value of the equal-strain model and γ reaches its maximum value for a fixed $'s_{33}Y$. Hence, to improve the

stress transfer in a composite, a polymer with a large μ and a small Y will be advantageous.

(c) In the hydrophone application, a 1-3 composite is subjected to a hydrostatic pressure. The stress on the composite will modify the equilibrium equation (2.1) of the polymer phase to

$$\left(\frac{2u}{L}\right) = s_{33}T_3 + s_{31}T_1 + s_{32}T_2 + s_{33}\mu \frac{L}{4} \left[\frac{\partial^2 u}{\partial r^2} + \left(\frac{1}{r}\right) \frac{\partial u}{\partial r} \right]. \quad (2.10)$$

Making use of the relation $s_{31} = s_{32} = -\sigma s_{33}$, where σ is the Poisson's ratio of the polymer, $T_1 = T_2 = T_3 = T$ in the hydrostatic condition, and $Y = 1/s_{33}$, Eq. (2.10) can be rewritten as

$$Y\left(\frac{2u}{L}\right) = (1-2\sigma)T + \frac{\mu L}{4} \left[\frac{\partial^2 u}{\partial r^2} + \left(\frac{1}{r}\right) \frac{\partial u}{\partial r} \right]. \quad (2.11)$$

The solution to this equation is

$$\left(\frac{2u}{L}\right) = (1-2\sigma) \frac{T}{Y} + \left[\left(\frac{2u}{L}\right)_0 - (1-2\sigma) \frac{T}{Y} \right] \frac{K_0(r/\xi)}{K_0(a/\xi)}. \quad (2.12)$$

The meaning of each quantity in Eq. (2.12) is the same as that in Eq. (2.7). Comparison between Eqs. (2.7) and (2.12) yields that the effect of hydrostatic pressure on a composite is to reduce the effective pressure on the polymer phase from T to $(1-2\sigma)T$. In the case of $\sigma=0.5$, this effective pressure becomes zero, a situation where the polymer becomes incompressible. On the other hand, Eq. (2.12) shows that the strain profile in the polymer phase is still described by the elastic constant ratio $2Y/\mu$, which is the same as that in the uniaxial stress situation. Hence, it is more appropriate to describe the reduction of the polymer strain level in the hydrostatic case as related to the reduction of the effective stress on its surface, rather than the change in the elastic constants of the material.

To find the total stress T_{total} exerted on the PZT rod, one has to calculate the strain of the PZT rod $(2u/L)_0$ in the composite under the hydrostatic pressure T . Using the reciprocal relation that the total force of the polymer phase on the PZT rod is equal in magnitude and opposite in sign to the total force of the PZT rod on the polymer phase, one can find T_{total} ,

T_{total}

$$= T \frac{1 + (1-2\sigma)F(a, \xi) - Y[s_h + (1-2\sigma)s_{33}F(a, \xi)]}{1 + s_{33}YF(a, \xi)} \times F(a, \xi), \quad (2.13)$$

where $s_h = s_{33} + 2s_{31}$ is the hydrostatic elastic compliance of the PZT rod, and a is the PZT rod radius. Hence, in the dilute limit, the hydrostatic piezoelectric constant d_h in the composite is related to the piezoelectric constant d_{ij} of the PZT rod by the equation

TABLE II. Hydrostatic piezoelectric charge constant for 1-3 composites with a 5% PZT volume content. In the calculation $s_{33}=590 \text{ pC/N}$ and $s_{31}=45 \text{ pC/N}$ are used.

s_{33}	$a=0.3 \text{ mm}$		$a=0.5 \text{ mm}$	
	0.02	0.1	0.02	0.1
ξ		$d_h \text{ (pC/N)}$		
1.0	106	55	60	39
0.5	51	34	24	19

$$d_h = \left[c_{d_{33}} \left(1 + (1-2\sigma)F(a, \xi) \right) - \frac{Y[s_h + (1-2\sigma)s_{33}F(a, \xi)]F(a, \xi)}{1 + s_{33}YF(a, \xi)} \right] v_0, \quad (2.14)$$

where v_0 is the volume fraction of PZT rods in the composite and $c_{d_{33}}$ and $c_{d_{31}}$ are the piezoelectric constants of PZT ceramics. Equation (2.14) is derived under the condition that the ceramic content in the composite is very low (dilute limit). Introducing Δ as the distance at which the polymer strain changes from $(2u/L)_0$ to $0.1(2u/L)_0$, we may define the criterion for the dilute limit in a 1-3 composite, that the distance between the two neighboring rods should be equal to or greater than $(2a + \Delta)$. For example, if the PZT rod radius is 0.25 mm, the dilute limit corresponds to about 5% or less PZT in a composite. Table II lists the d_h value calculated using Eq. (2.14) for composites with a 5% PZT rod of radius 0.3 mm and 0.5 mm. In the calculation, $\sigma=\frac{1}{3}$ is assumed for the polymer and $s_{31} = -\frac{1}{3}s_{33}$ is used for the PZT rod. The data indicate how d_h varies with PZT rod aspect ratio when the volume content of PZT is kept constant, and the effect of the polymer self-loading. The results are consistent with the existing experimental data.^{8,12,13}

IV. 1-3 COMPOSITE BEYOND THE DILUTE LIMIT

When the volume content of PZT rods in a composite becomes higher, as in most practical cases, the dilute approximation is not adequate in calculating the stress transfer properties between the PZT rods and polymer matrix. For a 1-3 composite as schematically drawn in Fig. 1, to solve the exact solution for the strain profile in the composite under either an electric field or a stress field can be quite involved, albeit it is not impossible. To avoid this complication and as a first-order approximation, we assume the solution for a 1-3 composite is a linear superposition of the solution in the dilute limit. Normally, the radius of the PZT rod used in 1-3 composites ranges from 0.1 to 0.5 mm, and as has been shown in the preceding section, for thin PZT rods, the strain decays rapidly as the polymer phase moves away from the PZT rod. Hence, if the volume percentage of PZT in the composite is not very high (<20%), one only needs to consider the effect of the nearest neighbor PZT rods in calculating the strain profile

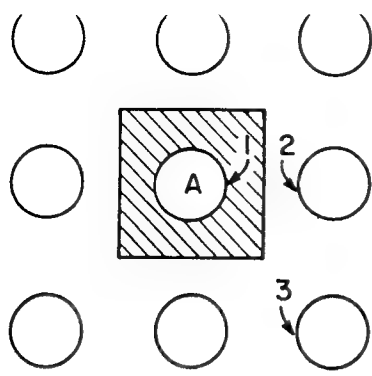


FIG. 8. Top view of a 1-3 composite. The area enclosed by the square is the unit cell and the circles are PZT rods. To calculate the polymer strain in the hatched area, only the nine PZT rods shown in the figure need to be considered if the ceramic content is less than 20%.

of the polymer phase in the hatched area of Fig. 8. Based on this consideration, the strain profile in the polymer phase of the unit cell can be approximated as

$$\left(\frac{2u}{L}\right) = A_0 \sum_{n=1}^9 K_0\left(\frac{|\mathbf{r} - \mathbf{r}_n|}{\xi}\right), \quad (3.1)$$

where the summation is over the nine PZT rods shown in Fig. 8 and \mathbf{r}_i is the center position of the i th rod. A_0 is the normalization factor, which will be determined from the boundary conditions that the strain at the polymer-PZT rod interface is equal to that of the PZT rod and all the PZT rods have the same strain level. It is clear that Eq. (3.1) cannot meet these conditions and A_0 determined from different boundary points will be different. However, it can be shown that even for a composite containing 20% PZT, the variation of A_0 calculated from different boundary points is less than 10%. Within this error, Eq. (3.1) can be used to describe the strain profile of the polymer phase in the unit cell containing the PZT rod A . To account for the variation of A_0 at a different boundary point, A_0 is calculated at points 1, 2, and 3 of the PZT-polymer boundary. This gives three different A_0 and the final value of A_0 is the averaged one over these three values,

$$A_0 = \left(\frac{1}{3}\right) \left(\frac{2u}{L}\right) \left(\frac{1}{L_1} + \frac{1}{L_2} + \frac{1}{L_3}\right), \quad (3.2)$$

where $(2u/L)_0$ is the strain of the PZT rod and $L_i = \sum_{n=1}^9 K_0(|\mathbf{a}_i - \mathbf{r}_n|/\xi)$, \mathbf{a}_i is the coordinate vector of the point labeled i in Fig. 8. From the results in Sec. III, d_{33} and d_h for the composite are, respectively,

$$d_{33} = v_0 [1 + A(a, \xi)] / [(1 + s_{33} Y) A(a, \xi)]^c d_{33}, \quad (3.3)$$

$$d_h = \left[c d_{33} \left(1 + (1 - 2\sigma) A(a, \xi) \right. \right. \\ \left. \left. - \frac{Y[s_h + (1 - 2\sigma) s_{33} A(a, \xi)] A(a, \xi)}{1 + s_{33} Y A(a, \xi)} \right) + 2 c d_{31} \right] v_0, \quad (3.4)$$

the meaning of each quantity is the same as that in Eq. (2.14), except $A(a, \xi)$, which is defined as

$$A(a, \xi) = \frac{A_0}{\pi a^2} \sum_{n=1}^9 \int K_0(|\mathbf{r}_n - \mathbf{r}|) dx dy, \quad (3.5)$$

where the integration is over the hatched area in Fig. 8. By assuming the strain in the polymer phase a constant, the above equations can be reduced to that derived earlier using the equal-strain approximation.¹⁴

Here d_h is calculated for 1-3 composites made of PZT-5A and spurs epoxy using Eq. (3.4). The parameters used in the calculation are obtained from the available literature.¹⁵ For a 1-3 composite with 10% PZT volume content and the rod radius $a = 0.3$ mm, the d_h values calculated are 55, 35, and 20 pC/N, respectively, for a sample thickness of $L = 4, 2$, and 1 mm. These numbers are comparable with the experimental values: 61, 32, 17 pC/N measured by Klicker for composites with the corresponding material parameters.⁸ For the composites with a higher volume fraction of PZT, the agreement between the theory and experiment becomes less satisfactory. This is what is expected from the assumption of this model.

V. CONCLUSIONS

In this paper, using the force equilibrium condition an elastic model is introduced to describe the deformation of 1-3 type composites under different driving conditions. Based on this, the effects of PZT rod aspect ratio, polymer shear and Young's moduli, as well as the spacing between PZT rods on the elastic coupling between the two components and the performance of composites are analyzed quantitatively. The theoretical results are in good agreement with experimental observations. Furthermore, using a double beam ultradilatometer, the strain profiles of several composites with simple structures were measured and the results can be described quite well by the theoretical predicted profiles. It is also shown that the strain profile measured in this manner can be used to describe the deformation of composites under a uniaxial or hydrostatic pressure.

ACKNOWLEDGMENT

We wish to thank Dr. Wally Smith for the stimulating discussions.

¹R. E. Newnham, D. P. Skinner, and L. E. Cross, *Mat. Res. Bull.* **13**, 525 (1978).

²R. E. Newnham, L. J. Bowen, K. A. Klicker, and L. E. Cross, *Mat. Eng.* **2**, 93 (1980).

³T. R. Gururaja, A. Safari, R. E. Newnham, and L. E. Cross, in *Electronic Ceramics*, edited by L. M. Levinson (Marcel Dekker, New York, 1987), Vol. 92.

⁴W. A. Smith and B. A. Auld, *IEEE Trans. Ultrason. Ferroelectrics., Freq. Controls* **38**, 40 (1991).

⁵W. A. Smith and A. A. Shaulov, *Ferroelectrics* **87**, 309 (1988).

⁶G. Hayward and J. A. Hossack, *J. Acoust. Soc. Am.* **88**, 599 (1990).

⁷B. A. Auld, H. A. Kunkel, Y. A. Shui, and Y. Wang, *Proc. 1983 IEEE Ultrason. Symp.* 554 (1983).

⁸K. A. Klicker, Ph.D. thesis, The Pennsylvania State University, 1980.

⁹W. A. Smith, *Proc. 1990 IEEE Ultrason. Symp.* 145 (1990).

¹⁰Q. M. Zhang, S. J. Jang, and L. E. Cross, *J. Appl. Phys.* **65**, 2808 (1989).

¹¹W. Cao, Q. M. Zhang, and L. E. Cross, *IEEE Trans. Ultrason. Ferroelectrics., Freq. Controls* (in press).

¹²T. R. Gururaja, Ph.D. thesis, The Pennsylvania State University, 1984.

¹³The d_3 values measured on the samples provided by FMI, Maine.

¹⁴M. J. Haun and R. E. Newnham, *Ferroelectrics* **68**, 123 (1986).

¹⁵In the calculation, $\sigma = \frac{1}{3}$ for the polymer phase and $s_{12} = \frac{1}{3} s_{11}$ for PZT rods are assumed; other parameters used in the calculation are from the data sheet of Morgan Matroc. Inc. and Refs. 8 and 12.

APPENDIX 35

Piezoelectric tubes and 1-3 type tubular composites as tunable actuators and sensors

Q. M. Zhang, H. Wang, and L. E. Cross

Materials Research Laboratory, The Pennsylvania State University
University Park, PA 16802

ABSTRACT

The piezoelectric actuators and sensors made of tubular structure can provide a great agility of the effective response in the radial direction. For a radially poled piezoelectric tube, the effective piezoelectric constant in that direction can be tuned to be positive, zero, and negative by varying the ratio of the outer radius (R_0) to the inner radius (r_0) of the tube. For a suitable ratio of R_0/r_0 , this effective constant can also be changed in sign or set to zero by adjusting the DC bias field level for tubes made of electrostrictive materials. Therefore, one can make a piezoelectric transducer with all the effective piezoelectric tensile constants having the same sign. The end capped thin wall tubes also exhibit exceptionally high hydrostatic response and the small size of the tubular structure makes it very suitable for integration into 1-3 composite which possesses low acoustic impedance and high hydrostatic response.

1. INTRODUCTION

The recent advance in the adaptive materials and structures has put increasing demands on new materials and material structures to broaden the range of material properties provided by the conventional materials.^{1,2} By integration of several materials into a composite or by structure modification, one can greatly improve the performance of devices. In this paper, we will examine the effective piezoelectric properties of a tubular structure and its composites formed from arrays of such tube for both actuating and sensing applications. We will show that for a radially poled ceramic tube, the competition between the piezoelectric d_{33} effect and d_{31} effect in the radial direction provides a convenient way to adjust the effective piezoelectric properties in that direction by changes in the tube radii. The small thickness of a thin wall tube also makes it practical to use field biased electrostrictive materials for actuators and sensors since only a low terminal DC voltage is required to produce substantial piezoelectric activities in the materials in this geometry and by adjusting the DC bias field level, the effective piezoelectric constant in the radial direction can be tuned from positive to zero, and to negative.

2. PIEZOELECTRIC RESPONSE OF A TUBE UNDER AN ELECTRIC FIELD

When a radially poled tube is subjected to an electric field along the radial direction, on the average, the strain in the axial direction equals $d_{31} E_m$, where d_{31} is the linear piezoelectric constant and E_m is the average field in the material. The dimensional change in the radial direction, however, is complicated. In this section, the solution of the elastic equation for the tubular structure under an electric field will be presented. It will be shown that with the same applied electric field, the outer diameter (OD) of the tube can either expand or contracts depending on the ratio of the OD to ID of the tube. This phenomenon is the direct consequence of the competition between the piezoelectric d_{33} and d_{31} effects which have opposite sign in producing the change in the tube OD under electric field.

For a tubular structure, it is convenient to use the cylindrical polar coordinate system, as shown in figure 1, in the analysis of the strain response of the sample under an electric field. The symmetry of

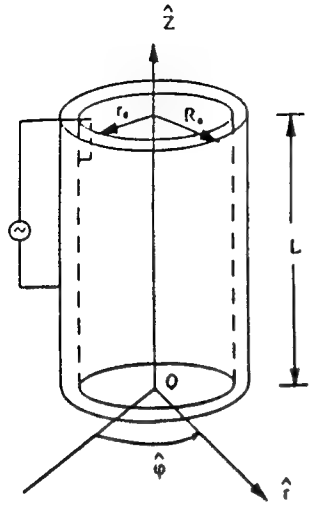


Figure 1: Schematic drawing of a radially poled ceramic tube with the outer radius R_0 and inner radius r_0 .

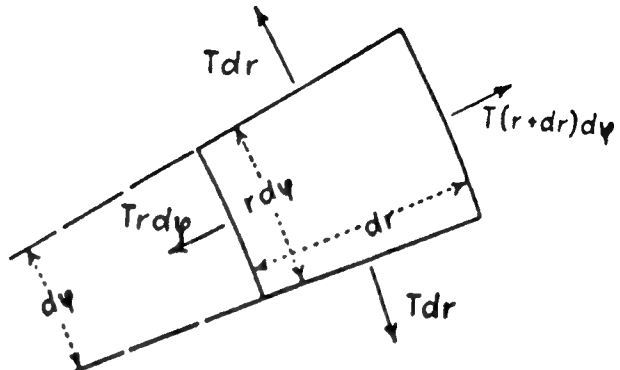


Figure 2: Forces on a segment of a tube in the plane perpendicular to the tube axis(z).

the problem requires that the ϕ -component of the displacement field $u_\phi=0$. For a thin wall tube, one can neglect the coupling terms containing both r and z in the displacement field \vec{u} and assume $\vec{u}=u_r(r)\hat{r}+u_z(z)\hat{z}$. Under this approximation, the non-zero strain component are:

$$u_{rr} = \frac{\partial u_r}{\partial r}, \quad u_{\phi\phi} = \frac{u_r}{r}, \quad \text{and} \quad u_{zz} = \frac{\partial u_z}{\partial z}.$$

The constitutive relations for the tube, therefore, are

$$\begin{aligned} T_z &= c_{11} u_{zz} + c_{12} u_{\phi\phi} + c_{12} u_{rr} - e_{31} E \\ T_r &= c_{11} u_{rr} + c_{12} u_{\phi\phi} + c_{12} u_{zz} - e_{33} E \\ T_\phi &= c_{12} u_{zz} + c_{11} u_{\phi\phi} + c_{12} u_{rr} - e_{31} E \end{aligned} \quad (1)$$

where T_z , T_r , and T_ϕ are the stress components in the three directions, c_{ij} is the elastic stiffness constant, e_{ij} is the piezoelectric stress constant, and E is the applied electric field on the tube wall along the r -direction. It is well known that the electric field is not a constant inside the tube wall and with a total

voltage V applied on the tube, $E = \frac{V}{r \ln(R_0/r_0)}$ ($r_0 \leq r \leq R_0$). In writing down equation (1), we also

made the approximation that the tube is isotropic elastically to simplify the analysis. The nonisotropic case will be addressed in the next section when we discuss the hydrostatic response of the end capped tubes. Both the experimental results which will be presented later in this section and the analysis in the next section show that the errors due to the isotropic approximation are not significant.

For a tube segment shown in figure 2, from the force balance consideration under the static condition, one can arrive at

$$\frac{\partial T_r}{\partial r} + \frac{T_r - T_\phi}{r} = 0 \quad (2)$$

Making use of the constitutive equation (eq. (1)), the basic elastic equations for this problem are

$$\frac{\partial}{\partial r} \left(\frac{1}{r} \frac{\partial}{\partial r} r u_r \right) = - \frac{e_{31} E}{r} \frac{s_{11}(1+\sigma)(1-2\sigma)}{1-\sigma} \quad (3)$$

$$\frac{\partial u_z}{\partial z} = \text{constant}$$

where σ is the Poisson's ratio and s_{11} is the elastic compliance. The solutions to eq. (3) are

$$u_r = ar + \frac{b}{r} + \frac{e_{31} V}{\ln p} \frac{s_{11}(1+\sigma)(1-2\sigma)}{1-\sigma} \quad (4)$$

and

$$u_z = c z$$

where $p=R_0/r_0$. a , b and c are the integration constants and can be determined from the boundary

conditions: $u_{zz}=d_{31}E_m$, where E_m is the average electric field in the tube ($E_m = \frac{2V}{(R_0+r_0) \ln(R_0/r_0)}$), and

at $r=R_0$ and r_0 , there is no external stress on the tube wall which implies $T_r=0$ at these two boundaries. Substituting eq. (4) into eq. (1) and using the boundary conditions, one can get

$$\begin{aligned} a &= E_m ((1-2\sigma) d_{33} - \sigma d_{31}) / (2(1-\sigma)) \\ b &= -R_0 r_0 E_m (d_{33} + \sigma d_{31}) / (2(1-\sigma)) \\ c &= d_{31} E_m \end{aligned} \quad (5)$$

In deriving eq. (5), we have used relation $e_{31}=c_{11}d_{31}+c_{12}(d_{31}+d_{33})$. All the strain components for the tube can be obtained from eqs. (4) and (5). Here we are more interested in finding out how the tube outer diameter changes with applied electric field as the ratio of R_0/r_0 varies since in most of the applications, this is the quantity of interests. Substituting a and b in equation (4) into the expression for u_r and setting $r=R_0$ yield the displacement of the tube outer wall $u_r(R_0)$

$$u_r(R_0) = E_m ((R_0+r_0) d_{31} + (R_0-r_0) d_{33}) / 2$$

This equation reveals that $u_r(R_0)$ can be changed from positive to zero, and to negative by varying the ratio of R_0/r_0 .

To illustrate the advantage of using thin wall tube for actuator applications, one can compare the piezoelectric response of a tube discussed here with a rod of radius R_0 and length L subjected to the same applied voltage V . For the rod, the field is applied along the axial direction and $u_{zz}=d_{33} V/L$ and $u_{rr}=d_{31} V/L$. For the tube sample, one can equivalently introduce the quantity u_r/R_0 as the effective strain in the radial direction

$$u_r(R_0)/R_0 = E_m ((1+r_0/R_0) d_{31} + (1-r_0/R_0) d_{33}) / 2 \quad (6)$$

Similar to a rod sample, we introduce the effective piezoelectric constants for the tube as if it were a rod poled axially,

$$u_{zz} = d_{33}^{\text{eff}} V/L \quad \text{and} \quad \frac{u_r}{R_0} = d_{31}^{\text{eff}} V/L \quad (7)$$

where L is the axial length of the tube and V is the voltage applied on the tube wall. From $u_{zz} = d_{31} E_m$ and equation (6), the effective piezoelectric constants can be deduced

$$d_{33}^{\text{eff}} = d_{31} \frac{2L}{(R_0+r_0)\ln(R_0/r_0)} \quad (8)$$

$$d_{31}^{\text{eff}} = \frac{L}{(R_0+r_0)\ln(R_0/r_0)} \left[\left(1 + \frac{r_0}{R_0}\right) d_{31} + \left(1 - \frac{r_0}{R_0}\right) d_{33} \right]$$

For thin wall tubes with L much larger than R_0 , which is the case in most of the applications, both d_{33}^{eff} and d_{31}^{eff} can be exceptionally large. This demonstrates that the tubular structure has great advantage over the regular ceramic rod for actuator application. Besides that, by choosing $(1+r_0/R_0) |d_{31}| > (1-r_0/R_0) |d_{33}|$, the effective d_{33} and d_{31} of the tube will have the same sign. By adjusting the ratio R_0/r_0 , one can also continuously vary d_{31}^{eff} of the tube from positive to zero and to negative.

To compare with the theoretical prediction, the displacement field $u_r(R_0)$ and u_{zz} of a radially poled PZT-5 tube were measured using a double beam laser dilatometer.³ The ceramic tubes used were manufactured by Morgan Matroc, Inc., Vernitron Div. with $R_0=0.635$ mm and $r_0=0.381$ mm. From the data acquired and using eqs (4), (5) and (6), we get $d_{33}=289$ pC/N and $d_{31}=-141.3$ pC/N for the tube material. For most of commercially available PZT materials, the ratio of d_{33}/d_{31} ranges from 2.15 to 2.3.⁴ The measured ratio here ($d_{33}/d_{31}=2.05$) is slightly below that range which we believe is the result of the approximations used in the derivation. The effective piezoelectric constants defined in eq. (7) for the tube, therefore, are $d_{33}^{\text{eff}}=-8180$ pC/N and $d_{31}^{\text{eff}}=-3220.5$ pC/N, the two coefficients have the same sign as predicted by eq. (8) and they are exceptionally large.

The small thickness of the tube wall also makes it possible to use electric field biased electrostrictive materials for the actuator application since only a small bias voltage is required here to induce substantial piezoelectric responses in the materials. Shown in figure 3 is the DC field induced piezoelectric constants of lead magnesium niobate (PMN)-lead titanate (PT) with a composition of 0.9PMN-0.1PT (the data is taken from ref. 5). Clearly, the ratio of the piezoelectric constants d_{33}/d_{31} for this material is bias field dependent. At the bias field level 1 kV/cm, $d_{33}=400$ pC/cm and $d_{31}=-200$ pC/cm, while at the bias field 3 kV/cm, $d_{33}=1000$ pC/cm and $d_{31}=-400$ pC/cm. In figures 4(a) and 4(b), we show how d_{33}^{eff} and d_{31}^{eff} of a tube made of this material will vary as the ratio of r_0/R_0 changes for these two cases. It can be seen that the cross-over points where d_{31}^{eff} changes sign are different for the two cases. Hence, for a suitable ratio of r_0/R_0 , by tuning the DC bias field level, both sign and magnitude of d_{31}^{eff} of the tube can be varied. In figure 5, the dependence of $-d_{31}^{\text{eff}}/d_{31}$ on the ratio of d_{31}/d_{33} is shown explicitly for a tube with $r_0/R_0=0.4$.

3. THE HYDROSTATIC RESPONSE OF END CAPPED TUBES AND 1-3 TYPE TUBULAR COMPOSITES

The availability of small size ceramic tubes makes it attractive to integrate them into 1-3 type piezoceramic-polymer composites for large area applications and to provide more flexibility for further material property modification. Before the discussion on the composite properties, we will briefly derive the expression for the hydrostatic response of end capped tubes first since this is the most commonly used mode of piezo-tubes as hydrostatic sensor.⁶

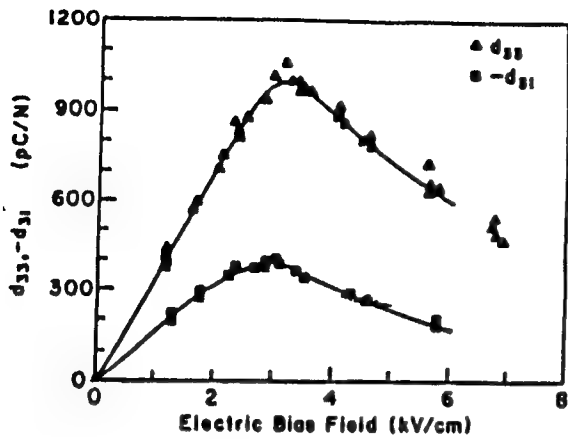


Figure 3: DC bias field induced piezoelectric constants of 0.9 PMN-0.1 PT at room temperature

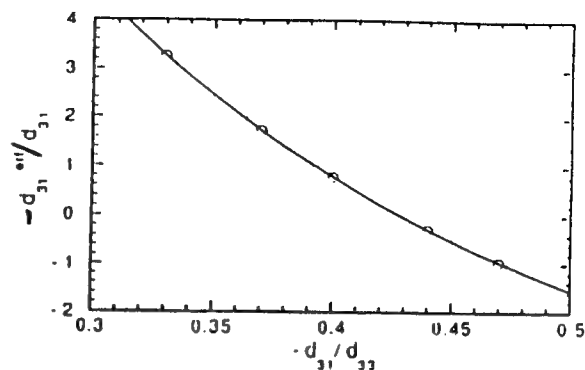


Figure 5: Dependence of d_{31}^{eff} on the ratio d_{31}/d_{33} for a tube with $r_o/R_o = 0.4$.

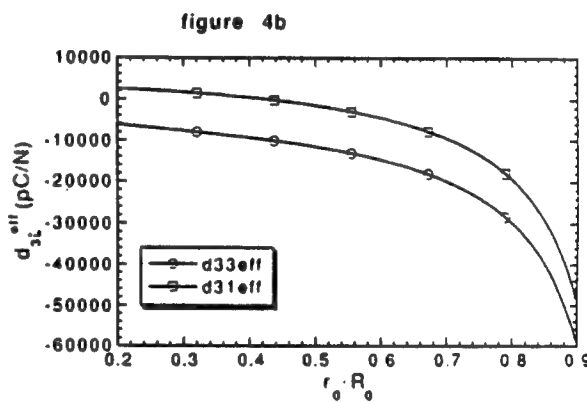
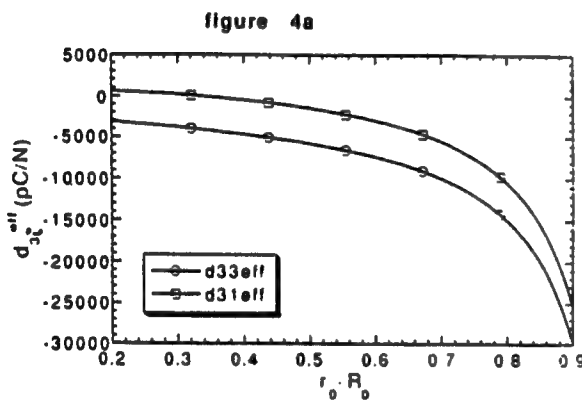


Figure 4: (a) Dependence of d_{31}^{eff} on r_o/R_o for tubes with $d_{33} = 400$, $d_{31} = -200$ and $L/R_o = 15$; (b) with $d_{33} = 1000$, $d_{31} = -400$, $L/R_o = 0.4$.

Similar to the derivations presented in the preceding section, the displacement field of a tube under hydrostatic pressure, when expressed in the cylindrical coordinate system, is $u_\phi = 0$ and $\vec{u} = u_r(r)\hat{r} + u_z(z)\hat{z}$. (for an isotropic material, this is the exact form of the displacement field and for a poled ceramic tube, the error in using this form of the displacement field, as will be shown later, is less than 10%.) Since all the external forces are applied on the surfaces of the tube, there is no internal body force in the tube wall, eq (3) becomes:

$$\frac{\partial r u_r}{r \partial r} = \text{const.} \quad \text{and} \quad \frac{\partial u_z}{\partial z} = \text{const.} \quad (9)$$

The solutions to the equations are:

$$u_r = a r + b/r \quad \text{and} \quad u_z = c z \quad (10)$$

The non-zero strain components are:

$$u_{rr} = a - b/r^2, \quad u_{\phi\phi} = a + b/r^2, \quad \text{and} \quad u_{zz} = c \quad (11)$$

where a , b , and c are the integration constants. The boundary conditions which will be used to determine them are: since the two ends of the tube are sealed, there is no pressure inside the tube, at $r=r_0$, $T_r = 0$; at $r=R_0$, $T_r = -p$; and at $z=0$ and $z=1$, the stress in the axial direction is $T_z = -p R_0^2/(R_0^2 - r_0^2)$, where $-p$ is the applied hydrostatic pressure. For an anisotropic tube, the constitutive relations are:

$$\begin{aligned} T_z &= c_{11} u_{zz} + c_{12} u_{\phi\phi} + c_{13} u_{rr} \\ T_r &= c_{33} u_{rr} + c_{13} u_{\phi\phi} + c_{13} u_{zz} \\ T_\phi &= c_{12} u_{zz} + c_{11} u_{\phi\phi} + c_{13} u_{rr} \end{aligned} \quad (12)$$

where c_{ij} are the elastic stiffness coefficients of the poled ceramics. Substituting the strain components in eq. (11) into eq. (12) and omitting the term in T_z having r dependence, one can obtain a , b , c :

$$a = \frac{-p R_0^2}{R_0^2 - r_0^2} \left[\frac{c_{13} - c_{11}}{c_{13}(c_{12} + c_{13}) - c_{11}(c_{13} + c_{33})} \right] \quad (13a)$$

$$b = \frac{-r_0^2 R_0^2}{R_0^2 - r_0^2} \frac{p}{c_{33} - c_{13}} \quad (13b)$$

$$c = \frac{-p R_0^2}{R_0^2 - r_0^2} \left[\frac{c_{12} - c_{33}}{c_{13}(c_{12} + c_{13}) - c_{11}(c_{13} + c_{33})} \right] \quad (13c)$$

From eqs. (11), (12) and (13), the hydrostatic response of the tube can be calculated from the relation

$$D_3 = d_{31} T_z + d_{31} T_\phi + d_{33} T_r \quad (14)$$

where D_3 is the electric displacement in the poling direction. The value of d_h can be found by taking the average charge produced in the inner and outer surfaces of the tube wall and divided it by the outer surface area of the tube. This yields from eq. (14):

$$d_h = \frac{1}{2} \left\{ d_{33} + \frac{R_0}{R_0 - r_0} \left[1 + \left(\frac{c_{13}^2 + c_{12}^2 - c_{11}^2 - c_{12}c_{33}}{c_{13}(c_{13} + c_{12}) - c_{11}(c_{13} + c_{33})} \right) + \frac{c_{11} - c_{13}}{c_{33} - c_{13}} \frac{r_0}{R_0} \right] d_{31} \right\} \quad (15)$$

Using the elastic stiffness coefficients for PZT-5H,⁴ for a tube with $R_0=0.635$ mm and $r_0=0.381$ mm, eq. (15) predicts $d_h=-657$ pC/N or $2.4 d_{31}$. If the tube R_0 is doubled while keeping the wall thickness the same, the d_h value can reach -1786 pC/N. Hence, for thin wall tubes, an exceptionally large hydrostatic response can be achieved.

For an elastically isotropic tube d_h can be found by simplifying eq. (15) using the isotropic conditions $c_{11}=c_{33}$, $c_{12}=c_{13}$:

$$d_h = \frac{1}{2} \left\{ d_{33} + \frac{R_0}{R_0 - r_0} \left[2 + \frac{r_0}{R_0} \right] d_{31} \right\} \quad (16)$$

For the PZT-5H tube just calculated, the calculated d_h value is -594 pC/N ($2.17 d_{31}$) when eq. (16) is

Experimental measurements were performed on several PZT-5 tubes ($R_0=0.635$ mm and $r_0=0.381$ mm) with two ends sealed and radially poled (the dielectric constant ϵ for this group of sample is around 1700 at the atmospheric pressure). d_h was measured through the direct piezoelectric effect where the charge induced on the electrodes of a sample is measured when the sample is subjected to a hydrostatic pressure. d_{31} and d_{33} were measured using the double beam laser interferometer.³ For this group of samples, the d_h was in the range from -330 pC/N to -400 pC/N and d_{31} from -140 pC/N to -160 pC/N. The ratio between experimentally measured d_h and d_{31} (on average) is 2.45 which is very close to that predicted from eq. (15). Clearly, to make a quantitative prediction about the hydrostatic response of a tubular structure, one may be required to include the elastic anisotropy in the calculation.

In analogy to the situation discussed in the preceding section, one can also manipulate the piezoelectric response of a tube to the stress field in the radial direction by changing the ratio of r_0/R_0 for tubes made of piezoelectric materials or the DC bias field for tubes made of electrostrictive materials. Here, we will use the result just derived for the hydrostatic response of a tube as an example. In eq. (14), the hydrostatic response of a tube comes from three terms, one is from the pressure in the axial direction and the other two from the pressure in the radial direction. The electric displacement D_3^r due to the pressure in the radial direction is

$$D_3^r = d_{31}T_\phi + d_{33}T_r$$

Hence, the partial piezoelectric response d^r of the tube to the pressure in the radial direction is

$$d^r = \frac{1}{2} \left\{ d_{33} + \frac{R_0}{R_0 - r_0} \left[\left(\frac{c_{13}^2 + c_{12}^2 - c_{11}^2 - c_{12}c_{33}}{c_{13}(c_{13} + c_{12}) - c_{11}(c_{13} + c_{33})} \right) + \frac{c_{11} - c_{13}}{c_{33} - c_{13}} \frac{r_0}{R_0} \right] d_{31} \right\} \quad (17)$$

Obviously, the opposite sign of d_{33} and d_{31} provides a convenient way to change d^r in eq. (17). One can easily verify that by varying the ratio of R_0/r_0 , d^r changes continuously from positive to zero, and to negative. Similar to the actuator case, for suitable ratio of r_0/R_0 , one can also change the sign of the effective radial response here by using electrostrictive materials with different DC bias field level. Furthermore, for a tube made of electrostrictive material, its piezoelectric response can be turned off by setting the DC bias field zero. This result as well as the result in the preceding section indicate that the range of the effective piezoelectric properties of the materials can be considerably broadened by using the tubular structures.

To calculate the hydrostatic figure of merit for this tubular sensor, we notice that in practice, the quantity $d_h g_h$ is a measure of the product of the charge and voltage produced in a unit volume material. For a tubular material, its effective volume is $\pi R_0^2 L$, where L is the tube length when the end capped tube is regarded as a rod with its radius equal to R_0 . Hence, the effective figure of merit for the tube is

$$d_h g_h = \frac{1}{2\epsilon\epsilon_0} \ln\left(\frac{R_0}{r_0}\right) \left(d_{33} + d_{31} \left(\frac{R_0}{R_0 - r_0} \right) \left(2 + \frac{r_0}{R_0} \right) \right)^2 \quad (18)$$

Here, we have used d_h result for an isotropic tube (eq (16)). One can easily expand the result to elastically anisotropic materials. Clearly, for a thin wall tube a large figure of merit can be obtained.

We now discuss the properties of 1-3 tubular composites. A typical 1-3 tubular composite is schematically drawn in figure 6. For the composite discussed here, the tubes are radially poled and the composite is electrode on the two end faces. Hence, special arrangement is required to ensure a proper electric connections between the electrodes at the tube walls and the composite end faces. This kind of composite can be used for large area actuator and sensor applications, as well as smart materials where both sensor and actuator are integrated into one structure. Here, we only discuss the properties associated with the sensor applications.

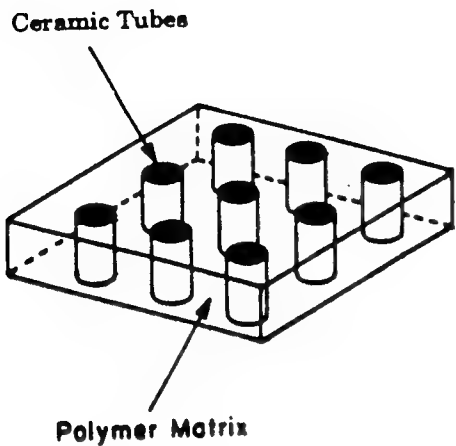


Figure 6: Schematic drawing of a 1-3 tubular composite.

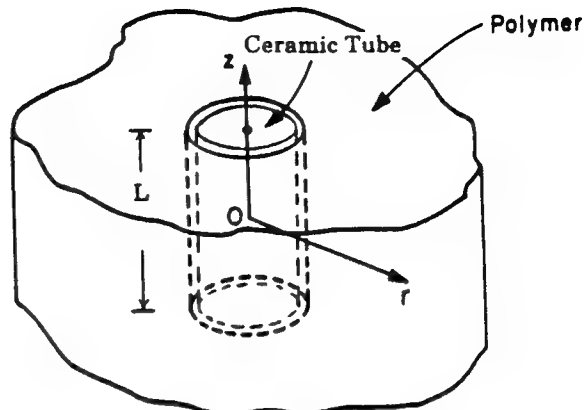


Figure 7: Schematic drawing of 1-3 tubular composite with only one tube embedded in an infinite extended polymer matrix.

When tubes are integrated into a 1-3 type ceramic-polymer composite, as has been demonstrated in our earlier publications, there is a stress transfer between the polymer matrix and the ceramic tubes in the z-direction.^{7,8} This stress transfer is the result of the difference in the elastic constants between the two constituent phases and is through the shear force in the two phases. Due to this stress transfer, the piezoelectric response of the tube in the axial direction is enhanced. To provide a physical picture of how the hydrostatic response of a tubular 1-3 composite changes as the elastic properties of the two constituent phases and their geometric parameters are varied, we will treat quantitatively the composite schematically drawn in figure 7. This composite corresponds to the tubular composite in the dilute limit. However, since only the polymer matrix close to the ceramic-polymer interface participates the stress transfer, the result can also be applied to the composite with finite ceramic content.

The procedure of calculating how much stress is transferred from the polymer phase to the ceramic rod is similar to that outlined in the earlier publications.^{7,8} Under hydrostatic pressure p , the surface displacement field u_z of the polymer phase in the z-direction should satisfy the following equation

$$\frac{2u_z}{L} = -(s_{11} + 2s_{12})p + \frac{s_{11}\mu L}{4} \left(\frac{\partial^2 u_z}{\partial r^2} + \frac{\partial u_z}{r \partial r} \right) \quad (19)$$

where p is the hydrostatic pressure, s_{ij} is the elastic compliance of the polymer phase, μ is the shear modulus of the polymer phase, and L is the thickness of the composite in the z-direction. The solution to eq. (19) is the zeroth-order Hankel function $K_0(\rho)$ and

$$\frac{2u_z}{L} = \frac{(1-2\sigma)p}{Y} + A K_0(r/\xi) \quad (20)$$

where A is an integration constant and $\xi = L/(2\sqrt{2Y/\mu})$, the strain decay length in the polymer phase. In eq. (20), we have made use of the relations $s_{12} = -\sigma s_{11}$ and $Y = 1/s_{11}$, where Y and σ are the Young's modulus and the Poisson's ratio of the polymer, respectively. The total force f transferred from the

polymer phase to the ceramic tube is, therefore

$$f = Y \int_{R_0}^{\infty} 2\pi r A K_0(r/\xi) dr$$

Two boundary conditions are needed to determine f . The first one is the condition that at the ceramic tube-polymer interface, the z -component of the strain in the two phases should be equal, and the second is the relation between the z -component of the strain in the ceramic tube and the stress field

$$u_{zz} = -\frac{pR_0^2(1-\sigma^c)s_{11}^c}{R_0^2 - r_0^2} + \frac{f s_{11}^c}{\pi(R_0^2 - r_0^2)} \quad (21)$$

where s_{11}^c and σ^c are the elastic compliance and the Poisson's ratio of the ceramic tube, respectively. Hence, the total stress in the axial direction of the tube is

$$T_z = -\frac{pR_0^2}{A_0} \left(1 + \frac{A_0(1-2\sigma)/(R_0^2 Y s_{11}^c) - (1-2\sigma)^c}{1 + K_0(p_0) A_0 (2K_1(p_0) Y s_{11}^c R_0 \xi)} \right) \\ = -\frac{pR_0^2}{A_0} \gamma \quad (22)$$

where γ is introduced as the stress amplification factor, $A_0 = (R_0^2 - r_0^2)$, $p_0 = R_0/\xi$, and $K_1(p)$ is the first order Hankel function. In figure 8, we plot γ as a function of the aspect ratio R_0/L for a 1-3 tubular composite made of PZT-5H tube with $R_0 = 0.635$ mm and $r_0 = 0.381$ mm and spurs epoxy.⁹ Apparently, for thin and long tubes, the stress amplification factor is large. This is similar to that obtained earlier for 1-3 composites made of ceramic rods.^{7,8}

Using the results from the single tube and equation (22), one can write down the effective hydrostatic piezoelectric strain coefficient for 1-3 tubular composites

$$d_h^{\text{eff}} = \frac{L}{R_0} v_c (d_{33} + \frac{R_0}{R_0 - r_0} (1 + \gamma + \frac{r_0}{R_0}) d_{31}) \quad (23)$$

where v_c is the volume content of the ceramic tubes in the composite which is defined as $v_c = \pi R_0^2/a$, and a is the unit cell area of the composite. For a composite in the low ceramic volume content, γ in eq. (22) is equal to that in eq. (23). With increased volume content, the dependence γ on the material properties of the constituent phases will become more complicated and one may not be able to derive the analytical expression for γ except in some special cases. In this paper, we will not pursue this further and only point out that in the composite, there is always a stress transfer between the two phases ($\gamma > 1$), the general rule to increase this stress transfer is basically the same as that for the dilute composite case.

The effective hydrostatic figure of merit for 1-3 tubular composites is

$$d_h^{\text{eff}} g_h^{\text{eff}} = \frac{v_c}{2\epsilon\epsilon_0} \ln\left(\frac{R_0}{r_0}\right) \left\{ d_{33} + \frac{R_0}{R_0 - r_0} \left(1 + \frac{r_0}{R_0} + \gamma\right) d_{31} \right\}^2 \quad (24)$$

For the comparison, in table I, we present the experimental values of the hydrostatic response of an end capped ceramic tube, a 1-3 composite with tube inside air backing, and a 1-3 composite with tube inside epoxy backing. All 1-3 composites had the volume content of 23.3 % ceramic tube and the dimensions of the tubes are: $R_0 = 0.635$ mm, $r_0 = 0.381$ mm, and $L = 9$ mm. The polymer matrix was made of spurs epoxy. In the composite with epoxy backing, the tube inside was filled with spurs epoxy. d_{31} listed in

the table was calculated using the single tube result where the ratio $d_{33}/d_{31}=2.2$ was used. From this d_{31} , γ was calculated from eq. (24). Clearly, the γ value here is much smaller than that shown in figure 8 ($R_0/L=0.07$ here). One of the reasons for this is that figure 8 is for the composite in the dilute limit, the γ value for composites with finite ceramic content should be smaller than that in figure 8. The imperfect stress transfer between the two phases and the depoling effect of the tubes during the epoxy curing may also be responsible for this reduction of γ . Although the data in table I show that the hydrostatic responses of the composites tested are not as high as that of the single tube, the difference is not very large. As the volume content of the ceramic tube and other parameters in a composite are varied, the effective hydrostatic figure of merit for 1-3 tubular composites will change. In the optimum condition, one would expect that $d_h^{\text{eff}}g_h^{\text{eff}}$ for a tubular 1-3 composite may exceed that of a single tube. Apparently, further experimental and theoretical work is required to address this issue. Further more, the figure of merit of 1-3 tubular composites is much higher than that of 1-3 composites made of ceramic rods.⁸

4. SUMMARIES AND ACKNOWLEDGEMENT

In this paper, the effective piezoelectric responses of the tubular structure and its composites were evaluated both theoretically and experimentally. When used as actuators, the effective piezoelectric constant in the radial direction of a tube can be changed from positive to zero and to negative by adjusting the ratio of R_0/r_0 for piezoelectric materials or the DC bias field for electrostrictive materials. Therefore, the effective piezoelectric constants along the axial direction and the radial direction can both have the same sign. For the sensor applications, the two ends sealed tube exhibits exceptionally high hydrostatic response and analogues to the situation of actuators, the pressure response in the radial direction can be adjusted by the ratio of R_0/r_0 for piezoelectric materials or the DC bias field for the

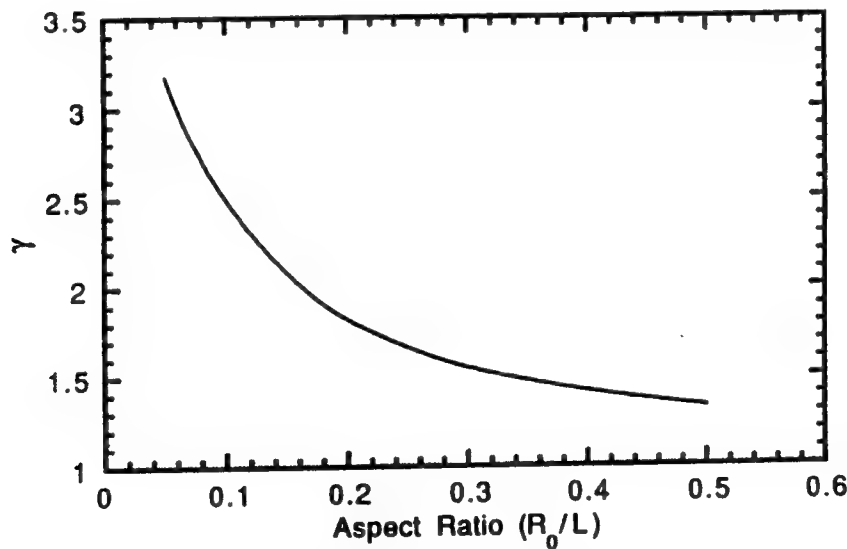


Figure 8: The stress amplification factor γ as a function of the aspect ratio R_0/L of the ceramic tube for the composite drawn in figure 7 with PZT-5H ceramic tube and spurs epoxy

electrostrictive materials. For large area applications, these tubes can be readily integrated into 1-3 composite structure which provides low acoustic density and high piezoelectric activity. The effectiveness of the stress transfer between the polymer phase and the ceramic tube in 1-3 composite makes it possible to back fill the inside of the ceramic tube which increases the mechanical integrity of the tubular structure while keeps the piezoelectric response of the composite almost intact.

This work was supported by the Office of Naval Research.

REFERENCES

1. R. E. Newnham and G. R. Ruschan, "Smart Electroceramics," *J. Am. Ceram. Soc.* **74**, 463 (1991).
2. R. E. Newnham, Q. C. Xu, S. Kumar, and L. E. Cross, "Smart Ceramic," *Ferro.* **102**, 259 (1990).
3. Q. M. Zhang, S. J. Jang, and L. E. Cross, "High-frequency strain response in ferroelectrics and its measurement using a modified Mach-Zehnder interferometer," *J. Appl. Phys.* **65**, 2807 (1989).
4. See the data sheet of Morgan Matroc, Inc., Vernitron Div.
5. D. J. Taylor, D. Damjanovic, A. S. Bhalla, and L. E. Cross, "Large Hydrostatic Piezoelectric Coefficient in Lead Magnesium Niobate: Lead Titanate Ceramic," Annual Report of the Materials Research Laboratory, The Pennsylvania State University (1991).
6. R. A. Langevin, "The Electro-Acoustic Sensitivity of Cylindrical Ceramic Tubes," *J. Acoust. Soc. Am.* **26**, 421 (1954); "Handbook of Hydrophone Element Design Technoledgy", NUSC Technical Document 5813 (1978).
7. Q. M. Zhang, Wenwu Cao, H. Wang, and L. E. Cross, "Characterization of the performance of 1-3 type piezocomposites for low frequency applications," *J. Appl. Phys.* (Feb. 1993).
8. Wenwu Cao, Q. M. Zhang, and L. E. Cross, "Theoretical study on the static performance of piezoelectric ceramic-polymer composites with 1-3 connectivity," *J. Appl. Phys.* **72**, 5814 (1992).
9. The data used are: $Y=3.1 (10^9 \text{ N/m}^2)$, $\mu=1.148 (10^9 \text{ N/m}^2)$, and $\sigma=0.35$ for spurs epoxy (from C. G. Oakley, Ph. D. Thesis, The Pennsylvania State University, 1991); $s_{11}^c=1.64 (10^{-11} \text{ m}^2/\text{N})$, and $\sigma=0.31$ (ref. 4).

Table I Hydrostatic properties of the end capped tube and 1-3 tubular composites

	ϵ	$d_h^{\text{eff}} (\text{pC/N})$	$d_b^{\text{eff}} g_h^{\text{eff}} (10^{-15} \text{ m}^2/\text{N})$	$d_{31} (\text{pC/N})$	γ
End capped tube	2,945	-14,330	10,000	-235	1
Composite (air backing)	2,922	-5,502	6,389	-235	2.11
Composite (epoxy backing)	2,944	-4,970	5,172	-235	

APPENDIX 36

Piezoelectric tubes and tubular composites for actuator and sensor applications

Q. M. ZHANG, H. WANG, L. E. CROSS

Materials Research Laboratory, The Pennsylvania State University, University Park, PA 16802, USA

Piezoelectric actuators and sensors made with a tubular structure can provide a great agility of effective response in the radial direction. For a radially poled piezoelectric tube, the effective piezoelectric constant in that direction can be tuned to be positive, zero or negative by varying the ratio of the outer radius (R_0) to the inner radius (r_0) of the tube. For a suitable ratio of R_0/r_0 , this effective constant can also be changed in sign or set to zero by adjusting the d.c. bias field level for tubes made of electrostrictive materials. Therefore, one can make a piezoelectric transducer with all the effective piezoelectric tensile constants having the same sign. End-capped thin-walled tubes also exhibit an exceptionally high hydrostatic response, and the small size of the tubular structure makes it very suitable for integration into a 1-3 composite which possesses low acoustic impedance and high hydrostatic response.

1. Introduction

The recent advance in adaptive materials and structures has put increasing demands on new materials and material structures to broaden the range of material properties provided by conventional materials [1, 2]. The novel concept of piezocomposites is one such example which combines two or more materials with complementary properties to expand the effective properties of the composite beyond those of each individual component [3, 4]. With the existing materials, by structure modifications, one can also greatly improve the performance of devices. In this paper, we will examine the effective piezoelectric properties of a tubular structure and its composites formed from arrays of such tubes for both actuating and sensing applications. For a radially poled ceramic tube, the competition between the piezoelectric d_{33} effect and d_{31} effect in the radial direction provides a convenient way to adjust the effective piezoelectric properties in that direction by changes in the tube radii. The small thickness of a thin-walled tube also makes it practical to use field-biased electrostrictive materials for actuators and sensors, since only a low terminal d.c. voltage is required to produce substantial piezoelectric activities in materials with this geometry.

2. Piezoelectric response of a tube under an electric field

When a radially poled tube is subjected to an electric field along the radial direction, on the average, the strain in the axial direction equals $d_{31}E_m$, where d_{31} is the linear piezoelectric constant and E_m is the average field in the material. The dimensional change in the radial direction, however, is complicated. In this section, the solution of the elastic equation for the tubular structure under an electric field will be presented. It

will be shown that with the same applied electric field, the outer diameter (o.d.) (or the inner diameter (i.d.)) of the tube can either expand or contract depending on the ratio of the o.d. to i.d. of the tube. This phenomenon is a direct consequence of competition between the piezoelectric d_{33} and d_{31} effects, which have opposite sign in producing the change in the tube o.d. under an electric field.

For a tubular structure, it is convenient to use the cylindrical polar coordinate system, as shown in Fig. 1, in the analysis of the strain response of the sample under an electric field. The symmetry of the problem requires that the ϕ component of the displacement field $u_\phi = 0$. For a thin-walled tube one can neglect the coupling terms containing both r and z in the displacement field u and assume $u = u_r(r)^\hat{r} + u_z(z)^\hat{z}$. Under this approximation, the non-zero strain components are

$$u_{rr} = \frac{\partial u_r}{\partial r} \quad u_{\phi\phi} = \frac{u_r}{r} \quad u_{zz} = \frac{\partial u_z}{\partial z}$$

The constitutive relations for the tube, therefore, are

$$\begin{aligned} T_z &= c_{11}u_{zz} + c_{12}u_{\phi\phi} + c_{12}u_{rr} - e_{31}E \\ T_r &= c_{11}u_{rr} + c_{12}u_{\phi\phi} + c_{12}u_{zz} - e_{33}E \\ T_\phi &= c_{12}u_{zz} + c_{11}u_{\phi\phi} + c_{12}u_{rr} - e_{31}E \end{aligned} \quad (1)$$

where T_z , T_r and T_ϕ are the stress components in the three directions, c_{ij} is the elastic stiffness constant, e_{ij} is the piezoelectric stress constant, and E is the applied electric field on the tube wall along the r direction. It is well known that the electric field is not a constant inside the tube wall and with a total voltage V applied on the tube, $E = V/r \ln(R_0/r_0)$ ($r_0 \leq r \leq R_0$). In writing down Equation 1, we also made the approximation that the tube is isotropic elastically to simplify the analysis. The non-isotropic case will be addressed in

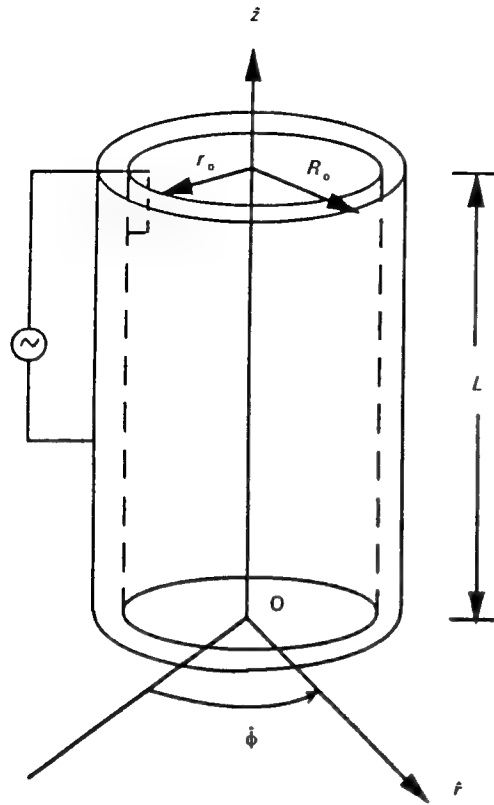


Figure 1 Schematic drawing of a radially poled ceramic tube with outer radius R_0 , inner radius r_0 and total length L . The electric field is applied on the tube wall along the radial direction.

the next section when we discuss the hydrostatic response of end-capped tubes. Both the experimental results which will be presented later in this section and the analysis in the next section show that the errors due to the isotropic approximation are not significant.

Making use of the constitutive Equation 1 and the static equilibrium condition, we can derive the basic elastic equations for this problem [5]:

$$\frac{\partial}{\partial r} \left[\frac{1}{r} \left(\frac{\partial(ru_r)}{\partial r} \right) \right] = - \left(\frac{e_{31} E}{r} \right) \frac{s_{11}(1+\sigma)(1-2\sigma)}{1-\sigma}$$

$$\frac{\partial u_z}{\partial z} = \text{constant} \quad (2)$$

where σ is Poisson's ratio and s_{11} is the elastic compliance. The solutions to Equation 2 are

$$u_r = ar + \frac{b}{r} + \left(\frac{e_{31} V}{\ln \rho} \right) \frac{s_{11}(1+\sigma)(1-2\sigma)}{1-\sigma}$$

$$u_z = cz \quad (3)$$

where $\rho = R_0/r_0$. a , b and c are the integration constants which can be determined from the boundary conditions: $u_{zz} = d_{31} E_m$, where E_m is the average electric field in the tube and $E_m = 2V/[(R_0 + r_0) \times \ln(R_0/r_0)]$; at $r = R_0$ and r_0 there is no external stress on the tube wall, which implies $T_r = 0$ at these two boundaries. Substituting Equation 3 into Equa-

tion 1 and using the boundary conditions, one can get

$$a = E_m \frac{(1-2\sigma)d_{33} - \sigma d_{31}}{2(1-\sigma)}$$

$$b = -R_0 r_0 E_m \frac{d_{33} + \sigma d_{31}}{2(1-\sigma)}$$

$$c = d_{31} E_m \quad (4)$$

All the strain components for the tube can be obtained from Equations 3 and 4. Here we are more interested in finding out how the tube outer diameter changes with applied electric field as the ratio R_0/r_0 varies since in most of the applications, this is the quantity of interest. Substituting a and b in Equation 4 into the expression for u_r and setting $r = R_0$ yields the displacement of the tube outer wall $u_r(R_0)$:

$$u_r(R_0) = E_m \frac{(R_0 + r_0)d_{31} + (R_0 - r_0)d_{33}}{2}$$

This equation reveals that $u_r(R_0)$ can be changed from positive to zero, and to negative, by varying the ratio of R_0/r_0 .

To illustrate the advantage of using thin-walled tubes for actuator applications, one can compare the piezoelectric response of a tube discussed here with a rod of radius R_0 and length L subjected to the same applied voltage V . For the rod, the field is applied along the axial direction and $u_{zz} = d_{33} V/L$ and $u_{rr} = d_{31} V/L$. For the tube sample, one can equivalently introduce the quantity u_r/R_0 as the effective strain in the radial direction:

$$\frac{u_r(R_0)}{R_0} = E_m \frac{[1 + (r_0/R_0)]d_{31} + [1 - (r_0/R_0)]d_{33}}{2} \quad (5)$$

Similar to a rod sample, we introduce the effective piezoelectric constants for the tube as if it were a rod poled axially:

$$u_{zz} = d_{33}^{\text{eff}} \frac{V}{L} \quad \frac{u_r}{R_0} = d_{31}^{\text{eff}} \frac{V}{L} \quad (6)$$

where L is the axial length of the tube and V is the voltage applied on the tube wall. From $u_{zz} = d_{31} E_m$ and Equation 5, the effective piezoelectric constants can be deduced as

$$d_{33}^{\text{eff}} = d_{31} \frac{2L}{(R_0 + r_0) \ln(R_0/r_0)}$$

$$d_{31}^{\text{eff}} = \frac{L}{(R_0 + r_0) \ln(R_0/r_0)} \times \left[\left(1 + \frac{r_0}{R_0} \right) d_{31} + \left(1 - \frac{r_0}{R_0} \right) d_{33} \right] \quad (7)$$

For thin-walled tubes with L much larger than R_0 , which is the case in most of the applications, both d_{33}^{eff} and d_{31}^{eff} can be exceptionally large. This demonstrates that the tubular structure has great advantage over the regular ceramic rod for actuator application. Besides that, by choosing $[1 + (r_0/R_0)]|d_{31}| > [1 - (r_0/R_0)]|d_{33}|$, the effective d_{33} and d_{31} of the tube will have the same sign. By adjusting the ratio

R_0/r_0 , one can also continuously vary d_{31}^{eff} of the tube from positive to zero and to negative.

To compare with the theoretical prediction, the displacement field $u_r(R_0)$ and u_{zz} of a radially poled PZT-5 tube were measured using a double-beam laser dilatometer [6]. The ceramic tubes used were manufactured by Morgan Matroc, Inc., Vernitron Divisions, with $R_0 = 0.635$ mm and $r_0 = 0.381$ mm. From the data acquired and using Equations 3, 4 and 5, we got $d_{33} = 289 \text{ pC N}^{-1}$ and $d_{31} = -141.3 \text{ pC N}^{-1}$ for the tube material. For most of the commercially available PZT materials, the ratio d_{33}/d_{31} ranges from 2.15 to 2.3 [7]. The measured ratio here ($d_{33}/d_{31} = 2.05$) is slightly below that range which we believe is the result of the approximations used in the derivation. The effective piezoelectric constants defined in Equation 6 for the tube, therefore, are $d_{33}^{\text{eff}} = -8180 \text{ pC N}^{-1}$ and $d_{31}^{\text{eff}} = -3220.5 \text{ pC N}^{-1}$; the two coefficients have the same sign as predicted by Equation 7 and they are exceptionally large.

The small thickness of the tube wall also makes it possible to use electric field-biased electrostrictive materials for the actuator application, since only a small bias voltage is required here to induce substantial piezoelectric responses in the materials. In field-biased electrostrictive materials, it has been shown that the ratio of the piezoelectric constants d_{33}/d_{31} is bias field-dependent [8]. Hence, for a suitable ratio R_0/r_0 , by tuning the d.c. bias field level, both sign and magnitude of d_{31}^{eff} of the tube can be varied.

3. The hydrostatic response of end-capped tubes

The availability of small-sized ceramic tubes makes it attractive to integrate them into 1-3 type piezoceramic-polymer composites for large-area applications and to provide more flexibility for further material property modification. Before a detailed discussion on the composite properties, we will derive the expression for the hydrostatic response of end-capped tubes in this section since this is the most commonly used mode of piezo-tubes as hydrostatic sensors [9, 10]. Again here, the ratio R_0/r_0 provides a convenient way to adjust the piezoelectric response of the sensor in the radial direction.

Similar to the derivations presented in the preceding section, the displacement field of a tube under hydrostatic pressure, when expressed in the cylindrical coordinate system, is $u_\phi = 0$ and $u = u_r(r)\hat{r} + u_z(z)\hat{z}$. (For an isotropic material, this is the exact form of the displacement field and for a poled ceramic tube, the error in using this form of the displacement field, as will be shown later, is less than 10%.) Since all the external forces are applied on the surfaces of the tube, there is no internal body force in the tube wall and Equation 2 becomes

$$\frac{1}{r} \left(\frac{\partial(ru_r)}{\partial r} \right) = \text{const.} \quad \frac{\partial u_z}{\partial z} = \text{const.} \quad (8)$$

The solutions to the equations are

$$u_r = ar + \frac{b}{r} \quad u_z = cz \quad (9)$$

The non-zero strain components are

$$u_{rr} = a - \frac{b}{r^2} \quad u_{\phi\phi} = a + \frac{b}{r^2} \quad u_{zz} = c \quad (10)$$

where a , b and c are the integration constants. The boundary conditions which will be used to determine them are: since the two ends of the tube are sealed, there is no pressure inside the tube and at $r = r_0$, $T_r = 0$; at $r = R_0$, $T_r = -p$; and at $z = 0$ and $z = 1$, the stress in the axial direction is $T_z = -pR_0^2/(R_0^2 - r_0^2)$, where $-p$ is the applied hydrostatic pressure. For the purpose of comparison, we will determine the integration constants a , b and c in Equation 9 for both elastically isotropic tubes and anisotropic tubes. For the anisotropic tube, the constitutive relations are

$$\begin{aligned} T_z &= c_{11}u_{zz} + c_{12}u_{\phi\phi} + c_{13}u_{rr} \\ T_r &= c_{33}u_{rr} + c_{13}u_{\phi\phi} + c_{13}u_{zz} \\ T_\phi &= c_{12}u_{zz} + c_{11}u_{\phi\phi} + c_{13}u_{rr} \end{aligned} \quad (11)$$

where c_{ij} are the elastic stiffness coefficients of the poled ceramics. Following the convention in the literature, in Equation 11, 3 is referred to the poling direction (\hat{r} direction), 1 the \hat{z} direction, and 2 the $\hat{\phi}$ direction. Substituting the strain components in Equation 10 into Equation 11 and omitting the term in T_z having r dependence, one can obtain a , b , c :

$$a = \frac{-pR_0^2}{R_0^2 - r_0^2} \left(\frac{c_{13} - c_{11}}{c_{13}(c_{12} + c_{13}) - c_{11}(c_{13} + c_{33})} \right) \quad (12a)$$

$$b = \frac{-r_0^2 R_0^2}{R_0^2 - r_0^2} \left(\frac{p}{c_{33} - c_{13}} \right) \quad (12b)$$

$$c = \frac{-pR_0^2}{R_0^2 - r_0^2} \left(\frac{c_{12} - c_{33}}{c_{13}(c_{12} + c_{13}) - c_{11}(c_{13} + c_{33})} \right) \quad (12c)$$

Therefore, the stress distribution in the tube is given by

$$T_r = \frac{-pR_0^2}{R_0^2 - r_0^2} \left(1 - \frac{r_0^2}{r^2} \right) \quad (13a)$$

$$\begin{aligned} T_\phi &= \frac{-pR_0^2}{R_0^2 - r_0^2} \left[\frac{c_{13}^2 + c_{12}^2 - c_{11}^2 - c_{12}c_{33}}{c_{13}(c_{12} + c_{13}) - c_{11}(c_{13} + c_{33})} \right. \\ &\quad \left. + \frac{c_{11} - c_{13}}{c_{33} - c_{13}} \left(\frac{r_0^2}{r^2} \right) \right] \end{aligned} \quad (13b)$$

$$T_z = \frac{-pR_0^2}{R_0^2 - r_0^2} \quad (13c)$$

In writing down Equation 13c, we omitted a term $(c_{12} - c_{13})b/r^2$, which is less than 7% of the total T_z . Since T_z itself is one of the boundary condition used to derive the integration constants a , b and c and is equal to $-pR_0^2/(R_0^2 - r_0^2)$, the appearance of this extra term in the expression for T_z derived using Equations 11 and 12 is clearly unphysical and is the error resulted from the approximation made regarding the displacement field for the tube under hydrostatic pressure.

However, the small size of this error (less than 7%) indicates the validity of this approximation.

From the stress distribution equations, the hydrostatic response of the tube can be calculated from the relation

$$D_3 = d_{31}T_z + d_{31}T_\phi + d_{33}T_r \quad (14)$$

where D_3 is the electric displacement in the poling direction. The value of the hydrostatic piezoelectric constant d_h can be found by taking the average charge produced in the inner and outer surfaces of the tube wall and dividing it by the outer surface area of the tube. This yields, from Equation 14,

$$d_h = \frac{1}{2} \left\{ d_{33} + \frac{R_0}{R_0 - r_0} \right. \\ \times \left[1 + \left(\frac{c_{13}^2 + c_{12}^2 - c_{11}^2 - c_{12}c_{33}}{c_{13}(c_{13} + c_{12}) - c_{11}(c_{13} + c_{33})} \right) \right. \\ \left. \left. + \frac{c_{11} - c_{13}}{c_{33} - c_{13}} \left(\frac{r_0}{R_0} \right) \right] d_{31} \right\} \quad (15)$$

In Equation 15, we have taken the tube outer surface as the total electroded area to calculate d_h . Using the elastic stiffness coefficients for PZT-5H [7], for a tube with $R_0 = 0.635$ mm and $r_0 = 0.381$ mm, Equation 15 predicts $d_h = -657 \text{ pC N}^{-1}$ or $2.4d_{31}$. If the tube R_0 is doubled while keeping the wall thickness the same, the d_h value can reach -1786 pC N^{-1} . Hence, for thin-walled tubes, an exceptionally large hydrostatic response can be achieved.

Equation 13 can be reduced to the stress field of an elastically isotropic tube by using the isotropic conditions $c_{11} = c_{33}$, $c_{12} = c_{13}$. It can be shown that the result thus obtained is the exact solution to the tube stress field, and similarly d_h can be found by simplifying Equation 15 using the isotropic condition

$$d_h = \frac{1}{2} \left[d_{33} + \frac{R_0}{R_0 - r_0} \left(2 + \frac{r_0}{R_0} \right) d_{31} \right] \quad (16)$$

For the PZT-5H tube just calculated, the calculated d_h value is -594 pC N^{-1} ($2.17d_{31}$) when Equation 16 is used.

Experimental measurements were performed on several PZT-5 tubes ($R_0 = 0.635$ mm and $r_0 = 0.381$ mm) with two ends sealed and radially poled (the dielectric constant ϵ for this group of sample is around 1700 at atmospheric pressure). d_h was measured through the direct piezoelectric effect, where the charge induced on the electrodes of a sample is measured when the sample is subjected to a hydrostatic pressure. d_{31} and d_{33} were measured using a double-beam laser interferometer [6]. For this group of samples, d_h was in the range from -330 to -400 pC N^{-1} and d_{31} from -140 to -160 pC N^{-1} . The ratio between the experimentally measured d_h and d_{31} (on average) is 2.45, which is very close to that predicted from Equation 15. Clearly, to make a quantitative prediction about the hydrostatic response of a tubular structure, one may be required to include the elastic anisotropy in the calculation.

By analogy with the situation discussed in the preceding section, by varying the ratio of R_0/r_0 one can

also manipulate the response of the tube to the stress field in the radial direction. Here, we will use the result just derived for the hydrostatic response of a tube as an example. In Equation 14, the hydrostatic response of a tube comes from three terms: one is from the pressure in the axial direction and the other two from the pressure in the radial direction. The electric displacement D'_3 due to the pressure in the radial direction is

$$D'_3 = d_{31}T_\phi + d_{33}T_r$$

Using the result of Equation (13) and taking the average charge produced at the tube inner wall and outer wall, one can obtain the partial piezoelectric response d' of the tube to the pressure in the radial direction

$$d' = \frac{1}{2} \left\{ d_{33} + \frac{R_0}{R_0 - r_0} \right. \\ \times \left[\left(\frac{c_{13}^2 + c_{12}^2 - c_{11}^2 - c_{12}c_{33}}{c_{13}(c_{13} + c_{12}) - c_{11}(c_{13} + c_{33})} \right) \right. \\ \left. \left. + \frac{c_{11} - c_{13}}{c_{33} - c_{13}} \left(\frac{r_0}{R_0} \right) \right] d_{31} \right\} \quad (17)$$

Obviously, the opposite sign of d_{33} and d_{31} provides a convenient way to change d' in Equation 17. One can easily verify that by varying the ratio R_0/r_0 , d' changes continuously from positive to zero, and to negative. Taking the elastically isotropic tube as an example and assuming $d_{33}/d_{31} = 2.2$ in Equation 17, when $r_0/R_0 = 0.375$, d' becomes zero. That is, the tube now becomes insensitive to the pressure wave in the radial direction. Similar to the actuator case, for suitable ratio of r_0/R_0 , one can also change the sign of the effective radial response here by using electrostrictive materials with different d.c. bias field levels. This result, as well as the result in the preceding section, indicates that the range of the effective piezoelectric properties of the materials can be considerably broadened by using tubular structures.

To calculate the hydrostatic figure of merit d_{hg_h} for this tubular sensor, we notice that in practice, the quantity is a measure of the product of the charge and voltage produced in unit volume of material. For a tubular material its effective volume is $\pi R_0^2 L$, where L is the tube length when the end-capped tube is regarded as a rod with its radius equal to R_0 . The capacitance of the tube is

$$C = \frac{2\pi L \epsilon_0 \epsilon}{\ln(R_0/r_0)}$$

where ϵ is the dielectric constant of the material. Since the total charge produced by the tube is equal to $2\pi R_0 L d_h$ and the voltage is equal to this charge divided by the capacitance of the tube, the effective figure of merit for the tube is

$$d_{hg_h} = \frac{1}{2\epsilon\epsilon_0} \ln\left(\frac{R_0}{r_0}\right) \\ \times \left[d_{33} + d_{31} \left(\frac{R_0}{R_0 - r_0} \right) \left(2 + \frac{r_0}{R_0} \right) \right]^2 \quad (18)$$

Here, we have used the d_h result for an isotropic tube (Equation 17). One can easily expand the result to elastically anisotropic materials. Clearly, for a thin-walled tube a large figure of merit can be obtained.

4. 1-3 tubular composites

A typical 1-3 tubular composite is schematically drawn in Fig. 2. For the composite discussed here, the tubes are radially poled and the composite is electroded on the two end-faces. Hence, a special arrangement is required to ensure proper electric connections between the electrodes at the tube walls and the composite end-faces. This kind of composite can be used for large-area actuator and sensor applications, as well as "smart" materials where both sensor and actuator are integrated into one structure. In this section, we only discuss the properties associated with sensor applications.

When tubes are integrated into a 1-3 type ceramic-polymer composite, as has been demonstrated in our earlier publications, there is a stress transfer between the polymer matrix and the ceramic tubes in the z direction [11, 12]. This stress transfer is a result of the difference in the elastic constants between the two constituent phases and is through the shear force in the two phases. Due to this stress transfer, the piezoelectric response of the tube in the axial direction is enhanced. To provide a physical picture of how the hydrostatic response of a tubular 1-3 composite changes as the elastic properties of the two constituent phases and their geometric parameters are varied, we will treat quantitatively the composite schematically drawn in Fig. 3. This composite corresponds to the tubular composite in the dilute limit. However, since only the polymer matrix close to the ceramic-polymer interface participates the stress transfer, the result can also be applied to the composite with finite ceramic content.

The procedure of calculating how much stress is transferred from the polymer phase to the ceramic rod

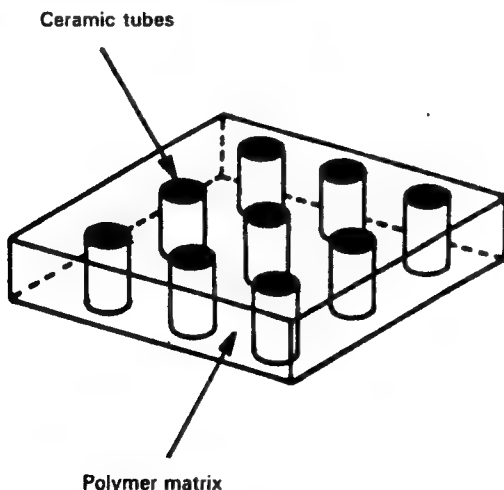


Figure 2 Schematic drawing of 1-3 tubular composite where the ceramic tubes are embedded in a polymer matrix. The ceramic tubes are either end-capped or filled inside with epoxy.

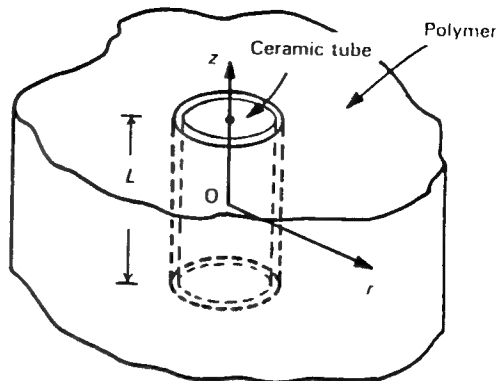


Figure 3 A single tube 1-3 composite. The ceramic tube is end-capped.

is similar to that outlined in the earlier publications, [11, 12]. Under hydrostatic pressure p , the surface displacement field u_z of the polymer phase in the z direction should satisfy the equation

$$\frac{2u_z}{L} = -(s_{11} + 2s_{12})p + \frac{s_{11}\mu L}{4} \left[\frac{\partial^2 u_z}{\partial r^2} + \frac{1}{r} \left(\frac{\partial u_z}{\partial r} \right) \right] \quad (19)$$

where p is the hydrostatic pressure, s_{ij} is the elastic compliance of the polymer phase, μ is the shear modulus of the polymer phase, and L is the thickness of the composite in the z direction. The solution to Equation 19 is the zero-order Hankel function $K_0(p)$ and

$$\frac{2u_z}{L} = -\frac{(1-2\sigma)p}{Y} + AK_0(r/\xi) \quad (20)$$

where A is the integration constant and $\xi = L/[2(2Y/\mu)^{1/2}]$ defines the strain decay length in the polymer phase. In Equation 20 we have made use of the relations $s_{12} = -\sigma s_{11}$ and $Y = 1/s_{11}$, where Y and σ are the Young's modulus and Poisson's ratio of the polymer, respectively. The total force f transferred from the polymer phase to the ceramic tube is therefore

$$f = -Y \int_{R_0}^{\xi} 2\pi r A K_0(r/\xi) dr$$

Two boundary conditions are needed to determine f . The first one is the boundary condition that at the ceramic tube-polymer interface, the z component of the strain in the two phases should be equal, and the second is the relation between the z component of the strain in the ceramic tube and the stress field

$$u_{zz} = -\frac{pR_0^2(1-2\sigma^c)s_{11}^c}{R_0^2 - r_0^2} + \frac{fs_{11}^c}{\pi(R_0^2 - r_0^2)} \quad (21)$$

where s_{11}^c and σ^c are the elastic compliance and Poisson's ratio of the ceramic tube, respectively. Equation 21 can be derived by following the procedure outlined in the preceding section. Hence, the amount of stress transferred from the polymer matrix to the

ceramic tube is

$$\frac{f}{\pi A_0} = -\frac{pR_0^2}{A_0} \left(\frac{A_0(1-2\sigma)/(R_0^2 Y s_{11}^c) - (1-2\sigma^c)}{1 + K_0(\rho_0)A_0/[2K_1(\rho_0)Y s_{11}^c R_0 \xi]} \right) \quad (22)$$

where $A_0 = (R_0^2 - r_0^2)$, $\rho_0 = R_0/\xi$ and $K_1(\rho)$ is the first-order Hankel function. Since the polymer phase is subjected to a hydrostatic pressure, the Poisson's ratio effect causes a reduction of the effective pressure at the polymer faces from $-p$ to $-p(1-2\sigma)$. As shown in Equation 22, this reduces the stress transfer from the polymer phase to the ceramic tube. To increase the stress transfer, one should choose polymers with a small Poisson's ratio. The total stress in the axial direction of the tube is

$$T_z = -\frac{pR_0^2}{A_0} \left(1 + \frac{A_0(1-2\sigma)/(R_0^2 Y s_{11}^c) - (1-2\sigma^c)}{1 + K_0(\rho_0)A_0/[2K_1(\rho_0)Y s_{11}^c R_0 \xi]} \right) \quad (23)$$

$$T_z = -\frac{pR_0^2}{A_0} \gamma \quad (23)$$

where γ is introduced as the stress amplification factor. In Fig. 4 we plot γ as a function of the aspect ratio R_0/L for a 1-3 tubular composite made of PZT-5H tube with $R_0 = 0.635$ mm and $r_0 = 0.381$ mm and Spurrs epoxy. The data used are: $Y = 3.1 \times 10^9$ N m $^{-2}$, $\mu = 1.148 \times 10^9$ N m $^{-2}$, and $\sigma = 0.35$ for spurs epoxy (from Oakley [13]; $s_{11}^c = 1.64 \times 10^{-11}$ m 2 N $^{-1}$) and $\sigma = 0.31$ [7]. Apparently, for thin and long tubes, the stress amplification factor is large. This is similar to that obtained earlier for 1-3 composites made of ceramic rods [11, 12].

Using the results from section 3 and Equation 23, one can write down the effective hydrostatic piezoelectric strain coefficient for 1-3 tubular composites as

$$d_h^{\text{eff}} = \frac{L}{R_0} v_c \left[d_{33} + \frac{R_0}{R_0 - r_0} \left(1 + \gamma + \frac{r_0}{R_0} \right) d_{31} \right] \quad (24)$$

where v_c is the volume content of ceramic tubes in the composite which is defined as $v_c = \pi R_0^2/a$, and a is the unit cell area of the composite. For a composite of low ceramic volume content, γ in Equation 22 is equal to that in Equation 24. With increased volume content,

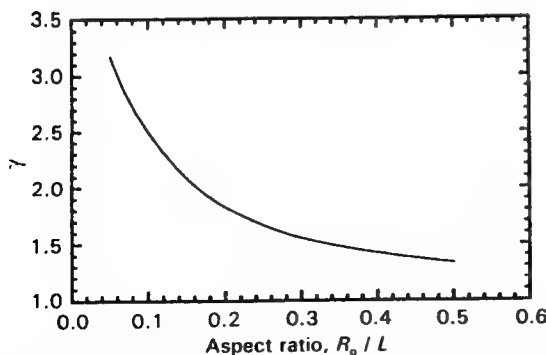


Figure 4 The stress amplification factor γ (Equation 23) as a function of the aspect ratio R_0/L of the ceramic tube for the composite drawn in Fig. 3 with PZT-5H ceramic tube and spurs epoxy.

the dependence of γ on the material properties of the constituent phases will become more complicated and one may not be able to derive the analytical expression for γ except in some special cases. In this paper, we will not pursue this further and only point out that in the composite, there is always a stress transfer between the two phases ($\gamma > 1$); the general rule to increase this stress transfer is basically the same as that for the dilute composite case.

In the limit of $v_c \rightarrow 1$, Equation 24 is reduced to that for a single tube when regarded as a rod with similar dimensions:

$$d_h^{\text{eff}} = \frac{L}{R_0} \left[d_{33} + \frac{R_0}{R_0 - r_0} \left(2 + \frac{r_0}{R_0} \right) d_{31} \right] \quad (25)$$

Equation 16 can be converted to Equation 25 by using the area of the tube end (πR_0^2) as the effective electrode area instead of the area of the tube outer wall. Similarly, one can also derive the effective hydrostatic figure of merit for 1-3 tubular composites as

$$d_h^{\text{eff}} g_h^{\text{eff}} = \frac{V_c}{2\epsilon\epsilon_0} \ln \left(\frac{R_0}{r_0} \right) \times \left[d_{33} + \frac{R_0}{R_0 - r_0} \left(1 + \frac{r_0}{R_0} + \gamma \right) d_{31} \right]^2 \quad (26)$$

As $v_c \rightarrow 1$ ($\gamma \rightarrow 1$), the result is reduced to that for a single tube sensor (Equation 18).

For comparison, in Table I we present the experimental values of the hydrostatic response of an end-capped ceramic tube, a 1-3 composite with tubes having inside air backing, and a 1-3 composite with tubes having inside epoxy backing. All 1-3 composites had a volume content of 23.3% ceramic tube and the dimensions of the tubes are $R_0 = 0.635$ mm, $r_0 = 0.381$ mm and $L = 9$ mm. The polymer matrix was made of spurs epoxy. In the composite with epoxy backing, the tube inside was filled with Spurrs epoxy. d_{31} listed in the table was calculated using Equation 25 where the ratio $d_{33}/d_{31} = 2.2$ is used. From this d_{31} , γ was calculated from Equation 26. Clearly, the γ value here is much smaller than that shown in Fig. 4 ($R_0/L = 0.07$ here). One of the reasons for this is that Fig. 4 is for the composite in the dilute limit; the γ value for composites with a finite ceramic content should be smaller than that in Fig. 4. The imperfect stress transfer between the two phases and the depoling effect of the tubes during epoxy curing may also be responsible for this reduction of γ . Although the data in Table I show that the hydrostatic responses of the composites tested are not as high as that of the single tube, the difference is not very large. As the volume content of the ceramic tube and other parameters in a composite are varied, the effective hydrostatic figure of merit for 1-3 tubular composites will change. In the optimum condition, one would expect that $d_h^{\text{eff}} g_h^{\text{eff}}$ for a tubular 1-3 composite may exceed that of a single tube. Apparently, further experimental and theoretical work is required to address this issue. Furthermore,

TABLE I Hydrostatic properties of the end-capped tube and 1-3 tubular composites

	ϵ	$d_h^{\text{eff}} (\text{pCN}^{-1})$	$d_h^{\text{eff}} g_h^{\text{eff}} (10^{-15} \text{m}^2 \text{N}^{-1})$	$d_{31} (\text{pCN}^{-1})$	γ
End-capped tube Composite	2945	-14330	10000	-235	1
Air backing	2922	-5502	6389	-235	2.11
Epoxy backing	2944	-4970	5172	-235	

the figure of merit of 1-3 tubular composites is much higher than that of 1-3 composites made of ceramic rods [12].

If there was no stress transfer from the polymer phase to the ceramic tubes in these tubular composites, one would get for this 1-3 composite $d_h^{\text{eff}} = 3339 \text{ pCN}^{-1}$ and $d_h^{\text{eff}} g_h^{\text{eff}} = 2353 \times 10^{-15} \text{ m}^2 \text{N}^{-1}$, which are much smaller than the values listed in Table I. This clearly demonstrates the importance of the stress transfer between the two phases in a 1-3 composite.

One interesting feature from Table I is that the hydrostatic response of the 1-3 tubular composite with epoxy backing does not differ very much from that with air backing. That is, the epoxy filling inside a tube does not change the stress distribution in the tube wall significantly except to transfer stress in the z direction. This can be understood by considering the following fact: the elastic moduli of the ceramic tube are much higher than those of epoxy, and as a result the ceramic tube wall practically shields the epoxy filling inside the tube from seeing the pressure in the radial direction. Conversely, the epoxy inside the tube does not exert a significant amount of stress on the ceramic tube wall in the radial direction. Therefore, the epoxy filling inside a tube provides an effective way to enhance the mechanical strength while keeping the hydrostatic response of the composite almost intact.

5. Summary

In this paper, the effective piezoelectric responses of the tubular structure and its composites were evaluated both theoretically and experimentally. When used as actuators, the effective piezoelectric constant in the radial direction of a tube can be changed from positive to zero and to negative by adjusting the ratio R_0/r_0 for piezoelectric materials or the d.c. bias field for electrostrictive materials. Therefore, the effective piezoelectric constants along the axial direction and the radial direction can both have the same sign. For sensor applications, the tube with two ends sealed exhibits an exceptionally high hydrostatic response and, analogous to the situation with actuators, the pressure response in the radial direction can be adjusted by the ratio R_0/r_0 for piezoelectric materials or

the d.c. bias field for the electrostrictive materials. For large-area applications, these tubes can be readily integrated into a 1-3 composite structure which provides a low acoustic density and high piezoelectric activity. The effectiveness of the stress transfer between the polymer phase and the ceramic tube in a 1-3 composite makes it possible to back-fill the inside of the ceramic tube, which increases the mechanical integrity of the tubular structure while keeping the piezoelectric response of the composite almost intact.

Acknowledgements

The authors wish to thank Dr J. Powers for many stimulating discussions. The technical assistance of Mr H. Chen is greatly appreciated. This work was supported by the Office of Naval Research.

References

1. R. E. NEWNHAM and G. R. RUSCHAN, *J. Amer. Ceram. Soc.* 74 (1991) 463.
2. R. E. NEWNHAM, Q. C. XU, S. KUMAR and L. E. CROSS, *Ferro.* 102 (1990) 259.
3. R. E. NEWNHAM, D. P. SKINNER and L. E. CROSS, *Mater. Res. Bull.* 13 (1978) 525.
4. W. A. SMITH, in Proceedings of 1990 IEEE International Symposium on Appl. of Ferro., (Urbana, Illinois, 1990) p. 145.
5. L. D. LANDAU and E. M. LIFSHITZ, "Theory of Elasticity" (Pergamon, 1986).
6. Q. M. ZHANG, S. J. JANG and L. E. CROSS, *J. Appl. Phys.* 65 (1989) 2807.
7. PZT-5 data sheet, 1991 (Morgan Matroc, Inc., Vernitron Division, OH).
8. D. J. TAYLOR, D. DAMJANOVIC, A. S. BHALLA and L. E. CROSS, in Annual Report of the Materials Research Laboratory (The Pennsylvania State University, University Park, PA, 1991) p. 50.
9. R. A. LANGEVIN, *J. Acoust. Soc. Amer.* 26 (1954) 421.
10. "Handbook of Hydrophone Element Design Technology", NUSC Technical Document 5813 (1978).
11. Q. M. ZHANG, WENWU CAO, H. WANG and L. E. CROSS, *J. Appl. Phys.* 73 (1993) 1403.
12. WENWU CAO, Q. M. ZHANG and L. E. CROSS, *ibid.* 72 (1992) 5814.
13. C. G. OAKLEY, PhD Thesis, The Pennsylvania State University (1991).

Received 23 November
and accepted 8 December 1992

ACTUATOR STUDIES

APPENDIX 37

FLEXENSIONAL "MOONIE" ACTUATORS

R. E. Newnham, A. Dogan, Q. C. Xu, K. Onitsuka, J. Tressler, and S. Yoshikawa
International Center of Actuators and Transducers

Materials Research Laboratory
The Pennsylvania State University
University Park, PA 16802

ABSTRACT

In recent years, piezoelectric and electrostrictive ceramics have been used in many actuators applications. A new type of composite actuator, which is based on the concept of a flexensional transducer, has been developed. (1-6) This ceramic-metal composite actuator, or "moonie" consists of either a piezoelectric ceramic disk or a multilayer stack sandwich between two specially designed metal end caps. This new design provides a sizeable displacement, as well as a large generative force. In other words, it bridges the gap between the two most common types of actuator; the multilayer and bimorph (7).

INTRODUCTION

The basic configuration of the ceramic-metal composite actuator (moonie) is shown in Figure 1. The metal end caps serve as mechanical transformers for converting and amplifying the lateral motion of the ceramic into a large axial displacement normal to the end caps. Both the d_{31} ($=d_{32}$) and d_{33} coefficients of the piezoelectric ceramic contribute to the axial displacement of the composite.

Sample Preparation and Measurement Technique

The composite actuators were made from electrode PZT-5A, PMN-PT, or multilayer ceramic disks (11-12.7 mm in diameter and 1 mm thick) and end caps (11-12.7 mm in diameter with thickness ranging from 0.3 to 3.0 mm). Shallow cavities 8.5 to 9.0 mm in diameter and about 200 μm center depth were machined into the inner surface of each of the end caps. The end caps were machined from brass, phosphor bronze, and acrylic. The ceramic disk and the end caps were bonded together around the

circumference, taking care not to fill the cavity or short circuit the electrodes. Composite actuators were also stacked together to get higher displacement by using silver epoxy at the centers of end caps.

The displacement of the composite actuator in the low frequency range was measured with a Linear Voltage Differential Transducer (LVDT) having a resolution of approximately 0.05 μm . The effective piezoelectric coefficient, which is a device property, was measured at the center of the samples using a modified Berlincourt d33 meter at a frequency of 100 Hz. Resonant frequencies were obtained with a Hewlett-Packard Spectrum Analyzer HP-3585A or Network Analyzer HP-3577A.

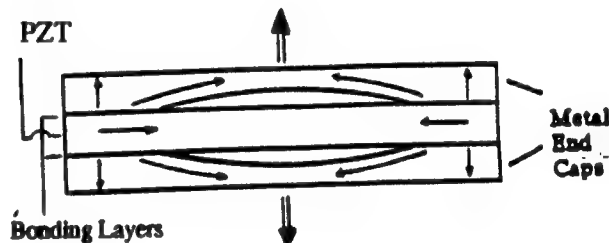


Figure 1. The geometry of the ceramic-metal composite actuator "Moonie". Arrows describe the direction of displacement.

FEA Modeling

Two commercially available FEA programs (ANSYS and SAP90) were used in this study for frequency response analysis. The relationship between admittance and frequency was calculated using 3-D axisymmetric piezoelectric elements in ANSYS. For the displacement analysis, the relationship between

displacement and applied electric field was calculated using 2D axisymmetric elements in SAP90. Each model was divided into three parts: the end cap, the PZT ceramic, and the bonding layer. Material parameters used in this analysis were Young's modulus, density, Poisson's ratio, piezoelectric constants, and dielectric constants.

EXPERIMENTAL RESULTS

Thickness Dependence of Displacement Values

Figure 2 shows the displacement at the cap center for composite actuators with different brass thickness at the same electric field, 1000 kV/mm. The results show that a composite actuator with 0.30 mm brass thickness can produce a displacement about 20 times larger than that of PZT alone. The displacement amplification is inversely related to the thickness of the metal end caps. FEA calculation agreed very well with the experimental results.

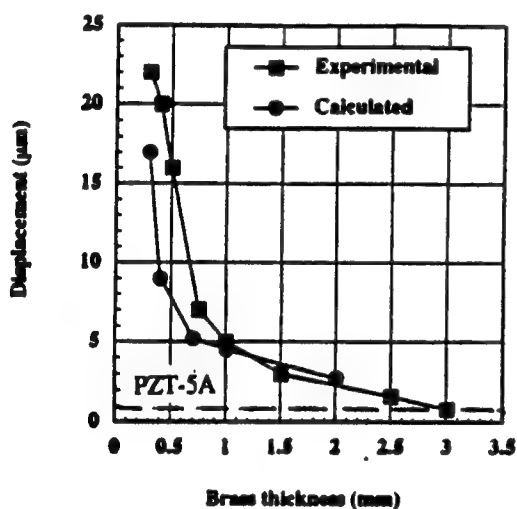


Figure 2. Comparison of the displacement calculated by FEA with experimental results as a function of end cap thickness.

Frequency Response of a Moonie Actuator

From the frequency response analysis, the lowest three resonant frequencies were calculated. Figure 3 shows the admittance spectrum of the moonie plotted as a function of the frequency from 10 to 300 kHz. The resonance peaks appearing at 50, 187, and 210 kHz, correspond to the lowest three flexextensional vibration modes. The first flexextensional mode can be effectively utilized up to nearly 50 kHz. Based on

these results, the coupling coefficient of the first mode was calculated to be 20%.

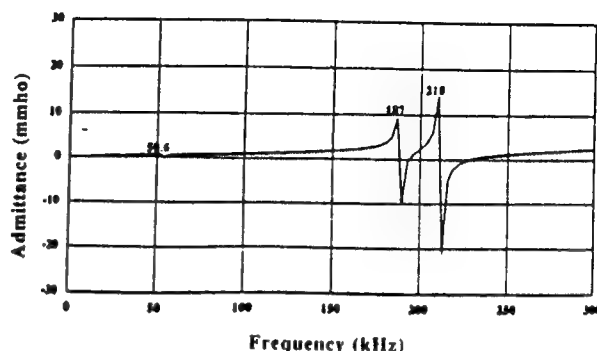


Figure 3. Admittance spectrum of the moonie (FEA)

Figure 4 compares the first flexextensional resonant frequency calculated by FEA with those obtained experimentally, for a range of brass end cap thickness. FEA calculation agreed very well with the experimental results. The first resonant frequency is approximately proportional to the square root of the brass end cap thickness.

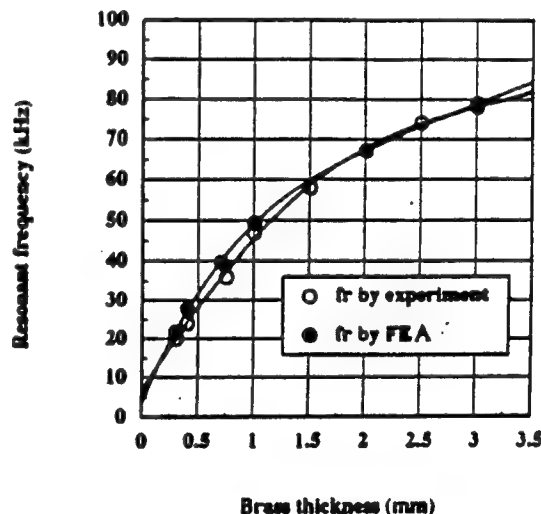


Figure 4. End cap thickness dependence of first resonance frequency.

Load Effect on Displacement of a Moonie Actuator

Normally, the displacement decreases when a load is applied to the actuator. Figure 5 shows the displacement profile across the exterior surface of the

moonie when four different loads are applied over an area 3 mm^2 under an applied E-field of 1 kV/mm . By increasing the load, the center displacement is gradually suppressed. The calculated maximum generative force of the moonie is 300 gf.

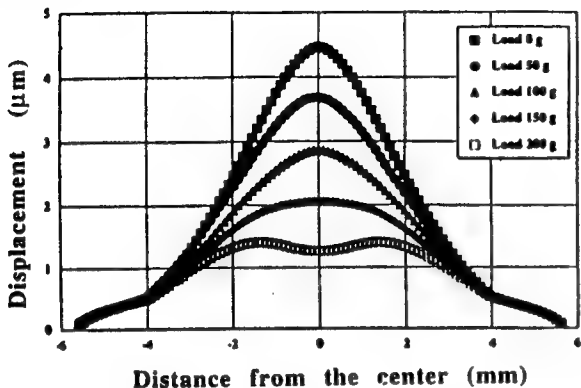


Figure 5. Calculated displacement profile across the exterior surface of the moonie actuator under the application of different loads.

Maximum Generative Force of the Moonie

Even though the flexural motion and displacement are the largest at the center of the end caps, the generative force is low. Fig. 6 shows the applied force-displacement relation of a moonie actuator operated at 1 kV/mm . A moonie actuator with 0.30 mm thick brass caps can withstand 210 gf while sacrificing 20% of its displacement value (load applied at the center of the end caps over 1 mm^2). The maximum generative force of the moonie actuator with 0.30 mm thick brass end caps should be around 350 gf (i.e. the intercept on the force axis). The reason for the saturation near 150 gf is probably due to the increasing contact surface of the LVDT measurement tip.

Trade-off Between Maximum Generative Force and Displacement

The position dependence of displacement is shown in Fig. 7 for the moonie actuator with 0.30 mm thick brass end caps. A displacement of about $22 \mu\text{m}$ was obtained at the center of the moonie. Displacement decreases dramatically when moving from the center to the edge. Conversely, generative force increases when moving from the center to the edge, where it approaches that of PZT ceramic. Therefore, it

becomes possible to tailor the desired actuator properties by changing the contact area over the brass end caps.

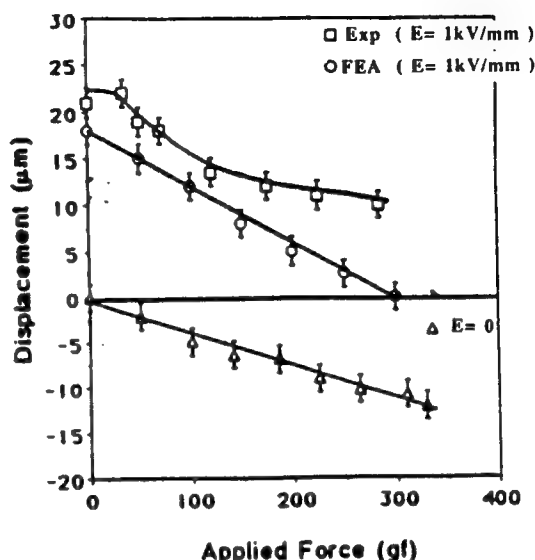


Figure 6. Displacement-applied force relation.

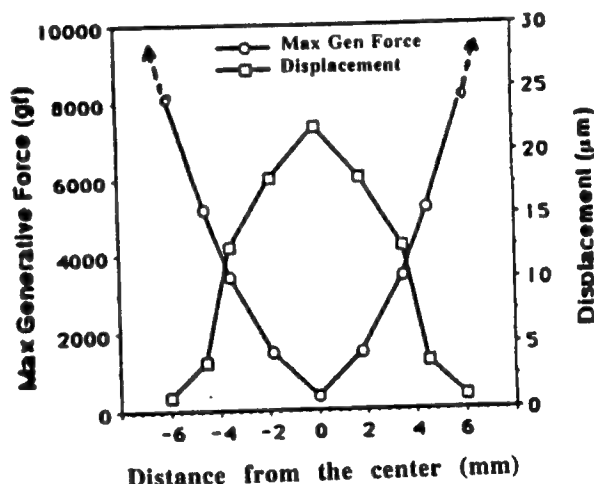


Figure 7. Position dependence of maximum generative force and displacement.

End Cap Material Effect

Four end cap materials: brass, aluminum, stainless steel and plastic were used for estimating their effect on the displacement of the moonie actuator. Since

they have different densities, Poisson's ratios, and Young's modulus, displacement is expected to be different for each end cap material.

Fig. 8 shows the effect of cap material on the displacement of the moonie actuator as a function of the cap thickness when applying a 1kV/mm electric field. It is observed that the lower the Young's modulus, the higher the displacement over the entire cap thickness range. All three metals, stainless steel, brass, and aluminum, show little difference in displacement when greater than 0.5 mm thick. Below a thickness of 0.5 mm, differences in displacement appear.

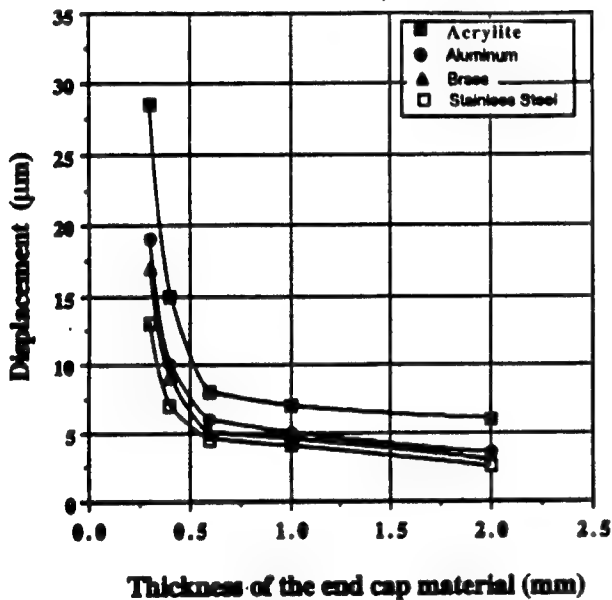


Figure 8. The effect of end cap material on the displacement value of moonie actuator.

Multistacked Moonie Actuator

A doubly stacked moonie actuator was fabricated by bonding together with silver epoxy two identical brass capped moonie actuators at the center of the cap. Figure 9 shows the displacement versus electric field curves for a doubly-stacked actuator driven by PZT-5A. A displacement of about 40 μm was obtained under an electric field of 1 kV/mm, which is almost twice the simple moonie displacement and nearly 20 times that of an uncapped ceramic. Displacement for the uncapped ceramic is also shown for comparison.

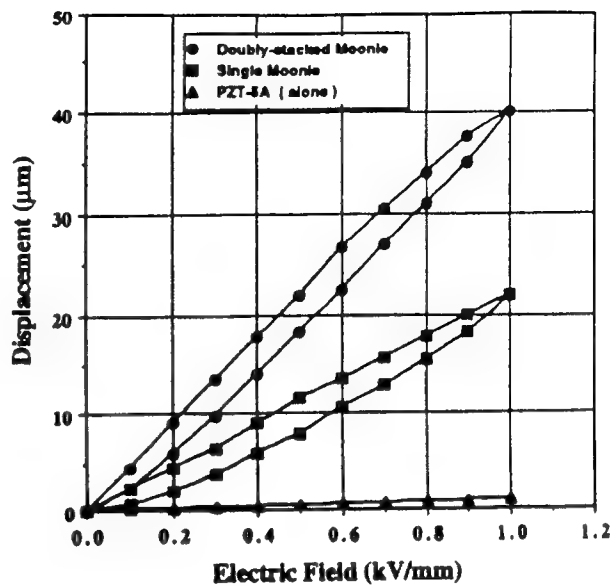


Figure 9. Displacement characteristic of a doubly-stacked moonie actuator.

Integrated Sensor and Actuator

By integrating both sensing and actuating functions into a single composite, the moonie device can be utilized for active vibration control. The prototype design (Fig. 10) consists of a 0.10 mm thick PZT-5A sensor, 2.5 mm on edge, imbedded within the upper end cap of a standard moonie actuator (11 mm in diameter, 3mm thick). External sinusoidal vibrations normal to the end cap surface are detected by the sensor. Then, via a feedback loop, a signal of appropriate amplitude and phase is applied to the actuator so that it effectively cancels the external vibration.

The sensitivity of the sensor was found by applying a sinusoidal AC electric field to the actuator portion of the device and observing the subsequent vibration signal on an oscilloscope. The minimum and maximum electric fields into the moonie actuator for which the sensor could detect a sinusoidal vibration signal were 200 mV/mm and 370V/mm, respectively. These minimum and maximum electric fields thus define the dynamic displacement range that the sensor is capable of detecting as being between 0.35 nm and 0.65 μm (as calculated by finite element analysis)

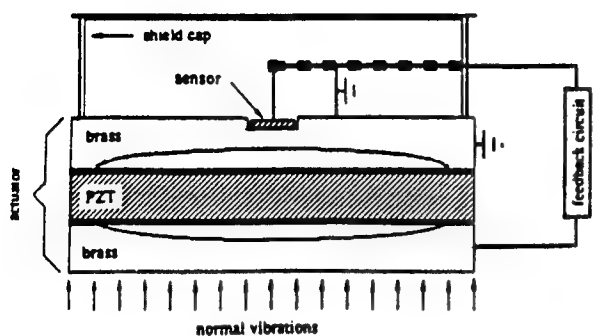


Figure 10. Integrated sensor and actuator.

The data in Figure 11 show that when the feedback circuit is activated, the prototype integrated sensor/actuator design can completely suppress the effects of an external vibration between 100 Hz and at least 2500 Hz. Over this frequency range, the electric field applied to the moonie actuator was nearly constant and its phase shift remained at nearly 180° due to the short propagation time as a result of the moonie actuator being in close proximity to the external vibration.

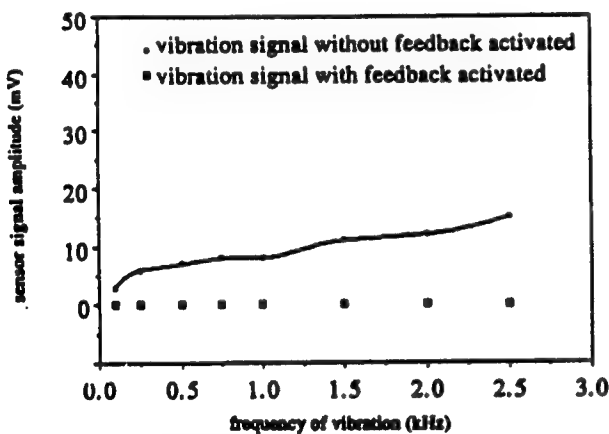


Figure 11. Sensor signal response both with and without the feedback circuit activated.

ACKNOWLEDGEMENT

The authors wish to thank Dr. L.E.Cross, and Dr .K. Uchino. The authors also wish to thank Dr. M. Megherhi of Piezo Kinetics Inc. for his technical support.

REFERENCES

1. R.E.Newnham, Q.C.Xu and S. Yoshikawa "Transformed stress direction-acoustic transducer" U.S Patent # 4,999,819 (March 12,1992).

2. Q.C.Xu, S.Yoshikawa, J.Belsick, R.E.Newnham, "Piezoelectric composites with high sensitivity and capacitance for use at high pressures.IEEE Transactions on Ultrasonics, Ferroelectrics and Frequency Control 38 [6] 634-39 (1991).

3. Y.Sugawara, K.Onitsuka, S.Yoshikawa, Q.Xu, R.E.Newnham, and K.Uchino, "Metal-Ceramic Composite Actuators " J.Am.Ceram.Soc.75[4]996-98(1992).

4. Q.C. Xu, A. Dogan, J. Tressler, S.Yoshikawa, and R.E.Newnham, "Ceramic-Metal Composite Actuator" IEEE Ultrasonic Symposium Proceedings (Florida, 1991).

5. A.Dogan, Q.C. Xu, K. Onitsuka, S.Yoshikawa, K. Uchino and R.E.Newnham. " High Displacement Ceramic-Metal Composite Actuators (Moonie)". Ferroelectric Special Issue for IMF-8 (in press).

6. K. Onitsuka, A.Dogan, Q.C. Xu, J. Tressler, S. Yoshikawa, and R.E.Newnham."Design Optimization for Ceramic-Metal Composite Actuators (Moonie)". Ferroelectric Special Issue for IMF8 (in Press).

7. K. Uchino "Piezoelectric and Electrostrictive Actuators", Morikita Publication, Tokyo, Japan, 1986.

APPENDIX 38

HIGH DISPLACEMENT CERAMIC METAL COMPOSITE ACTUATORS (MOONIES)

AYDIN DOGAN, QICHANG XU, KATSUHIKO ONITSUKA,
SHOKO YOSHIKAWA, KENJI UCHINO, ROBERT E. NEWNHAM
Intercollege Materials Research Laboratory, The Pennsylvania State University
University Park, PA 16802

(Received August 9, 1993)

Abstract The two most common type of piezoelectric actuators are the multilayer actuator with internal electrodes and the cantilevered bimorph actuator^[1]. A new type of composite ceramic actuator is the multilayered multistacked moonie (multi-multi moonie). Normal multilayer actuators produce a large generative force, but only a small displacement. Conversely, bimorphs produce large displacements but the forces are very small. The moonie actuator combines the advantages of both, producing a large displacement as well as a reasonably large generative force.

INTRODUCTION

The objective of this work was to fabricate and to evaluate the performance of a composite actuator that combines the piezoelectric d_{33} and d_{31} coefficients of a ceramic disk to generate large displacements with moderately high force. Figure 1 shows the basic configuration of the ceramic-metal composite actuator (moonie). The composite actuator is called the "moonie" because the shallow cavities under the metal endcaps are shaped like half moons^[2,3]. The metal end caps serve as mechanical transformers for converting and amplifying the lateral motion of the ceramic into a large axial displacement normal to the end caps. Both the d_{31} and d_{33} coefficients of the piezoelectric ceramic contribute to the axial displacement of the composite.

Sample Preparation

The composite actuators were made from electroded PZT-5A (Piezo Kinetics Co.) disks (12.7 mm in diameter and 1mm thick) and brass end caps (12.7 mm in diameter with

thicknesses ranging from 0.3 to 2.5 mm). Shallow cavities 9.0 mm in diameter with a 200 μm center depth were machined into the inner surface of each of the caps. The PZT disk and the end caps were bonded around the circumference using Emerson & Cumming epoxy (Eccobond 45LV), taking special care not to fill the cavity. The thickness of the epoxy bonding layer was approximately 20 μm . Moonies with a multilayer actuator instead of a ceramic disk were also fabricated by a similar process in order to decrease the applied voltage.

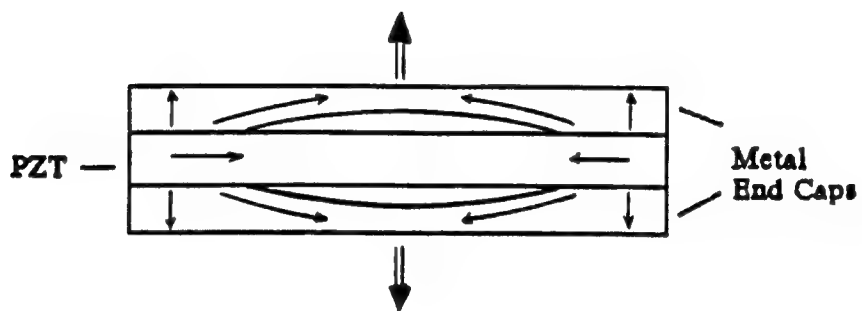


FIGURE 1. The geometry of the ceramic-metal composite actuator "Moonie".
Arrows describe the direction of displacement.

Measurement Technique

The displacement of the composite actuator was measured using a Linear Voltage Differential Transducer (LVDT) at 0.01 Hz, which had a resolution of approximately 0.05 μm . Results were confirmed by an eddy current type non-contact displacement transducer. For generative force measurements, force was applied to the surface of the moonie using a wide angle curved tip with diameter 12 mm and the experiment was stopped before causing any permanent deformation to the end caps. The piezoelectric coefficient d_{33} was measured at the center of the sample using a modified Berlincourt d_{33} meter at a frequency of 100 Hz. The same coefficient was measured by converse piezoelectric effect using a double beam laser interferometer. The results were in good agreement.

EXPERIMENTAL RESULTS

Thickness Dependence of Displacement Values

Figure 2 shows the displacement at the cap center versus electric field for composite actuators with different brass thicknesses. The displacement of the uncapped PZT ceramic is also shown for comparison. The results show that a composite actuator with 0.30 mm brass thickness can produce a displacement about 20 times larger than that of PZT alone. The displacement amplification is inversely related to the thickness of the metal end caps. FEA calculation agreed very well with the experimental results.

Thickness Dependence of Effective d_{33} and Resonance Frequency

Figure 3 shows the dependence of the effective d_{33} coefficient and the first resonance frequency on brass thickness. The effective d_{33} is inversely proportional to h_m (h_m =metal end caps thickness), and the first resonance frequency is roughly proportional to $(h_m)^{1/2}$. By reducing the thickness of the end caps, the effective d_{33} values increase dramatically. An effective piezoelectric d_{33} coefficient of about 13,000 pC/N, approximately 30 times that of PZT-5A, was obtained for a brass thickness of 0.30 mm.

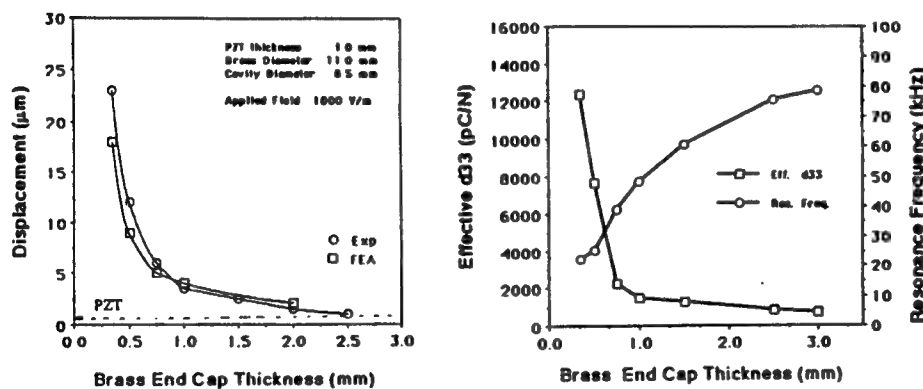


FIGURE 2. Displacement - brass endcaps thickness relation (on the Left)

FIGURE 3. Effective d_{33} & resonance freq. - brass end caps thickness relation

Maximum Generative force of the Moonie

Even though the flexural motion and displacement are the largest at the center of the moonie, the generative force is low. Figure 4 shows the applied force-displacement relation of a moonie actuator operated at 1 kV/mm. A moonie actuator with 0.30 mm thick brass caps can withstand a 210 gf while sacrificing 20% of its displacement value (load applied at the center of the end caps over 1 mm²). The maximum generative force of the moonie actuator with 0.3 mm thick brass end caps should be around 350 gf (i.e the intercept on the force axis). The reason for the saturation near 150 gf is probably due to the increasing contact surface of the LVDT measurement tip.

Trade-off Between Maximum Generative Force and Displacement

The position dependence of displacement is shown in Figure 5 for the moonie actuator with 0.30 mm thick brass end caps. A displacement of about 22 μm was obtained at the center of the moonie. Displacement decreases dramatically when moving from the center to the edge. Conversely generative force is smaller at the center of the moonie actuator. The generative force increases when moving from the center to the edge, where it approaches that of PZT ceramic. Therefore, it is possible to tailor the desired actuator properties by changing the contact area over the brass end caps.

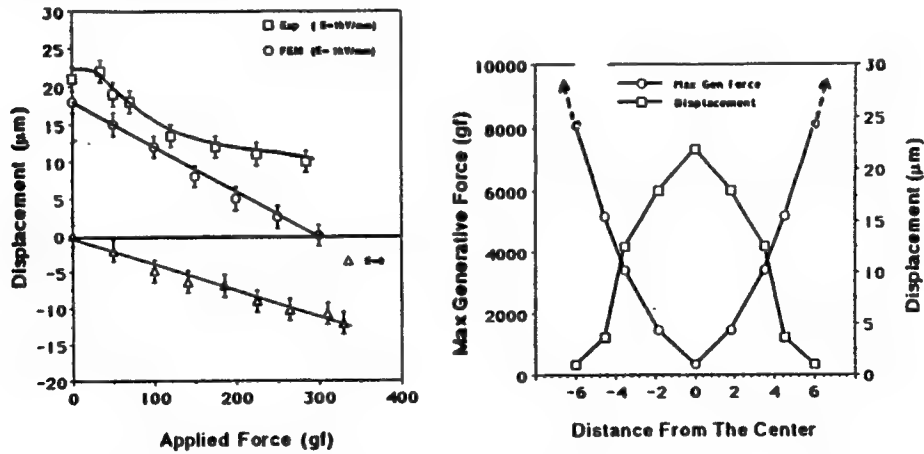


FIGURE 4. Displacement-applied force relation (on the left)

FIGURE 5. Position dependence of max. generative force and displacement

Multilayer Multistacked Moonie Actuator

A multilayer actuator can also be used as the ceramic element in the moonie design, making it possible to decrease the applied voltage without losing the high displacement. A moonie with a multilayer is called a "multilayer moonie". Even higher displacement values can be obtained by stacking multilayer moonies together, which is called a "multi-multi moonie". Figure 6 shows the basic design of the multi-multi moonie. The displacement characteristics of different actuators with the same size and under the same applied voltage are compared in Figure 7. The multi-multi moonie, which has a 10 mm diameter and 10 mm total thickness and consists of 5 multilayer moonie, shows more than 105 μm displacement. However, the interstacke bonding layers cause an increase in hysteresis and a reduction in the total displacement. A standard multilayer actuator of the same thickness shows only a 7.5 μm displacement. Therefore, it is possible to amplify the displacement value almost 15 times using the multi-multi moonie design.

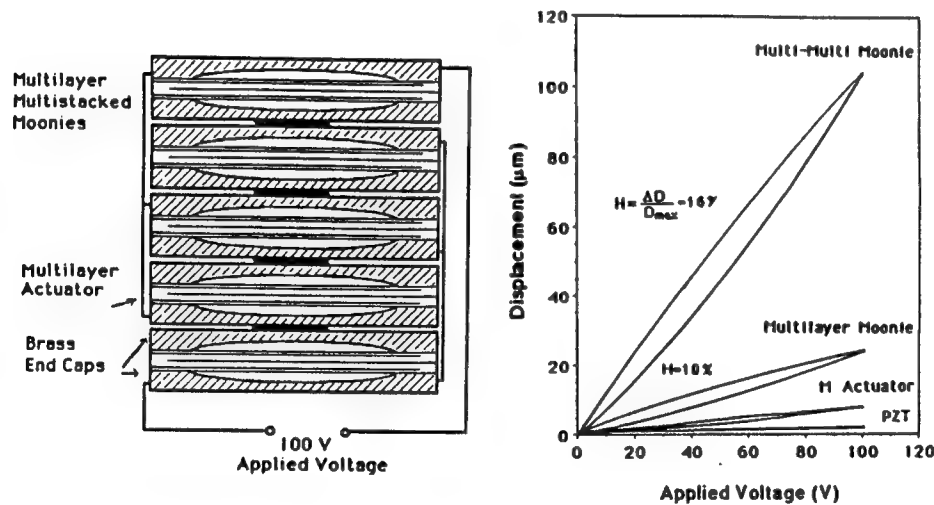


FIGURE 6. Structure of multilayer-multistacked moonie (on the left)

FIGURE 7. Comparison of displacement values of several actuators

CONCLUSION

Three important criteria for actuators are displacement, generative force, and response time. The properties of the moonie actuator (10 mm in diameter with 0.3 mm thick end caps, ≈ 1.7 mm in total thickness) can be summarized as: displacement ≈ 22 μm , maximum generative force ≈ 350 gf, response time ≈ 100 μsec . Moreover, there is a trade off among these criteria. The moonie actuator gives displacement of 22 to over 100 μm , maximum generative force of 350 gf to several kgf, and response time of 20 to 100 μsec . By altering some of the dimensions on the moonie design, it is easy to tailor an actuator with desired properties. Figure 8 compares the important characteristics of the two most common actuators with the moonie actuator. The moonie actuator is a versatile performer that fills the gap between the multilayer actuator and the bimorph actuator and covers a wide range in the actuator field.

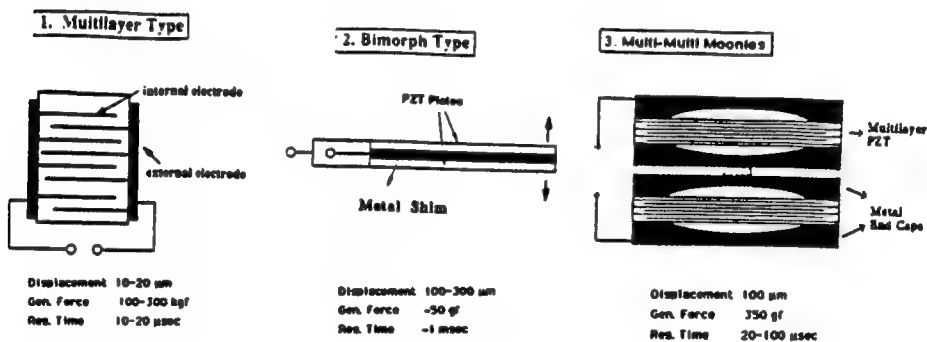


FIGURE 8. Comparison of multi-multi moonie with other actuators

REFERENCES

1. K.Uchino, Piezoelectric/Electrostrictive Actuator (Morikita Publishers, Tokyo 1986)
2. Y.Sugawara, K.Onitsuka, S.Yoshikawa, Q.C.Xu, R.E.Newnham and K.Uchino, *J. Am. Ceram.Soc.* **74**, No 4, pp.996, 1992
- 3.Q.C.Xu, A. Dogan, J. Tressler, S. Yoshikawa, and R.E.Newnham, IEEE Ultrasonic Symposium Proceedings (Florida, 1991)

APPENDIX 39

MANUFACTURING TECHNOLOGY OF MULTILAYERED TRANSDUCERS

Kenji Uchino

International Center for Actuators and Transducers

Materials Research Laboratory, The Pennsylvania State University
University Park, PA 16802

ABSTRACT

Multilayer structures have been investigated intensively in the application fields of ferroelectric ceramics; dielectrics, piezoelectrics and electrooptics. General problems for manufacturing actual devices are discussed and possible solutions are introduced in this paper, focusing on particle and grain size effects on properties, electrode materials and designs, and reliability issues of hybrid structures. Key words to the future trend will be "finer" and "hybridization."

INTRODUCTION

In the recent application fields of ferroelectric ceramics, multilayered structures have been investigated intensively, aiming at miniaturization and hybridization of the devices. Figure 1 exemplifies multilayer, multimorph and multi-moonie structures. This paper reviews the applications of these devices first, then the preparation processes, and finally current problems are pointed out and possible solutions are introduced.

Key words to the future trend will be "finer" and "hybridization." Layers thinner than 10 μm will be used instead of the present 100 μm sheets. Non-uniform configurations or hetero-structures of the materials, layer thickness or the electrode pattern will be adopted for practical devices.

APPLICATIONS OF MULTILAYERED CERAMICS

Multilayered structures are widely utilized in the application fields of dielectrics, piezoelectrics and electrooptics.

Multilayered Dielectrics

Electrostatic capacitance of a multilayer capacitor is given by the following formula:

$$C = n\epsilon\epsilon_0 S / (L/n), \quad (1)$$

where ϵ is the relative permittivity of the material, n the number of layers, S area, and L is the total thickness of the capacitor. Note that the capacitance increases drastically in proportion to the square of the number of layers, when the total size is fixed. The conventional capacitor of 10 μF with 30 μm layer thickness used to have 70 mm^3 in volume size. With decreasing the layer thickness down to 10 μm , the device volume could be reduced into 7.7 mm^3 .¹⁾

Multilayered substrates are also very promising for making a hybrid structure of an electrical circuit. Figure 2 shows a sectional view of a monolithic multicomponents-ceramic for a voltage controlled crystal oscillator,²⁾ where resistors and capacitors are included in the substrate.

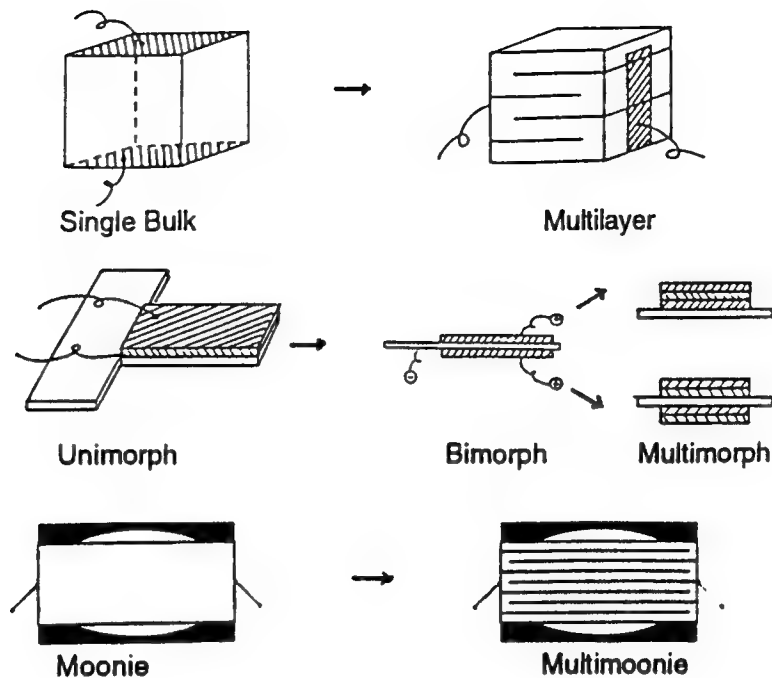


Fig.1 Examples of multilayer, multimorph and multi-moonie structures.

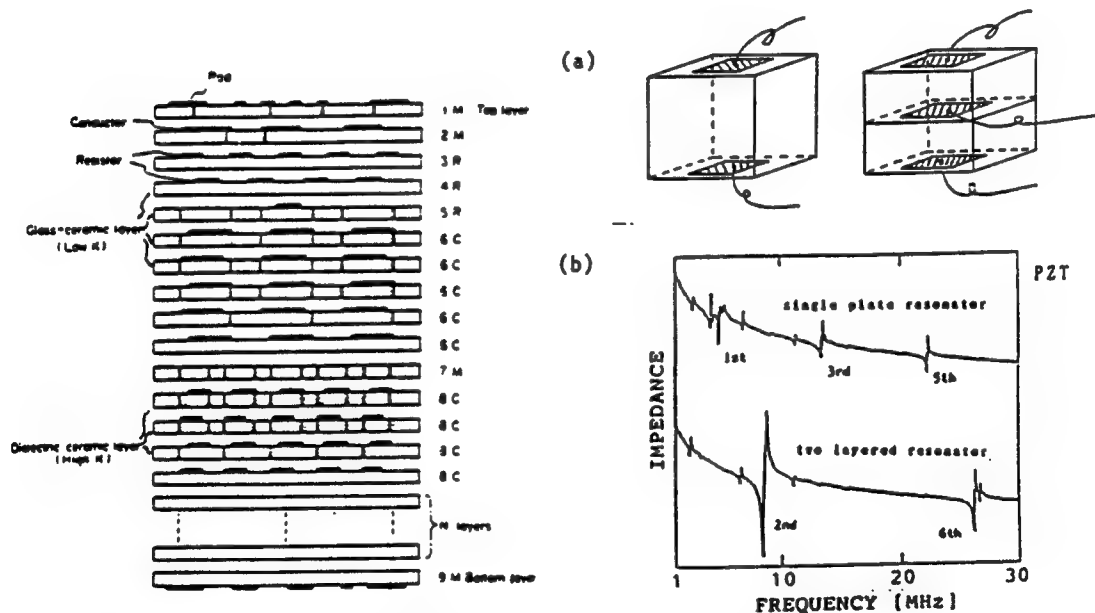


Fig.2 Section view of a monolithic multicomponent ceramic.

Fig.3 (a) Single- and two-layer piezo-resonators. (b) Impedance curves.

Piezoelectric Multilayers

A two-layered piezoelectric resonator has been proposed for a higher-order mode oscillator.³⁾ Figure 3(a) illustrates single- and two-layered structures and Fig. 3(b) shows impedance curves for these two resonators as a function of frequency. It is notable that the second-order harmonic mode is significant in the two-layered structure compared with the fundamental mode.

Multilayer piezoceramics have been applied to actuators. First example is found in an ultrasonic linear motor.⁴⁾ The merits of the usage of a multilayer structure are low drive voltage and a large value of ratio of input electrical energy over volume. The motor consists of a metal fork and a piezoelectric element (Fig. 4(a)) and the motion of the fork legs is illustrated in Fig. 4(b). The maximum speed of 30 cm/s and the maximum load (thrust) of 10 N were realized for the input energy of 0.7 W with an efficiency of 16 %.

Second example is a dot matrix printer.⁵⁾ The displacement of 16 μm in a 20 mm-long piezo-actuator is magnified by 30 times with a hinge lever mechanism as shown in Fig. 5(a). And 24 head elements are arranged to make a printer head for Chinese characters (Fig. 5(b)). The printing speed of 100 characters /sec is 3 times quicker than the conventional electromagnetic printer.

Thirdly, a deformable mirror is introduced,⁶⁾ which is useful for the phase matching of the light wave in image detectors such as an astronomic telescope. The device consists of three plates of lead magnesium niobate based (PMN) electrostrictive ceramics bonded together with a glass mirror. Each ceramic plate possesses a different electrode pattern to generate focus or coma aberration on the mirror surface (See Fig. 6(a) and (b)).

A laser beam scanner is the most recent application of a multi-moonie actuator.⁷⁾ The moonie consists of a thin multilayer ceramic element and two metal plates with a narrow moon-shaped cavity bonded together, and can amplify the small displacement induced in a piezoelectric ceramic. The moonie with a size of 5mm x 5mm x 2.5mm can generate a 18 μm displacement under 60 V, which is an order of magnitude as large as the generative displacement of the multilayer with the same size. This compact actuator has been applied to make a miniaturized laser beam scanner for laser printers (Fig. 7).

Multilayer Electrooptic Devices

In order to reduce the half-wavelength voltage (i. e. drive voltage), the multilayer structure is also used in electrooptic devices. Figure 8 shows a PLZT (lead lanthanum zirconate titanate) light valve with internal electrodes. An order of magnitude smaller voltage (100V) is sufficient to drive the valve in comparison with the usual shutter.

A recent application is found in a 2-dimensional display for projection type TV's.⁸⁾ Hundreds of PLZT sheets are stacked alternately with plate-through and separate electrodes, as shown in Fig. 9(a). Plate-through and separate electrodes are used for horizontal and vertical addressing, respectively. A pixel consists of a pair of PLZT sections beside a plate-through electrode (Fig. 9(b)). Figure 9(c) shows a character "F" projected on a screen.

PREPARATION PROCESS OF MULTILAYERED STRUCTURES

Two preparation processes are possible for multilayered ceramic devices: one is a cut-and-bond method and the other is a tape-casting method. Figures 10(a) and 10(b) show the flow-charts of the both methods. The tape-casting method requires expensive fabrication facilities and sophisticated techniques, but is suitable for mass-production.

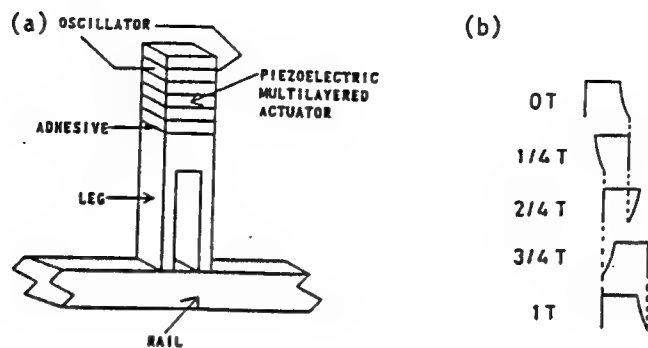


Fig.4 (a) Structure of an ultrasonic linear motor. (b) Motion of the fork legs.

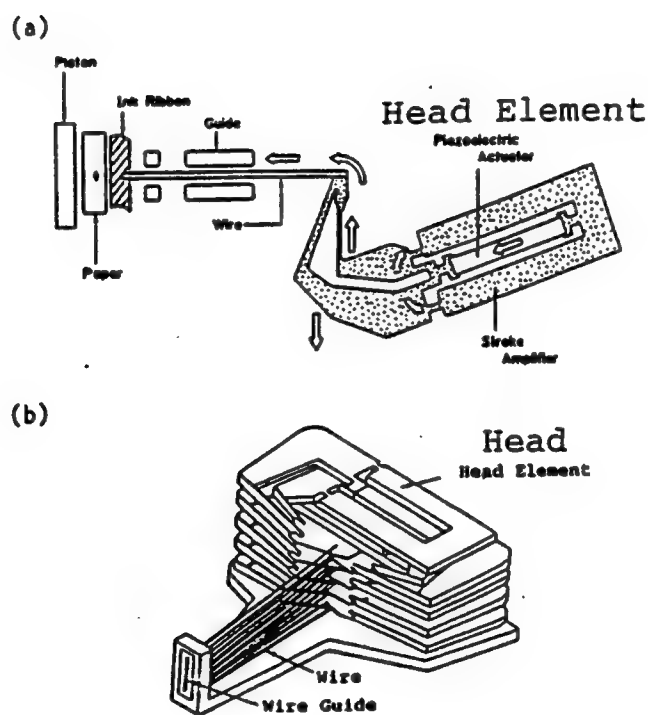


Fig. 5 (a) Printer head element consisting of a multilayer piezoceramic.
 (b) Dot matrix printer head.

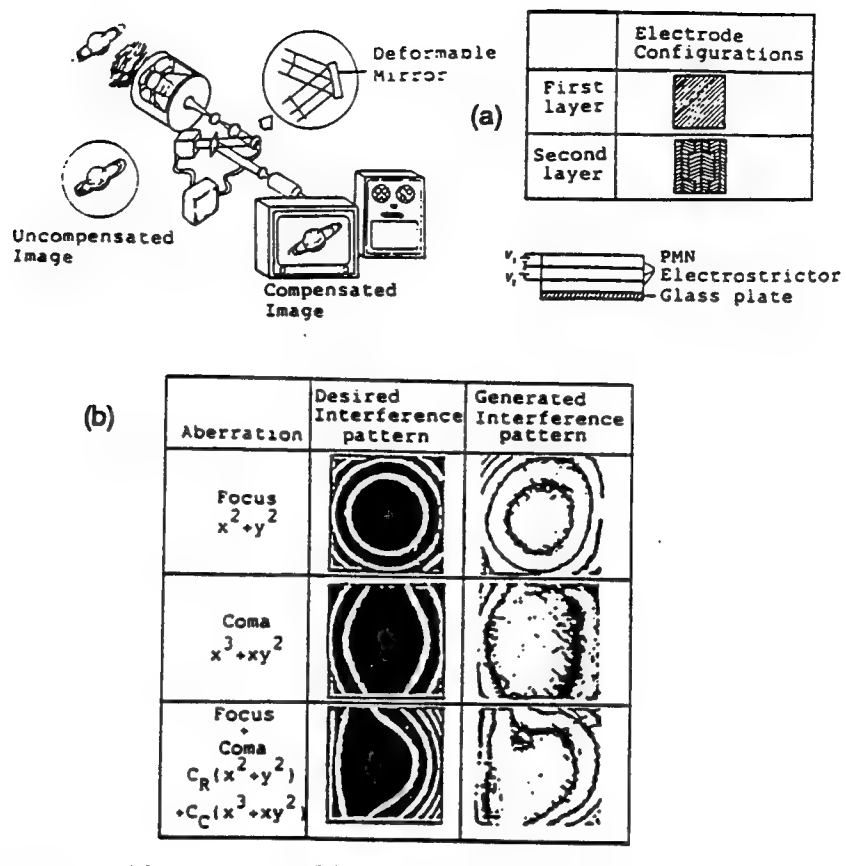


Fig.6 (a) Structure of a multi-morph deformable mirror. (b) Actual control of wavefront.

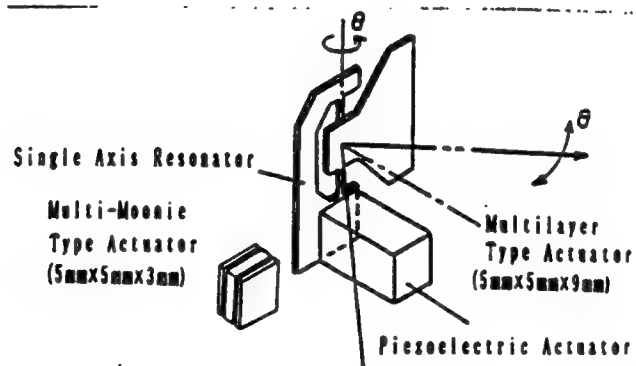


Fig.7 Laser beam scanner utilizing a piezoelectric multi-moonie actuator.

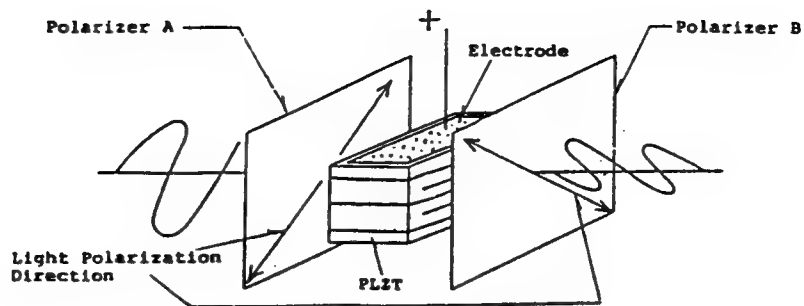


Fig.8 PLZT light valve.

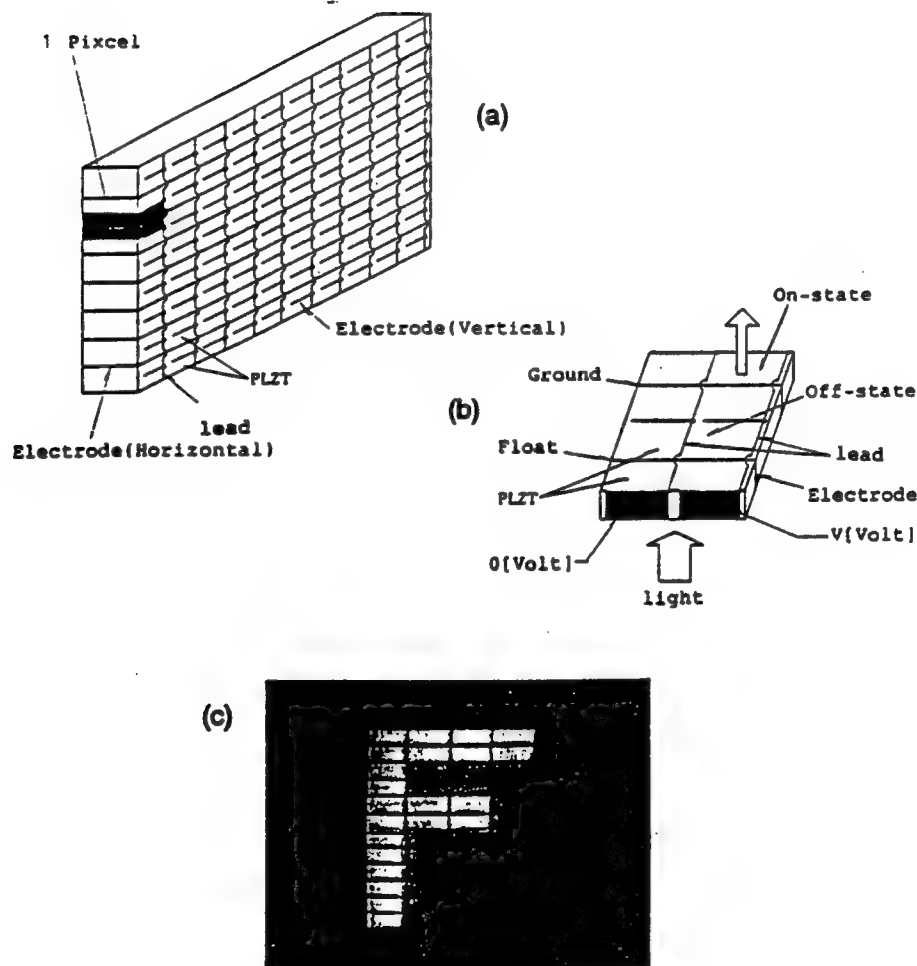


Fig.9 (a) Design of a 2-dimensional display. (b) Operation principle of a pixel.
(c) An example image on the screen.

APPENDIX 40

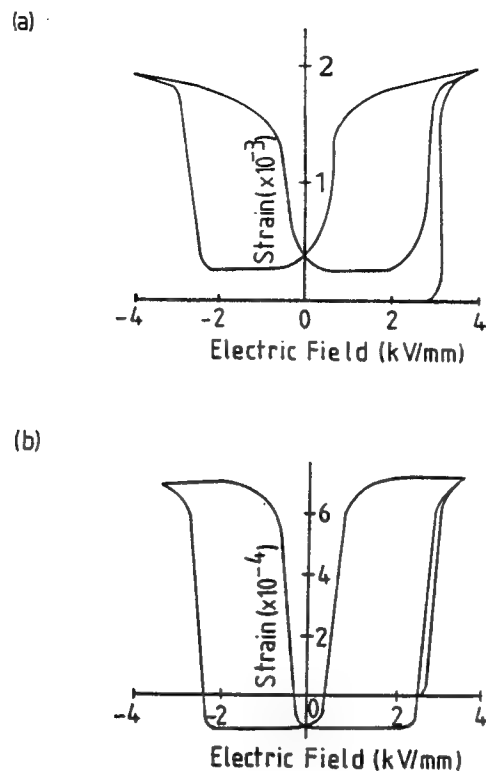


FIGURE 2 Longitudinally (a) and transversely (b) induced strains in the PNZST ceramics under an electric field cycle.

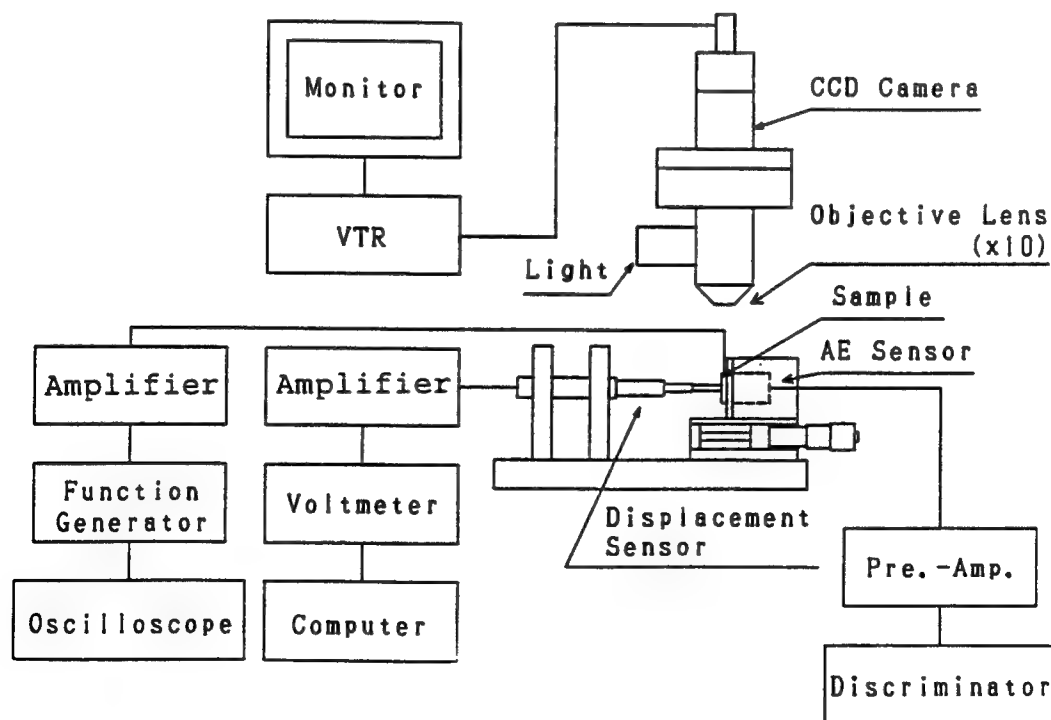


FIGURE 3 Measuring system for the crack propagation experiments.

IK-C40), a displacement sensor (Millitron, Nr. 1301) and an acoustic emission (AE) sensor (NF Circuit Design Block, AE-905). The Charge Coupled Device used here had 400,000 pixels, and 1 μm length on the sample was magnified up to 1 mm on the TV monitor. The crack propagation process was recorded in a VCR (Mitsubishi HV-V36). The AE measuring system has been newly attached, in comparison with the previous set up in Reference 1. The sample was driven by a triangular electric field of $E_{\max} = 40 \text{ kV/cm}$ at 0.1 Hz.

3. RESULTS

3.1 Clamping Effect

The clamping effect on the strain in the multilayer model actuator is illustrated in Figure 4, where l_0 is the length of the plate-through electrode (6 mm) and l_e is the length of the shorter electrode. The displacement of the actuator with the electrode ratio of $l_e/l_0 = 1$ is almost uniform across the actuator face. On the other hand, the displacement of the sample with $l_e/l_0 = 0.85$ or 0.61 is reduced remarkably outside the electrode edge, i.e., in the electrostrictively inactive region. Therefore, a large internal stress should be induced near the boundary between the active and inactive portions of the multilayer model actuator. The clamping effect becomes even bigger by enlarging the inactive region.

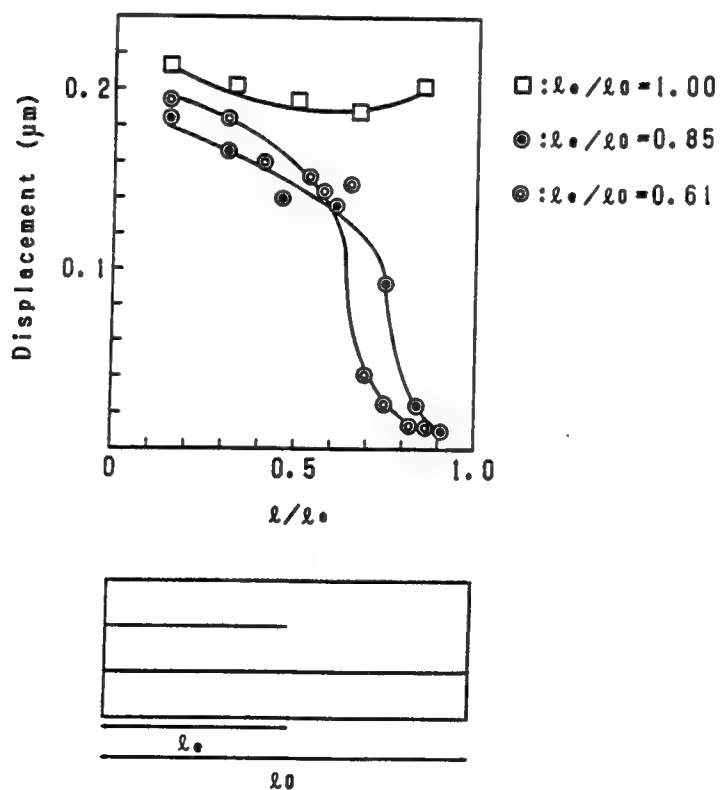


FIGURE 4 Clamping effect in the multilayer model actuators with an interdigital electrode configuration.

3.2 Crack Propagation

Crack generation and propagation resulting from the internal stress was observed and recorded dynamically using a CCD microscope and a VTR recorder.

Figure 5 shows a typical crack propagation process observed for a sample having a layer thickness of 200 μm . Although some pores exist in the sample, the uniform

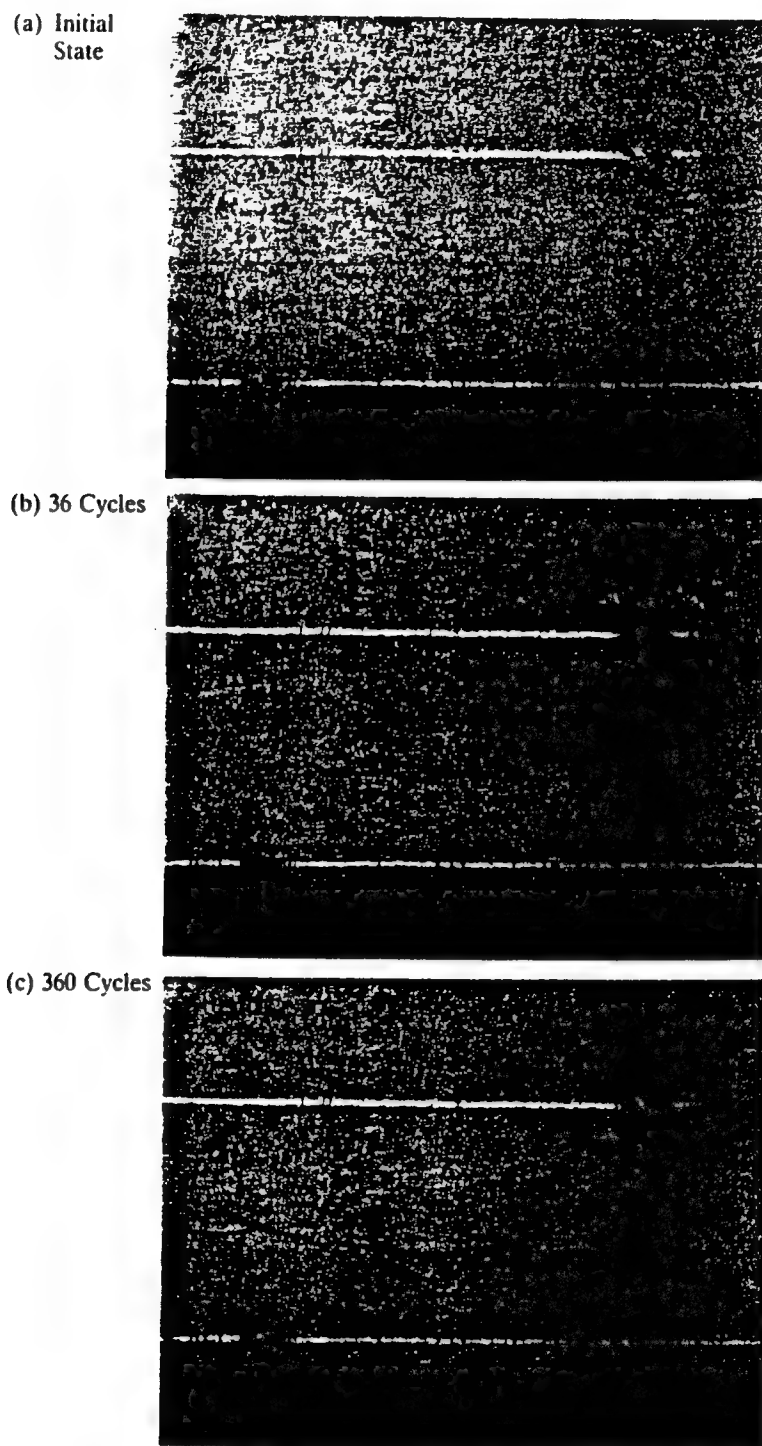


FIGURE 5 Crack generation and propagation process in the multilayer model actuator.

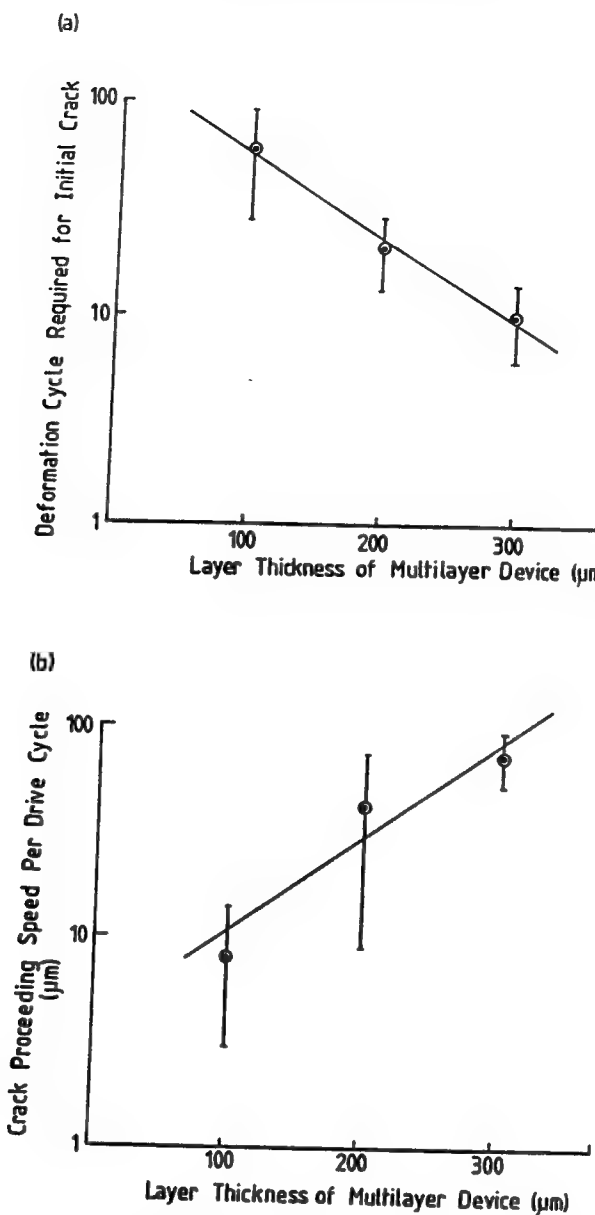


FIGURE 6 Layer thickness dependence of the critical deformation cycle required for the initial crack generation (a), and of the crack propagation speed per drive cycle (b).

existence might not give significant effect on the crack propagation mechanism. The series of pictures was copied from the VCR tape. The crack initiates between the electrodes slightly inside the electrode edge after 36 electric field cycles in this sample. The crack then propagates along the center area between the electrode pair (48 cycles), then finally branching around the electrode edge after 360 cycles. It is noteworthy that the crack opens widely under the electric field and closes at zero field.

This result is different from that of piezoelectric multilayer model actuator. In the case of piezoelectric actuators, the crack is initiated at the electrode edge and propagates in three directions from the electrode edge: two cracks move toward the other electrostrictively inactive region, and one moves toward the ceramic-electrode interface.

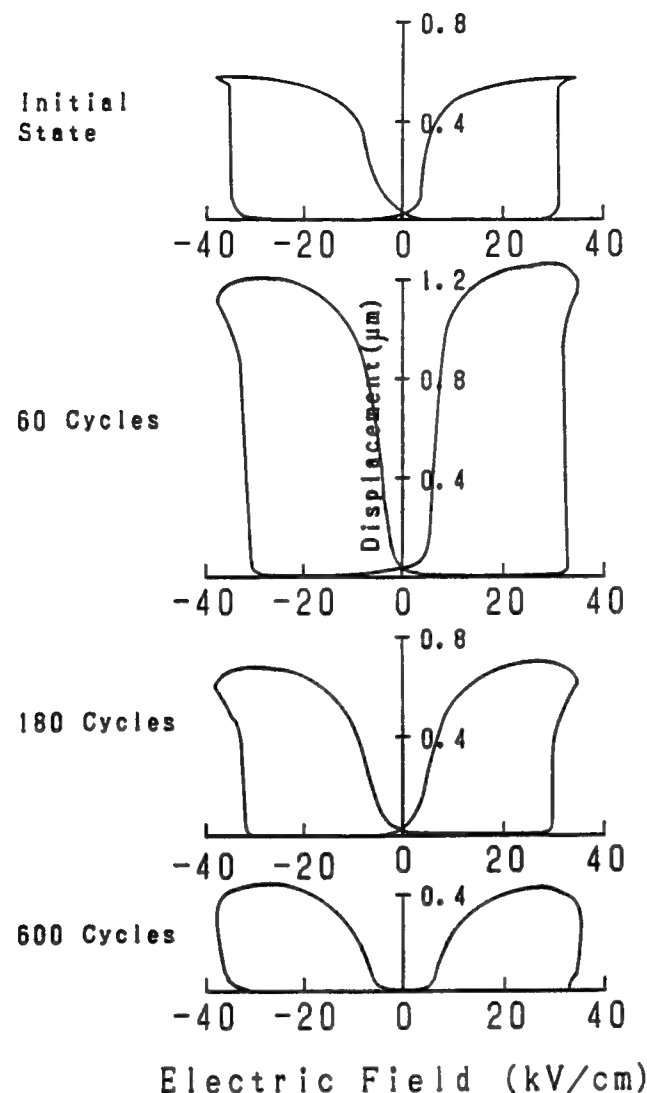


FIGURE 7 Variation of the displacement during the destruction ($\text{Pb}_{0.99}\text{Nb}_{0.02}[(\text{Zr}_{0.7}\text{Sn}_{0.3})_{0.955}\text{Ti}_{0.045}]_{0.98}\text{O}_3$).

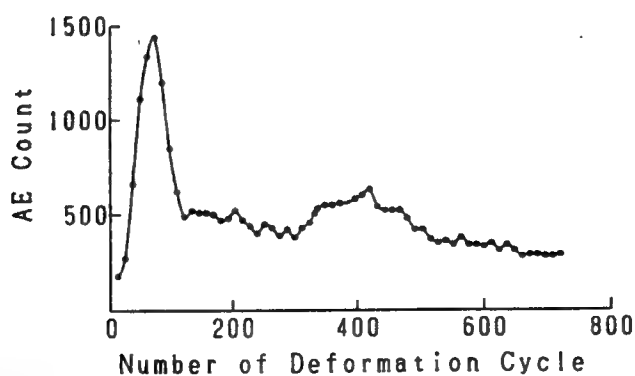


FIGURE 8 Changes in acoustic emission count during the fracture process ($\text{Pb}_{0.99}\text{Nb}_{0.02}[(\text{Zr}_{0.7}\text{Sn}_{0.3})_{0.955}\text{Ti}_{0.045}]_{0.98}\text{O}_3$).

The difference is probably due to the difference in internal stress distribution. The sign of the longitudinally-induced and transversely-induced strains is opposite in the piezoelectrics, while in antiferroelectrics undergoing a phase change rather isotropic expansive strains are induced in the both directions. Therefore, the internal stress distribution in antiferroelectrics differs from that of piezoelectrics. Theoretical calculations of the internal stress distribution are now in progress.

Similar crack propagation processes were observed in the samples with layer thicknesses of 100 μm and 300 μm , when driven by the same electric field. However, significant differences were recognized in the fracture toughness. Figures 6(a) and 6(b) plot the layer thickness dependence of the critical deformation cycles required for the initial crack generation and of the crack propagation speed per drive cycle.

It is very interesting that a dramatic improvement in the fracture toughness is observed in the thinner layer sample, even though the driving electric field is the same for all three samples.

The reason is not clear, but it may be related to the ratio between the grain size ($\sim 5 \mu\text{m}$) and the layer thickness. This result reminds us of a general empirical rule of dielectric ceramics: with reducing the film thickness, the electrical breakdown field increases remarkably. Further investigation is required.

3.3 Displacement Change During Failure

The destruction of the device brings a change in the induced displacement. Figure 7 shows the variation of the induced displacement during the crack propagation process for the model actuator with a layer thickness of 200 μm . The initial displacement of about 0.6 μm doubles after 60 cycles. This can probably be attributed to the bending deformation associated with the crack opening and closing process. Further increases in the number of deformation cycles leads to a decrease in the magnitude of the displacement. This observation can be explained by a decrease of the effective electric field in the ceramics caused by the narrow air gap associated with crack formation.

3.4 Variation of Acoustic Emission Count

Acoustic emission events (AE) were counted during the destruction process of the sample with a layer thickness of 200 μm (Figure 8). The AE count increases remarkably after the crack initiation, reaching a maximum at 60 cycles, where the crack propagation speed is maximum and the largest displacement is observed. Later, the acoustic emission count leveled off after the crack was completed.

In the previous paper, we suggested that the acoustic emission might be a good predictor for recent experiments actuator failure.⁷ This results supports this suggestion.

4. SUMMARY

- (1) In order to investigate crack propagation mechanism in antiferroelectric multilayer actuators, we have fabricated model actuators which generate high speed

cracks. The fracture generation and propagation was observed dynamically during cyclical electric fields using a CCD microscope. Simultaneous measurements of the induced displacement and acoustic emission were also carried out.

(2) The crack begins slightly inside the edge of the internal electrode and propagates along the center area between the pair electrodes. Later crack branches are generated around the electrode edge. This result is different from that of a piezoelectric actuator.

(3) Reducing the layer thickness of the ceramic actuator, leads to a drastic improvement in fracture toughness.

REFERENCES

1. T. Yano and S. Takahashi, *Trans. IEICE*, **J71-C11**, 1576 (1988).
2. S. Moriyama and F. Uchida, *JSPE*, **50**, 718 (1984).
3. Atsushi Furuta and Kenji Uchino, *J. Am. Ceram. Soc.*, **76**, 1615 (1993).
4. Sadayuki Takahashi, Atsushi Ochi, Masatomo Yonezawa, Takeshi Yano, Takeshige Hamatsuki and Izumo Fukui, *Jpn. J. App. Phys.*, **22**, 157 (1983).
5. D. Berlincourt, H. H. Kruger and B. Jaffe, *J. Phys. Chem. Solids*, **25**, 659 (1964).
6. K. Uchino, *MRS Int'l. Mtg. on Adv. Mtls.*, **9**, 489 (1989).
7. Terukiyo Hirose and Kenji Uchino, *Ferroelectrics*, **87**, 295 (1988).

APPENDIX 41

Destruction Mechanisms in Ceramic Multilayer Actuators

Hideaki ABURATANI¹, Shuichi HARADA², Kenji UCHINO^{1,2}, Atsushi FURUTA³
and Yoshiaki FUDA³

¹*International Center for Actuators and Transducers, The Pennsylvania State University,
University Park, Pennsylvania 16802, USA*

²*NF Electronic Instruments Inc., 1352 South Atherton Street, State College, Pennsylvania 16801, USA*

³*Tokin Corporation, 6-7-1 Koriyama, Taihakku, Sendai 982*

(Received November 29, 1993; accepted for publication February 19, 1994)

Destruction mechanisms were investigated in electrostrictor, piezoelectric and phase-change antiferroelectric ceramic multilayer actuators with an interdigital electrode configuration. Simultaneous observations were done by three different methods; visual observation with a charge coupled device (CCD) microscope, field-induced strain and acoustic emission (AE) measurements. During a cyclic electric field application, the crack was initiated from the edge of an internal electrode and propagated obliquely to another electrode in the piezoelectric sample, while in the antiferroelectric, the crack was initiated between a pair of electrodes and propagated parallel to the electrodes. The field-induced strain curve exhibited asymmetric and enhanced strains in all the samples during the crack propagation, probably due to the internal delaminations. The AE count also increased drastically before the destruction.

KEYWORDS: acoustic emission, actuator, antiferroelectric, crack, electrostrictor, piezoelectric, stress

1. Introduction

Ceramic multilayer actuators are applicable to precise positioners, because of their quick response, large generative force and high electromechanical transduction capability. They are becoming key components in semiconductor manufacturing processes, precision cutting machines etc.¹⁻⁵ With the expanding the applications, the durability and reliability of the actuators have become very important issues.

Figure 1(a) shows a typical interdigital electrode configuration of a multilayer-type actuator. In this structure, at the boundary between electrostrictively active and inactive parts (around the electrode edge region), the internal stress concentration should arise under an electric field. This internal stress concentration may cause self-destruction.⁶ The magnitude of the maximum tensile stress was estimated to be as large as the destruction strength of the ceramic (1×10^8 Pa). Our group was the first to visually observe the dynamic crack initiation and propagation process using a charge coupled device (CCD) microscope.⁷

This paper describes more systematically the destruction process in three different ceramic actuator materials: piezoelectric, electrostrictive and phase-change materials. Moreover, three different observation techniques were used simultaneously in this study: visual observation with a CCD microscope, field-induced strain measurement and acoustic emission (AE) monitoring. The results indicate that the AE count is one of the best destruction-prediction methods for establishing an "intelligent" actuator system with a safety mechanism.

2. Experimental

The multilayer model actuators used in this study were prepared by the tape casting method (Fig. 1(b)). This model actuator simulating the interdigital electrode configuration had two electrostrictively active layers with an electrode gap of 200 μ m. Two electrode

side gaps (0.5 mm and 3 mm) were formed to change the electric field concentration (see (i) and (ii) in Fig. 1(b)). The three compositions $0.9\text{Pb}(\text{Mg}_{1/3}\text{Nb}_{2/3})\text{O}_3 - 0.1\text{PbTiO}_3$ (PMN-PT), $\text{Pb}((\text{Ni}_{1/3}\text{Nb}_{2/3}), \text{Zr}, \text{Ti})\text{O}_3$ (PNNZT) and $\text{Pb}_{0.99}\text{Nb}_{0.02}((\text{Zr}_{0.7}\text{Sn}_{0.3})_{0.955}\text{Ti}_{0.045})_{0.98}\text{O}_3$ (PNZST) were chosen as examples of electrostrictive, piezoelectric and phase-change (antiferroelectric) materials, respectively. The magnitudes of the field-induced strains are 0.1%, 0.2% and 0.4%, respectively. For investigation of the effect of the layer thickness, the AE count of the piezoelectric PNNZT with 100 μ m and 150 μ m, and antiferroelectric PNZST with 100 μ m and 300 μ m electrode gap samples were also measured.

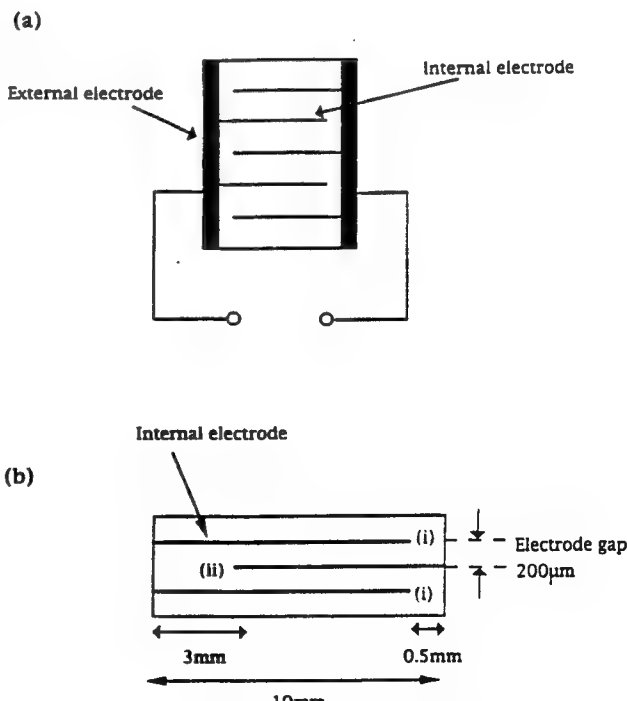


Fig. 1. (a) Actuator with interdigital electrodes. (b) Model actuator used in the experiment.

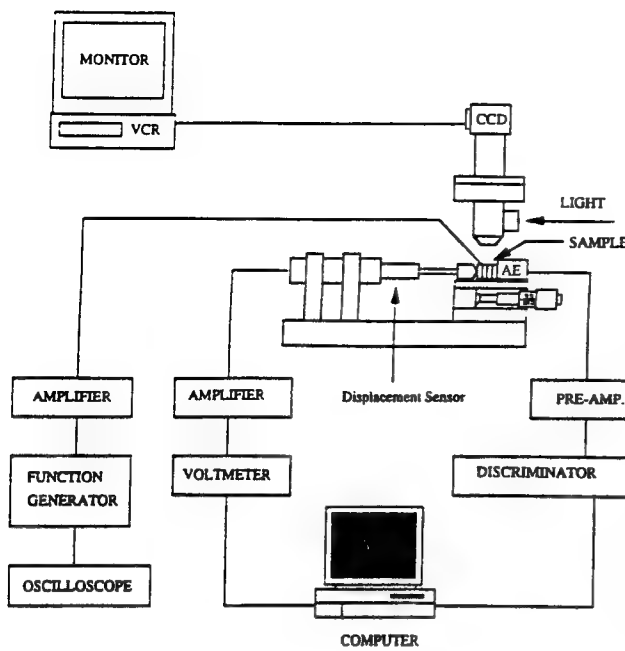


Fig. 2. Measuring system of the destruction mechanism.

Figure 2 shows the measuring system consisting of a microscope (ELMO, Model MS-VII-A) with a CCD (Toshiba, Model IK-C40), a displacement sensor (Millitron, Model 1301) and an acoustic sensor (NF Corporation, AE-905USF116). An excessively large electric field was applied (NF Corporation, Model 4045) in order to accelerate the actuator collapse. The samples were bipolar-driven at 1 Hz by a triangular electric field of ± 2.0 kV/mm for the electrostrictor and piezoelectric, and ± 4.0 kV/mm for the antiferroelectric. The crack propagation process was recorded by VCR, and the induced strain and the AE count data were stored in a computer.

3. Results and Discussion

3.1 Crack propagation

Figure 3 shows typical cracking patterns in the piezoelectric PNNZT. The crack is usually initiated at the edge of the internal electrode ((i) in Fig. 3(a)) and propagates obliquely outward to another electrode and outward of the electrode ((ii) in Fig. 3(b)). The crack was initiated preferentially in the area (i) to area (ii) of Fig. 1(b). At the same time, delamination is generated between the electrode and ceramic interface ((iii) in Fig. 3(b)), so as to form a final Y-shaped crack branch. This result coincides with theoretically expected electric field/stress-distribution.⁶⁾ Occasionally, a crack which propagates vertically between a pair of internal electrodes is observed, only when an internal defect is located near the electrode ((iv) in Fig. 3(b)).

On the other hand, in the antiferroelectric PNZST, the crack is initiated between the electrodes, grows along the center area, and branches at the electrode edge area (Fig. 4). The difference between the Y-shaped crack location in the piezoelectric and the phase-change materials may be caused by the differ-

ence in the strain induction mechanism: that is, both the field-induced longitudinal and transverse strains in the antiferroelectric are expansive (i.e., the Poisson's ratio is negative), unlike the normal piezoelectric or electrostrictive material.

In both the piezoelectric and antiferroelectric sam-

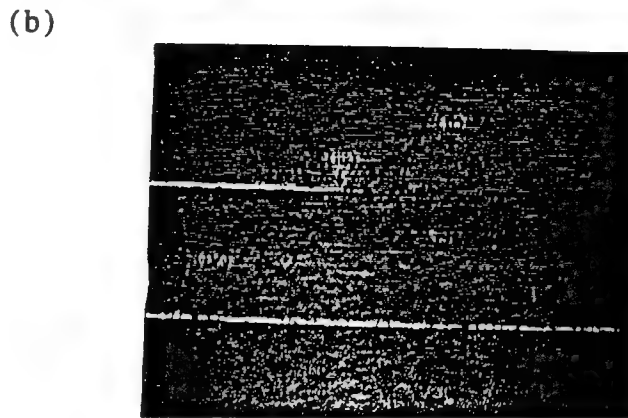
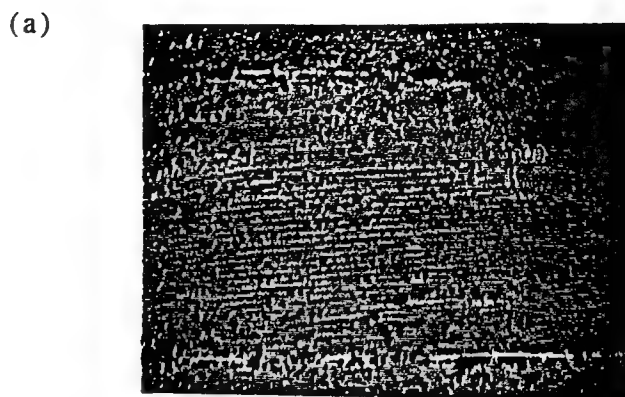


Fig. 3. Cracking patterns in piezoelectric PNNZT.

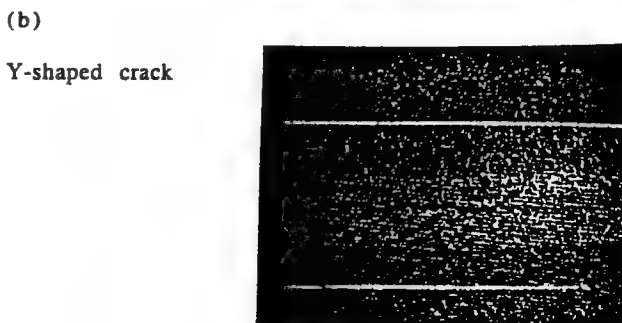
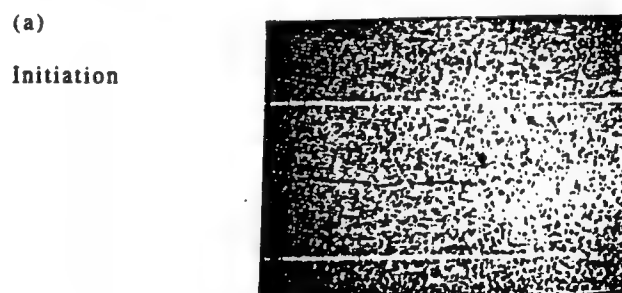


Fig. 4. Cracking pattern in phase-change PNZST.

ples, the destruction processes were easily observed; however, in the electrostrictor the crack propagation was not detected clearly, probably due to the small induced strain level.

3.2 Displacement changes during the destruction

The induced strain changes are shown in Fig. 5. During the crack propagation, the magnitude of the induced strain is increased by 20~40 percent in all samples, with rather asymmetric characteristics compared with the initial state. This enhancement is probably due to the crack opening and closing motions under the field.

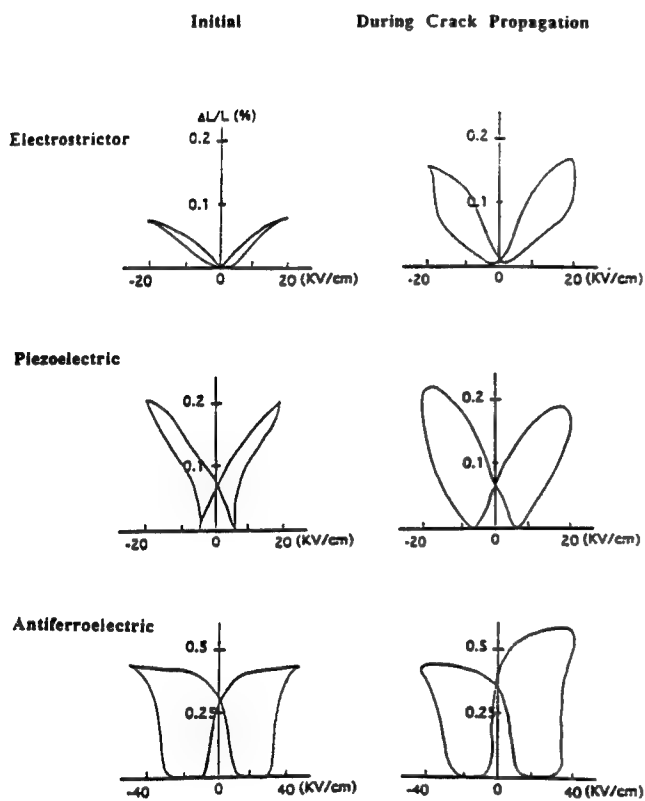


Fig. 5. Induced strain changes during the crack propagation.

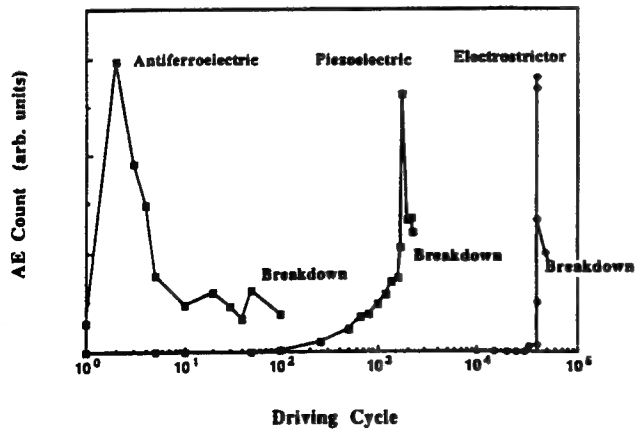


Fig. 6. AE counts accumulated in one drive cycle.

3.3 Acoustic emission

Figure 6 plots the AE counts accumulated in one drive cycle, as a function of total driving cycle for the three samples. All the samples show a remarkable in-

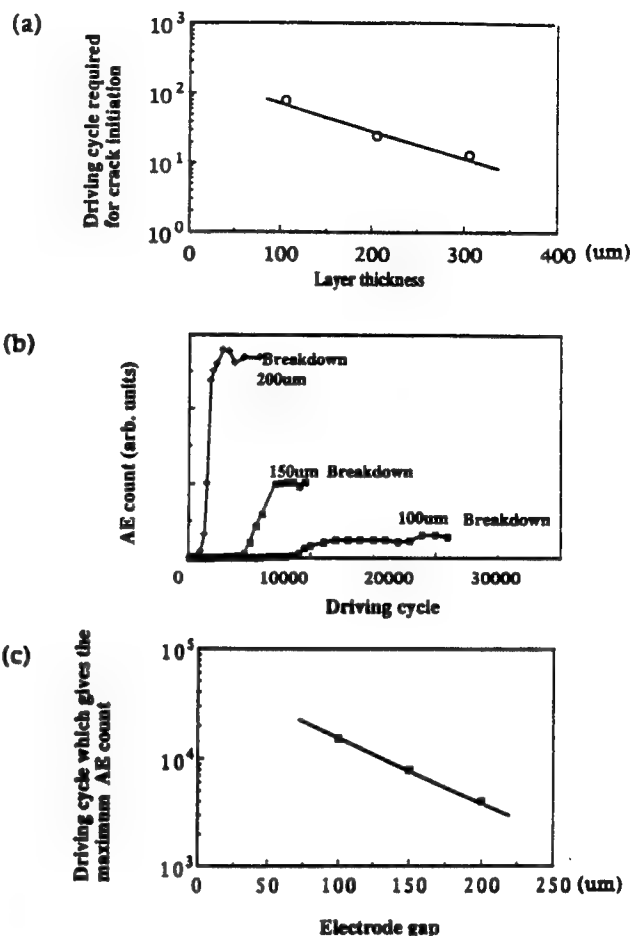


Fig. 7. Layer thickness dependence of the device durability. (a) Electric-field cycle required to initiate the crack in PNZST, (b) AE count change, and (c) electric field cycle necessary to generate the maximum AE count in PNNZT.

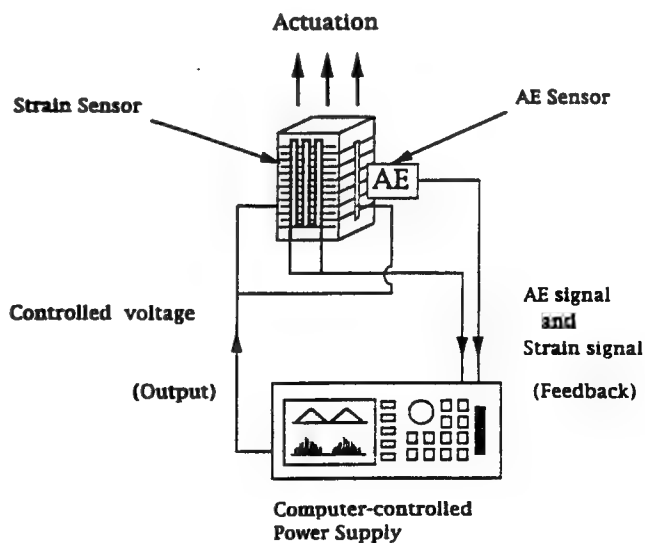


Fig. 8. Intelligent actuator system.

crease in the AE count during the crack propagation and leveling-off after the crack is completed. The significant difference in the breakdown cycle (i.e., durability) among the three samples is probably attributed to the magnitude of the maximum strain; that is, 0.1% in the electrostrictor, 0.2% in the piezoelectric and 0.4% in the antiferroelectric samples.

3.4 Layer thickness dependence of the destruction

A very important empirical rule was clarified during a series of experiment; the durability of the devices is remarkably improved with reducing thickness of the ceramic layers. Figure 7(a) shows the electric-field cycle required to initiate the crack (CCD observation in the antiferroelectric PNZST). Figure 7(b) shows the AE count change for samples with different layer thickness and Fig. 7(c) plots the electric field cycle necessary to generate the maximum AE count (in the piezoelectric PNNZT) as a function of layer thickness. The drive lifetime increases exponentially with decreasing layer thickness.

4. Conclusions

Three different techniques were adopted to clarify the destruction mechanisms of ceramic multilayer actuators: a CCD microscope, induced displacement measurement and acoustic emission monitoring. Somewhat different crack propagation processes were observed

depending on the actuator materials: The crack initiated at the edge of the electrode and formed a Y-shaped crack in the piezoelectric; the crack initiated between the electrodes, propagated in both directions and branched around the electrodes edge area (Y-shaped crack between the electrodes) in the antiferroelectric. Enhancement in the field-induced-strain and in the AE count was observed during the crack propagation.

Finally, an intelligent actuator system with a safety mechanism is proposed in Fig. 8. If the destruction manifestation of the actuator is detected by the AE monitor, the total actuator system will be safely stopped without causing any damage to the controlled system.

Acknowledgment

This work was supported by the Office of Naval Research through Contract No. N00014-92-J-1510.

- 1) K. Uchino: *Piezoelectric/Electrostrictive Actuators* (Morikita, Tokyo 1986).
- 2) K. Uchino: MRS Bull. **18** (1993) 42.
- 3) E. Kouno: CIRP Ann. **33** (1984) 369.
- 4) S. Moriyama and F. Uchida: JSPE **50** (1984) 718.
- 5) T. Yano and S. Takahashi: Trans. IEICE J71-C11 (1988) 1576.
- 6) S. Takahashi, A. Ochiai, M. Yonezawa, T. Yano, T. Hamatsuki and I. Fukui: Ferroelectrics **50** (1983) 181.
- 7) A. Furuta and K. Uchino: J. Am. Ceram. Soc. **76** (1993) 1615.

APPENDIX 42

Destruction Detection Techniques for Safety Piezoelectric Actuator Systems

K. UCHINO AND H. ABURATANI

ABSTRACT

Destruction mechanisms in electrostrictor, piezoelectric and phase-change antiferroelectric ceramic multilayer actuators with an interdigital electrode configuration were investigated. Simultaneous observations were done by four different methods; visual observation with a CCD-microscope, field-induced strain, acoustic emission (AE) and surface potential measurements. During a cyclic electric field application, the crack was initiated from the edge of an internal electrode and propagated obliquely to another electrode in the piezoelectric sample, while in the antiferroelectric, the crack was initiated between a pair of electrodes and propagated parallel to the electrodes. The field-induced strain curve exhibited asymmetric and enhanced strains in all the samples during the crack propagation, probably due to the internal delaminations. The AE count increased and the surface potential decreased drastically just before the destruction.

INTRODUCTION

The expanding number of applications of ceramic actuators has made the reliability of the devices much more important (Kouno, 1984; Moriyama and Uchida, 1984; Yano and Takahashi, 1988; Uchino 1986, 1993). Safety will be the number one priority in ceramic actuator systems, because sudden collapse of the actuator often causes serious problems.

We have been proposing an "intelligent actuator system" containing a position drift compensation mechanism and a safety feedback function, as illustrated in Fig.1 (Aburatani et al., 1994). The latter function can stop an actuator drive safely without causing any serious damages onto the work, e. g. in a precision lathe machine. This paper reports three possible predictors for the actuator failure; induced-displacement monitoring, acoustic emission (AE) counting and surface voltage measurement.

Figure 2(a) shows a typical interdigital electrode configuration of a multilayer type piezoelectric actuator. In this structure, at the boundary

Kenji Uchino, International Center for Actuators and Transducers, Materials Research Laboratory, The Pennsylvania State University, University Park, PA 16802
Hideaki Aburatani, University Park, PA 16802

between electrostrictively active and inactive parts, around the electrode edge region, the internal stress concentration should arise under an electric field applied and may cause self-destruction (Takahashi et al., 1983). The magnitude of the maximum tensile stress was estimated as large as the destruction strength of the ceramic (1×10^8 Pa). Our group was the first to visually observe the dynamic crack initiation and propagation processes using a charge coupled device (CCD) microscope (Furuta and Uchino, 1993).

In this paper, the destruction process has been investigated in three different ceramic actuator materials: piezoelectric, electrostrictive and phase-change materials, using simultaneous four different observation techniques: visual observation with a CCD microscope, field induced strain, acoustic emission (AE) and surface potential measurements. The results indicate that the AE count and potential monitoring are the best destruction-prediction methods to establish an "intelligent" actuator system.

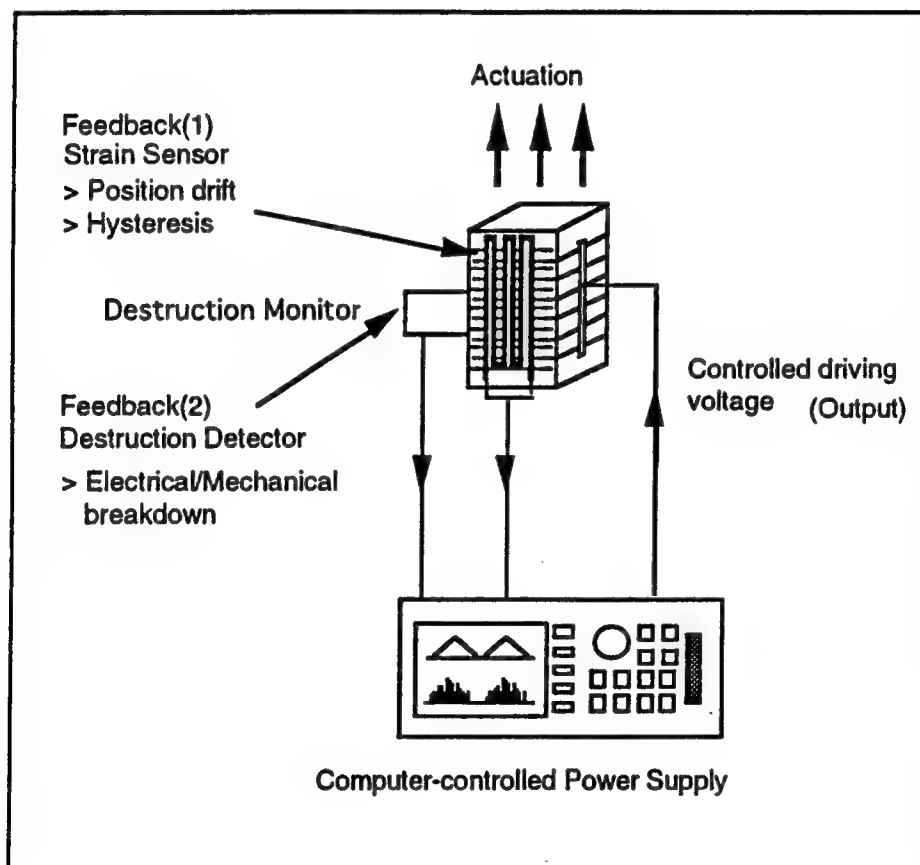


Figure 1 Intelligent actuator system

EXPERIMENTS

The multilayer model actuators used in this study were prepared by a tape casting method (Fig. 2(b)). This model actuator simulating the interdigital electrode configuration had two electrostrictively active layers with an electrode gap 200 μ m. Two electrode side gaps (0.5mm and 3mm) were made to change the electric field concentration. The three compositions $0.9\text{Pb}(\text{Mg}_{1/3}\text{Nb}_{2/3})\text{O}_3\text{-}0.1\text{PbTiO}_3$ (PMN-PT), $\text{Pb}((\text{Ni}_{1/3}\text{Nb}_{2/3})\text{Zr,Ti})\text{O}_3$ (PNNZT) and $\text{Pb}_{0.99}\text{Nb}_{0.02}((\text{Zr}_{0.7}\text{Sn}_{0.3})\text{O}_{0.955}\text{Ti}_{0.045})\text{O}_{0.98}\text{O}_3$ (PNZST) were chosen for the examples of electrostrictive, piezoelectric and phase-change (antiferroelectric) materials, respectively. The magnitudes of the field-induced strains are 0.1%, 0.2% and 0.4%, respectively.

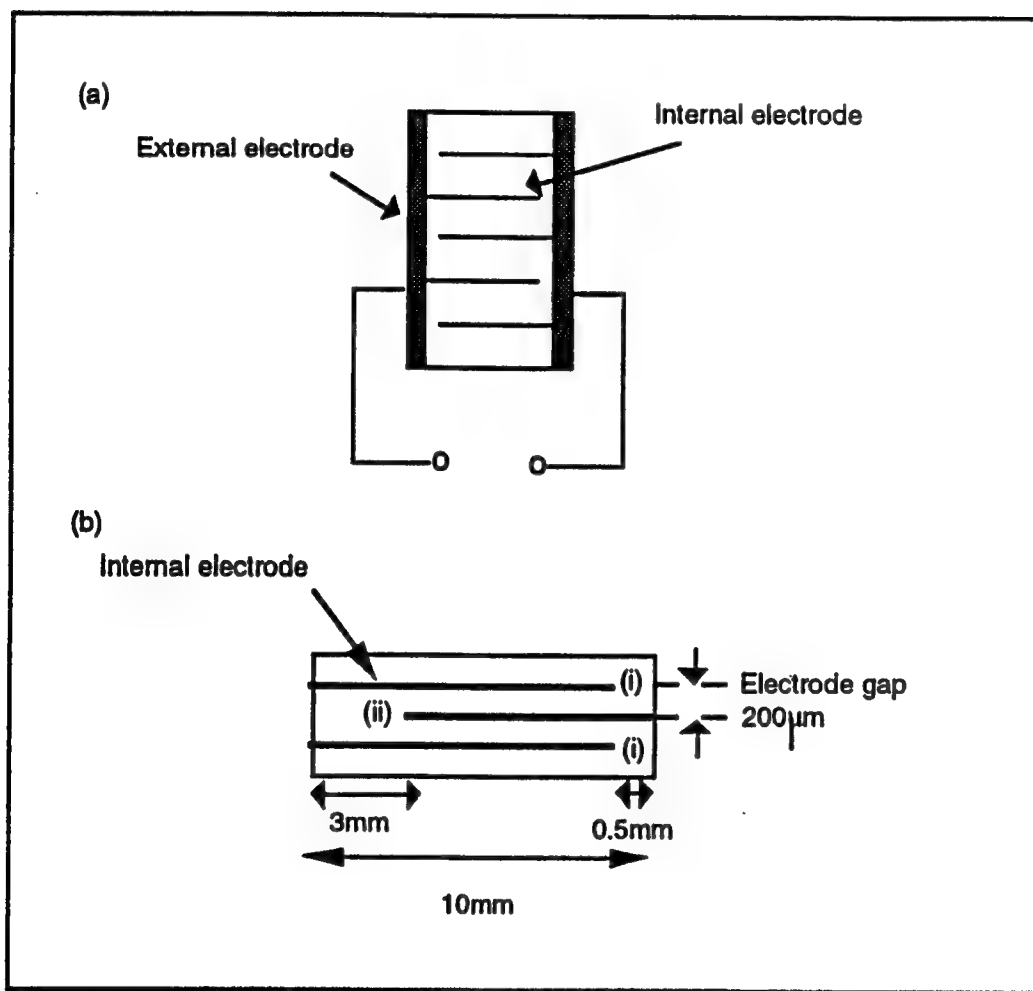


Figure 2 (a) Actuator with interdigital electrodes
 (b) Model actuator used in the experiment

Figure 3(a) shows the measuring system consisting of a displacement sensor (Millitron, Model 1301), an acoustic sensor (NF Corporation, AE-905USF 116) and a voltage meter. An additional surface electrode was coated on the actuator sample near the internal electrode edge to monitor the potential change (Fig. 3(b)). An exaggeratedly large electric field was applied (NF Corporation, Model 4045) in order to accelerate the actuator collapse. The samples were bipolar-driven at 1 Hz by a triangular electric field of $\pm 2.0\text{kV/mm}$ for the electrostrictor and piezoelectric, and $\pm 4.0\text{kV/mm}$ for the antiferroelectric. The crack propagation process was recorded in a VCR, and the induced strain, the AE count and the surface potential data were stored in a computer.

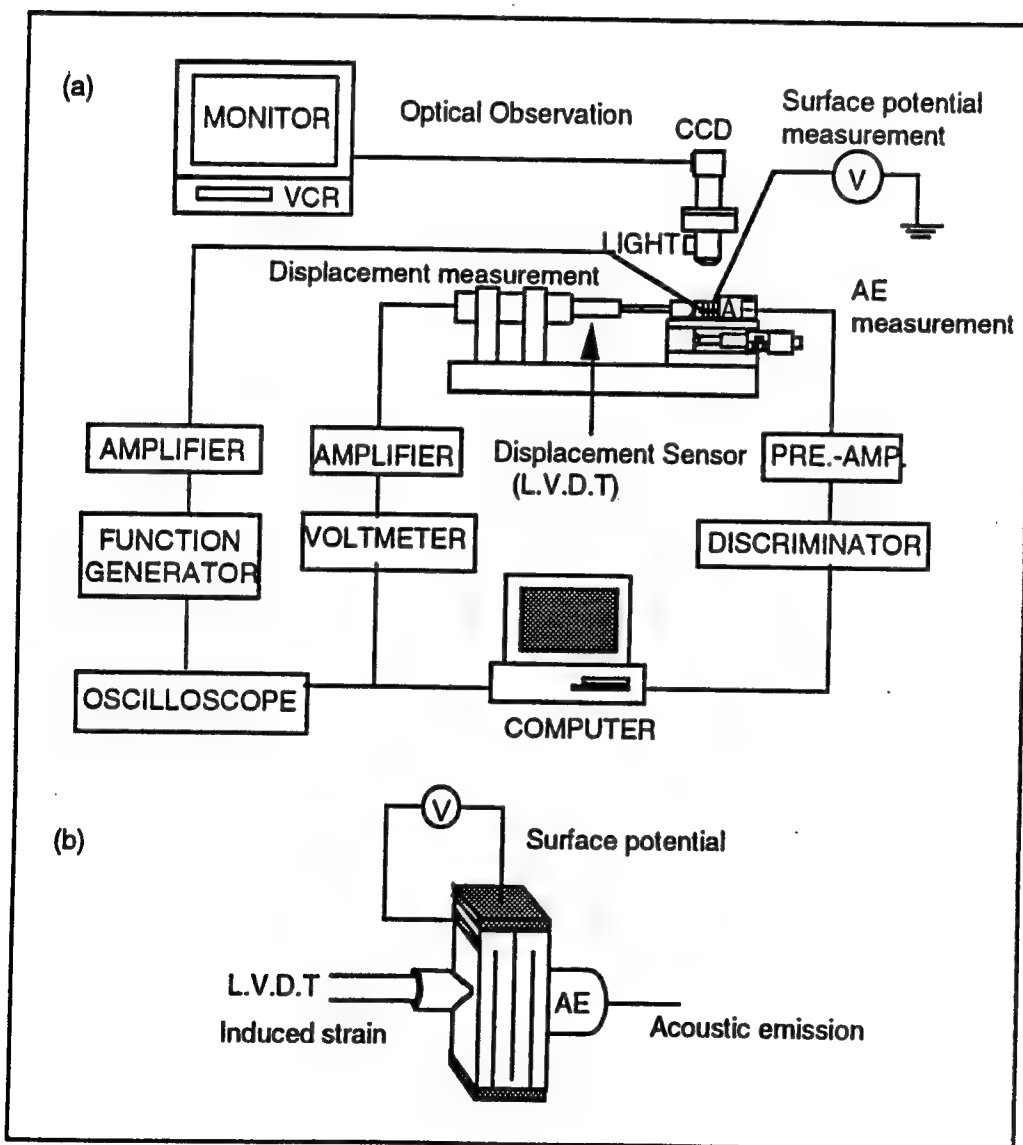


Figure 3 (a) Measurement system
 (b) Sample for surface potential measurement

RESULTS AND DISCUSSIONS

(1) CRACK PROPAGATION

Figure 4(a) shows a typical cracking pattern observed in the piezoelectric PNNZT. The crack is usually initiated at the edge of the internal electrode and propagates obliquely to another electrode and outward of the electrode. The crack was initiated preferentially in the area(i) to the area(ii) of Fig. 2(b). At the same time, the delamination is generated on the electrode-ceramic interfaces, so as to make a final Y-shaped crack branch. This result coincides with theoretically expected electric field/stress distribution (Takahashi et al., 1983). On the contrary, in the antiferroelectric PNZST, the crack is initiated between the electrodes, grows along the center area, and branches at the electrode edge area (Fig. 4(b)). The difference of the Y-shaped crack location between the piezoelectric and the phase-change materials may be caused by the difference in the strain induction mechanism: that is, both the field-induced longitudinal and transverse strains in the antiferroelectric are expansive (i. e. the Poisson's ratio is negative) unlike the normal piezoelectric or electrostrictive material.

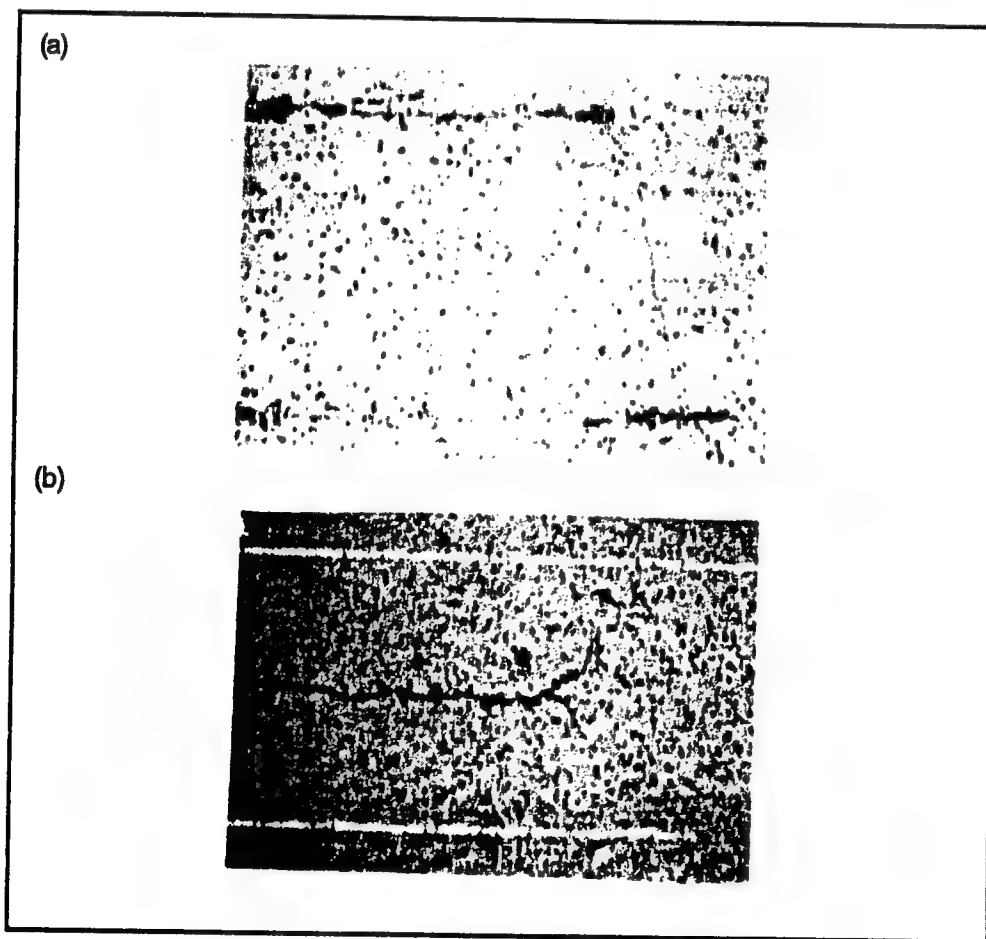


Figure 4 (a) Cracking pattern in piezoelectric PNNZT
(b) Cracking pattern in phase-change PNZST

(2) DISPLACEMENT CHANGES DURING THE DESTRUCTION

The induced strain changes are shown in Fig. 5. During the crack propagation, the magnitude of the induced strain is increased by several tens % in all samples, with rather asymmetric characteristics compared with the initial state. This enhancement is probably due to the crack opening and closing motions under the field.

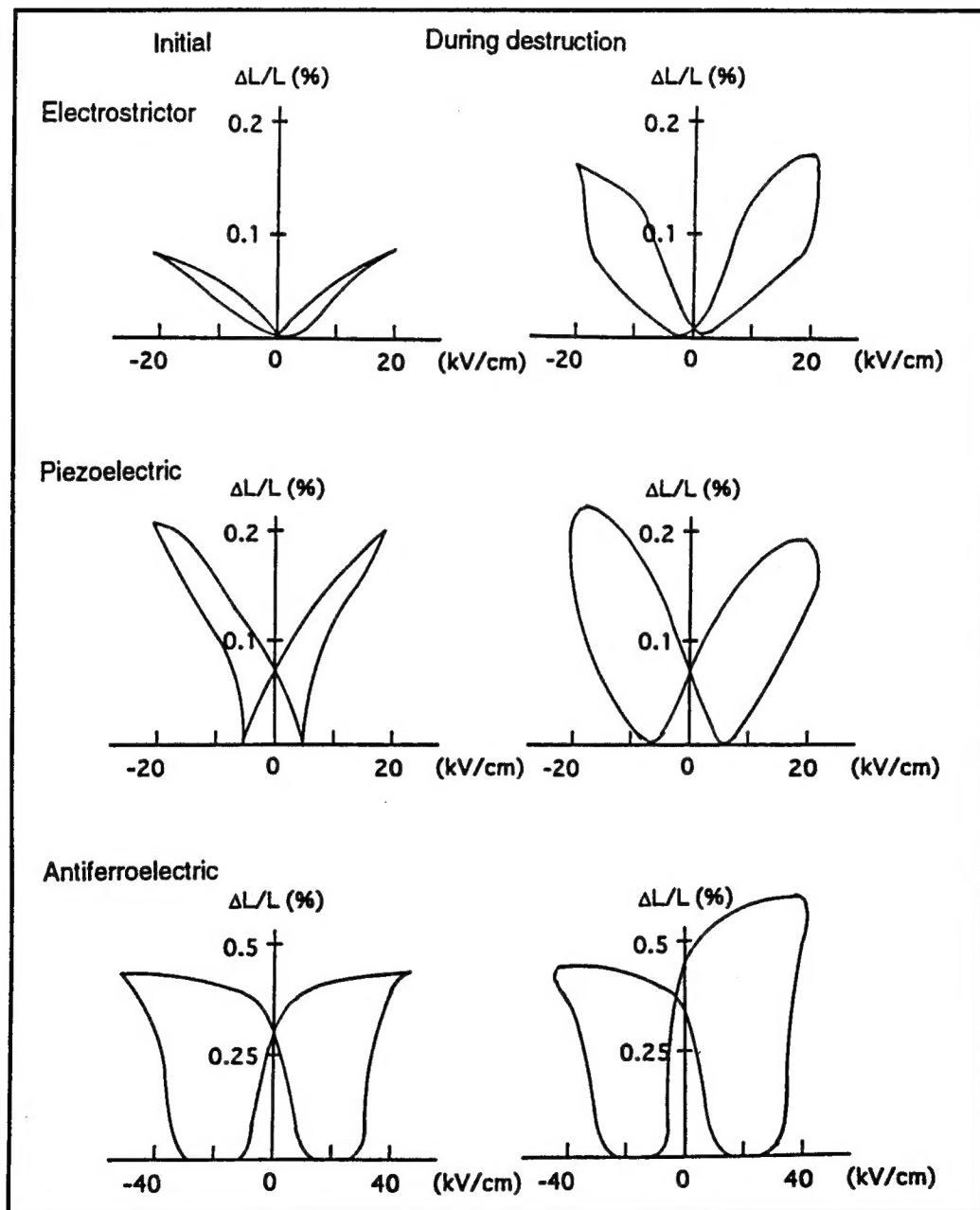


Figure 5 Induced strain change

(3) ACOUSTIC EMISSION

Figure 6 plots the AE count accumulated in one drive cycle, as a function of total driving cycle for the three samples. All the samples show a remarkable increase of the AE count during the crack propagation and leveling-off after the crack completed. The significant difference in the break down cycle (i. e. durability) among the three samples is probably attributed to the magnitude of the maximum strain; that is, 0.1% in the electrostrictor, 0.2% in the piezoelectric and 0.4 % in the antiferroelectric samples.

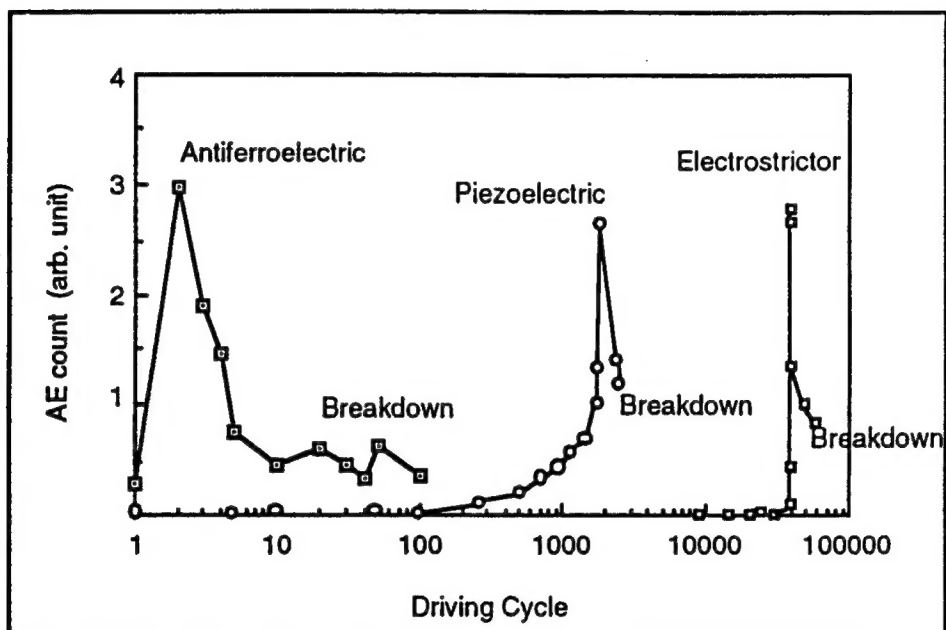


Figure 6 AE count accumulated in one driving cycle

(4) SURFACE POTENTIAL CHANGE

The surface potential change was monitored through the surface electrode. Figure 7(a) shows an example curve obtained for a piezoelectric sample during a voltage cycle, which resembles the polarization-electric field curves. The peak-to-peak surface potential is shown in Fig. 7(b) as a function of drive cycle, where the AE count is also plotted. A drastic change at the initial stage is mainly due to the reorientation of the spontaneous polarization. It is noteworthy that the surface potential drop was detected according to the crack propagation and the AE count increase. The complete crack inside the device (i. e. air gap) may decrease the surface voltage.

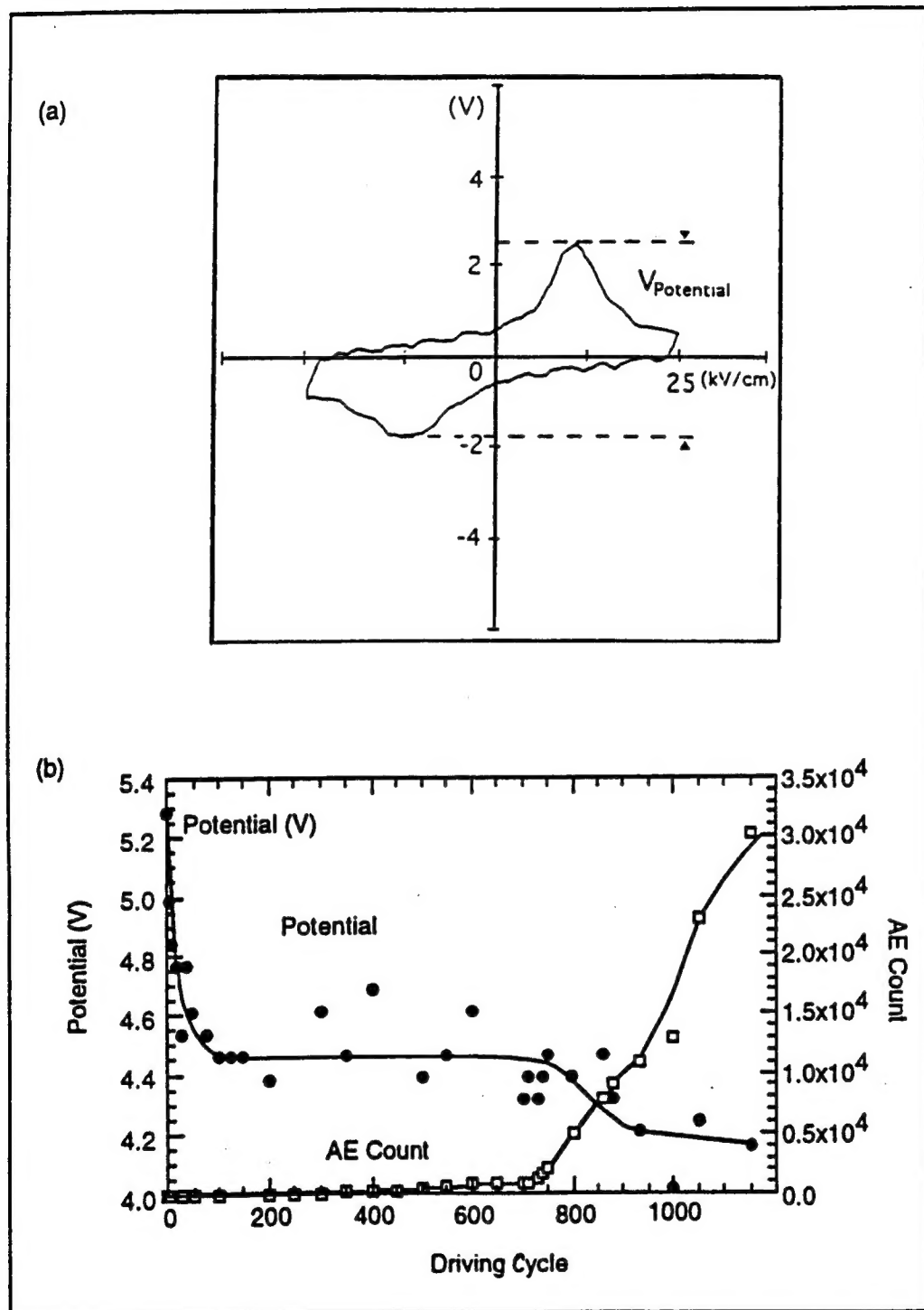


Figure 7 (a) Surface potential curve for the piezoelectric PNNZT
 (b) Peak-to-peak potential change as a function of driving cycle

CONCLUSIONS

Three different techniques were adopted to monitor the destruction of ceramic multilayer actuators: induced displacement, acoustic emission and surface potential change measurements. Enhancement in the field induced strain was observed during the crack propagation, but this is sometimes confused as thermal effect. On the contrary, drastic change in the AE count is a good predictor for the collapse of the actuator, and the surface potential monitoring will be another alternative. If the destruction symptom of the actuator is detected by one of these monitoring methods, the total actuator system will be safely stopped without causing any damages to the controlled thing..

ACKNOWLEDGEMENT

This work was supported by the Office of Naval Research through Contract No. N00014-92-J-1510.

REFERENCES

Aburatani, H. , S. Harada, A. Furuta, Y. Fuda and K. Uchino. 1993, " Destruction Mechanism in Ceramic Multilayer Actuator", Japanese Journal of Applied physics (in print)

Furuta, A. and K. Uchino. 1993, "Dynamic Observation of Crack Propagation in Piezoelectric Multilayer Actuators" Journal of American Ceramic Society, 76 (6): 1615.

Kouno, E. 1984, "A Fast Response Piezoelectric Actuator for Servo Correction of System Errors in precision Engineering" CIRP Ann., 33 (1): 369.

Moriyama, S., and Uchida, F. 1984, "Precision X-Y Stage with a Piezo-Driven Fine Table", JSPE, 50 (4): 718.

Takahashi, S., A. Ochiai, M. Yonezawa, T. Yano, T. Hamatsuki and I. Fukui. 1983, "Internal Electrode Piezoelectric Ceramic Actuator", Ferroelectrics, 50: 181.

Uchino, K. 1986, "Piezoelectric /Electrostrictive Actuators", Morikita, Tokyo, Japan.

Uchino, K. 1993, "Ceramic Actuators : Principles and Applications", Materials Research Society Bulletin, 18 (4): 42.

Yano, T. and S. Takahashi. 1988, "Utilization of Piezoelectric Stiffened Effects on Impact Printer Heads," Trans. IEICE, J71-C11: 1576.